University of Southampton
Faculty of Engineering and the Environment
Aerodynamics and Flight Mechanics Research Group

Toward a Physics Based Entrainment Model for Simulation of Helicopter Brownout

Gregory Teofil Jasion
Thesis for the degree of
Doctor of Philosophy

March 2013

UNIVERSITY OF SOUTHAMPTON

ABSTRACT

FACULTY OF ENGINEERING AND THE ENVIRONMENT
AERODYNAMICS AND FLIGHT MECHANICS RESEARCH GROUP

Doctor of Philosophy

TOWARD A PHYSICS BASED ENTRAINMENT MODEL FOR SIMULATION OF HELICOPTER BROWNOUT

by Gregory Teofil Jasion

Brownout is the name given to the degraded visual environment that can develop around a helicopter as it operates in dusty conditions. The dust cloud produced reduces visibility and makes landing the helicopter extremely difficult, there is potential for damage to the aircraft or even loss of life. This thesis works towards understanding the physical processes occurring in the generation of the dust cloud and the application of this understanding in a computational model for dust entrainment.

Current brownout simulations use empirical entrainment models originally developed for aeolian sand movement. These models use parameters fitted to experimental evidence, whilst they may recreate the dust conditions of certain scenarios there is need for a physical model that can produce accurate results for prospective aircraft or scenarios.

The physical brownout system is a multiphase system made up of particle dynamics of the scales less than a millimetre and fluid scales as large as metres. In this thesis computational modelling of particle systems, fluid systems and multiphase flow systems are used to understand how the rotor wake entrains particles.

A model scale 3D unsteady rotor simulation was performed both in and out of ground effect. The flow compares well with experimental results. The ground vortex interaction is quantified. The model scale analysis is complemented by a full scale but steady, 2D, axisymmetric rotor flow analysis. The steady flow is demonstrated to provide sufficient aerodynamic force to lift typically medium sized particles from the ground.

The Discrete Element Method is a Lagrangian particle simulation method, in this thesis it is investigated numerically and then the physical behaviour is assessed in a simulation of a probe indentation experiment. The dynamic behaviour matched the experiment well. The Discrete Element Method is recommended as a particle modelling method for a brownout modelling solution.

Modelling brownout is extremely difficult due to the range of scales involved. This thesis provides an in depth understanding of the helicopter flow field at small and large scales and the aerodynamic forces and entrainment mechanisms of particles on the ground in the wake of a helicopter.

Publications:

- G. Jasion, J.S. Shrimpton, M. Danby, and K. Takeda. Performance of numerical integrators on tangential motion of dem within implicit flow solvers. *Computers & Chemical Engineering*, 35(11):2218–2226, 2011
- G. Jasion and J.S. Shrimpton. Prediction of brownout inception beneath a full-scale helicopter downwash. *Journal of the American Helicopter Society*, 57(4):1–13, 2012
- G.T. Jasion, M. Danby, and J.S. Shrimpton. Suitability of parameters and models in the discrete element method for simulation of mesoscale powder indentation experiments. *Particle & Particle Systems Characterization*, accepted - pending reviewer corrections

Contents

List of Figures

List of Tables

Declaration of Authorship

I, Gregory Teofil Jasion, declare that the thesis entitled

"Toward a Physics Based Entrainment Model for Simulation of Helicopter Brownout"

and the work presented in the thesis are both my own, and have been generated by me as the result of my own original research. I confirm that:

- this work was done wholly while in candidature for a research degree at this University.
- no part of this thesis has previously been submitted for a degree or any other qualification at this University or any other institution.
- where I have consulted the published work of others, this is always clearly attributed.
- where I have quoted from the work of others, the source is always given. With the exception of such quotations, this thesis is entirely my own work.
- I have acknowledged all main sources of help.
- where the thesis is based on work done by myself jointly with others, I have made clear exactly what was done by others and what I have contributed myself. Appendix A is an extension of work by Tuley *et al*. [4], computational code was provided by Tuley and adapted to solve tangential forces and tangential analytical solutions by myself for this work. Appendix A contains some results from Tuley *et al*. [4], reproduced with permission, and this is clearly identified in text. Appendix C used code developed by Danby [6] for a 2D case, this was adapted for a 3D case and significantly altered for improved performance by myself, this chapter also includes some of the results of the 2D study performed by Danby [6] and some experimental results from experimental work published in [7].
- parts of this work have been published as:
  - G. Jasion, J.S. Shrimpton, M. Danby, and K. Takeda. Performance of numerical integrators on tangential motion of dem within implicit flow solvers. *Computers & Chemical Engineering*, 35(11):2218–2226, 2011
  - G. Jasion and J.S. Shrimpton. Prediction of brownout inception beneath a full-scale helicopter downwash. *Journal of the American Helicopter Society*, 57(4):1–13, 2012
  - G.T. Jasion, M. Danby, and J.S. Shrimpton. Suitability of parameters and models in the discrete element method for simulation of mesoscale powder indentation experiments. *Particle & Particle Systems Characterization*, accepted - pending reviewer corrections

Signed:
Date:

Acknowledgements

I would like to thank my supervisor John Shrimpton for his support and patience throughout the project. Thanks are also due to Glynn Thomas who became my advisor for the final year and Kenji Takeda who advised during my first year. A big thank you to Matthew Danby who helped me with my first paper and Sina Haeri who helped me with the Hartree code.

I would like to acknowledge Iridis 3, the University of Southampton's compute facility, that was used throughout the project and in particular for Chapter 4, 5 and 6. I would also like to thank the Microsoft Institute of High Performance Computing at the University of Southampton for computational facilities that were invaluable for simulations conducted in Appendix C.

My colleagues were invaluable on many fronts ensuring my sanity and helping with tips and tricks for every occasion.

A big thank you to my family, their continuing encouragement kept me going.

Nomenclature

Roman

A	area
A_i	actual fractional error
A_c	acceleration parameter
a_i	position of particle 'a' of an interacting pair
A_p	projected area of a particle
A_v	Hamaker constant
b_i	position of particle 'b' of an interacting pair
C	coefficient
c	damping coefficient
C_F	coefficient of friction
C_L	coefficient of lift
C_P	coefficient of power
C_T	coefficient of thrust
D	diameter
D_p	particle diameter
E	Young's Modulus
e	coefficient of restitution
E_i	ordered error estimator
e_{ijk}	permutation symbol
F	force
f	correction factor
f_j	fluid quantity for grid, $j = 1, 2, 3$
F_n, i	force vector in the normal direction
F_L^+	nondimensional lift force
F_t, i	force vector in the tangential direction

g	gravitational acceleration
g_i	gravitational acceleration vector
g_j	spatial discretisation function, $j = 1, 2, 3$
h	grid spacing
I_{ij}	angular inertia tensor
k	turbulent kinetic energy
k_n	normal particle stiffness
k_t	tangential particle stiffness
L	angular momentum
m	mass
M_i	moment vector
m_p	particle mass
$\dot{m}$	mass flux
m_{eff}	effective mass
m_{ratio}	mesh refinement ratio
n_i	normal vector
P	power
p	pressure
p_c	order of convergence
Q	mass flux
R	rotor radius
r	radial coordinate
r_a	contact radius of the asperity
r_c	vortex core radius
Re_{rot}	particle rotation Reynolds Number
Re_p	particle Reynolds Number
r_g	grid refinement ratio
r_p	particle radius
S	source term
s	particle surface coordinate
S_{ij}	mean rate of strain tensor
St	Stokes Number

T	thrust
t	time
t_{rev}	rotor revolution time
U	velocity
U_i	mean velocity vector
u_i	particle velocity vector
u^+	mean velocity normalised by the friction velocity
u_{rel}	relative velocity
u_*	friction velocity
u_{*i}	threshold impact velocity
u_{*t}	threshold friction velocity
u_∞	velocity far downstream
v_i	fluid velocity vector
v_{ind}	induced velocity at the rotor
x	Cartesian coordinate
x_i	position vector
y	Cartesian coordinate
y^+	non-dimensional wall distance
z	Cartesian or cylindrical vertical coordinate
z_d	rotor disk height

Greek

Γ	circulation
$\gamma_1(\phi)$	skewness of ϕ
Γ_v	circulation of tip vortex
δ	boundary layer thickness
δ_ν	eddy viscosity parameter
δ_c	cohesion overlap
δ_{ij}	Kronecker delta
δ_n	normal overlap
δ_t	tangential overlap
ϵ	rate of turbulent dissipation
η	Kolmogorov length scale

θ circumferential angle

κ von Karman constant

μ viscosity

μ_t turbulent viscosity

ν kinematic viscosity

ξ_i vortex path

ρ density

σ material surface energy

τ time scale

τ_{sh} Shields parameter

τ^*_{sh} critical Shields parameter

τ_{ref} reference wall shear stress

τ_w wall shear stress

ϕ characteristic variable

ψ wake age

Ω rotor rotation rate

ω frequency

$\omega_{f,i}$ fluid vorticity vector

ω_i angular velocity vector

Ω_{ij} rate-of-rotation tensor

Subscripts

a particle 'a' of an interacting pair

b particle 'b' of an interacting pair

B Basset force

disk rotor disk

D drag force

f fluid

Fr friction force

G gravity force

IGE In Ground Effect

i, j, k, l tensor subscripts

L kift force

M Magnus force

OGE Out of Ground Effect

P pull-off force

p particle

S Saffman force

T total force

Abbreviations

ADM Actuator Disk Method

ALM Actuator Line Method

ASM Actuator Surface Method

BTV Blade Tip Vortices

BVI Blade Vortex Interaction

DEM Discrete Element Method

FFT Fast Fourier Transform

GVI Ground Vortex Interaction

IGE In Ground Effect

NS Navier Stokes

ODE Ordinary Differential Equation

OGE Out of Ground Effect

RANS Reynolds Averaged Navier Stokes

Chapter 1

Introduction

This chapter gives a brief overview of the problem of helicopter dust entrainment, the physical processes involved and the necessity for further understanding in this topic. The aims of the thesis are stated and the structure of the thesis is explained.

1.1 Context

Brownout is the name given to the occurrence of thick clouds of dust generated by helicopters during landing and take off in dusty conditions. If the dust envelopes the helicopter the visibility of the pilot is degraded to the extent that only brown dust can be seen; the phenomenon is therefore likened to redout and blackout effects associated with high g-force manoeuvres. Whiteout is the name for the snow equivalent of brownout. Pilots attempting to land rotor craft in this degraded visual environment take a large risk; without visual cues the craft is likely to drift which could result in roll-over and the loss of the aircraft and crew. The United States Air Force reported [8] that brownout had claimed more helicopters than any other threat. It is claimed that the phenomenon cost the US military $100 million in 2006 [9]. The condition has a variety of impacts on operations including formation flying and troop insertion and generally poses an increased mission risk [10]. Brownout also has an impact on civil operations, several brownout incidents have been reported over the last few years [11].

The underlying process by which brownout occurs can be summarised as:

1. The air flow from the helicopter down wash spreads out across the ground surface.
2. The particles on the surface experience aerodynamic forces from the near ground flow.
3. The aerodynamic force on each particle must first overcome the cohesive forces and gravity that keep the particle stationary before motion begins.
4. The particle is lifted into the flow by one of several hypotheses proposed: either by an unsteady ejection event in the flow [12], by rolling and bouncing the particle off of an asperity on the surface [13] or through resonance [14].
5. The liberated particle is now acted upon by the aerodynamic forces and gravity. For larger particles saltation will probably result; that is the particle will fall back down to the surface and collide with other particles on the ground.
6. This collision can liberate further particles via two means; the first is ballistic [15], the direct transfer of kinetic energy through collision, the second is the wake of the incident particle entraining finer particles [16]. The indirect effect of displacing the larger particles is that this may expose smaller particles that were previously hidden from the flow.
7. The particle described in stage 5 will be entrained if it is small and follows the flow. The particle will still be influenced by gravity and so will drop out of the cloud if the aerodynamic forces are not strong enough to keep it entrained. The size of the particle will dictate how long it takes to fall, small particles will linger for much longer, these particles make up the majority of the visual obscuration.

The process enumerated above highlights the large range of scales involved. In this problem there are flow features defined by the rotor diameter of the order of several meters and there are particles of the order of microns reacting to the flow. Similarly modelling the mechanics of saltation and brownout inception requires the tracking of many thousands of interacting particles. Combining knowledge from the different length and time scales of the problem is one of the primary challenges of this research area.

A complete brownout simulation is one that incorporates a flow solver, to reproduce the wake from the helicopter, with a dust entrainment or flux model, to calculate how much dust leaves the ground, and a particle motion routine to calculate the progress of the particles over time. There have been a small number of complete simulations developed and they are discussed in detail in Chapter 2. These simulations use a variety of flow solving methods to

calculate the rotor wake but for the entrainment model they all use a derivative of the aeolian mass flux model developed by Bagnold [17]. Bagnold developed the model to describe the aeolian motion of desert sand with the assumptions of steady parallel flow, these assumptions are not entirely valid for a helicopter wake. The entrainment models based on this method are somewhat empirical with parameters tuned for the cases required. Whilst they may produce good results for the cases they are tuned to models of this nature cannot be relied on for *a priori* brownout assessment of speculative craft or scenarios. The current gap in the knowledge is a physics based deterministic brownout model. Creating a physics based deterministic brownout model would provide a unique research tool that is not just capable of recreating the dust clouds that are witnessed; it would enable the capacity to assess brownout behaviour at the design stage and investigate design modifications for mitigation on existing aircraft. A model of this kind would also be invaluable in simulation based training of pilots.

1.2 Aims

This study is an investigation of the brownout phenomenon and a foundation for the development of a computational model to simulate particle entrainment in helicopter flows. The project aims to:

- Approach the problem from multiple scales, ranging from the full scale helicopter flows of the order of meters to the particle-particle interactions of the order of microns.
- Investigate the fluid-particle forces and discover, for the scales of the near ground rotor wash, the dominant forces.
- Identify characteristic features of the rotor flow, how they pertain to entrainment, how they relate to the rotor that generated them and thereby create a relationship between the rotor and entrainment.
- Develop particle modelling methods to be able to simulate large systems of particles and assess their suitability for simulating the dynamics of the particle bed.

1.3 Thesis structure

This thesis investigates Brownout entrainment at several different scales and the thesis is organised to reflect this.

Chapter 2 is a comprehensive literature review. Previous studies, both experimental and numeric, attempting to understand the brownout phenomena are presented. Current state-of-the-art brownout simulations are described and their entrainment models reviewed. Entrainment models from other disciplines are also described highlighting possible features that can be utilised in the rotorwash context. At a smaller scale literature of the entrainment mechanisms of a single particle are presented followed by an overview of the current understanding of the saltation transport mechanism and how it relates to this work.

Chapter 3 explains the numerical tools that will be used throughout the fluid-dynamics chapters of this work, primarily Chapters 4, 5 and 6. The forces a particle is subjected to when moving through a fluid are gathered from the literature. The Navier Stokes (NS) equations used by numerical flow solvers are given and Reynolds Averaged NS (RANS) equations are presented for the simulations in Chapter 6. Basic flow scales are taken from a full scale helicopter experiment and used to assess the particle-fluid forces nondimensionally.

Brownout is the result of low level flight of rotorcraft and fittingly the investigation starts there with two rotorcraft flow field simulations. Chapter 4 presents the first: an unsteady 3D simulation demonstrating all the flow features and rotor tip vortices but at a reduced scale. A rotor is modelled using an actuator line method producing the classic helical wake. A further 4 simulations are conducted at different rotor heights from the ground. Features of the near wall flow field are discussed qualitatively and compared with experimental results from the literature. Quantitative assessments of the near wall flow features are made in Chapter 5 and related to entrainment. Statistical analysis of the vortex paths and wall shear stresses are performed and the decay of coherent structures in the flow is assessed. The mechanism by which vortices throw particles upwards is identified and explained in this chapter.

A second rotor flow field simulation is performed in Chapter 6 at full scale but time averaged and 2D axisymmetric. This simulation is calibrated against published experimental results of a full scale helicopter. The results provide us with real world velocity and length scales for a helicopter downwash. The particle fluid forces are applied to this flow field utilising the real world scales.

Brownout is a multiphase problem; the rotor wake discussed in detail in the previous chapters is responsible for entraining sand particles, modelling these sand particles is the subject of Chapter 7 and Appendices A & C. A common modelling method for granular systems is the Discrete Element Method (DEM) and this is defined in Chapter 3. DEM is a Lagrangian particle model, it uses numerical integrators to progress the positions of the particles. The performance of that numerical system is evaluated in Appendix A.

Before entrainment the sand particles lie in a vast bed with each particle resting in contact with a number of peers; Appendix C applies the Discrete Element Method to a similarly large system of particles. DEM practitioners calibrate the model parameters in a number of different ways commonly as bulk properties or on the scale of single particle interactions. The simulation here attempts to bridge the gap between these calibration scales by modelling a powder penetrometry experiment performed by Danby [6]. The experiment consisted of a probe driven into a pot of powder at a constant speed, the resistive forces on the probe were recorded. The force trace on the experimental probe is compared with that in the simulation. The meso-scale behaviour of particle rearrangement due to the probe has similar complexity to the process of saltation bombardment from a large bed.

The final chapter summarises the conclusions of the work presented in this thesis. Further work is suggested combining and advancing the success of simulation Chapters 4, 5, 6 and Appendix C.

Chapter 2

Review of Helicopter Brownout Modelling

Modelling brownout is difficult because it requires understanding of several physical processes over a wide scale range. This review starts with the early comprehensive models of wind blown sand, then walks through the attempts over the last 50 years to understand and model the entrainment of dust into rotor wakes. The final sections discuss entrainment models with additional features and the use of Lagrangian particles.

2.1 Why is brownout such a problem?

Helicopters have been in production for over 50 years, during this time they have been used in a number of military and civilian roles. Helicopters are inherently useful in a roles that require vertical take-off or landing (VTOL), low speed flight or hover, and landing at unprepared sites. Helicopters find use in urban transport, off-shore transport, search and rescue as well as troop deployment and attack roles. All of these operations cause an effect seldom experienced by fixed wing aircraft - the aircraft interacts with wake it has itself generated. Through training a helicopter pilot learns how to avoid hazardous situations like the vortex ring state - descending at a specific rate that results in the tip vortices in the vicinity of the blades. Brownout and whiteout, however, are environmentally dependent and somewhat unavoidable. Brownout occurs during landing and take off when fine sand or dust is entrained in the rotor wash reducing the visibility of the pilot, whiteout is caused by the entrainment of snow.

Pilots can attempt to keep ahead of the developing dust cloud by approaching the landing zone with significant forward velocity, a technique called roll-on landing, but just before the final touchdown the helicopter is enveloped in the dust. In standard landing or roll-on landing the final moment before touchdown is a dangerous moment. It is imperative that the pilot maintains heading and does not allow the aircraft to translate laterally. To be able to achieve the desired level of control the pilot will rely on visual clues such as a mark on the tarmac or a tuft of grass. During brownout, however, the visibility is greatly reduced to the point that all visual cues are obscured making landing a difficult and dangerous task.

If the dust cloud could be controlled to allow the pilot some visibility of the ground then this would make landing in dusty environments safer. Additionally, controlling the dust cloud could be used to reduce dust ingestion into engine air intakes. The capacity to model the development of a dust cloud in a brownout scenario enables the evaluation of the brownout characteristics of a device or design prior to production. The tool could also be used to: design retro-fit devices for brownout mitigation, train pilots, develop optimum landing manoeuvres or provide dust cloud data for the simulation of novel radar systems that aim to see through dust.

2.2 Wind blown sand

To begin to understand the brownout problem we look first at wind blown sand, a subject explored by Bagnold [17] during time in the Libyan desert in the 1940's and 50's. Wind transports sand using three mechanisms illustrated in Fig. 2.1:

- large particles creep (5 mm) - they are pushed along the bed by the wind and collisions from smaller airborne particles.
- medium sized particles saltate (0.5 mm) - a skipping mechanism. Sand particles leave the surface, through collision or aerodynamic forces, then are blown some distance before they collide with the bed at speed causing further saltation or creep. This process can be sustained in an equilibrium causing massive sand transport.
- small particles become suspended (5μm). They are light enough to be carried a considerable height and distance by the flow, these particles can be ejected from the ground by saltating particles or by the flow. Suspended particles are responsible for visual obscuration during brownout.

Bagnold [17] was by no means the first to observe the movement of sand by wind, however, he was the first to attempt to identify underlying principles of the process. Bagnold identified many of the challenges that still exist when studying the problem of sand entrainment, namely

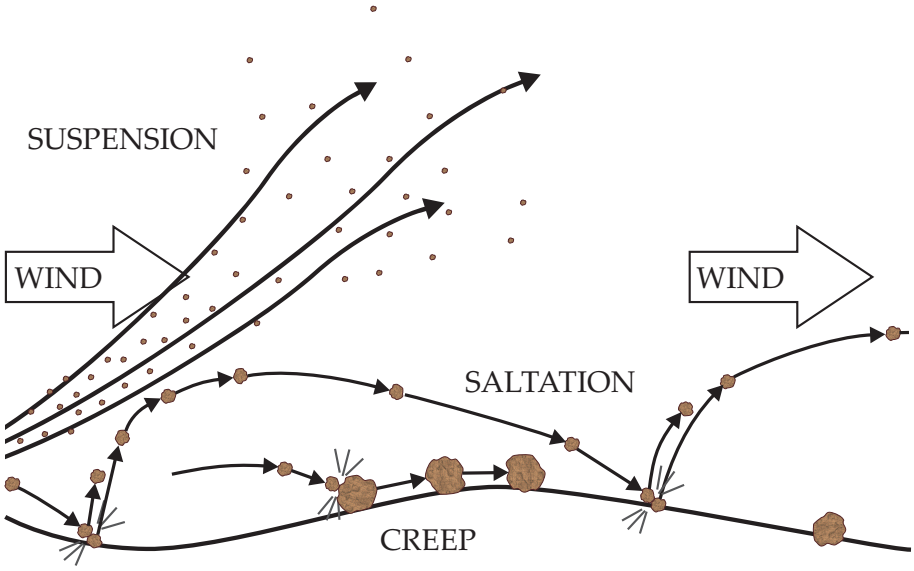

Figure 2.1: The 3 different aeolian transport mechanisms: creep, saltation and suspension. Saltating particles tend to leave the surface at a very steep angle and collide with a much shallower one [17].

the effect on the flow from carrying heavy particles in high concentration and the effect of the deformable bed surface that must affect the flow. Nevertheless Bagnold defines a series of expressions to find the transport rate of sand by wind, expressions that are still used in studies of wind blow sand in 2011 [18].

Bagnold [17] conducted observations in the natural desert and experiments in a laboratory wind tunnel observing the motion of sand grains in wind. Bagnold made several interesting observations: a static-threshold velocity exists at which sand motion begins, this is followed by a lower dynamic-threshold velocity which is the velocity required to maintain the saltation. That is to say, at wind speeds insufficient to disturb sand grains on the surface saltation is maintained by the impacts of falling particles. Bagnold discovered that the velocity profile of the air is dramatically altered by the motion of sand grains as momentum is transferred from the fluid phase to the solid phase.

Inception of sand particles by the aerodynamic forces alone, Bagnold observed, first occurs by inducing the particles to roll along the surface. Once the particles have gathered sufficient speed they then start to bounce along the surface causing saltation and a sand cloud to emerge. Particles released by saltation have a near vertical trajectory upwards and make impact at a shallow angle, illustrated in Fig. 2.1.

Sand motion was quantified by Bagnold [17]. The methodology was used by Wachspress *et al*. [19] and is included later in Section 2.6.

Iversen *et al*. [20] took the relations of Bagnold and others and sought to apply them to Martian aeolian sand transport. The dynamics of Martian sand are of little interest in this thesis, however, to relate the expressions of Bagnold to the lower density Martian atmosphere Iversen expands the expressions of Bagnold to change the significance of inter-particle forces. Iversen found that the trends Bagnold identified, relating threshold velocity to friction velocity and particle size, were not as universal as Bagnold believed. Iversen *et al*. found that the mass flux varied with particle size distribution, particle shape, and the different manifestations of inter-particle forces explored in detail in Chapter 3.

Wachspress [21] describes the difficulty of using an entrainment model from literature in a brownout context given that most aeolian entrainment models are based on 3 assumptions: 1) flat ground, 2) parallel flow, 3) steady flow. Wachspress [21] argues that helicopters always land

on flat ground and the flow nearest the wall will be parallel but the rotor wash will definitely be unsteady and full of strong vortex structures. This author believes that the flat ground assumption mentioned previously is akin to the zero pressure gradient condition familiar in flat plate boundary layers, however, an impinging jet with radial wall jet flow must have a strong pressure gradient.

2.3 Early studies of helicopter dust entrainment

An early published study by Leese of the US Army looked at helicopter 'Blast Effects' a term referring to dust cloud creation from the near ground rotor wash [22]. The study was conducted to get a better understanding of how dust, snow and foreign objects are blown into the air by the helicopter downwash.Leese [22] hoped to find a relationship between the full-scale helicopters tested and model-scale rotors used in more controlled tests, but was unable to identify scaling properties with confidence. Leese also examined using ground sheeting to prevent the dust pick-up. Leese identified the region of peak particle pick-up as one rotor diameter away from the hub.

Shortly after Rodgers [23] conducted a full scale experimental study on the dust cloud generated by helicopter down wash. Dust samplers were mounted on the fuselage of several helicopters to determine the size distribution of airborne particles for different heights of hover. The result indicate that the stronger flow, when the helicopter is closer to the ground, is capable of entraining large and small particles alike, but a weaker down wash can only entrain the smaller particles. Rodgers [23] also described the dust cloud around a helicopter as seen from another helicopter above it, he described a doughnut shaped dust cloud with a helicopter clearly visible from above but shrouded from the sides.

2.4 Impinging jets as a first approach

The time averaged flow beneath a helicopter is not dissimilar to an impinging jet. This section contains a description of the cases where experiments using jets have been conducted in an effort to better understand brownout.

Bradshaw and Love [24] conducted an experiment using an impinging jet. The jet was positioned normal to a smooth surface at a height of approximately 8 jet radii. A stagnation region forms beneath the jet, the static pressure is at a peak and a hemispherical like region of increased static pressure forms. The peak skin friction was approximately 1 jet radius from the jet centre, the edge of the free jet. This is due, Bradshaw explained, to the radial velocity peaking under the influence of the pressure gradient.

Morse and Newhouse [25] used a ducted fan to investigate the erosive effects of an impinging jet at heights between $z_d = R$ and $6R$. The ducted fan used had a very high disk loading, approximately an order of magnitude higher than a typical helicopter. A variety of soil conditions were tested for erodibility under the fan; vegetation, hard packed surfaces and wet soil showed little erosion, loose surfaces eroded rapidly.

Haehnel [26] investigated brownout by experiment using a jet impinging on a bed of loose sand. The rig used a high speed jet position directly above a large bed of sand or glass beads, the erosion of the bed was recorded. Haehnel found the mass flux to fit the model described by Eq. (2.1):

$$q = C/g(\tau_w - \tau_c) \tag{2.1}$$

where g is the gravitational constant, C is a constant with units of m^{-1}, τ_w is the wall shear stress and τ_c is the critical wall shear stress based on experimental observations or on the empirical relationship described by:

$$\tau_c = B^2 \left(\Delta\rho g d_p + \frac{C}{d_p} \right) \tag{2.2}$$

where $\Delta\rho = \rho_s - \rho_f$ the difference between particle and fluid densities, B and C are constants found from experiment to be $B = 0.1109$ and $C = 3 \times 10^{-4}$ N/m for aeolian flows. Haehnel found, by experiment, critical shear stress for glass beads and sand to be $0.059\,\mathrm{m}^2\mathrm{s}^{-2}$ and $0.15\,\mathrm{m}^2\mathrm{s}^{-2}$. Eq. (2.2) is defined for uniform parallel flow and as such is not strictly appropriate. The results also show a large variance in the results for sand, where size and shape are not as controlled as they are for glass beads, supporting evidence for saltation through initial stimulation of large particles. Haehnel concluded that it was possible to model entrainment rates if models were based on the Reynolds stresses, i.e. the turbulent fluctuations, but not on average velocity properties. The entrainment function, Eq. (2.1), could be added as the source term to a particle transport equation. A CFD solver could model the dust as an Eulerian concentration continuum. Alternatively the mass flux can be discretised to produce a number of particles to be injected into the near wall flow and then tracked using Lagrangian frame and particle-fluid forces. The main difference between this experiment and rotor based entrainment is that the rotor flow has strong vortex-ground interaction as shown by the results of Lee *et al*. [27], whilst Haehnel includes the fluctuation flow properties these are still Reynolds averaged and do not include the peak stresses from vortex events. In this project a deterministic entrainment model is sought but the results and empirical models presented by Haehnel are useful for validation.

2.5 Qualities of the rotor wake within the context of entrainment

The driving force behind the brownout condition and the entrainment process is the helicopter down wash. Here the features of the helicopter flow are described.

The helicopter flow is a 3 dimensional, highly complex, unsteady flow. The main flow features a strong axial jet and tip vortices shed by each rotor blade that are convected downwards, additional features include blade-vortex interaction; when a rotor blade travels through a tip vortex, interactions with the fuselage and flow interactions with the tail rotor [28]. A full scale helicopter tuft study by Wadcock *et al*. [29] showed that operating close to the ground adds to the complexity of the flow introducing separation and reversed flow on the fuselage and ground.

The helical vortex produced by the rotor tips break up over time. Computational work by Kenny [31] shows a clear break up of the helicopter's primary vortex filament into a multitude of smaller secondary-vortices as it interacts with the ground, in agreement with several experimental studies looking at vortex rings impacting on a wall [32, 33, 16, 34]. In each case the vortex generates secondary and even tertiary vortices as it approaches the wall and a region of higher speed flow is visible between the vortices and the ground. This region of high speed flow could be responsible for the particle entrainment. Figure 2.2 clearly shows the primary vortices sweeping across the ground, two or three are identifiable as concentric rings in the dust before the bulk separation. The photo also shows secondary features aligned with the flow, these could be secondary vortices.

The flow travelling near to the ground will develop a boundary layer. The boundary layer is host to eddy structures that transport high energy fluid to the surface and low energy fluid into

Figure 2.2: A Merlin EH101 Helicopter in a dust cloud [30]

the bulk flow. Particles respond to the flow in the boundary layer but the flow will also be effected by the presence of the particles. Particle resuspension is a result of the particle-fluid coupling on the ground plane. The boundary layer is described in more detail in Section 3.2.1.

2.5.1 Vortex ground interaction

Lee *et al*. [27] used Digital Particle Image Velocimetry (PIV) to look at the blade vortex ground interaction and the near ground velocity profile for a model rotor in ground effect. They conclude that the flow becomes an unsteady radially expanding wall jet, and that the vortex filaments shed from the rotors normally diffuse naturally when the rotor is high enough from the ground. However, when the rotor is close to the ground the filaments spread out across the surface causing them to spin up before turbulence in the wall jet quickly shears the vortices and accelerates their diffusion.

Nathan and Green [35] applied PIV to a rotor IGE both hovering and advancing in a series of wind tunnel experiments, the wind tunnel was equipped with a rolling road. Nathan and Green [35] found the wake structure results in a large recirculation ahead of the moving rotor, employing the moving ground causes the recirculation vortex to become more concentrated and closer move closer to the aircraft. A secondary effect of the tighter vortex is a strong region of opposed vorticity at the wall ahead of the recirculation zone. This shows that viscous ground—vortex interaction has a big effect on the vortex behaviour.

2.5.2 Vortex filament straining

Ramasamy and Leishman [36] studied the effects of vortex filament straining and viscous diffusion. The vortex filaments reside in the vicinity of the wake boundary and are stretched by the expansion of the wake. The tip vortex is composed of a viscous core of fluid that rotates in a solid-body like fashion and surrounded by a fluid with a swirl velocity that asymptotically reduces to zero with distance from the core. The width of the core is measured between to the two peaks in swirl velocity. Viscous diffusion causes the vortex size to grow over time and the swirl velocity to reduce, straining the filament causes the vortex to reduce in width and conservation of momentum causes it to then spin faster. For IGE rotor flows the consequences

are very interesting, as the tip vortices approach the ground they are stretched and spin faster potentially increasing entrainment.

Self induced instabilities in helical vortex structures are observed both in and out of ground effect. Several different instabilities are identified by Widnall [37] in an analytical study on helical filaments in an axial free stream. Experimental observations of helical vortex wakes in a free stream are made by Sørensen *et al*. [38], several modes of breakdown are observed. In the case of a hovering rotor the wake behaves differently, Lee *et al*. [27] found vortex pairing within a few disk diameters down stream. Vortex pairing involves neighbouring filaments moving around each other and eventually merging. Lee *et al*. continued the observations to a rotor in ground effect and found the vortex pairing effect can push some vortices very close to the ground which could also dramatically increase entrainment, this finding was confirmed by Johnson *et al*. [39].

2.5.3 Observations of dust entrainment from rotors

Gillies *et al*. [40] carried out a recent full scale experimental study measuring dust emission from low level rotor craft flight. Gillies *et al*. found that the dust emission is reduces as the forward travel speed increases, it was speculated this is due to reduced residence time over any specific location and the change in pressure distribution over the rotor as a result of the varying pitch of the blades, required for controlling the aircraft.

The Sandblaster project [41] gathered data of rotor craft dust emission including particle size and concentrations. They conclude that larger airframes, with a higher disk loading, generate the densest dust clouds and are also capable of entraining the largest particles; concentrations of fine particles are similar for all airframes.

Johnson *et al*. [39] conducted a multiphase PIV study to quantify the entrainment mechanisms for an IGE rotor flow. The study captured vortex ground interactions with fascinating results involving the flow field around the vortices themselves, stagnation bubbles and particle-vortex trapping. Johnson questions the validity of the threshold velocity dust models used in most brownout models comparing the upwash sources. The vertical flow in the turbulent boundary layer, for which the threshold velocity model was designed, is a result of only the turbulence where as an IGE rotor flow contains significant vertical flow from vortex events.

2.6 Computational models of helicopter dust entrainment

In recent years several numerical models describing the complete brownout process have been presented. Amongst the work present are models developed by Wachspress *et al*. of Continuum Dynamics [19], Phillips and Brown of Glasgow University [42], D'Andrea and Scorcelletti of Augusta Westland [43] and Syal *et al*. and Thomas *et al*. of the University of Maryland [44]Thomas *et al*. [45]. The aim of these developments is to create a complete brownout simulation package by incorporating CFD with a particle motion method and an entrainment model. A short account of each of the entrainment models used in the simulations of Wachspress *et al*. [19], Phillips and Brown [42] and Thomas *et al*. [45] is given here.

The simulation developed by Wachspress *et al*. [19] incorporates a Lagrangian tracking model with a vortex transport CFD model. The objective was to develop a deterministic real time brownout simulation. Wachspress *et al*. uses an entrainment criteria based on a threshold friction velocity, the velocity at a reference height is supplied by the CFD model this is then used to find the shear stress on the ground via a logarithmic boundary layer profile. If the friction velocity generated by the flow field is greater than the threshold the particle is put into motion.

Wachspress *et al*. used an entrainment model based on Bagnold [17] who developed a basic expression from studying movement of sand dunes. The entrainment flux is found by first

finding the threshold drag velocity, u_{*t}, and comparing it with the friction velocity. The friction velocity, u_*, is found at any point in the flow by comparing a velocity in the flow at a reference height with a velocity profile, Eq. (2.3):

$$u(y) = 5.75u_* \log\left(y/k_r\right) \tag{2.3}$$

where $u(y)$ is the horizontal flow velocity at a height y, k_r is a roughness parameter. Wachspress *et al*. use $y = 0.3$m, $k_r \simeq 1/30^{\text{th}}$ of the diameter and the sphericity accounted for with a factor of 0.75. The threshold drag velocity is found using an expression by Shao and Lu [46]:

$$u_{*t} = B\sqrt{\frac{\rho_p - \rho_f}{\rho_f} g d_p + \frac{C}{\rho_f d_p}} \tag{2.4}$$

Bagnold [17] offered values for B and C based on his observations of sand dunes, Wachspress *et al*. offers variation based on the helicopter brownout models and observations but the values are very much subjective. Bagnold observed that finer particles require a higher threshold velocity, but studies have shown that if larger particles are mixed with the fine particles then that threshold lowers significantly. The former concept is confirmed by the studies of Rodgers [23] discussed above supporting the notion of saltation of large particles as a catalyst to entrainment.

The effects of saltation are incorporated into the Wachspress *et al*. entrainment model by addition of the impact threshold, u_{*i}:

$$u\left(y\right) = 5.75u'_* \log\left(y/k'\right) + u_{*i} \tag{2.5}$$

where u'_* is the altered drag velocity, k' is the increased surface roughness and u_{i*} is the impact threshold velocity at $y = k'$. The impact threshold velocity is the velocity required at height k' to maintain saltation.

The mass flux of particles injected into the flow is given as:

$$Q = C\left(v_{ref} - u_{*t}\right)^3 \tag{2.6}$$

The flux rate, Q, is based on Eulerian models that state the mass flux is proportional to the cube of the difference between the threshold velocity and the wall tangential fluid velocity, v_{ref} at the reference height and C is a constant chosen to empirically match observations for rotor wash flow. The quantity of particles entrained per unit area is found using a particle distribution function. Once entrained the particles are carried through the flow by the drag force based on the relative velocity.

The model proposed by Wachspress *et al*. is empirical and correlates with several different data sources. This saltation model is driven by an unsteady CFD code such that the velocity values put into the the model are instantaneous. The entrainment flux expression is a macroscopic expression based on observation, there is no appreciation of how the flow interacts with the surface particles and since the expression was defined for aeolian transport the idiosyncrasies of the vortical rotor down wash are not appreciated.

The second brownout model reviewed was developed by Phillips and Brown [42]. Unlike the Wachspress *et al*. model which uses a Lagrangian approach the Phillips and Brown particle model is Eulerian. The particles are modelled as a continuum in the flow. The entrainment model is subsequently a source term, S_p, in a particle transport equation, Eq. 2.7:

$$\frac{\delta}{\delta t}\rho_p + \left(v + v_g\right) \cdot \nabla\rho_p = S_p + \nu_p \nabla^2 \rho_p + \text{other nonequilibrium terms} \tag{2.7}$$

where v is the local flow velocity, v_g is the fallout velocity due to gravity, ν_p is the particle

diffusion constant.

The source term, S_p, is a sub-model much like that of Wachspress *et al*. [19]; Phillips and Brown used a similar threshold expression to Eq. 2.4 and used wind tunnel data from Lu and Shao [47] to find values of B and C. The model is simplified to only use one roughness scale, one particle diameter and therefore has a uniform threshold velocity. A horizontal flux model, Eq. 2.8, from White [48] is used to determine the number of particles that are saltated:

$$Q = Ecv^3 \frac{\rho}{g} \left(1 - \frac{v_t}{v}\right) \left(1 + \frac{v_t^2}{v^2}\right) \tag{2.8}$$

where Q is the mass flux, E is the ratio of erodible to total surface area, $c = 0.261$ is an empirical constant, v_t is the threshold velocity calculated similarly to above, Eq. (2.4). A fraction of those are fully entrained, that fraction is determined by the clay content of the soil base. An empirical relationship gives the source term:

$$S_P = Qe^{13.4f-6.0}$$

where $f = 0.1$ is the clay fraction.

This model seems over simplified, it seems that the entrainment flux is solely dependant on the near ground velocity. The boundary layer profile is estimated using that velocity and steady parallel turbulent boundary layer theory, this may not hold during the passage of near ground vortices. The entrainment model is handled in much the same was as a wall function in a CFD code but this is developed based on the steady parallel flows from aeolian research such as Bagnold [17]. The flow features that make the rotor flow significant are ignored in the entrainment model and all saltation is assumed to happen in a fixed near wall region.

The model is validated qualitatively based on flow visualisations and footage of helicopters operating in dusty conditions and the agreement seems impressive. It is yet to be reported if the simulation can accurately model other helicopters or phenomena that were not involved in the parameter tuning process.

Perhaps the most effective simulation is that performed by Thomas *et al*. [45], the flow is modelled using a combination of the vortex wake methods and Eulerian methods to achieve excellent wake simulations. A Bagnold style entrainment mechanism is used to entrain particles which are then modelled using in the Lagrangian frame with the drag force calculated from the flow field. The simulation is performed at a model scale replicating the experimental setups of Lee *et al*. [27] and Johnson *et al*. [39], the numerical results were validated against the experiments and showed good agreement of both flow and particle motion. The 'vortex trapping' phenomenon described by Johnson *et al*. [39] was recreated by the simulation. While this method is not a full scale helicopter brownout simulation it includes many of the features and is perhaps the most validated.

The simulations of Wachspress *et al*. [19] and Phillips and Brown [42] aim to deliver an accurate brownout simulation package incorporating flow fields, dust clouds and visualisation. The parameters are tuned to the results expected such that the behaviour is now correct, the advantage is computational speed the disadvantage is that the model is probably not valid outside of the parameter window used to define it. The simulations of Thomas *et al*. [45] show great capability, the entrainment matches experiments well but there is still room for a more comprehensively resolved particle bed and physics based entrainment by fluid forces of particles from the bed. A physics based deterministic model is capable of predicting results for cases outside of the parameter fitting window, prediction can then be used in development and testing of helicopter operations or modifications to reduce the dangers of brownout operations. Further, the physics based entrainment model would be valid for all manner of industrial dry powder

multi-phase flows.

2.6.1 Alternative entrainment models

The basic aeolian saltation models do not always capture the unsteady effects or the effect of near wall vortices. Unsteady aeolian dust entrainment is investigated by Bauer *et al*. [49], Butterfield [50], Spies and McEwan [51]. In each study conditional averaging and event detection are used to consider sweep and ejection events but their results were inconclusive. Sterk *et al*. [52] found that the fluctuation events, sweeps and ejections, contribute positively and negatively to shear stress but only positively to saltation and streamwise velocity, they conclude that the driving variables are wind speed and fluctuations not shear stress as is commonly considered in the Bagnold model.

Cao [12] uses the average bursting frequency for parallel, uniform and steady turbulent flows. A bursting period relationship is related to the friction velocity $T_B = \nu T_B^+ / u_*^2$ where T_B is the bursting period and $T_B^+ = 100$ is the non-dimensional bursting period found from literature. The concept of a bursting period could be used, perhaps drawing parallels to the frequency of rotor tip vortex impacts with the ground or the turnover time of a vortex structure. Aerosols from reactor explosions were studied by Ardey and Mayinger [53]; entrainment following a sudden pressure wave is greater than the equivalent steady flow case, this supports the importance of vortical events in rotor wash entrainment.

Marchioli *et al*. [54] looked at the power of near wall turbulent events to eject particles from the surface, the power analysis focused on the boundary layer of a wavy wall. The vortical structures seen by Marchioli *et al*. reach into the shear layer and strong sweep and ejection events occur. The vortices are identified as the principle driver for particle resuspension with Stokes number being the controlling parameter. The helicopter flow may not have the same structure but it also features unsteady vortical structures, these structures could cause the particles to be entrained in like manner.

Marchioli *et al*. [54] and Cao [12] both produce entrainment functions with agreeable results in the parallel flow case, but there appears to be an absence of understanding between the single particle leaving a surface and the surface mass flux approach. A function that is capable of expressing the entrainment from a finite event whilst maintaining the capacity to integrate with a full brownout model is a likely solution for an entrainment model in such an inhomogeneous flow as that of an IGE rotor-wash.

2.6.2 Lagrangian forces acting to entrain particles

The methods described previously have applied a large scale flow system to a bulk entrainment method. The following section considers the entrainment of discrete particles by flow forces.

Substantial work has been carried out on the subject of entraining particles from surfaces. Hall [55] conducted experiments on cylinders in a wind tunnel to discover the lift forces on a wall bounded particle in a turbulent boundary layer. Smaller scales have been experimented with particles residing in the shear layer by Mollinger *et al*. [56]. Any particle on a particle bed in a flow will be affected by aerodynamic forces of lift and drag, inter-particle cohesion forces and gravity. For the particle to leave the surface the lift force must overcome gravity and adhesion to a surface or cohesion to the particles in the bed. Ziskind *et al*. [57] present an analytical solution to the entrainment of a particle positioned on top of two or three particles, they conclude that the most likely entrainment mechanism is for the particle to roll due to the drag force as the drag is much greater than the lift. Particle cohesion and resuspension are explored in more detail in Chapter 3.

Ibrahim *et al*. [58] performed experiments exploring micro particle detachment from a surface of known roughness. Ibrahim reports the detached fraction of the particles over time as the flow is accelerated. The particles sit within the viscous sublayer, defined in Chapter 3, and are sparsely arranged in a monolayer, particle sizes between 30μm and 110μm were tested. The sample of larger particles was completely detached within 5ms, the smallest sample was 80% detached by 24ms. The model derived by Ibrahim is not a saltation entrainment as the particles are sparse but shows that particles beginning the entrainment process require a threshold velocity and time. Ibrahim refers to Soltani and Ahmadi [59] who found, through direct numerical simulation, that micro particle detachment is heavily dependent on burst-sweep events in the boundary layer, these fluctuations provide extra intensity to the flow and help entrainment.

2.7 Summary

The present literature has made steps into the methods and understanding required to solve the problem of brownout, but have done so from different starting points and with different motivations. At present a deterministic physics based brownout entrainment model is not available. The entrainment model in the brownout simulations reviewed above is too generalized to support a research and development platform aiming to provide accurate dust clouds from speculative craft or environments. These entrainment models may lack the capacity to adapt to varied sand properties and they operate irrespective of the intricacies of how the rotor flow interacts with the ground plane.

Bridging Lagrangian particle simulations with a rotor flow field simulation allows a combination of the macroscopic rotor flow field with the microscopic particle bed and particle-flow forces. Particle-flow forces are reported in Chapter 3, these are applied to a full scale steady flow in Chapter 6. An unsteady rotor simulation is performed in Chapter 4, the flow results are applied to a Lagrangian particle model in Chapter 5. Chapter 7 discusses the concept of particle entrainment from a deterministically modelled particle bed.

Chapter 3

Fluid and Particle System Modelling

This thesis explores one physical system composed of two phases; the fluid phase and the solid particulate phase. This chapter explains the governing physics and the techniques used to model these phases.

The first section describes the Navier-Stokes equations (NS) that describe the fluid flow and the Lagrangian equations that govern particle motion.

In Section 3.2 the NS equations are expressed in axisymmetric coordinates and the Reynolds averaged equations that are solved in Chapter 6 are presented. Section 3.2.1 explains the $k-\epsilon$ turbulence model, this is followed by a description of turbulent boundary layers, both used in the analysis in Chapter 6.

Expressions for the forces experienced by a particle in a flow are given in Section 3.3. The inter-particle forces and methods to model particle interaction dynamics are presented in Section 3.4. The Discrete Element Method (DEM) is a technique to model large systems of particles, it is used in Appendices A and C, the framework of the DEM is defined in Section 3.4.4.

The governing equations for fluids and particles in Sections 3.1, 3.3 and 3.4 are nondimensionalised in Sections 3.5 and 3.6. Analysis of the nondimensional equations allows assessment of the importance of terms in the expression. The nondimensionalised equations are analysed in Chapter 6 in the context of a full scale rotor flow.

3.1 Governing equations of fluid and particle motion

The motion of fluids is governed by mass conservation and the Navier-Stokes equations. In an Eulerian Cartesian coordinate system the continuity equation is defined by Eq. (3.1) [60, p. 76]:

$$\frac{\partial \rho}{\partial t} + \frac{\partial}{\partial x_i}(\rho v_i) = 0 \tag{3.1}$$

where ρ is the fluid density, t is time, x_i is the position vector and v_i is the fluid velocity vector. In an incompressible flow this expression is simplified to $\left(\frac{\partial v_i}{\partial x_i}\right) = 0$. The Navier-Stokes equations are defined in Eq. 3.2 [60, p. 76]:

$$\frac{\partial}{\partial t}(\rho v_i) + \frac{\partial}{\partial x_j}(\rho v_i v_j) = \rho g_i - \frac{\partial p}{\partial x_i} + \frac{\partial \tau_{ij}}{\partial x_j} + \rho F_i \tag{3.2}$$

with

$$\tau_{ij} = \mu \left(\frac{\partial v_i}{\partial x_j} + \frac{\partial v_j}{\partial x_i} - \frac{2}{3}\delta_{ij}\frac{\partial v_l}{\partial x_l} \right) \tag{3.3}$$

where g_i is the gravity vector, p is pressure and δ_{ij} is the Kronecker delta. The terms in Eq. 3.2 from left to right are: the temporal, the convection, the gravity body force, the pressure gradient, the diffusion and the user defined body force, F_i, with units of N/kg.

The particle motion is described in the Lagrangian frame in order that the motion of each particle can be solved individually. The forces on a particle are the sum of the fluid forces, gravity and particle interaction forces, Eq. 3.4.

$$\frac{du_i}{dt} = F_{\text{fluid},i} + F_{\text{gravity},i} + F_{\text{particle},i} \tag{3.4}$$

where u_i is the particle velocity vector and $F_{\phi,i}$ is a force vector incorporating the mass of the particle with units of N/kg.

The rotational equation of motion is defined using the angular momentum equation:

$$\frac{dL_i}{dt} = M_i = e_{ijk} F_j x_k \tag{3.5}$$

where L_i is the angular momentum defined as clockwise positive, M_i is the sum of the moments, e_{ijk} is the permutation symbol and x_k is the perpendicular distance from the applied force to the centre of rotation - typically the particle radius. Then:

$$L_i = I_{ij}\omega_j \tag{3.6}$$

where I_{ij} is the angular inertia tensor and ω_j is the angular velocity. The angular inertia of a particle is orientation dependent; for a sphere, however, it is not and reduces to the scalar parameter $\frac{2}{5}mr_p^2$:

$$I_{\text{sphere},ij} = \delta_{ij}\frac{2}{5}mr_p^2 \tag{3.7}$$

We can then replace $I_{\text{sphere},ij}$ with a single scalar value and treat it similarly to the mass in the rectilinear momentum equation to yeild:

$$\frac{d\omega_i}{dt} = M_i \tag{3.8}$$

where the units for $M_{\phi,i}$ are N/kgm.

3.2 Axisymmetric and Reynolds averaged flow equations

In Chapter 6 a simple flow simulation was implemented to obtain a downwash velocity field, the simulation performed was incompressible, steady, 2D axisymmetric and non-swirling. The axial, radial and swirl coordinate directions are indicated by z, r and θ respectively with corresponding velocities v_z, v_r and v_θ. For 2D steady axisymmetric non-swirling flows the mass continuity equation is given as [60, p. 76]:

$$\frac{1}{r}\frac{\partial(\rho r v_r)}{\partial r} + \frac{\partial(\rho v_z)}{\partial z} = 0 \tag{3.9}$$

The instantaneous conservation of momentum equations for 2D steady axisymmetric geometries, from Schlichting [60, p. 79], are for the axial direction:

$$\rho\left(v_r\frac{\partial v_z}{\partial r} + v_z\frac{\partial v_z}{\partial z}\right) = F_z - \frac{\partial p}{\partial z} + \frac{1}{r}\frac{\partial r\tau_{rz}}{\partial r} + \frac{\partial \tau_{zz}}{\partial z} \tag{3.10}$$

and in the radial direction:

$$\rho\left(v_r\frac{\partial v_r}{\partial r} + v_z\frac{\partial v_r}{\partial z}\right) = F_r - \frac{\partial p}{\partial r} + \frac{1}{r}\frac{\partial r\tau_{rr}}{\partial r} + \frac{\partial \tau_{rz}}{\partial z} - \frac{\tau_{\theta\theta}}{r} \tag{3.11}$$

where the viscous stresses, τ_{ij} are:

$$\begin{aligned}
\tau_{rr} &= \mu\left(2\frac{\partial v_r}{\partial r}\right)\\
\tau_{\theta\theta} &= \mu\left(2\frac{v_r}{r}\right)\\
\tau_{zz} &= \mu\left(2\frac{\partial v_z}{\partial z}\right)\\
\tau_{rz} &= \mu\left(\frac{\partial v_z}{\partial r} + \frac{\partial v_r}{\partial z}\right)
\end{aligned} \tag{3.12}$$

Reynolds decomposition is a method of representing the instantaneous velocity field, v_i, by separating the mean velocity field, $\overline{V_i}$, from the fluctuations: $v_i' = v_i - \overline{V_i}$. The mean of the fluctuations is zero but the mean of the covariances or Reynolds stresses is not zero, $\overline{v_i'v_j'} \neq 0$. The Reynolds averaged mass continuity equation for the 2D non-swirling axisymmetric flow is then found through substitution of $v_i = \overline{V_i} + v_i'$ into Eq. 3.9 and averaging over time:

$$\frac{\partial \overline{V_z}}{\partial z} + \frac{1}{r}\frac{\partial}{\partial r}\left(r\overline{V_r}\right) = 0 \tag{3.13}$$

The Reynolds averaged momentum conservation equations for 2D non-swirling axisymmetric flows [61, p. 110] are: for the axial direction:

$$\begin{aligned}
\frac{\partial}{\partial z}(\rho\overline{V_z}\,\overline{V_z}) + \frac{\partial}{\partial z}(\rho\overline{v_z'^2}) + \frac{1}{r}\frac{\partial}{\partial r}(r\rho\overline{V_z}\,\overline{V_r}) + \frac{1}{r}\frac{\partial}{\partial r}\left(r\rho\overline{v_r'v_z'}\right) &= -\frac{\partial \overline{P}}{\partial z} + \frac{\partial}{\partial z}\left[\mu\left(2\frac{\partial \overline{V_z}}{\partial z}\right)\right]\\
&\quad + \frac{1}{r}\frac{\partial}{\partial r}\left[r\mu\left(\frac{\partial \overline{V_z}}{\partial r} + \frac{\partial \overline{V_r}}{\partial z}\right)\right] + F_z
\end{aligned} \tag{3.14}$$

and for the radial direction:

$$\frac{\partial}{\partial z}(\rho\overline{V_z}\,\overline{V_r}) + \frac{\partial}{\partial z}(\rho\overline{v_z' v_r'}) + \frac{1}{r}\frac{\partial}{\partial r}(r\rho\overline{V_z}\,\overline{V_z}) + \frac{1}{r}\frac{\partial}{\partial r}(r\rho\overline{v_r'^2}) = -\frac{\partial\overline{P}}{\partial r} + \frac{1}{r}\frac{\partial}{\partial z}\left[r\mu\left(\frac{\partial\overline{V_r}}{\partial z} + \frac{\partial\overline{V_z}}{\partial r}\right)\right] + \frac{1}{r}\frac{\partial}{\partial r}\left[r\mu\left(2\frac{\partial\overline{V_r}}{\partial r}\right)\right] - 2\mu\frac{\overline{V_r}}{r^2} + F_r \quad (3.15)$$

where F_z, F_r are the external body forces, μ is the dynamic viscosity and $\overline{P}$ is the average static pressure.

3.2.1 Turbulence model

Turbulence broadly refers to the unsteady fluctuations in a flow field, these range from very large scale eddies in the flow down to the smallest scales where fluid viscosity converts the kinetic energy of these fluctuations into heat. Turbulence is characteristically unsteady but overall the statistics of the flow can be characterised as stationary if there is a steady mean flow. The flow can be separated into steady and fluctuating components, as in Reynolds decomposition, $v_i' = v_i - \overline{V_i}$.

The $k-\epsilon$ model

The $k-\epsilon$ model provides approximations of the turbulent energy, k, and the rate of turbulent dissipation, ϵ. If the instantaneous flow velocity is described as $v_i = \overline{V_i} + v_i'$, then the turbulent kinetic energy is $k = \frac{1}{2}\left(\overline{v_i' v_i'}\right)$. The dissipation rate, ϵ, is defined as $\epsilon = 2\nu\overline{e_{ij}' e_{ij}'}$ where e_{ij}' is the fluctuating component of the rate of deformation tensor and ν is the kinematic viscosity. The model works by accounting for the transfer of energy from the mean flow to the turbulent kinetic energy and through to viscous dissipation, in words the equation for the transport of k or ϵ is:

Rate of change of k or ϵ	+	transport of k or ϵ by convection	=	transport of k or ϵ by diffusion	+	Rate of production of k or ϵ	-	Rate of destruction of k or ϵ

The calculated values of k and ϵ can be used to give velocity and length scales, ϵ is the dissipation rate and is therefore associated with the smallest eddies but because energy in largest eddies is assumed to cascade through to the smallest scales the energy is balanced. Therefore ϵ can be used to find the length scale of the larger eddies which extract energy from the mean flow:

$$v_{\text{turb}} = k^{\frac{1}{2}} \qquad l_{\text{turb}} = \frac{k^{\frac{3}{2}}}{\epsilon} \quad (3.16)$$

The time scale of the larger eddies, the turn over time, can then be defined as:

$$\tau = \frac{k}{\epsilon}$$

The characteristic scales of the smallest eddies are the Kolmogorov scales, the Kolmogorov length scale is:

$$\eta \equiv \left(\frac{\nu^3}{\epsilon}\right)^{1/4} \quad (3.17)$$

the time and velocity scales follow:

$$\tau_\eta \equiv \left(\frac{\nu}{\epsilon}\right)^{1/2}$$

$$v_\eta \equiv (\nu\eta)^{1/4}$$

The $k-\epsilon$ model is a popular and widely used turbulence model but assumes that the Reynolds stresses are a function of the mean flow gradients, this is convenient for the calculation but is not always true in high strain regions and near the stagnation point.

The realizable $k-\epsilon$ model

To model the turbulence in Chapter 6 the two equation realizable $k-\epsilon$ model was chosen. Unlike the traditional $k-\epsilon$ model the realizable version has noticeable improvements for flows with vorticity and rotation over the standard $k-\epsilon$ model and performs better where there are regions of high shear or stagnation. It was anticipated that the jet flow modelled here will have stagnation and high levels of vorticity. The model is realizable because "the eddy viscosity formulation is based on the realizability constraints; the positivity of normal Reynolds stresses and the Schwarz' inequality for turbulent shear stresses"[62]. Shih [62] originally derived the model to solve the axisymmetric jet anomaly, a known weakness of the standard $k-\epsilon$ model, the model has also been validated for a number of other flow cases. The case modelled here would suffer the same anomaly with the traditional $k-\epsilon$ model.

The k equation in 2D axisymmetric coordinates is:

$$\frac{\partial}{\partial z}(\rho k\overline{V_z}) + \frac{1}{r}\frac{\partial}{\partial r}(r\rho k\overline{V_r}) = \frac{\partial}{\partial z}\left[\left(\mu + \frac{\mu_t}{\sigma_t}\right)\frac{\partial k}{\partial z}\right] + \frac{1}{r}\frac{\partial}{\partial r}\left[\left(\mu + \frac{\mu_t}{\sigma_t}\right)\frac{\partial k}{\partial r}\right] + G_k - \rho\epsilon + S_k \quad (3.18)$$

where S_k is the source term and G_k in axisymmetric coordinates is:

$$G_k = -\rho\left[\left(\overline{v_z'v_z'}\frac{\partial\overline{V_z}}{\partial z} + \overline{v_z'v_r'}\frac{\partial\overline{V_r}}{\partial z}\right) + \left(\overline{v_r'v_z'}\frac{1}{r}\frac{\partial}{\partial r}\left(r\overline{V_z}\right) + \overline{v_r'v_r'}\frac{1}{r}\frac{\partial}{\partial r}\left(r\overline{V_r}\right)\right)\right]$$

The dissipation rate, ϵ, in 2D axisymmetric coordinates is modelled as:

$$\frac{\partial}{\partial z}(\rho\epsilon\overline{V_z}) + \frac{1}{r}\frac{\partial}{\partial r}(r\rho\epsilon\overline{V_r}) = \frac{\partial}{\partial z}\left[\left(\mu + \frac{\mu_t}{\sigma_t}\right)\frac{\partial\epsilon}{\partial z}\right] + \frac{1}{r}\frac{\partial}{\partial r}\left[r\left(\mu + \frac{\mu_t}{\sigma_t}\right)\frac{1}{r}\frac{\partial}{\partial r}(r\epsilon)\right] + \rho C_1 S_\epsilon - \rho C_2\frac{\epsilon^2}{k+\sqrt{\nu\epsilon}} + S_\epsilon \quad (3.19)$$

where S_ϵ is the dissipation rate source term.

The realizable model uses the same eddy viscosity expression as other $k-\epsilon$ models:

$$\mu_t = \rho C_\mu\frac{k^2}{\epsilon}$$

but differs from other $k-\epsilon$ models because C_μ is not constant, instead it is dependant on the rate of rotation, strain and turbulent fields:

$$C_\mu = \frac{1}{A_0 + A_s\frac{kV^*}{\epsilon}}$$

where

$$V^* \equiv \sqrt{S_{ij}S_{ij} + \widetilde{\Omega}_{ij}\widetilde{\Omega}_{ij}}$$

and

$$\widetilde{\Omega}_{ij} = \overline{\Omega_{ij}}$$

where $\overline{\Omega_{ij}}$ is the mean rate of rotation tensor when viewed in a rotating reference frame with angular velocity:

$$\overline{\Omega_{ij}} = \frac{1}{2}\left(\frac{\partial \overline{V_r}}{\partial z} - \frac{\partial \overline{V_z}}{\partial r}\right)$$

The constants A_0 and A_s are:

$$A_0 = 4.04, \quad A_s = \sqrt{6}\cos\phi$$

$$\phi = \frac{1}{3}\cos^{-1}(\sqrt{6}W), \quad W = \frac{S_{ij}S_{jk}S_{ki}}{\widetilde{S}^3}, \quad \widetilde{S} = \sqrt{S_{ij}S_{ij}}, \quad S_{ij} = \left(\frac{\partial v_j}{\partial x_i} + \frac{\partial v_i}{\partial v_j}\right)$$

where S_{ij}, mean rate of strain tensor, is expressed in axisymmetric coordinates as:

$$S_{ij} = \frac{1}{2}\left(\frac{\partial \overline{V_z}}{\partial z} + \frac{\partial \overline{V_r}}{\partial z} + \frac{1}{r}\frac{\partial}{\partial r}\left(r\overline{V_z}\right) + \frac{1}{r}\frac{\partial}{\partial r}\left(r\overline{V_r}\right)\right)$$

The model constants used in Eq. 3.18 and 3.19 are:

$$C_{1\epsilon} = 1.44, \quad C_2 = 1.9, \quad \sigma_k = 1.0, \quad \sigma_\epsilon = 1.2$$

The boundary conditions for the $k-\epsilon$ model are:

- outlet or axis: $\partial k/\partial n = 0$ and $\partial \epsilon/\partial n = 0$
- walls: a wall treatment must be used. If the near wall mesh resolution is very good, $y^+ \approx 1$, then the standard turbulence models can be applied to this region with good result. If the nearest mesh cell is somewhat larger, e.g. $y^+ \approx 30$, then the viscous region is not resolved and a wall function must be used. The wall function is composed of a mean velocity formulation functions for the turbulent properties [63].

At the axis boundary the Fluent solver assumes the value in the adjacent cell. The wall treatment used in this case was the two layer model [64] which is sensitised to the pressure gradient. The two layer model divides the near wall region into a fully turbulent region and a viscosity affected region, the boundary between these regions is given by:

$$\mathrm{Re}_y \equiv \frac{\rho y\sqrt{k}}{\mu} = 200$$

In the viscous-affected region, $\mathrm{Re}_y < 200$, k is calculated as normal but the viscosity is computed from $\mu_t = \rho C_\mu l_{mu}\sqrt{k}$ where the length scale is computed with $l_\mu = yC_l^*\left(1 - e^{-\mathrm{Re}_y/A_\mu}\right)$. For ϵ we use $\epsilon = k^{3/2}/l_\epsilon$ where the length scale is computed from $l_\epsilon = yC_l^*\left(1 - e^{-\mathrm{Re}_y/A_\epsilon}\right)$. The constants take the values: $C_l^* = \kappa C_\mu^{-3/4}$, $\quad A_\mu = 70$, $\quad A_\epsilon = 2C_l^*$ [65].

Turbulent boundary Layers

A simple overview of the turbulent boundary layer is presented. In a viscous flow over a surface the no-slip condition will cause a boundary layer to be manifest. In a steady uniform flow the boundary layer will grow and eventually trip from laminar to turbulent, this can occur earlier if there are roughness elements or an adverse pressure gradient. The fully turbulent boundary layer has several sublayers, they can be characterised by the nondimensional height parameter y^+, defined as:

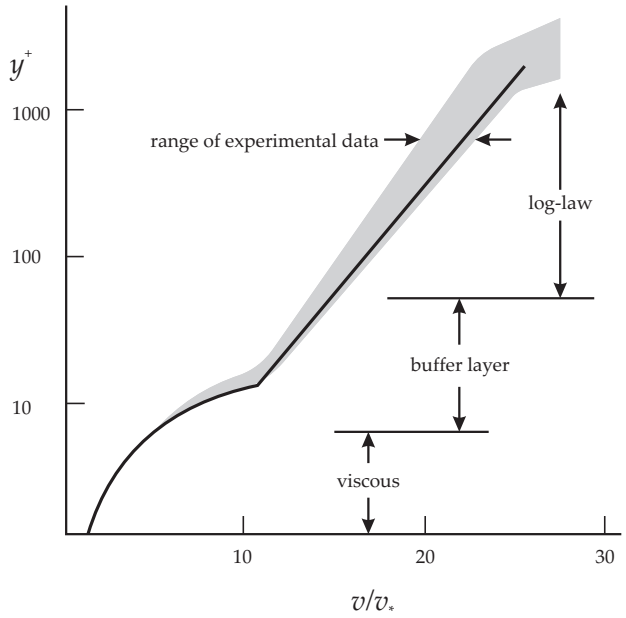

Figure 3.1: Velocity distribution of the turbulent boundary layer, the grey area represents the experimental error [66].

$$y^+ \equiv \frac{v_* y}{\nu} \tag{3.20}$$

where y is the normal distance from the wall, ν is the kinematic viscosity and v_* is the friction velocity:

$$v_* = \sqrt{\frac{\tau_w}{\rho_f}} \tag{3.21}$$

where τ_w is the wall shear stress, Eq. 3.22.

$$\tau_w = \mu_f \frac{\delta v_r}{\delta z}_{\text{wall}} \tag{3.22}$$

where μ_f is the viscosity of air, $\frac{\delta v_r}{\delta z}_{\text{wall}}$ is the radial velocity gradient at the wall. A nondimensional velocity related to y^+ in the boundary layer is, in its general form, $v^+ = \frac{V}{v_*}$, where V is the local free stream velocity.

The first sublayer is the viscous sublayer: $v^+ = y^+$, this layer is very thin $y^+ < 5$. The flow is dominated by viscous shear, the flow velocity tends to zero at the wall as do the size of the eddies. The relationship between the distance from the wall and the velocity is linear. In the log-law layer: $(30 < y^+ < 500)$ both the viscous effects and the inertial effects are important and the velocity is given by:

$$v^+ = \frac{1}{\kappa} \ln y^+ + B \tag{3.23}$$

where κ is the von Karman constant and $B = 5.5$. In the buffer layer, $(5 < y^+ < 30)$, neither expression is entirely accurate but a midpoint of $y^+ = 11$ is usually used to divide the buffer region between the viscous sublayer and the log-law layer.

The outer layer, $0.02 < \frac{y}{\delta} < 0.2$, is inertia dominated though still within the boundary layer. Another log relationship $\frac{V_{max} - V}{v_*} = \frac{1}{\kappa} \ln\left(\frac{y}{\delta}\right) + C$, where C is a constant, takes the velocity asymptotically to free stream at $y = \delta$.

In three dimensional turbulence eddies exist at scales as large as the characteristic of their cause for example the width of a bluff body and as small as the Kolmogorov scale, defined by the

viscous dissipation of turbulence by fluid viscosity. The scales of those eddies are particularly important when concerned with particle-fluid forces and entrainment, discussed in more detail in Chapter 6. In a radially expanding flow, such as would be found around an impinging jet, the developing boundary layer will decelerate as it expands, effectively an adverse pressure gradient, which can cause early separation. As a result the rate of development of the boundary layer in the longitudinal direction will be higher than that of a 2D planar boundary layer.

3.3 Particle-fluid forces

In this section the forces experienced by a particle in a fluid with relative velocity are presented. First the original expressions valid for creeping flow are presented and then each force is presented in detail with the correction coefficients that extend their usage to faster flows with higher $\mathrm{Re_p}$, Eq. 3.28.

In 1885 Boussinesq [67] detailed an expression for the transient hydrodynamic force on a sphere in creeping flow conditions ($\mathrm{Re} \ll 1$). Three years later Basset [68], seemingly independent of Boussinesq, produced an identical expression. This expression has come to be known as the 'Boussinesq Basset equation' to describe the motion of a sphere in a creeping flow.

$$F(t) = \text{drag} + \text{added mass force} + \text{Basset force} \tag{3.24}$$

$$F(t) = -6\pi r_p \mu_f \left|u_i - v_i\right| - \frac{1}{2} m_f \frac{\mathrm{d}\left|u_i - v_i\right|}{\mathrm{d}t} - 6r_p^2 \sqrt{\pi\, \mu_f \rho_f} \int_0^t \frac{\frac{d}{d\tau}\left|u_i - v_i\right|}{\sqrt{t-\tau}} \mathrm{d}\tau \tag{3.25}$$

where u_i is the velocity of the particle, v_i is the velocity of the fluid, m_f is the mass of fluid of the same volume as the sphere, μ_f is the dynamic viscosity of the fluid and r_p is the radius of the particle.

The force is composed of three parts, the first is commonly known as Stokes drag, the second is the added mass term proposed by Poisson [69] and the third term is the history term or 'Basset force', associated with the development of the boundary layer and wake [70].

Since the creation of this expression the terms have been extended to larger ranges of Re, typical in real world examples, and the additional force expressions due to shear, rotation and the influence of walls on these forces have been described. Summing all these forces produces the equation of motion for a particle in a fluid:

$$\frac{\mathrm{d}u_i}{\mathrm{d}t} = F_{D,i} + F_{A,i} + F_{B,i} + F_{M,i} + F_{S,i} + F_{G,i} \tag{3.26}$$

where the forces, $F_{\phi,i}$, are identified by their subscripts; D is drag, A is the added mass, B is the Basset force, M is the Magnus force, S is the Saffman lift force and G is the gravity force. Forces, $F_{\phi,i}$, have the units N/kg .

Of these forces only the Magnus force produces a torque on the particle. The rotational equation of motion is defined as:

$$\frac{d\omega_i}{dt} = M_{M,i} \tag{3.27}$$

where $M_{M,i}$ is the moment from the Magnus effect, the units of $M_{M,i}$ are N/kgm.

3.3.1 Particle characterisation

Before defining the particle forces it is important to identify the particle characterisation parameters: Reynolds number, Stokes number and the Froude number. The Reynolds number is

a familiar flow parameter that indicates the ratio of inertial to viscous flow forces, particle Reynolds number is defined as:

$$\mathrm{Re_p} = \frac{\rho_f d_p \left| u_i - v_i \right|}{\mu_f} \tag{3.28}$$

where ρ_f is the fluid density, d_p is the particle diameter, u_i is the particle velocity, v_i is the fluid velocity and μ_f is the fluid dynamic viscosity.

The Stokes number parameter is the ratio of characteristic time scales of the particle, τ_p , to the time scales of the fluid, τ_f. The Stokes number indicates how well a particle will follow specific flow features: a high Stokes number, $\tau_p \gg 1$, indicates the particle is unreactive to this flow and a Stokes number close to unity, $\tau_p \approx 1$, or lower predicts the particle will follow the flow very closely.

$$\mathrm{St} = \frac{\tau_p}{\tau_f} \tag{3.29}$$

where τ_p is the particle relaxation time given by Eq. 3.30.

$$\tau_p = \frac{\rho_p D_p^2}{18 \mu_f} \tag{3.30}$$

The Froude number is the ratio of inertia to weight forces and is often used in hydrodynamic scenarios:

$$\mathrm{Fr} = \sqrt{\frac{g_0 x_0}{u_0^2}} \tag{3.31}$$

These characteristic parameters are used throughout definition and description of the particle force expressions.

3.3.2 Drag

Drag is the term for the resistive force encountered when a fluid passes around a body, it is generally expressed as:

$$F_{D,i} = \frac{1}{2} \frac{C_D A_p \rho_f}{m_p} \left(u_i - v_i \right) \left| u_i - v_i \right| \tag{3.32}$$

where C_D is the drag coefficient and A_p is the projected area of the particle. The drag coefficient varies with the particle Reynolds number, Eq. 3.28. The drag coefficient, C_D, is first defined for Stokes flow where $\mathrm{Re_p} \ll 1$:

$$C_D = \frac{24}{\mathrm{Re_p}} \tag{3.33}$$

Schiller and Neumann [71] proposed a correction for C_D that is valid for $\mathrm{Re_p} < 800$ this was later validated by Bagchi [72]:

$$C_D = \frac{24}{\mathrm{Re_p}} (1 + 0.15 \mathrm{Re_p}^{0.687}) \tag{3.34}$$

3.3.3 Basset force

The 'history term' or Basset force describes the time taken for a wake and boundary layer to develop on a particle undergoing relative acceleration. Events such as the particle rapidly coming to a halt or reversing its direction would cause the particle to travel through its own wake altering the force on the particle. Particles respond to fluctuations in the fluid in a similar

way; the Stokes number is the ratio of characteristic time scales of the particle to the fluid, Eq. 3.29. It is important to note the acceleration term is relative to the fluid, $\mathrm{d}u_{\mathrm{rel}}/\mathrm{d}t$, so for $\mathrm{St} \gg 1$ in a highly turbulent fluid the accelerations relative to the fluid could be very large indeed as the flow changes rapidly relative to the particle, but for $\mathrm{St} \ll 1$ the opposite is true.

In the context of down wash, there are a variety of flow conditions. There are highly turbulent regions, strong wall jet like regions, stagnation regions, strong velocity and pressure gradients and vorticity. Attempting to generalise a particle in this entire flow in terms of $\mathrm{Re_p}$ or St is not easy, though the following events are significant:

- Full entrainment (from stationary on the wall to moving with the fluid) will see the particle under go very large accelerations, from rest on the surface to full entrainment into the flow with velocity of the order of $10\mathrm{ms}^{-1}$

- Once entrained in the flow field the Stokes number, St, is an indicator of the likely fluid-relative-accelerations of the particle.

The original Basset force can be expressed as:

$$F_{B,i} = 6\frac{r_p^2}{m_p}\sqrt{\pi\rho_f\mu_f}\int_0^t \frac{1}{\sqrt{t-\tau}}\frac{\delta(u_i - v_i)}{\delta\tau}\mathrm{d}\tau \tag{3.35}$$

where $t - \tau$ is the time since the last acceleration. Modifications have been proposed by Odar and Hamilton [73] introducing a coefficient to account for acceleration, Eq. 3.36:

$$C_B = 2.88 + \frac{3.12}{(0.12 + A_c)^3} \tag{3.36}$$

$$A_c = \frac{|u_{\mathrm{rel}}|^2}{2r_p\frac{d|u_i - v_i|}{dt}}$$

where A_C is the acceleration number. Tsuji et al. [74] confirmed the result by Odar and Hamilton [73] for $\mathrm{Re}_p < 16000$ in an extensive gas-solid experimental study.

Reeks and McKee [75] offer a correction for the case where there is some initial velocity, Eq. 3.37, the Basset history force can then be expressed as:

$$F_{B,i} = 6\frac{C_B r_p^2}{m_p}\sqrt{\pi\rho_f\mu_f}\left[\int_0^t \frac{1}{\sqrt{t-\tau}}\frac{\delta(u_i - v_i)}{\delta\tau}\mathrm{d}\tau + \frac{(u_i - v_i)_0}{\sqrt{t}}\right] \tag{3.37}$$

where $(u_i - v_i)_0$ is the initial relative velocity. Many studies will ignore Basset force using a justification that it is negligible if the accelerations are small or the density ratio is large. Dorgan & Loth [76] introduce their work on the history force as only important where particle motion is dominated by the drag force, and is susceptible to high periods of acceleration. Furthermore they quote Armenio & Fiorotto [77] who claim that the history force is only significant for density ratios of order 1 and below. Johnson [78] presents the ratio of Basset force to Stokes drag and shows that the Basset force is negligible when the fluid density is much lower than the particle density. In this case the density ratio is large and the drag force is dominant, however, the turbulent nature of the flow means high accelerations are to be expected.

Integrating the time history can be a strain on computational resources for large systems. There are several proposed methods to reduce the cost, for example a time truncation system proposed by Dorgan [76].

3.3.4 Transverse forces

Shear and rotation in the flow field cause transverse forces on particles in the flow, sometimes referred to as the Faxen terms. A relative rotation gives rise to the Magnus force and a shear gradient contributes to the Saffman force.

Magnus Force

Relative rotation gives a force much like swing on a cricket ball, this is due to the relative slip velocities on opposite sides of the particle producing a pressure difference, an effect known as the Magnus lift force. The original expression derived by Magnus is given as:

$$F_{M,i} = \frac{\pi r_p^3 \rho_f}{m_p} e_{ijk} \Omega_j (u_k - v_k) \tag{3.38}$$

where Ω_j is the relative rotational velocity of the particle with respect to the fluid. The force is orthogonal to the plane defined by the axis of rotation and the relative velocity.

The effect is said to be significant for $\mathrm{Re_p} \gg 1$, [70, p. 193], but the original expression is only valid for creeping flows. Work has been carried out on correction factors to give an expression for the force at larger $\mathrm{Re_p}$ [70, p. 193], the extended expression is presented here, Eq. 3.39:

$$F_{M,i} = \frac{1}{2} \frac{1}{m_p} C_{L,M} \rho_f A \left| u_l - v_l \right| \frac{e_{ijk} \Omega_j (v_k - u_k)}{|\Omega_l|} \tag{3.39}$$

where $C_{L,M}$ is the Magnus correction coefficient. The correction coefficient is given by Oesterle and Bui-Dinh [79]:

$$C_{L,M} = 0.45 + \left(\frac{\mathrm{Re_{rot}}}{\mathrm{Re_p}} - 0.45 \right) \exp\left(-0.05684 {\mathrm{Re_{rot}}}^{0.4} {\mathrm{Re_p}}^{0.3} \right), \quad \mathrm{Re_{rot}} < 140 \tag{3.40}$$

where $\mathrm{Re_{rot}}$ is the Reynolds number based on the rotation of the sphere:

$$\mathrm{Re_{rot}} = \frac{\rho_f \left| \Omega_i \right| d_p^2}{\mu_f}$$

The rotation of the fluid relative to the particle will cause rotation of the particle, the Magnus effect also describes moments on the particle, White and Schultz [48] expressed this in the 2 dimensional case as:

$$M_M = \pi \mu \frac{D_p^3}{I} \left(\omega - \frac{1}{2} \frac{\partial u}{\partial y} \right) \tag{3.41}$$

Rubinow and Keller [80], calculated the integral of the torque, $e_{ijk} r_j F_{M,k}$, over the surface of the sphere to obtain this expression for the total moment:

$$M_{M,i} = -8\pi\mu \frac{r_p^3}{I} \Omega_i \left[1 + o(\mathrm{Re_p}) \right] \tag{3.42}$$

where the symbol o means $o\left(\mathrm{Re_p}\right) / \mathrm{Re_p} \to 0$ as $\mathrm{Re_p} \to 0$, [79]. Lain et al. [81] used the results of Dennis et al. [82] to express the torque produced from the Magnus effect with a coefficient to extend the applicable range:

$$M_{M,i} = \frac{\rho_f}{2} \frac{r_p^5}{I} C_M \left| \omega_{\mathrm{rel}} \right| \left(\omega_{f,i} - \omega_{p,i} \right)$$

where, $u_{\text{rel}} = \left|\omega_{f,i} - \omega_{p,i}\right|$. Given that, for a sphere:

$$I = \frac{2m_p r_p^2}{5} \tag{3.43}$$

this reduces to:

$$M_{M,i} = \frac{15}{16}\frac{\rho_f}{\rho_p}\pi C_M \left|\omega_{\text{rel}}\right| \left(\omega_{f,i} - \omega_{p,i}\right) \tag{3.44}$$

where the coefficient C_M is defined as:

$$C_M = 64\pi \text{Re}_{\text{rot}}^{-1}, \quad \text{Re}_{\text{rot}} < 32$$

$$C_M = 12.9\text{Re}_{\text{rot}}^{-0.5} + 128.4\text{Re}_{\text{rot}}^{-1}, \quad 32 < \text{Re}_{\text{rot}} < 1000 \tag{3.45}$$

Saffman force

The Saffman lift force is generated by shear in the flow in much the same way as the Magnus force, it is expressed as:

$$F_{L,i} = 6.46 C_{L,s}\frac{\mu_f r^2}{m_p}\left|u_{\text{rel}}\right| \left(\frac{\partial u_i}{\partial x_j}\right)^{\frac{1}{2}} \nu^{-0.5}$$

The original Saffman force expression is only valid for the condition $\text{Re}_\text{p} \ll 1$, but the lift coefficient $C_{L,s}$ extends for higher Re_p:

$$C_{L,s} = \left(1 - 0.3314\sqrt{\beta_L}\right)\exp\left(-\frac{\text{Re}_\text{p}}{10}\right) + 0.3314\sqrt{\beta_L}, \quad \text{Re}_\text{p} \leq 40$$

$$C_{L,s} = 0.0524\sqrt{\beta_L \text{Re}_\text{p}}$$

$$\beta_L = \text{Re}_\text{p}\frac{\left|\omega_{\text{rel}}\right|}{\left|u_{\text{rel}}\right|}, \quad 0.005 < \beta_L < 0.4$$

Crowe [83] states the Saffman force is actually just a special case of the Magnus force for a particle in shear flow at the limit $\text{Re} \to 0$. Qualitatively this seems possible since the rotation of the fluid can be found from shear quantities. Quantitatively this can be explored by looking at the nondimensional values of the forces as calculated in Section 6.4. Saffman and Magnus forces appear frequently in the literature but their exact nature and contribution is still very much debated [83, 84]. The experimental study by Zhou [84] looked at the contribution of Saffman and Magnus forces on the trajectories of saltating sand in a wind tunnel, the Magnus force was significant but the Saffman force was not. The nondimensional analysis in Chapter 6 will yield a result.

3.3.5 Added mass

A particle moving through a fluid will pull a significant volume of the fluid with it, Poisson [69] found this volume to be half that of the sphere and this was later confirmed by Green [85]. The added mass force can then be expressed by Eq. 3.46:

$$F_{A,i} = \frac{\mathrm{d}u_i}{\mathrm{d}t}\frac{1}{2}\frac{m_f}{m_p} = \frac{2}{3}\frac{\pi r_p^3 \rho_f}{m_p}\frac{\mathrm{d}u_i}{\mathrm{d}t} = \frac{1}{2}\frac{\rho_f}{\rho_p}\frac{\mathrm{d}u_i}{\mathrm{d}t} \tag{3.46}$$

where m_f is the mass of the fluid that would occupy the volume of the particle. The effect of added mass is dependant on the density ratio between the particle and the fluid. For sand in air this ratio is about 2200:1 [70] therefore added mass can be neglected.

3.3.6 Pressure force

The pressure force is the force associated with local pressure gradients in the fluid, Eq. 3.47. It is included in some multiphase simulations [86] and not in others [87]. The second term on the right simplifies to $\frac{1}{\rho_p}$ which is small for large particle densities, as such the pressure force does not become significant until the pressure gradient approaches the same order as ρ_p.

$$F_{p,i} = -\frac{\mathrm{d}p}{\mathrm{d}x_i}\frac{4\pi r_p^3}{3m_p} = -\frac{\mathrm{d}p}{\mathrm{d}x_i}\frac{1}{\rho_p} \tag{3.47}$$

where $\frac{\mathrm{d}p}{\mathrm{d}x_i}$ is the pressure gradient vector at the particle position.

3.3.7 Gravity and buoyancy

The gravity and buoyancy forces are both body forces that can be considered constant through out all situations. Combining the two expressions of gravitational acceleration and buoyancy due to differences in fluid and particle density results in:

$$F_{g,i} = \frac{1}{6}\pi d_p^3 \frac{\left(\rho_p - \rho_f\right)}{m_p} = \left(1 - \frac{\rho_f}{\rho_p}\right) g_i$$

As with the added mass expression, Section 3.3.5, the sand in air density ratio is 2200:1 therefore the effect of buoyancy can be neglected, this reduces the above equation to the familiar force of gravity acting on a mass:

$$F_{g,i} = g_i \tag{3.48}$$

3.3.8 Near wall effects

In boundary layers the no-slip condition at the wall can cause anisotropic 3D structures to appear, such as pairs of counter rotating spanwise vortices, or hairpin vortices. Marquille et al. [88] used DNS to model the channel flow separation over a bump in the wall, the vortices after separation are described as intense. These near wall structures lead to regions of high and low shear stress that can trap and eject particles. Particles entrained in turbulence will accumulate in certain regions of the flow namely those of high strain, low acceleration and low vorticity [89] [90]. In turbulence at low Reynolds number heavy particles cluster in low vorticity regions as they are spun out of the vortices. Particles will cluster in regions of low vorticity relative to their own response time. Goto and Vassilicos [90] show particle clustering becomes more defined as $\mathrm{St} \to 1$.

The effect of preferential concentration also occurs in wall bounded turbulence with particles gathering in the regions of low shear stress. The regions of low shear stress are also synonymous with the so called sweep and ejection events that sweep faster moving fluid toward the wall and eject slow fluid by the wall into the free stream. The particles will be observed to collect in these regions, then there is a potential for ejection events to pull these particles out of the boundary layer and entrain them into the flow.

The presence of entrained particles has been shown to increase the thickness of the boundary layer through increased diffusion similar to roughness. Wachspress [21] uses a correction factor

Author	p	q	Range
Saffman[95]	6.46	3	$\mathrm{Re}_\mathrm{p}^* \ll 1$
Leighton and Acrivos[96]	9.22	4	$\mathrm{Re}_\mathrm{p}^* \ll 1$
Hall[55]	20.9	2.31	$\mathrm{Re}_\mathrm{p}^* > 6$
Mollinger et al.[91]	56.9	1.87	$0.6 < \mathrm{Re}_\mathrm{p}^* < 4$

Table 3.1: Coefficients for lift expressions of a particle on a wall, Rabinovich [93]

.

proposed by Bagnold [17] in their entrainment model described in Section 2.6.

Particles in close proximity with a wall will experience an enhanced lift effect. There have been several studies, both experimental and numerical, for particles in linear shear flow bounded by a wall, however, for particles in a turbulent boundary that are large enough to not sit entirely within the sublayer the expression is best defined using the results of Mollinger and Nieuwstadt [91] for the lower Re_p ranges and Hall [55] for the larger Re_p ranges.

Particles on a wall

Following Mollinger and Nieuwstadt [91] the nondimensional lift force can be expressed in the form:

$$F_L^+ = p\left(a^+\right)^q \tag{3.49}$$

where:

$$F_L^+ = \frac{\tilde{F_L}}{\rho\nu^2}$$

and the nondimensional radius, a^+ is:

$$a^+ = \frac{av_*}{\nu}$$

where v_* is the shear velocity and $a^* = 0.5\mathrm{Re}_\mathrm{p}^*$ the shear Reynolds number, $\mathrm{Re}_\mathrm{p}^* = D_p u_* / \nu$. In recent work by Zeng [92] and Rabinovich [93] values for p and q in different limits of Re_p^* were collected, presented here in Table 3.1. For the low values of Re_p^* the chosen expression follows Leighton and Acrivos [94] as this fits experimental data better in the range $\mathrm{Re}_\mathrm{p}^* < 0.6$. It is important to note that the values developed by Hall and Mollinger et al. were for turbulent boundary layers rather than linear shear layers as was the case for the others. For this reason the present study will be using these relationships primarily.

The majority of particles will have larger Re_p^* and these are governed by the results obtained by Hall [55] who conducted a series of experiments with a large particle on the floor of a wind tunnel in the Boundary layer. Hall used a variety of configurations including the probe particle placed between larger particles as well as resting on top of them. Since in our case the objective is to model the fluid forces likely occurring on a particle of sand that is part of a bed of sand the configurations tested by Hall are very relevant.

Particles near the wall

The force expression in Eq. 3.49 is only relevant for a particle sitting on the wall. The effect of the proximity of the wall have been realised by Zeng [92] for a particle that is up to a distance of $y = 4D_p$ away from the wall. The expression proposed by Zeng is given as a ratio of lift coefficients created to fit various models and results, this is especially useful because it saves using either of the lift coefficients explicitly, simply the influence of the wall:

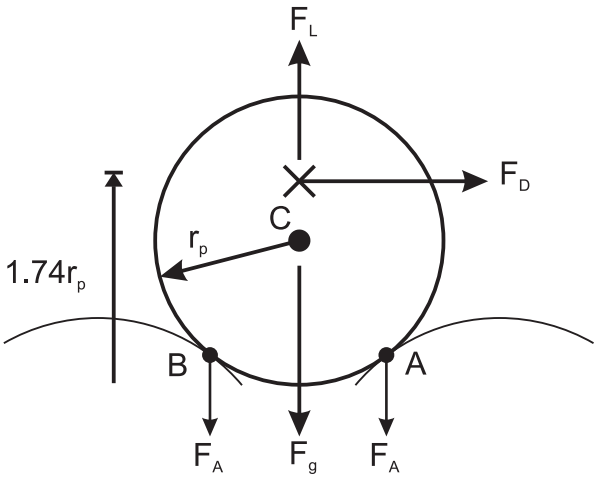

Figure 3.2: Forces acting on a particle at rest on two particles.

$$\frac{C_{Ls}}{C_{Ls,w}} = \exp\left(-0.5\delta\left(\frac{\mathrm{Re}}{250}\right)^{\frac{4}{3}}\right)\left[\exp\left(\alpha(\mathrm{Re})\delta^{\beta(\mathrm{Re})}\right) - \lambda(\delta,\mathrm{Re})\right] \tag{3.50}$$

where C_{Ls} and $C_{Ls,w}$ are the lift and wall lift coefficients respectively, the nondimensional wall distance is given by $\delta = y/D_p - 0.5$, $\mathrm{Re} = \mathrm{Re}_\mathrm{p}^* = 2a^+$ and α, β and λ are functions below:

$$\alpha = -\exp(-0.3 + 0.05 * 2a^+)$$

$$\beta = 0.8 + 0.02a^+$$

$$\lambda = (1 - \exp(-\delta))\left(\frac{a^+}{125}\right)^{\frac{5}{2}}$$

3.4 Particle-particle forces

The ground surface in the scenario considered is made up of sand, this surface is a collection of discrete particles, it is porous, and it is erodible. For the particles to be moved the fluid forces acting on those particles must first overcome the particle-particle cohesion, for the particle to be entrained the forces on the particle must then overcome gravity as illustrated in Fig. 3.2. The cohesive forces consist of electrostatics, mechanical stresses, chemical bonds and van der Waals forces. Electrostatics and van der Waals forces do not require contact.

3.4.1 Static adhesion

There are a number of well known models for simulating the effects of resuspension with cohesive forces present. The Derjaguin model [97] developed in the 1970s proposed deformation on the materials by mechanical stresses, the forces were entirely compressive and within the Hertzian contact region, the force was based on the van der Waals force. Later in the 1970s Johnson et al. [98] proposed a popular model that became known as the JKR model, this model was proposed after Johnson saw that contact radii were significantly larger than those predicted by Derjaguin *et al*. [97]. JKR uses the surface energy to account for the adhesive forces, again all forces exist within the contact zone. Derjaguin *et al*. proposed a more advanced model that accounted for tensile stresses but also now assumed the contact shape was Hertzian, this became

known as the DMT model. The Hertzian shape assumption resulted in the forces being half located in the contact region and half outside it. Rimai at al. [99] summarised these two models and then conducted experiments on particles of 1μm and 10μm but the results were unable to draw distinction between the DMT and JKR models, nevertheless Rimai noted that the JKR model did a reasonable job of predicting the contact area at separation.

Adhesion forces between particles and between particles and surfaces are of concern to a number of industries including semiconductors and aerosols. The situation of a bed of particles was captured by Ziskind, Fichman and Gutfinger (ZFG) [57] with the idea of particles sitting on one or two asperities, as in Fig. 3.2. ZFG modelled the fluid forces and applied moments to the particle about the asperity, these moments can liberate the particle provided there is a sufficient lift force to overcome gravity. This method allows inception by the drag force, which is orders of magnitude greater than lift. The concept of particle resonance was dismissed by Vainshtein [100] claiming that the particles are resuspended at much lower frequencies than particle resonance.

The adhesion models used by ZFG include the DMT and JKR model. It is claimed that DMT is designed for small or hard particles, whilst JKR is suited to large or soft particles.

ZFG includes a van der Waals force, Eq. 3.51, from Israelachvili [101], however, this does not contribute the majority of the cohesive force:

$$F_v = \frac{A_v r_p}{6\,|n_i|^2} \tag{3.51}$$

where A_v is the Hamaker constant, ZFG used an approximation of $A \simeq 10^{-19}$J, $|n_i|$ is the distance — ZFG uses roughness heights for this distance. Eichenlaub *et al*. [102] used the same expression from the DMT approximation, Eichenlaub *et al*. [102] conducted experiments using two separate methods and reported the Hamaker constant for SiO_2- SiO_2 as 65.5×10^{-21}J and 69.6×10^{-21}J. Ackler [103] reported Hamaker values of 66×10^{-21}J, the same result is reported by French [104].

3.4.2 Adhesion models

The JKR adhesion model:

$$\frac{r_a^3 E_{\text{eff}}}{r_p} = F_p + 3\pi\sigma r_p + \sqrt{6\pi\sigma r_p F_p + (3\pi\sigma r_p)^2} \tag{3.52}$$

where F_p is the pull off force, r_a is the contact radius or radius of the asperity, E_{eff} is the effective Young's modulus and σ is the surface energy. E_{eff} can be found using:

$$\frac{1}{E_{\text{eff}}} = \frac{3}{4}\left(\frac{1-\sigma_p'^2}{E'} + \frac{1-\sigma_p^2}{E}\right)$$

where σ_p and σ_p' are the Poisson's ratio of the two bodies. For like bodies:

$$E_{\text{eff}} = \frac{2}{3}\left(\frac{E}{1-\sigma_p 2}\right)$$

The DMT adhesion model is not explicitly given but ZFG employs an approximation from Maugis [105]:

$$F_{P,\text{DMT}} = \frac{r_a^3 K}{r_p} - 2\pi\sigma r_p \tag{3.53}$$

Equations 3.52 and 3.53 give a relationship between the adhesive force and the contact radius. Following the analysis of ZFG we can presume that at the point of inception the contact

radius is reduced to zero and this provides a pull off force, F_{P0}:

$$F_{P0,\mathrm{JKR}} = \frac{3}{2}\pi\sigma \min\left(r_p, r_a\right) \tag{3.54}$$

$$F_{P0,\mathrm{DMT}} = 2\pi\sigma \min\left(r_p, r_a\right) \tag{3.55}$$

where $\min\left(r_p, r_a\right)$ is used because the model presumes that the smaller particle adheres to the larger particle as if the large particle was a smooth surface.

Experimental results by Jones *et al*. [106] give particle-particle pull of forces for glass ballotini as 20-40nN for 6μm particles and $10 - 20$nN for 35μm particles. Using Eq. 3.54 the surface energy, $1.2 \times 10^{-4} < \sigma < 2.8 \times 10^{-3}\mathrm{Jm}^{-2}$. Experimental results for a smooth substrate by Ibrahim *et al*. [58] for smooth glass spheres on a substrate gives a force 34nN for 72μm diameter with a surface energy of $2 \times 10^{-4}\mathrm{Jm}^{-2}$. These results agree with each other though it is noted there will be a large range in the actual surface energies of naturally occurring sand, similar to that seen in the experiments of Jones *et al*. [106].

3.4.3 Friction

Tangential motion of two bodies in contact is opposed by friction. Friction is traditionally expressed as:

$$F_{Fr} = C_{Fr}F_N \tag{3.56}$$

where C_{Fr} is the friction coefficient and F_N is the normal force. This is the maximum, the frictional force is equal and opposite to the applied tangential force until the Coulomb condition is met, at which point the particle will slip and the resistive force will equal Eq. 3.56. The direction of frictional force is tangential to the plane of contact and in the same plane as the applied force and the distance vector between the two particles:

$$t_i = -e_{ijk}n_j e_{klm}\hat{n}_l f_m$$

where f_m is the unit vector for the direction of applied force and n_l is the unit vector from particle centre a_i to particle centre b_i:

$$\hat{n}_i = \frac{b_i - a_i}{|b_i - a_i|} \tag{3.57}$$

The frictional force is dependent on the normal force. For a particle on a surface the friction then becomes:

$$F_{Fr,i} = t_i C_{Fr}\left(F_{g,i} + P_{0,i} - F_{M,i} - F_{S,i}\right) \tag{3.58}$$

Experimental work by Jones [106] using AFM supports the use of linear expressions and a friction coefficient. Jones found that typically for glass ballotini $C_{Fr} \simeq 0.5$.

Whether the particles initially roll or slide is determined by the relative strengths of the adhesion and frictional forces and, to some extent, the arrangement of the particles. This is discussed in more detail in section 6.4.2 .

The moment generated by frictional forces is simply the frictional force with a moment arm of the radius:

$$M_{Fr} = \frac{m_p}{I}e_{ijk}r_i F_{Fr,j}$$

where r_i is the vector from the centre of the particle to the contact point and I is the moment of inertia of a sphere, Eq. (3.43).

$$M_{Fr} = \frac{5}{2r_p^2} e_{ijk} r_i F_{Fr,j} \tag{3.59}$$

3.4.4 Introduction to the Discrete Element Method

The Discrete Element Method was originally presented by Cundall and Strack [107] to model soil mechanics, but since then has been used to model grain silo dynamics [108], powder conveying [109], aerosol flows [110] and filtration and separation processes [111]. Most current use involving free motion and oblique impacts is based on work by Maw *et al*. [112], the assumptions specified are an essential part of models used in the literature [113, 114, 115, 116]. In each time step the forces acting on each particle are calculated using the soft-sphere contact model; this contact model allows two or more particles to overlap with the repulsion force calculated using a spring-dashpot system, Fig. 3.3. Additional particle interaction forces such as friction, cohesion and body forces such as gravity are commonly applied as required by the simulation. The forces are then integrated to calculate the velocity and position for the next time step. Integration of DEM with a flow solver is a logical step, the additional fluid forces from the flow solver output are added to the DEM forces (one-way coupled). If relevant the effect of the particles on the flow can also be accommodated (two-way coupled) by including the particle drag as a source term in the fluid momentum equations. The DEM is assessed numerically in Appendix A, and used in Appendix C to model a large system of particles in the simulation of an experiment.

Assumptions of the DEM

The DEM is typically combined with numerical integrators, time discretization results in some error this error is heavily dependent on time step and choice of numerical integrator. Error associated with time step and integrator choice is explored in detail in Appendix A.

The DEM is a model and, using the above implementation, assumes all particles are spherical, stiffness is uniform or follows a uniform model and inter-particle friction is appreciable using the stick slip model. As these are simply force expression that are included in the calculation process it is easy to include more advanced models for any of the forces. Examples of additional complexity include non-spherical shapes [117], rolling resistance [118], or stochastic surface asperity models as used by Prokopovich *et al*. [119].

Equations of motion

DEM is based on the soft-sphere approach; each particle is modelled as a sphere of finite mass, these are allowed to overlap and a repulsive force is calculated using a spring dashpot system with the overlap as the extent of spring compression, Fig. 3.3. There are two common methods for calculating the force from the overlap, δ_n, the linear model and the Hertzian model. The linear model is simply the product of the overlap and the stiffness, $F_n = \delta_n k_n$, where k_n is the stiffness with units of N/m. The Hertzian model takes account of the volume of the sphere that is compressed in the overlap, Eq. 3.63. The normal force is then calculated using the linear model as:

$$F_{n,i} = -\frac{n_i}{\left(n_j n_j\right)^{1/2}} \left(\delta_n k - c \frac{\mathrm{d}\delta_n}{\mathrm{d}t} \right) \tag{3.60}$$

where k_n is the inter-particle stiffness, n_i is the vector from the centre of particle a to particle b, c is the damping coefficient and δ_n is the particle overlap:

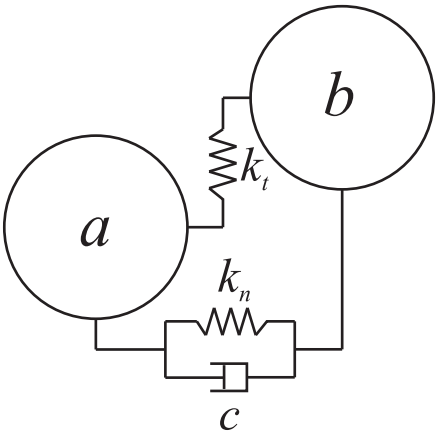

Figure 3.3: The soft sphere force model using normal spring-dashpot forces and tangential spring forces.

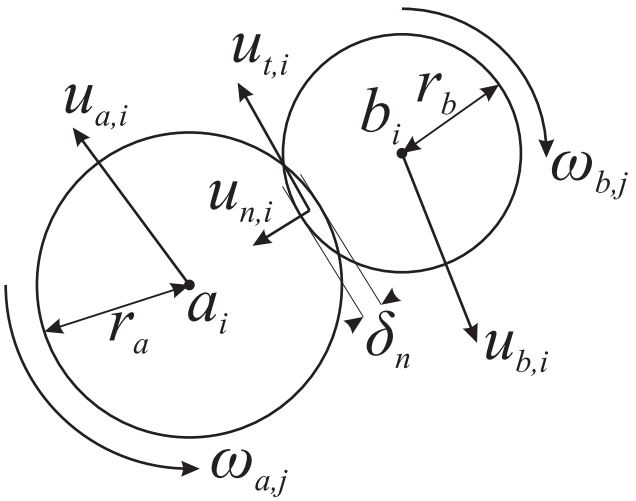

Figure 3.4: Definition of symbols during particle collision.

$$\delta_n = (r_a + r_b) - \sqrt{n_i n_i} \tag{3.61}$$

where r_a and r_b are the radii of particles a and b and the normal vector, n_i, is calculated as:

$$n_i = (b_i - a_i) \tag{3.62}$$

where a_i and b_i are the position vectors of particles a and b, Fig. 3.4 explains the symbols graphically. The Hertzian normal force model [7] is defined as:

$$F_{n,i} = -\frac{n_i}{\left(n_j n_j\right)^{1/2}} \left(\frac{4}{3} E_{\text{eff}} \sqrt{r_{\text{eff}}} \delta_n^{\frac{3}{2}} - c \frac{\mathrm{d}\delta_n}{\mathrm{d}t} \right) \tag{3.63}$$

where E_{eff} is the combined Young's modulus of the two particles, $r_{\text{eff}} = \frac{r_a r_b}{r_a + r_b}$ is the effective radius. If the particles are assumed to have identical properties then $E_{\text{eff}} = \frac{E}{1-\sigma^2}$.

The damping coefficient, c, is found from the coefficient of restitution, e, using a relationship derived by [120]:

$$c = 2 \ln e \sqrt{\frac{k m_{\text{eff}}}{\pi^2 + \ln^2 e}} \tag{3.64}$$

where e is the coefficient of restitution and the effective mass, m_{eff}, of contacting particles a and b is:

$$m_{eff} = \frac{m_a m_b}{m_a + m_b} \tag{3.65}$$

The frictional force is calculated in the plane normal to n_i acting in the opposite direction to the relative contact velocity, no damping is employed as friction is a dissipative force, this is typical in DEM simulation. The Coulomb condition distinguishes between sliding and elastic tangential forces by providing a maximum force, once reached the tangential force is capped to $C_f F_n$, this is the stick-slip model:

$$F_{t,i} = -\min\left(C_f F_n, k_t \delta_t\right) \frac{u_{t,i}}{\left(u_{t,j} u_{t,j}\right)^{1/2}} \tag{3.66}$$

where C_f is the friction coefficient, the normal force magnitude is $F_n = \sqrt{F_{n,i} F_{n,i}}$, k_t is the tangential stiffness, δ_t is the tangential displacement for this particle pair collision and $u_{t,i}$ is the relative tangential velocity. δ_t is the sum of the tangential motion already encountered for this contact pair:

$$\delta_t = \int_{t_{\text{start}}}^{t} u_t(t)\, \mathrm{d}t \tag{3.67}$$

where the integral is between the start of the contact, t_{start}, to present time, t.

Some particle systems experience cohesive forces, a simple cohesion model acts in a similar manner to the linear stiffness model but uses a larger radius of interaction:

$$F_{\text{coh},i} = -k_{\text{coh}} \delta_{\text{coh}} \frac{n_i}{\left(n_j n_j\right)^{1/2}} \tag{3.68}$$

where k_{coh} is the cohesion stiffness and δ_{coh} is the overlap of some cohesion radius r_{coh} using Eq. 3.61. The cohesion radius is typically larger than the particle radius to allow nearby particles to attract each other.

The simulation time step is calculated using the particle collision time period and a

resolution, a_{res}, to ensure a_{res} time steps are used over one collision:

$$\Delta t = \frac{1}{a_{\text{res}}}\sqrt{\frac{m}{k_n}} \tag{3.69}$$

The stiffness of a particle can be found from the Young's modulus material parameter by matching the Hertz force expression Eq. 3.63 with the linear force expression Eq. 3.60. This results in Eq. 3.70 [6].

$$k_n = \left(\frac{4}{15}\right)\frac{E}{1-\sigma^2}\sqrt{2r\delta_{\max}} \tag{3.70}$$

where $\delta_{\max}$ is an estimated maximum compression or overlap between the two particles. For nominal values of sand and an overlap of 1% this results in a very high value of $k \approx 10^6$N/m, giving a maximum time step of the order 1×10^{-10}. Simulating a physical process that takes several seconds would require a very large number of time steps and for complex systems this could be prohibitive. Instead a common compromise is to lower the stiffness, it has been shown that doing so can still yield realistic behaviour [121]. This compromise has been used in the simulations of Appendix C that involve tens of thousands of particles over time periods of several seconds.

Wall contact forces are modelled as one sided particle contacts. The force on the particle can be found using Eq. 3.60 or 3.63 but replacing δ_n with $\delta_{\text{wall}} = r_a - \sqrt{(w_i a_i)^2}$ where w_i is the position vector of a point on the wall closest to the particle centre. The linear and Hertzian wall normal force equations are defined in Eq. 3.71 and 3.72:

$$F_{n,\text{wall},i} = -\delta_{\text{wall}} k \frac{(w_i - a_i)}{\sqrt{(w_i - a_i)^2}} - c\frac{\mathrm{d}\delta_{\text{wall}}}{\mathrm{d}t} \tag{3.71}$$

$$F_{n,\text{wall},i} = -\frac{4}{3}\frac{(w_i - a_i)}{\sqrt{(w_i - a_i)^2}} E_{\text{eff}}\sqrt{r_a}\delta_{\text{wall}}^{\frac{3}{2}} - c\frac{\mathrm{d}\delta_{\text{wall}}}{\mathrm{d}t} \tag{3.72}$$

The force due to gravity for each particle is given as:

$$F_{g,i} = m_p g_i \tag{3.73}$$

similarly other forces, such as drag $F_{D,i}$, can be included in DEM model with relative ease using Eq. 3.32.

The complete equation of motion for a particle in a DEM system with walls, friction and cohesion is:

$$\frac{\mathrm{d}u_i}{\mathrm{d}t} = \frac{1}{m}\left(F_{n,i} + F_{t,i} + F_{n,\text{wall},i} + F_{t,\text{wall},i} + F_{\text{coh}} + F_{g,i} + F_{\phi,i}\right) \tag{3.74}$$

where $F_{\phi,i}$ represents optional forces such as drag or buoyancy.

Angular momentum is calculated using the tangential forces:

$$\frac{d\omega_i}{dt}\frac{2}{5}mr_p^2 = M_i = e_{ijk}F_{t,j}x_k \tag{3.75}$$

where ω_i is the angular velocity, M_i is the total moment and x_k is the vector from particle centre to centre of force, the contact centre $x_k = n_k - 1/2\delta_n$.

In the DEM these force equations are used to find the acceleration of each particle. The acceleration is integrated using a numerical integration scheme to give velocity and then position values at the next time step. The application of numerical integration schemes is discussed in detail in Section A.5. A complete explanation of how the DEM is practically applied in a many—particle simulation is given in Appendix C in which a dry powder penetrometry experiment is simulated numerically.

	description	symbol	ND
length scale	particle diameter	d_0	$d_0^* = \frac{x}{d_0}$
velocity scale	flow speed	u_0	$u^* = \frac{u_i}{u_0}$
fluid density scale	air density	ρ_{f0}	$\rho_f^* = \frac{\rho_f}{\rho_{f0}}$
particle density scale	particle density	ρ_{p0}	$\rho_p^* = \frac{\rho_p}{\rho_{p0}}$
viscosity scale	viscosity of air	μ_0	$\mu^* = \frac{\mu}{\mu_0}$
time scale	*derived*	$\frac{d_0}{u_0}$	$t^* = t\frac{u_0}{d_0}$
surface energy scale	surface energy of particle	σ_0	$\sigma^* = \frac{\sigma}{\sigma_0}$
Reynolds number	*derived*	$\frac{\rho_{f0} d_0 u_0}{\mu_{f0}}$	Re_0
gravity scale	magnitude of gravity	g_0	$g = g_0 g^*$
Froude number	*derived*	$\sqrt{\frac{u_0^2}{g_0 d_0}}$	Fr_0
density ratio	fluid to solid density	$\frac{\rho_{f_0}}{\rho_{p_0}}$	$\frac{\rho_{f_0}}{\rho_{p_0}}$

Table 3.2: Nondimensional parameters and numbers, their definition, meaning and symbol.

3.5 Nondimensional fluid equations

The equations that govern the fluid flow, namely the continuity and Navier-Stokes equations Eqs. 3.1 and 3.2, are nondimensionalised in this section. The nondimensional analysis allows the terms of the expression to be compared for relative importance and identifies familiar nondimensional numbers that indicate under which conditions the balance of terms change.

Table 3.2 lists nondimensional numbers used in this analysis; the derivations, symbols and meaning are also given.

The continuity equation, Eq. 3.1, is nondimensionalised to give Eq. 3.76:

$$\left[\frac{\rho_0 u_0}{x_0}\right]\frac{\partial \rho^*}{\partial t^*} + \left[\frac{\rho_0 u_0}{x_0}\right]\frac{\partial}{\partial x_i^*}(\rho^* u_i^*) = 0$$

$$\frac{\partial \rho^*}{\partial t^*} + \frac{\partial}{\partial x_i^*}(\rho^* u_i^*) = 0 \tag{3.76}$$

The Navier-Stokes equations, Eq. 3.2, are nondimensionalised for incompressible flows to give:

$$\frac{\partial}{\partial t^*}(\rho^* u_i^*) + \frac{\partial}{\partial x_j^*}(\rho^* u_i^* u_j^*) = \left[\frac{\mu_0}{x_0 u_0 \rho_0}\right]\frac{\partial}{\partial x_j^*}(\tau_{ij}^*) + \left[\frac{g_0 x_0}{u_0^2}\right]\rho^* g_i^* - \left[\frac{p_0}{\rho_0 u_0^2}\right]\frac{\partial p^*}{\partial x_i^*} + \left[\frac{F_0 x_0}{u_0^2}\right]\rho^* F_i^* \tag{3.77}$$

where the stress tensor τ_{ij}^* is:

$$\tau_{ij}^* = \mu^*\left(\frac{\partial u_i^*}{\partial x_j^*} + \frac{\partial u_j^*}{\partial x_i^*} - \frac{2}{3}\delta_{ij}\frac{\partial u_k^*}{\partial x_k^*}\right) \tag{3.78}$$

Using nondimensional numbers defined in Table 3.2 Eq. 3.77 can be simplified as:

$$\frac{\partial}{\partial t^*}(\rho^* u_i^*) + \frac{\partial}{\partial x_j^*}(\rho^* u_i^* u_j^*) = \frac{1}{\mathrm{Re}_0}\frac{\partial}{\partial x_j^*}(\tau_{ij}^*) - \frac{\partial p^*}{\partial x_i^*} + \mathrm{Fr}_0 \rho^* g_i^* + \mathrm{Fr}_{u0} \rho^* F_i^* \tag{3.79}$$

It is clear from Eq. 3.79 that the diffusion term is governed by the inverse of the Reynolds number. Flows with large Re are inertially dominated and as diffusion is a viscous phenomenon its influence over the flow diminishes. The relative importance of gravity is governed by the Froude number, Fr, the ratio of inertia to weight and in kind the external body force F_i^* is governed by the user Froude number,Fr_{u0}, the ratio of inertia to external force. Pressure scales with the convective term, the second term on the LHS in Eq. 3.79.

3.6 Nondimensional particle forces and moments

The particle-fluid forces introduced in Section 3.3 will be nondimensionalised in this section. nondimensionalising the forces gives an indication to the relative importance of the expressions.

The left hand side of Eq. 3.26 nondimensionalises to:

$$\frac{\mathrm{d}u_i}{\mathrm{d}t} = \frac{u_0^2}{d_0}\frac{\mathrm{d}u_i^*}{\mathrm{d}t^*}$$

Equation 3.26 becomes:

$$\frac{\mathrm{d}u_i^*}{\mathrm{d}t^*} = \frac{d_0}{u_0^2}\left[F_{D,i} + F_{B,i} + F_{M,i} + F_{L,i} + F_{G,i} + F_{A,i} + F_{Fr,i}\right] \tag{3.80}$$

Likewise for Eq. 3.8:

$$\frac{\mathrm{d}\omega_i}{\mathrm{d}t} = \frac{u_0^2}{d_0^2}\frac{\mathrm{d}\omega_i^*}{\mathrm{d}t^*}$$

$$\frac{\mathrm{d}\omega_i^*}{\mathrm{d}t^*} = \frac{d_0^2}{u_0^2}\left[M_{M,i} + M_{F,i}\right] \tag{3.81}$$

We now nondimensionalise the individual force expressions, where the d_0/u_0^2 scaling term is incorporated into each nondimensional force reference term $F_{\phi 0}$ to give:

$$\frac{\mathrm{d}u_i^*}{\mathrm{d}t^*} = F_{D0}F_{D,i}^* + F_{B0}F_{B,i}^* + F_{M0}F_{M,i}^* + F_L F_{L,i}^* + F_{G0}F_{G,i}^* + F_{A0}F_{A,i}^* + F_{Fr0}F_{Fr,i}^*$$

likewise for equation 3.81 the term d_0^2/u_0^2 is included to give:

$$\frac{\mathrm{d}\omega_i^*}{\mathrm{d}t^*} = M_{M0}M_{M,i}^* + M_{F0}M_{F,i}^*$$

Table 3.2 lists the non dimensional symbols and derivations.

3.6.1 Drag Force

$$F_{D,i} = \frac{\mathrm{d}u}{\mathrm{d}t} = \frac{1}{2}\frac{C_D}{m}A\rho_f\left(u_i - v_i\right)\left|u_{rel}\right| \tag{3.82}$$

where the drag coefficient, C_D is:

$$C_D = \frac{24}{\mathrm{Re_r}}f_d \tag{3.83}$$

$$f_d = 1, \quad \mathrm{Re_p} \ll 1$$

$$f_d = \left(1 + 0.15\mathrm{Re_p}^{0.687}\right), \quad \mathrm{Re_p} < 800 \tag{3.84}$$

combining Eqs. 3.28 and 3.83 with 3.82 and expanding gives us the expression:

$$F_{D,i} = \frac{1}{2}\frac{6}{\pi d_p^3 \rho_p}\frac{24\mu_f f_d}{\rho_f D\left|u_{rel}\right|}\frac{\pi D^2}{4}\rho_f \left|u_{rel}\right|\left(u_i - v_i\right)$$

simplifying:

$$F_{D,i} = 18\frac{\mu_f f_d}{\rho_p D^2}\left(u_i - v_i\right)$$

non dimensionalising and including d_0/u_0^2 gives:

$$F_{D,i} = 18\frac{d_0}{u_0^2}\frac{\mu_{f0}\mu_f^*}{\rho_{p0}\rho_p^* d_p^{*2} d_0^2} f_d u_0\left(u_i^* - v_i^*\right) = 18 f_d \frac{\mu_{f0}}{\rho_{p0} d_0 u_0}\frac{\mu_f^*}{\rho_p^* d_p^{*2}}\left(u_i^* - v_i^*\right) \tag{3.85}$$

simplifying:

$$F_{D,i} = F_{D0}F_{D,i}^* = \left[18 f_d \frac{\rho_{f0}}{\rho_{p0}}\frac{1}{\mathrm{Re}_0}\right]\left[\frac{\mu_f^*}{\rho_p^* d_p^{*2}}\left(u_i^* - v_i^*\right)\right] \tag{3.86}$$

3.6.2 Basset force

The extended Basset force:

$$F_{B,i} = 6\frac{C_B r_p^2}{m}\sqrt{\pi\rho_f\mu_f}\left[\int_0^t \frac{1}{\sqrt{t-\tau}}\frac{\delta(u_i - v_i)}{\delta\tau}\mathrm{d}\tau + \frac{(u_i - v_i)_0}{\sqrt{t}}\right]$$

nondimensionalise;

$$F_{B,i} = \frac{6}{4}C_B\frac{d_0}{u_0^2}\frac{d_0^2 D^{2*}}{\left(\frac{1}{6}\pi d_0^3 D^{*3}\rho_{p0}\rho_p^*\right)}\sqrt{\pi\rho_{f0}\rho_f^*\mu_0\mu^*}$$
$$\left(\int_0^t \frac{1}{\sqrt{\frac{d_0}{u_0}\left(t^* - \tau^*\right)}}\frac{u_0^2}{d_0}\frac{\mathrm{d}\left(u_i^* - v_i^*\right)}{\mathrm{d}\tau^*}\mathrm{d}\tau^*\frac{d_0}{u_0} + \frac{u_0\left(u_i^* - v_i^*\right)_0}{\sqrt{\frac{d_0}{u_0}t^*}}\right)$$

$$F_{B,i} = \frac{36}{4}\frac{d_0}{u_0^2}C_B\sqrt{\frac{u_0^2}{\pi^2 d_0^2 D^{2*}\rho_{p0}^2\rho_p^{2*}}\pi\frac{u_0}{d_0}\rho_{f0}\rho_f^*\mu_0\mu^*}$$
$$\left(\int_0^t \frac{1}{\sqrt{(t^* - \tau^*)}}\frac{\mathrm{d}\left(u_i^* - v_i^*\right)}{\mathrm{d}\tau^*}\mathrm{d}\tau^* + \frac{\left(u_i^* - v_i^*\right)_0}{\sqrt{t^*}}\right)$$

$$F_{B,i} = \frac{36}{4}C_B\sqrt{\frac{1}{\pi}\frac{\mu_0}{d_0 u_0\rho_{p0}}\frac{u^*}{D^*}\frac{\mu^*}{D^* u^*\rho_p^*}\frac{\rho_{f0}}{\rho_{p0}}}$$
$$\left(\int_0^t \frac{1}{\sqrt{(t^* - \tau^*)}}\frac{\mathrm{d}\left(u_i^* - v_i^*\right)}{\mathrm{d}\tau^*}\mathrm{d}\tau^* + \frac{\left(u_i^* - v_i^*\right)_0}{\sqrt{t^*}}\right)$$

This can be reduced to:

$$F_{B,i} = F_{B0}F^*_{B,i} = \left[\frac{9C_B}{\sqrt{\pi}}\left(\frac{\rho_{f0}}{\rho_{p0}}\frac{1}{\mathrm{Re}_0}\right)^{\frac{1}{2}}\right] \left[\left(\frac{1}{\mathrm{Re}^* t^*}\right)^{\frac{1}{2}}\left(\int_0^t \frac{1}{\sqrt{(t^*-\tau^*)}}\frac{\mathrm{d}\left(u_i^*-v_i^*\right)}{\mathrm{d}\tau^*}\mathrm{d}\tau^* + \frac{\left(u_i^*-v_i^*\right)_0}{\sqrt{t^*}}\right)\right] \tag{3.87}$$

3.6.3 Magnus force

$$F_{M,i} = \frac{C_M \pi r^3 \rho_f}{m} e_{ijk}\Omega_j(u_k - v_k)$$

nondimensionalise:

$$F_{M,i} = \frac{C_M \pi}{8}\frac{d_0}{u_0^2}\frac{d_0^3 D^{*3}\rho_{f0}\rho_f^*}{\left(\frac{1}{6}\pi d_0^3 D^{*3}\rho_{p0}\rho_p^*\right)}\frac{u_0^2}{d_0}e_{ijk}\Omega_j^*\left(u_k^* - v_k^*\right)$$

this reduces to:

$$F_{M,i} = F_{M0}F^*_{M,i} = \left[\frac{3}{4}C_M\frac{\rho_{f0}}{\rho_{p0}}\right]\left[e_{ijk}\Omega_j^*\left(u_k^* - v_k^*\right)\right] \tag{3.88}$$

3.6.4 Saffman force

The original Saffman lift expression can be expressed as:

$$F_{S,i} = 6.46\frac{\mu_f r^2}{m}\left|u_{rel}\right|\kappa^{0.5}\nu^{-0.5}$$

Including the correction factor, f_s, and extending gives the more general form of:

$$F_{S,i} = 6.44\frac{f_s r^2}{m}\sqrt{\mu_f\rho_f}\frac{e_{ijk}\left(u_j - v_j\right)\omega_{f,k}}{\sqrt{|\omega_{f,i}|}}$$

nondimensionalising:

$$F_{S,i} = \frac{6.44}{4}f_s\frac{d_0}{u_0^2}\frac{D^{*2}d_0^2}{\left(\frac{1}{6}\pi d_0^3 D^{*3}\rho_{p0}\rho_p^*\right)}\left(\rho_{f0}\rho_f^*\mu_0\mu^*\right)^{\frac{1}{2}}\left(u_0\left(\frac{d_0}{u_0}\right)^{1/2}\frac{e_{ijk}\left(u_j^* - v_j^*\right)\omega_{f,k}^*}{|\omega_{f,i}^*|^{\frac{1}{2}}}\right)$$

$$F_{S,i} = \frac{38.64}{4\pi}f_s\frac{1}{\left(u_0\rho_{p0}D^*\rho_p^*\right)}\left(\rho_{f0}\rho_f^*\mu_0\mu^*\right)^{\frac{1}{2}}\left(\left(\frac{d_0}{u_0}\right)^{1/2}\frac{e_{ijk}\left(u_j^* - v_j^*\right)\omega_{f,k}^*}{|\omega_{f,i}^*|^{\frac{1}{2}}}\right)$$

rearrange:

$$F_{S,i} = \frac{38.64}{4\pi}f_s\frac{1}{\left(u_0\rho_{p0}\right)}\left(\frac{d_0\rho_{fo}\mu_0}{u_0}\right)^{\frac{1}{2}}\left(\frac{\rho_f^*\mu^*}{D^{*2}\rho_p^{*2}}\right)^{\frac{1}{2}}\left(\frac{e_{ijk}\left(u_j^* - v_j^*\right)\omega_{f,k}^*}{|\omega_{f,i}^*|^{\frac{1}{2}}}\right)$$

with:

$$\mathrm{Re} = \frac{\rho_f u D}{\mu_f}$$

$$F_{S,i} = \frac{38.64}{4\pi}f_s\frac{\mu_0}{\left(u_0^2\rho_{p0}\right)}\left(\frac{d_0 u_0\rho_{fo}}{\mu_0}\right)^{\frac{1}{2}}\left(\frac{\rho_f^*\mu^*}{D^{*2}\rho_p^{*2}}\right)^{\frac{1}{2}}\left(\frac{e_{ijk}\left(u_j^* - v_j^*\right)\omega_{f,k}^*}{|\omega_{f,i}^*|^{\frac{1}{2}}}\right)$$

$$F_{S,i} = F_{S0}F^*_{S,i} = \left[3.07 f_s \frac{\mu_0}{\left(u_0^2 \rho_{p0}\right)} \left(\mathrm{Re}_0\right)^{\frac{1}{2}}\right] \left[\left(\frac{\mu^*}{D^{*2}\rho_p^*}\right)^{\frac{1}{2}} \left(\frac{e_{ijk}\left(u_j^* - v_j^*\right)\omega_{f,k}^*}{|\omega_{f,i}^*|^{\frac{1}{2}}}\right)\right] \tag{3.89}$$

3.6.5 Gravity

$$F_{g,i} = \left(1 - \frac{\rho_f}{\rho_p}\right) g_i$$

including the effects of buoyancy nondimensionalises to:

$$F_{g,i} = \frac{d_0}{u_0^2} \frac{1}{\rho_p^* \rho_{p0}} \left(\rho_p^* \rho_{p0} - \rho_f^* \rho_{f0}\right) g_0 g_i^*$$

assuming the density ratio is small this expression further reduces to:

$$F_{g,i} = \frac{d_0}{u_0^2} g_0 g_i^*$$

the Froude number, defined as $\mathrm{Fr}^2 = \frac{u^2}{gD}$, substitutes in to leave;:

$$F_{g,i} = F_{g0}F^*_{g,i} = \left[\frac{1}{\mathrm{Fr}_0^2}\right] g_i^* \tag{3.90}$$

3.6.6 Adhesion

The pull off force for the JKR and DMT adhesion models are defined as:

$$P_{0,JKR} = \frac{3}{2}\pi\sigma r_p$$

$$P_{0,DMT} = 2\pi\sigma r_p$$

using the previous notation these are rewritten as:

$$F_{P,i} = f_p \frac{\pi\sigma r_p}{m} r_i \tag{3.91}$$

where f_p depends on whether the JKR or DMT model is used, and given the value 1.5 or 2 respectively and r_i is the unit vector from particle centre to the contact point $r_i = \frac{x_{cont,i} - x_{p,i}}{|x_{cont,i} - x_{p,i}|}$ and is already nondimensional.
nondimensionalising Eq. 3.91:

$$F_{P,i} = f_p \frac{\pi\sigma r_p}{m} r_i = f_p \pi \frac{d_0}{u_0^2} \frac{\sigma_0 \sigma^*}{\left(\frac{1}{6}\pi d_0^3 D^{*3} \rho_{p0} \rho_p^*\right)} D^* d_0 r_i^*$$

$$F_{P,i} = 6 f_p \frac{\sigma_0}{d_0 u_0 \rho_{p0}} \frac{\sigma^*}{D^{*2}\rho_p^*} r_i^*$$

and simplifying:

$$F_{P,i} = F_{P0}F^*_{P,i} = \left[6 f_p \frac{\sigma_0}{d_0 u_0 \rho_{p0}}\right] \left[\frac{\sigma^*}{D^{*2}\rho_p^*} r_i^*\right] \tag{3.92}$$

3.6.7 Friction

The friction force is given as:

$$F_{Fr,i} = \frac{C_{Fr}}{m}\left(F_{P,i} + F_{g,i} - F_{S,i} - F_{M,i}\right)$$

$$F_{Fr,i} = C_{Fr}\left(F_{P0}F^*_{p,i} + F_{g0}F^*_{g,i} - F_{S0}F^*_{S,i} - F_{M0}F^*_{M,i}\right)$$

substituting the $F_{\phi 0}$ terms for each of the sources:

$$F_{Fr,i} = C_{Fr}\left(\left[6f_p\frac{\sigma_0}{d_0 u_0 \rho_{p0}}\right]F^*_{p,i} + \left[\frac{1}{\mathrm{Fr}_0^2}\right]F^*_{g,i}\right. \tag{3.93}$$

$$\left. - \left[3.07 f_s \frac{\mu_0}{\left(u_0^2\rho_{p0}\right)}\left(\mathrm{Re}_0\right)^{\frac{1}{2}}\right]F^*_{S,i} - \left[\frac{3}{4}C_M\frac{\rho_{f0}}{\rho_{p0}}\right]F^*_{M,i}\right) \tag{3.94}$$

3.6.8 Moments

Recall the momentum from the Magnus effect described in Eq. 3.44:

$$M_{M,i} = \frac{15}{16}\frac{\rho_f}{\rho_p}\pi C_M \left|\omega_{rel}\right|\left(\omega_{f,i} - \omega_{p,i}\right)$$

nondimensionalise:

$$M_{M,i} = \frac{15\pi}{16}\left(\frac{d_0}{u_0}\right)^2 C_M \frac{\rho_{f0}}{\rho_{p0}}\frac{\rho^*_f}{\rho^*_p}\left(\frac{u_0}{d_0}\right)^2\left|\omega^*_{rel}\right|\left(\omega^*_{f,i} - \omega^*_{p,i}\right)$$

which reduces to:

$$M_{M,i} = M_{M0}M^*_{M,i} = \left[\frac{15\pi}{16}C_M\frac{\rho_{f0}}{\rho_{p0}}\right]\left[\left|\omega^*_{rel}\right|\left(\omega^*_{f,i} - \omega^*_{p,i}\right)\right] \tag{3.95}$$

Similarly for the friction expression, Eq. 3.59:

$$M_{Fr,i} = \frac{5}{2r_p^2}e_{ijk}r_i F_{Fr,j}$$

$$M_{Fr,i} = \frac{5}{2r_p^2}e_{ijk}r_j\left(F_{p,k} + F_{g,k} - F_{S,k} - F_{M,k}\right)$$

nondimensionalise, where r^*_j is a nondimensional unit vector:

$$M_{Fr,i} = \left(\frac{d_0}{u_0}\right)^2\frac{10}{d_0^2 D^{*2}}e_{ijk}r^*_j\left(F_{P0}F^*_{p,k} + F_{g0}F^*_{g,k} - F_{S0}F^*_{S,k} - F_{M0}F^*_{M,k}\right)$$

$$M_{Fr,i} = \frac{5}{u_0^2}\frac{1}{D^{*2}}e_{ijk}r^*_j\left(F_{P0}F^*_{p,k} + F_{g0}F^*_{g,k} - F_{S0}F^*_{S,k} - F_{M0}F^*_{M,k}\right) \tag{3.96}$$

The friction plays a dominant role in the moment expression, the nondimensional reference term is a combination of the difference forces at work.

3.6.9 Final forms of the nondimensional particle equation

Equation 3.80 can now be expressed in terms of reference values, and nondimensional variables:

$$\frac{\mathrm{d}u^*_i}{\mathrm{d}t^*} = \left[F_{D0}F^*_{D,i} + F_{B0}F^*_{B,i} + F_{M0}F^*_{M,i} + F_{L0}F^*_{L,i} + F_{G0}F^*_{G,i} + F_{P0}F^*_{P,i} + F_{Fr0}F^*_{Fr,i}\right] \tag{3.97}$$

The reference values indicate the relative importance of the forces for the typical scenario. The nondimensional variables, F^*_ϕ, are typically of order 0. Calculation of the reference terms, F_{ϕ_0}, and substitution into Eq. (3.97) allows the identification of the significant forces for any given scenario. That analysis is performed in Chapter 6 applied to a full scale helicopter flow.

3.7 Chapter summary

This chapter outlines the numerical tools used throughout the thesis to describe various physical systems. This chapter described the governing equations of the fluid and particulate phases. The Navier-Stokes equations used to find the 3D unsteady rotor wake in Chapters 4 and 5 were defined in Section 3.1. The 2D axisymmetric flow equations and the turbulence model used in Chapter 6 were given in Section 3.2. The particle-fluid forces were identified from the literature in Section 3.3. The particle-particle forces were defined and the DEM simulation framework used in Appendices A and C was outlined in Section 3.4.4. The fluid and particle force expressions are nondimensionalised and described in Sections 3.6 and 3.6, these nondimensionalised expressions are analysed further in Chapter 6 using the reference values from a full scale helicopter flow field and the numerical tools now defined in this chapter.

Chapter 4

Model Scale Rotor Simulation: Method, Verification and Mean Flow Results

---

In this chapter an unsteady 3D rotor wake modelling method is described, implemented and verified against experimental results from the literature. This is a prelude to Chapter 5, the flow field verified in this chapter will be used to investigate particle entrainment mechanisms. The rotor is modelled using the actuator line method and the wake simulation is performed using an Eulerian finite volume Navier-Stokes solver within the commercial software package Ansys Fluent (ver. 12.0.16). Other methods of simulating rotor wakes are discussed in a literature review. Five rotor heights are considered, 4 heights near the ground and 1 height out of ground effect. The spatial discretisation error is assessed using Richardson extrapolation. The velocity field, vortex trajectories and power offset due to ground effect are compared with experimental data from the literature and found to be a reasonable match.

4.1 Introduction

This chapter describes the actuator line method used to model a 3D unsteady rotor wake and presents a number of different validations that are applied to the results. Different methods of modelling the rotor wake are reported from the literature in Section 4.2, the Actuator Line Method was chosen and the decision was justified in this section. The implementation of the Actuator Line Method (ALM) is provided in Section 4.3. The quality of the mesh is assessed using the Richardson extrapolation to approximate the grid free solution from 3 meshes of increasing resolution.

The results of the flow are directly compared with experimental data from the literature in Section 4.4.3. The vortex trajectories of two experiments from the literature using rotors IGE (In Ground Effect) and OGE (Out of Ground Effect) were used in the comparison. The rotor power is shown to decrease, while the thrust remains constant, as the rotor approaches the ground; this is compared with experimental results and analytical predictions. The flow fields are non-dimensionalised and compared with PIV results from the literature and the vortex trajectories are compared with two sets of experimental data.

Chapter 5 uses the flow fields generated in this chapter to consider particle entrainment as a result of the vortex ground interaction.

4.2 Review of rotor wake simulation methods

The rotor wake or downwash is defined as the air that has been affected by the rotor, this can include the flow around the blades and the flow further downstream. A rotor wake features a bulk throughput of fluid bound by the wake boundary, a blade tip vortex generated by each rotor blade, a root vortex generated at the root of each blade and a vortex sheet which is generally weaker than either the tip or root vortices but spans the length of the blade - the wake structure is illustrated in Fig. 4.1. The tip vortices are advected with the flow and form a distinctive helix along the wake boundary, the vortex sheet takes on the appearance of a screw. Fluid is entrained into the vortices causing them to grow in size and viscous effects diffuse the vortices over time; eventually the distinctive structures are lost. The smoke visualisations of Lee *et al*. [27] and the results produced in these simulations show all these features, Section 4.4.1.

Several methods have been developed for the simulation of flow around a rotor. The motivations of researchers differ greatly; for some the aim is to understand the flow over a specific blade geometry [122], for others the interaction between the main wake and fuselage is the focus. This chapter is concerned with the complex, unsteady, structures of the wake primarily involving ground — vortex interaction, this requires an IGE rotor wake simulation that models the Blade Tip Vortices (BTVs) and the viscous interaction with the ground.

There are broadly two categories of rotor wake modelling: first-principles methods and vortex tracking methods. First-principles or Eulerian methods solve the conservation of mass and momentum equations on a finite difference or finite volume mesh. Vortex tracking methods generate a wake structure composed of lifting line vortices. The vortex field is solved to produce a velocity field. Other means of evaluating the rotor wake include hybrid methods that combine the vortex wake methods with finite difference methods [123], vorticity embedding or vortex-lattice methods [28]. Here the two main methods will be described but further methods can be found in the reviews of Hariharan and Sankar [124], McCroskey [125] or Sanderse *et al*. [126].

The choice of method for how the wake is modelled is often closely linked to the way the rotor blades are modelled, however, it is often the case that only the blades and the near blade flow are solved.

This review is presented in 3 sections:

1. vortex methods, including the prescribed and free-wake methods, Section 4.2.1.
2. Eulerian wake methods, finite-volume flow solvers used in combination with a blade model, Section 4.2.2.
3. methods of modelling the rotor blades, from actuator disk to body fitted meshes on overset grids, Section 4.2.3.

4.2.1 Vortex methods

There are several different types of vortex method:

- prescribed wake
- free wake
- vortex blob

The simplest of these methods is the prescribed wake, Landgrebe [127]. The prescribed wake method models each blade as a bound vortex or lifting line, the wake is a finite series of straight line vortex filaments each with constant circulation. The flow around the blades is assumed to be two dimensional, radial velocity is neglected. Blade data such as C_L, C_D and α is used to find the circulation of the blade. The Biot-Savart law is used to find the velocity induced by each vortex filament. The method starts with an initial wake geometry which can be theoretical or based on experimental results, the flow field is calculated and the wake geometry is updated, based on the flow field.

Griffiths *et al*. [128] used a free-vortex, or free-wake, method to examine the performance of rotors IGE. The free vortex method was previously implemented by Brown and Whitehouse [129], the method used Lagrangian wake markers and the motion of each wake marker is governed by the velocity field. Each Lagrangian wake marker is periodically released from the blade and a vortex filament binds it to a neighbour in the past and future generating a string of discrete wake filaments emerging from each blade of the rotor. The velocity acting on any wake marker is found through summation of all the velocity induced by each vortex filament found by application of the Biot-Savart law for each filament. This summation is the most computationally demanding part of the method. Griffiths used two methods to model the ground, a symmetry or image condition and a grid of vortex singularities with variable vortex strength; both these methods are inviscid. The vortices themselves are subject to viscous diffusion and strain, both can be modelled for each vortex filament using the methods described by Ramasamy and Leishman [36]. The method assumes wake periodicity, Griffiths claims this a valid assumption but the instability of rotor wakes described by Widnall [37] mixed with the viscous forces involved in the vortex ground interaction gives rise to the suspicion that this assumption will only be valid for an inviscid rotor wake solution.

Bhagwat and Leishman [131] produce a time accurate free-vortex method to predict the wake through manoeuvres or control changes. The work identifies an important limitation of the free-vortex method, either an initial wake or a boundary condition is required to start the wake otherwise the initial vortex may be unstable. Li and Chen [132] make improvements to the numerical algorithm to halve the computation time. Li and Chen use the same initial vortex helix as Bagai and Leishman [133].

The work of Pulla [134] uses the free wake method with both a lifting line and a lifting surface. The lifting line is a line of bound vorticity providing lift, the panel used by Pulla is a 2D

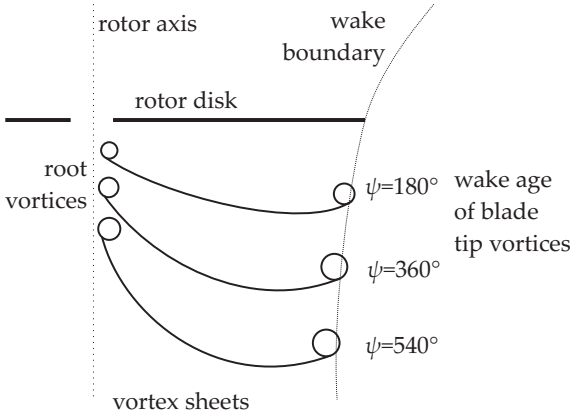

(a) An illustration of the wake structure slice showing the root and tip vortices, the vortex sheet and wake boundary for a rotor in hover OGE.

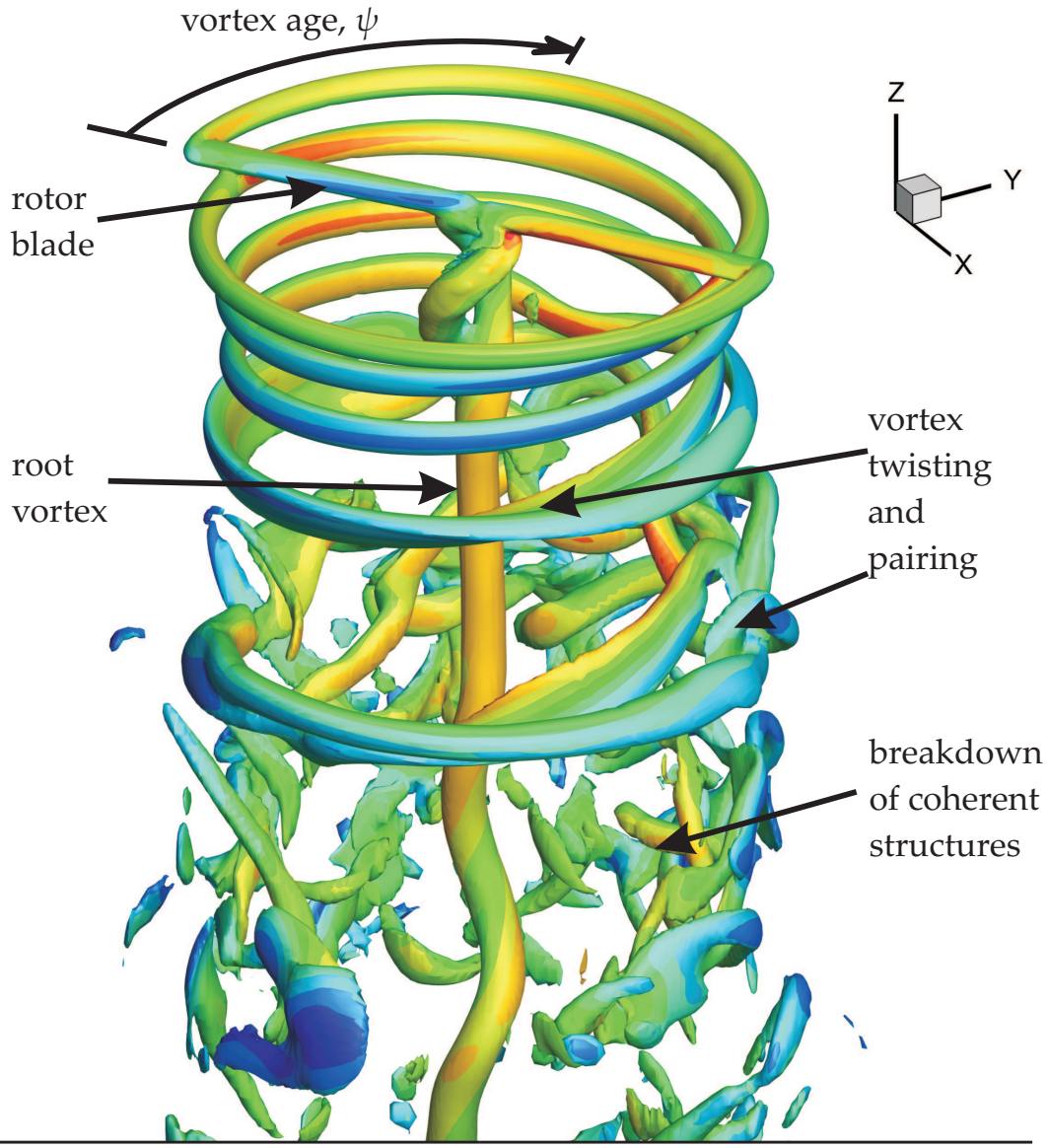

(b) The OGE rotor wake found using the methods described in this chapter. The 3D vortex structures are visualised using an iso-surface of vorticity. Coloured according to velocity magnitude from high, red, to low, blue.

Figure 4.1: The wake structure for a rotor in hover OGE.

grid of horseshoe vortices that distribute the lift over a finite aspect ratio wing. The lifting line considers only the tip vortex for the modelling of the wake but the lifting surface has several trailing vortex filaments along the span. A basic helix is used as an initial solution. The positions of the vortices match the experimental results of Light [135] and Caradonna and Tung [136] for the OGE case.

The vortex blob method, described by Lee and Na [137], is similar to the free-wake method but the vortex blobs are not bound to each other though they still represent a section of a vortex tube. Lee and Na state that the blob method is advantageous as it allows more complex interactions such as those involving co-axial rotors. However, Griffiths [130] used the free-vortex method to study a tandem rotor configuration with reasonable success compared with experimental results. The vortex blob method shares the same limitations for interaction with a ground plane though Lee and Na do not attempt to apply it to the IGE case.

Vortex methods are well established and used for a variety of helicopter studies, however, the inherently inviscid nature of the method does not help explore the viscous vortex-ground interactions.

4.2.2 Eulerian finite volume methods

Eulerian methods are often employed to simulate the flow over a specific blade geometry or around the complex geometry of the helicopter fuselage. They have the advantage that the full Navier-Stokes equations can be solved, including viscosity, but they have the disadvantage that the vorticity can numerically diffuse [138]. They are referred to as first-principles methods because the vortex generation is not seeded or prescribed as in the vortex solution but is a result of the forces on the fluid, the flow field is then determined by the rotor model and any boundary conditions on the grid.

An Eulerian method using a purpose built parallel finite volume code is presented by Allen [139]. A 4 bladed rotor is simulated through time using a body fitted mesh around each blade. The tip vortices seems to dissipate very rapidly; if the smoke visualisation experiments of Lee [27] are compared with the vorticity visualisation of the numerical results by Allen then the number of distinct vortices in the numerical results are significantly less. Xu and Weng [140] used the fifth order scheme to find the flow field around a hovering rotor and compare it to the MUSCL scheme. Details of these schemes can be found in [140]. Xu and Weng used a body fitted C-H mesh around the rotor blades embedded in a cylindrical background mesh. The results show a significantly larger number of distinct tip vortices, the evolution of the vortices matches experiments.

An adaptive grid refinement method is employed during the analysis of a rotor in hover by Wissink *et al*. [141]. The Eulerian solution is found using body fitted unstructured blade mesh overlayed on a structured mesh solved with a high order method to capture the wake. Two rotor capturing methods are used, the first uses a fused mesh but with a rotating coordinate system the second moves the body fitted mesh. The results of both these methods are similar to each other and are within 3% of the experimental result when comparing helicopter rotor efficiency.

Kalra *et al*. [142] use an overset mesh method for the blade and another that generates a helical mesh that tracks the BTVs. The overset mesh method enables the blade to have a body fitted high resolution mesh, $\simeq$1 million cells, that can move through the relatively coarser main mesh, $\simeq$10 million cells. An interpolation scheme is used to transfer data between the two meshes. The method manages to capture four or more revolutions of the helical BTV. Kalra *et al*. also place rotors IGE, with results that capture the trends of the experimental results of Lee *et al*. [27].

Advanced simulations by Thomas *et al*. [143] included an aeroelastic blade dynamics model

coupled with the solution of the flow. Thomas also used overset body fitted meshes to model the blade. Vorticity confinement models were developed by Steinhoff and Underhill [138] to help protect the tip vortices from diffusing too rapidly in finite grid methods. Boelens *et al*. [144] attempt to preserve vorticity by using a hybrid CFD-Lagrangian method and adaptive grids, the results appear to show a tip vortex helix persisting for two revolutions.

Brown and Whitehouse [129] developed the Vortex Transport Method (VTM) designed specifically to conserve vorticity; the same method is used by Philips and Brown [145] in a complete brownout simulation. The method uses a finite volume grid and solver to solve the vorticity transport equation, formulated from the curl of the Navier-Stokes equations. Like the Lagrangian free-wake models the method requires the vorticity in each cell to calculate the velocity field using a modified Biot-Savart law, but this computational expense is reduced by use of a multi-pole method. The VTM manages to preserve the vortex structures far longer than any other method seen in the literature. The method is incompressible and is inviscid for simplicity and because the majority of the flow is in the high Reynolds number regime. The viscous and compressibility effects around the blades are included by use of blade lookup tables. The method of images is also used to model the ground plane and the ground interaction is again inviscid as in the free-wake models.

4.2.3 Blade modelling methods

Different methods of modelling the rotor are described here. The actuator methods exert a force on the flow, they are sometimes referred to as permeable surfaces as the physical presence exerts a force on the fluid but no surface is modelled. The simplification means that no boundary layer is created by the blades in these methods making the immediate flow around the blades inaccurate, however, the method is primarily used by researchers concerned with the larger flow field and in particular the wake downstream of the rotor. Body fitted meshes, on the other hand, are possibly the best way to represent the blade allowing for full resolution of the flow over any specific blade geometry, the computational expense is the cost of this additional detail.

Actuator disk

The actuator disk is based on 1 dimensional momentum theory utilising a disk equivalent to the disk swept out by the blades and a pressure jump providing the thrust, for hover this is simply the weight of the helicopter. In finite volume Eulerian methods the force of the disk can be implemented by using the source term in the Navier-Stokes equation 3.2. The actuator disk method is used in Chapter 6. Sørensen and Kock [146] use an actuator disk method with a blade-element approach allowing the use of 2D aerofoil data to be included in the calculation.

Actuator line

The actuator line is an unsteady form of the actuator disk, a line applies thrust to the flow simulating each blade and each blade rotates around the hub. The actuator line is also implemented using the momentum source term in the Navier-Stokes equation, but more care must be taken on how the force is applied to the discretised space to ensure the force is smoothly applied and there are no jumps associated with the shape of the grid. The actuator line method (ALM) uses no physical surface to represent the mesh, just the force, for this reason the transonic effects and the blade pressure profiles are not present. The ALM is used to model the wake not the blade. Specific data on the blade, such as C_L and C_D, can be applied in much the same was the lifting line method used in the free wake methods previously. The ALM is extremely versatile by nature; since no body fitted blade grid is required the rotor can be easily moved and

implementation of multiple rotors is easy. Mikkelsen *et al*. [147] use the actuator line method to investigate a series of wind turbines positioned behind each other. The ALM is used routinely in wind turbine flow predictions, [148][149][150][38], though has found little use in helicopter studies.

Actuator panel

The actuator panel is an extension of the actuator line, instead of applying force to the flow along a line it is applied over a panel. This requires more computation but gives the opportunity for a more detailed force profile. Watters and Mason [151] implement the actuator surface through application of a discontinuity of the pressure and velocity field in the location of a rotor blade surface, it is stipulated as advantageous because the discontinuity occurs on a cell faces in the computational grid rather than having to distribute a force throughout computational cell volumes. Dobrev *et al.* [152] uses a grid of nodes as a surface and implements a pressure discontinuity across the surface. The immediate flow around the blade produces promising results that are a reasonable match with experiments.

Sliding meshes with body fitted rotor panels

Overset or moving meshes are the most popular methods of modelling the rotor blades in Eulerian helicopter simulations, and offer the chance to truly simulate a blades performance. The meshed blade models the blade surface as a solid wall with a no-slip condition. The Eulerian models previously mentioned, [139][140][141], all used body fitted meshed blades and some form of moving mesh. The body fitted blade mesh method is capable of returning pressure profiles, stall characteristics, compressibility effects or acoustic responses of a blade. The effect on the wake from changes to the geometry of the blade can be considered.

The simulation of rotor interaction with the tail rotor and with the fuselage is an important, albeit secondary, part of the helicopter wake [28]. Several works have added these additional complexities to their simulations [134] [153]. In this study only the main rotor OGE and IGE will be considered to first understand the primary flow, the secondary effects of the fuselage interactions and the tail rotor are left to future consideration.

In this work the primary focus is formulating an unsteady rotor wake simulation to gain deeper understanding of the vortex ground interaction that occurs and is likely the cause of dust inception during brownout. A method that includes viscous forces is required to simulate the boundary layer, the geometry of the rotor or helicopter are of no specific importance. The ALM method is simple to implement and can operate in a viscous flow.

4.3 Methodology

In this simulation the actuator line method is chosen as it is simple to implement but still capable of producing all the features of interest. Mikkelsen [148] explained the implementation of the actuator line method, the explanation is included here with additional details for implementing in Ansys Fluent. For simplicity no drag force was implemented, though induced drag is inherently present due to the tip vortices.

4.3.1 Implementation of the ALM

The ALM was implemented in the commercial flow solver Fluent (version 12.0.16) using a collection of User Defined Functions (UDFs) that provide values for additional source terms, S_i, in the momentum equation, Eq. (3.2). The blade is represented by a line of blade nodes,

momentum is applied to the cell volumes around each blade node using a Gaussian spreading function, the momentum vector is normal to the relative velocity and has no radial component. The `SOURCE` type of UDF is called for each cell volume in the fluid domain for each iteration in every time step, each time the UDF is called the following steps occur:

1. The parameters of the UDF are initialised - the radius of the rotor, R, number of blade nodes, n_b, weight of the helicopter, W_h, angular velocity, ω, location of the rotor hub, $x_{\text{hub},i}$, and where the root cut-out is, R_{cut}, defined in Table 4.1. Next the current fluid cell location, $x_{c,i}$, and velocity, $u_{c,i}$, are retrieved from Fluent.

2. A bounding box is defined around the rotor; for efficiency the UDF checks the location of the current cell, $x_{c,i}$, and if it is sufficiently outside of the rotor bounding box, such that the rotor could never apply force to it, the UDF returns zero.

3. If the cell is within the bounding box the locations of the blade nodes, $x_{b,n,i}$, are found analytically given the current simulation time t and blade node number n. In Cartesian coordinates:

$$x_{b,n,i} = x_{\text{hub},i} + \frac{2}{n_b}\left(n - \frac{n_b - 1}{2}\right) R \begin{bmatrix} \cos(\omega t) \\ \sin(\omega t) \\ 0 \end{bmatrix} \tag{4.1}$$

4. For this fluid cell the distance to each blade node is found, normalised by the length c_w and processed through a Gaussian PDF with standard deviation of c_w.

$$x_{\text{rel},n,i} = x_{c,i} - x_{b,n,i}$$

$$\hat{x}_{\text{rel},n} = \frac{\left|x_{\text{rel},n,i}\right|}{c_w}$$

$$G = \sum_{n=1}^{n_b} W_b \frac{1}{\sqrt{2\pi}} e^{\left(-\frac{\hat{x}_{\text{rel},n}^2}{2}\right)} \tag{4.2}$$

   where $W_b = W_h / n_b$ is the influence of each blade node, c_w is a characteristic cell width which should be larger than the largest cell width in the vicinity of the rotor to keep a smooth spreading. The force magnitude that will be applied to this fluid cell, G, has been found.

5. The momentum vector for this cell is required to be orthogonal to the incident velocity of the blade. This was found for the arbitrary node by first finding the rotational blade velocity of that cell, ωr_c, and then subtracting the fluid velocity of that cell, $u_{c,i}$, as shown in Fig. 4.3 and 4.2:

$$r_c = \left|x_{c,i} - x_{\text{hub},i}\right| \tag{4.3}$$

$$v_{\text{rel},j} = \begin{bmatrix} \omega r_c - \left(u_{c,x}\cos(\theta) - u_{c,y}\sin(\theta)\right) \\ 0 \\ -u_{c,z} \end{bmatrix} \tag{4.4}$$

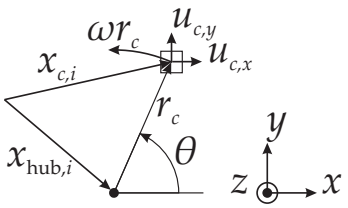

Figure 4.2: Cylindrical coordinate definition for the rotor model. Looking down on the rotor disk: radial distance, r_c, is measured from the hub, θ is measured from the x axis. The cell position, $x_{c,i}$, and velocity, $u_{c,x}$ and $u_{c,y}$, are defined in the Cartesian system. The velocity of the rotating blade is ωr_c at that cell position.

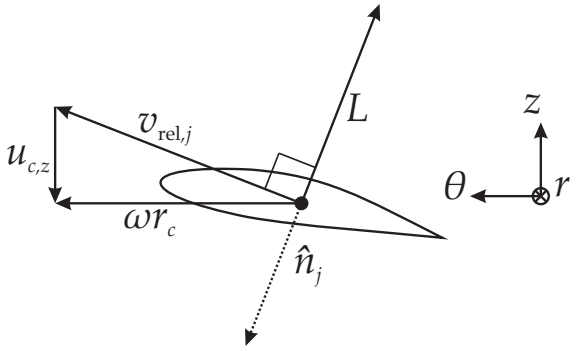

Figure 4.3: Relative velocity definition for the rotor model. A 2D slice, in the θ-z plane, through the blade location. The lift force L is reproduced by applying the ALM force in the $\hat{n}_j$ direction.

where $\theta = \tan_2^{-1} \frac{x_{c,y} - x_{\text{hub},y}}{x_{c,x} - x_{\text{hub},x}}$ is the absolute angle of the fluid cell position relative to the hub and the x axis in the r-θ plane, Fig. 4.2, and $v_{\text{rel},j}$ acts only in the θ-z plane, Fig. 4.3. Subscript $i = 1, 2, 3$ refers to cartesian directions x, y, z and subscript $j = 1, 2, 3$ refers to cylindrical coordinates r, θ, z. Taking the normal unit vector of $v_{\text{rel},j}$ and applying it back to the original 3D Cartesian coordinate system gives the orthogonality desired:

$$\hat{n}_j = \begin{bmatrix} v_{\text{rel},z} / |v_{\text{rel}}| \\ 0 \\ -v_{\text{rel},\theta} / |v_{\text{rel}}| \end{bmatrix} \tag{4.5}$$

The momentum source vector is then:

$$S_{c,i} = G C_{\text{vol}} \begin{bmatrix} -\hat{n}_\theta C_L \sin\theta \left(\frac{|v_{\text{rel}}|}{\omega r_c} \right)^2 \\ \hat{n}_\theta C_L \cos\theta \left(\frac{|v_{\text{rel}}|}{\omega r_c} \right)^2 \\ \hat{n}_z C_L \left(\frac{|v_{\text{rel}}|}{\omega r_c} \right)^2 \end{bmatrix} \tag{4.6}$$

where $C_L = f(1/r)$ is the lift coefficient idealised to provide a near uniform disk loading and C_{vol} is a volume factor given in Step 7. The disk loading provides constant circulation along the blade in the style of the idealised Joukowski rotor [154].

6. The blades of a real helicopter do not extend back to the centre of rotation, the root cut-out is implemented by reducing C_L to zero toward the hub without any discontinuity at the cut off.

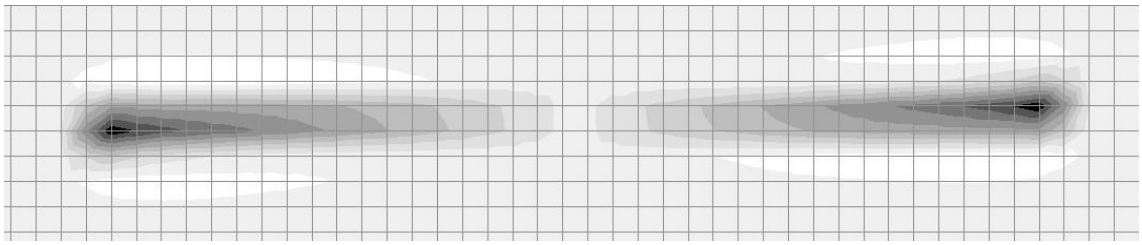

Figure 4.4: One iteration of the Actuator Line method applied to a uniform orthogonal grid, contours of vertical velocity - black is a maximum.

Name	symbol	Description
Disk radius	$R = 0.5$m	Distance from root to tip of the rotor blades.
Cut out radius	$R_{\text{cut}} = 0.05$m	Radius of the root cut out region.
Cell width	$c_w = 0.01$m	Representative cell width for use with the Gaussian spreading.
Helicopter weight	$W_h = 5$N	Weight of the helicopter.
Hub position	$x_{\text{hub},i} = [0, 0, z_d]$	where z_d is the rotor height, Table 4.2
Number of blade nodes	$n_b = 120$	The actuator line applies force around these points.
Angular velocity	$\omega = 47.1$ Rads^{-1}	Angular velocity of the blades.

Table 4.1: Parameters used in the ALM rotor simulation.

$$C_L = \begin{cases} \dfrac{1}{r_c}, & r_c > R_{\text{cut}} \quad (4.7) \\ \dfrac{1}{R_{\text{cut}}} \dfrac{r_c}{R_{\text{cut}}}, & r_c \leq R_{\text{cut}} \quad (4.8) \end{cases}$$

7. The UDF applies the momentum calculated to the volume of the cell, it expects units of N/m^3. The momentum G has units of N, it is scaled by a representative volume: $C_{\text{vol}} = 1/\left(2c_w^3\right)$.

8. Time step is chosen to ensure the blade tip node does not pass more than one grid cell in a time step.

The end result is a cylindrically shaped Gaussian spread of momentum source term around a prescribed rotor location. Running a single iteration of the UDF we can see the virtual blade, Fig. 4.4 illustrates the ALM applied on a course uniform mesh, practically this is an appropriate sanity check for the suitability of the UDF with a specific grid. Figure 4.4 shows the force applied at the tip is larger, however, the residence of the blade on any particular cell is proportional to $1/r$ — the time averaged result is a near uniform disk.

4.3.2 Solution methods

The characteristics of the simulation dictate the best choice of solution method. The rotor wake has strong vorticity, strong pressure gradients, mild swirl components, is highly unsteady and is incompressible. A pressure based transient solver was chosen for this simulation as compressibility is not an issue and we wish to capture the unsteady phenomenon. The PISO pressure-velocity coupling scheme is chosen because it is recommended for transient flows [155,

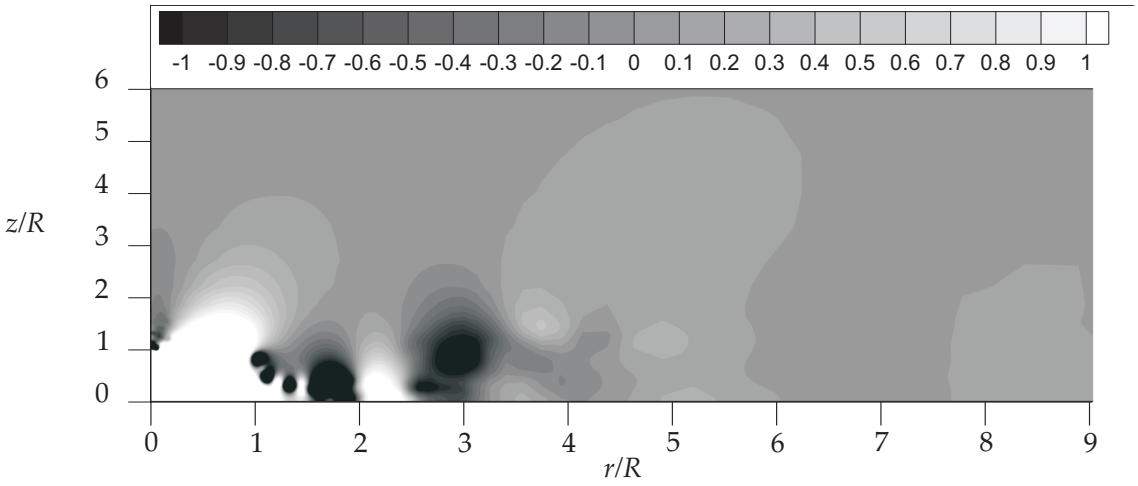

Figure 4.5: Static pressure contours at $t = 90t_{\text{rev}}$ for case $z_d/R = 0.5$, contour levels are $-1 < p_s < 1$ to examine the validity of a 0 total pressure boundary condition.

Ch.26.3.1]. For spatial discretization the PRESTO pressure scheme is noted for solving strong pressure gradients because it solves the pressure at each cell face rather than interpolating it, the momentum scheme was second order upwind. Temporal discretization was performed using a second order implicit method. Computational expense is an important issue; the mesh contained 3×10^6 cells and was run for 24000 time steps, computation took approximately 40 days using parallel processing with up to 36 processes. The simulations were run on the University of Southampton's supercomputer Iridis 3.

4.3.3 Boundary Conditions

The boundary conditions for the OGE case were all constant gauge pressure equal to zero, the constant pressure boundary is implemented by choosing a total gauge pressure, $p_0 = 0$ in this case, the static pressure at the boundary and the velocity are found from Bernoulli's equation, Eq. (4.9).

$$p_0 = p_s + \frac{1}{2}\rho_f |v_i|^2 \tag{4.9}$$

where p_s is the static pressure, $|v_i|$ is the velocity magnitude. The pressure boundary condition is chosen because there is no free stream and the ambient velocity is near zero but mass still needs to enter and leave the domain in an undetermined direction. The extent of the domain was chosen to be far from the rotor and the region of interest, peak wall stress at $r \approx 1.5R$, and sufficiently far radially that the vortices have dissipated. Figure 4.5 shows the static pressure contours around the gauge pressure of zero, it is clear that near the boundaries the pressure is already very close to gauge pressure of zero and pressure gradients near the boundary are also very low. It is therefore shown that the boundary condition and extent are unlikely to have a significant impact on the flow in the centre of the domain.

The boundary condition for the IGE cases were identical save for the no slip wall condition on the lower face. The wall applies the condition of zero velocity normal to the wall and zero velocity parallel to the wall at the surface. For the OGE case the lower boundary is also a constant pressure boundary.

4.3.4 Spatial resolution and temporal resolution of the ALM

The first mesh implemented for use with the ALM was a structured uniform mesh with the rotor hub in the centre. This was a useful way to test and develop the implementation of the ALM as seen in Fig. 4.4. Since the rotor hub was not moving in this simulation a structured cylindrical mesh was developed to provide a consistent pattern of fluid cells to be influenced by the ALM. That is to say the cylindrical mesh reduces the dependence on θ, however, unless the grid is 100% cylindrical and the rotor moves a whole number of cells per time step the output of the rotor will not be truly independent of θ. The chosen mesh reduces this dependence: it is composed of a central small rectangular block surrounded by 4 quadrants to make the cylinder, Fig. 4.6. In the r direction cells are concentrated in region from $R/\sqrt{2}$ to the blade tip, this annulus of concentrated cells contained the predicted wake boundary and vortex trajectory. In z cells are concentrated near the wall and at the disk. Cell distribution is uniform in the θ direction in the quadrants.

Time step, Δt, and grid spacing in the θ direction are linked by ω such that $\omega\Delta t < \Delta\theta$. This ensures blade nodes do not step more than a cell width in a single time step. Given the dimensions in Fig. 4.6 and ω, given in Table 4.1, Δt must be less than 8.3×10^{-4}s. The time step must also be smaller than the time scales of the flow. The vortex time scale is estimated using the vortex width, r_{vort}, measured from peak to peak swirl velocity, v_θ, given by Eq. (4.10) [156]:

$$v_\theta = \frac{\Gamma}{2\pi r_{\text{vort}}} \tag{4.10}$$

where Γ is the circulation and for a two bladed helicopter $\Gamma = T/(R^2\omega\rho_f)$, where T is thrust. The PIV results of Johnson *et al*. [39] show the vortex width to be approximately $r_{\text{vort}} = 3 \times 10^{-2}R$, this yields a swirl velocity of $v_{\text{vort},\theta} = 4.5\text{ms}^{-1}$ and a time scale of $\tau_{\text{vort}} = 2\pi r_{\text{vort}}/v_{\text{vort},\theta} = 0.02$s. To satisfy the rotor and vortex scales a time step of $\Delta t = 5 \times 10^{-4}$ was chosen.

Approximation of Kolmogorov scales

The Kolmogorov scales are the scales of the smallest structures in a flow, they are representative of the smallest scales in the turbulent energy cascade after which the kinetic energy is converted to heat. The Kolmogorov length scale, η, is dependent on the energy dissipation rate, ϵ, which is approximated using Eq. (4.11), where L is the eddy size and $u(L)$ is the characteristic velocity [61, Ch. 6]. The largest length scale eddies are assumed to be the blade tip vortices, their width is estimated as above from Johnson *et al*. [39] to be $r_{\text{vort}} = 3 \times 10^{-2}R$ and $v_{\text{vort},\theta} = 4.5\text{ms}^{-1}$ from Eq 4.10.

$$\epsilon \simeq \frac{u(L)^3}{L} \tag{4.11}$$

$$\eta \equiv \left(\frac{\nu^3}{\epsilon}\right)^{\frac{1}{4}} \tag{4.12}$$

The Kolmogorov length scale, Eq. (4.12), was estimate to be $\eta = 3 \times 10^{-5}$m, Kolmogorov velocities and time scales were estimated to be $v_\eta \simeq 0.5\text{ms}^{-1}$ and $\tau_\eta \simeq 5 \times 10^{-5}$s respectively. The average mesh cell size in the region $0.4 > r/R > 1.2$ is $l_{\text{cell}} = 9 \times 10^{-3}$m. The smallest physical fluid scales are approximately 300 times smaller than the numerical grid spacing. The Kolmogorov scales are based on the assumption that $\text{Re}_L \gg 1$ and that the turbulence is isotropic. It is clear that this turbulence is not isotropic as the vortex structures are part of a large helix with no other vortices of that magnitude departing from that original orientation. The Reynolds number of the energy containing scale is $\text{Re}_L \simeq 2 \times 10^3$, large enough that the scales are not affected by viscosity indicating that second Kolmogorov Hypothesis applies to this

case	rotor height, z_d	domain height $z_{\max}$
IGE-25	$0.50R$	$3.0R$
IGE-34	$0.68R$	$3.0R$
IGE-75	$1.50R$	$3.0R$
IGE-200	$4.00R$	$6.0R$
OGE	$4.00R$	$6.0R$

Table 4.2: Rotor simulation cases, rotor disk height from ground and number of cells in the grid.

direction at least. The Kolmogorov time scale, τ_η, is an order of magnitude smaller than the chosen time step. Consider the comparison between the structures in Fig. 4.9 – whilst it is clear that the smallest structures are not resolved numerically, the large structures appear to be well resolved and the transition from coherent structure to incoherent turbulence happens at a similar rate.

The objective of these simulations is to understand the evolution of the large structures, the tip vortices, through time and space. If the smallest scales are not resolved then the energy cascade is cropped short of the Kolmogorov scale and all the transfer of kinetic energy to heat energy happens at that scale, the large scales now lose energy more rapidly than they would. In isotropic turbulence the energy spectra could be compared against the $-5/3$ gradient to examine the rate of dissipation [61], here the turbulence is dominated by the rotor tip vortices and is therefore not isotropic. Presuming that not resolving the smallest scales causes an increase in dissipation the analysis is made with the understanding that the large scales are diffusing more rapidly than they should be. However, the following validations show that the level of resolution is sufficient to produce phenomena seen in experiments and in photographs of full scale helicopter dust entrainment.

Reference scales for nondimensionalisation

The flow field results are non-dimensionalised for verification in this chapter and analysis in Chapter 5. Velocities in the rotor wake are non-dimensionalised with the induced velocity, v_{ind}, based on the thrust, T, 4.13 from 1D momentum theory:

$$v_{\text{ind}} = \sqrt{T/2\rho A_{\text{disk}}} \tag{4.13}$$

where Figure 4.14e shows the mean velocity magnitudes of slices through the flow field. The non-dimensionalised velocity at the disk in Fig. 4.14e is 1, showing that in the OGE case the mean flow field through the disk is mostly uniform and approaches the 1D solution. For the IGE cases: as the rotor approaches the ground the velocity profile from hub to blade tip, $r = 0 \rightarrow R$, shifts from near uniform velocity and becomes more concentrated at the blade tip as the rotor approaches the ground.

Length and time are nondimensionalised by R, the blade radius, and $t_{\text{rev}} = 2\pi/\omega$, the blade revolution time. Using R/v_{ind} for the time scale is not very useful, but t_{rev} is associated with the frequency of vortex creation and helps characterize the vortex intermittency.

4.3.5 Rotor simulation cases

The rotor simulation was carried out using 4 different IGE heights and a single OGE height. In all cases the rotor was stationary with respect to the ground and the ambient fluid. The case names and rotor heights are summarised in Table 4.2.

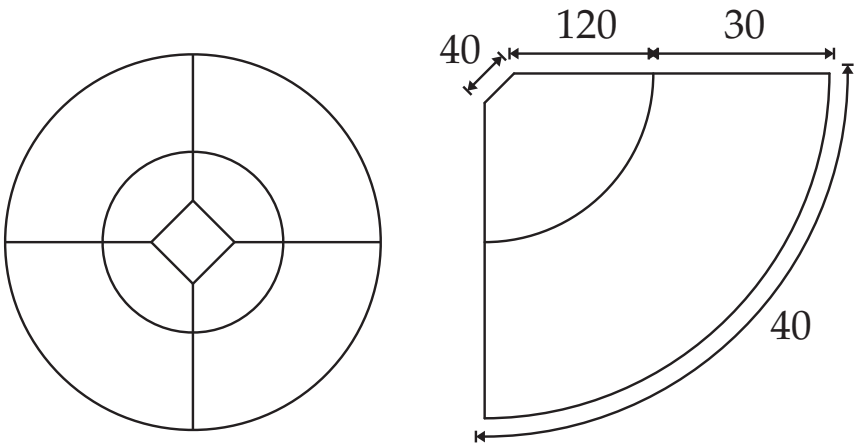

(a) The structured cylindrical mesh is composed of a small square core and 4 quadrants. The quadrant dimensions are given in cell number.

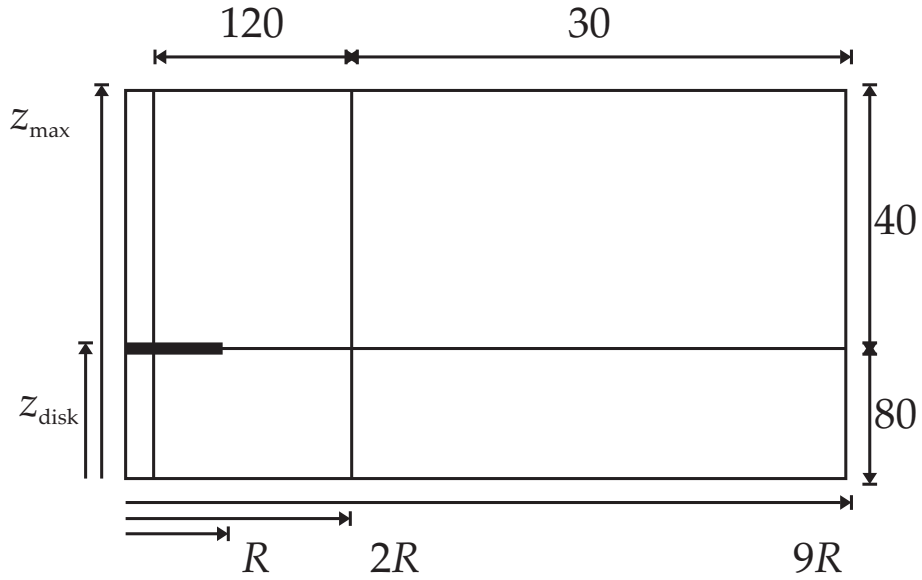

(b) Side view of a quadrant. Dimensions above and right are cell number, below and left are distance.

Figure 4.6: The grid shape and dimension, z_{disk} and z_{max} are defined in Table 4.2.

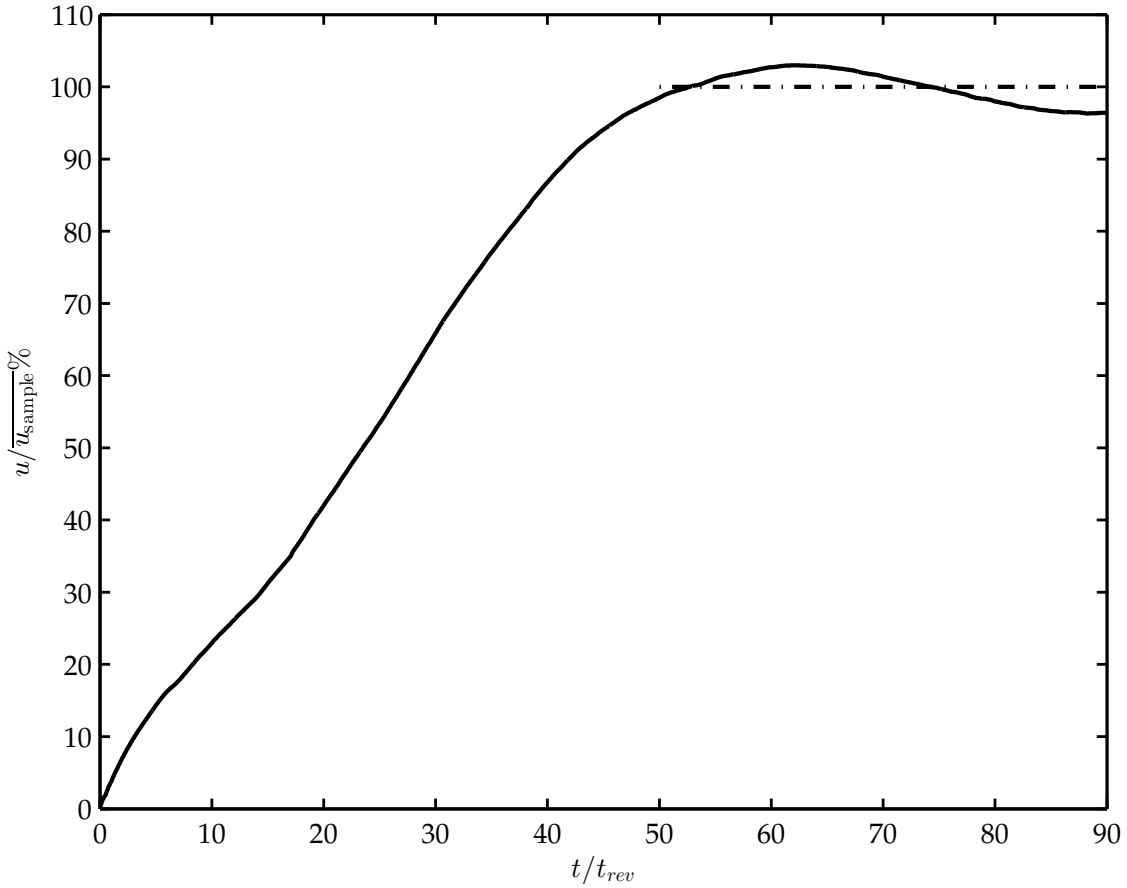

Figure 4.7: The average velocity magnitude of the entire domain over time presented as a percentage of the mean of the analysed data $50 < t_{\text{rev}} < 90$, for case $z_d/R = 0.5$.

4.3.6 Data captured during simulation

The 5 simulations performed exported 3 data sets:

1. a complete flow field every ten time steps.
2. a near wall slice in the vertical plane, from the ground to approximately $0.1z_d$ in height and from the rotor hub, $r = 0$, to the extent of the domain, $r = 9R$.
3. a volume encapsulating the rotor recording all the momentum added by the rotor in the current time step. This data set is recorded every ten time steps.

Additional data can be extracted post-process from the complete flow field in Item 1 as often as every 10^{th} time step, the majority of analysis in Chapter 5 is performed on full scale slices from the axis to the edge of the domain extracted every ten time steps.

4.3.7 Statistical stationarity

To be confident of any statistical analysis it must be first established whether the flow is statistically stationary. The mean velocity magnitude of the entire domain over time for case $z_d/R = 0.5$ is shown in Fig. 4.7. The velocity increases as the flow field develops and settles once the wake reaches the edge of the domain. The statistical analysis in this work is performed on data $50 < t_{\text{rev}} < 90$, in this region there appears to be a slow perturbation acting in the flow, this could be due to vortex interactions — regardless of the cause the magnitude of the perturbation is low $\pm 5\%$.

4.3.8 Using Richardson extrapolation to quantify the spatial discretisation error in the unsteady rotor simulations

The Rotor simulations were performed on a middle resolution grid, g_2, a higher resolution mesh, g_1, and a lower resolution mesh, g_3, were constructed for the $z_d/R = 0.5$ case to assess the error associated with the grid. The higher resolution mesh took considerably longer to run, as such it was not run to the extent that the entire flow domain can be considered statistically stationary. The alternative is to asses a specific quantity, in this case the tip vortex width, at a location $\psi = 0.1$Rad where the flow is statistically stationary in a relatively short time. This flow quantity was chosen as it the tip vortex is in a deterministic location and the width can be extracted of the vortex throughout time can be reliably found for each grid with relative ease.

The Richardson extrapolation [157][158] is a method that uses the known ratio in the grid spacing and the solution order to calculate an approximation of a flow quantity in a continuous, zero grid spacing, solution. In this case there are 3 grids, g_1, g_2, g_3, each with half the grid spacing, h_1, h_2, h_3, of the previous one. The solution is calculated using second order methods and should nominally have an order of convergence $p_c = 2$, however the order of convergence can be found directly from the results using Eq. (4.14):

$$p_c = \ln\left(\frac{f_3 - f_2}{f_2 - f_1}\right) / \ln\left(m_{\text{ratio}}\right) \tag{4.14}$$

where $f = \overline{2r_c}$ is the flow quantity compared - in this case the vortex width for each grid averaged across time and the spatial zone and $m_{\text{ratio}} = h_2/h_1 = 2$ is the mesh refinement fraction.

Richardson extrapolation

Richardson extrapolation [158] can be used to find an approximation of the continuum solution from known solutions with different grid spacings. The estimate of the continuum solution can also be used to assess the discretisation error associated with a certain grid resolution.

A flow quantity, f, can be considered as the sum of a series, Eq. (4.15):

$$f = f_{h=0} + g_1 h + g_2 h^2 + g_3 h^3 + \text{...higher order terms} \tag{4.15}$$

where $g_{1,2,3}$ are functions independent of grid spacing, h is the grid spacing and $f_{h=0}$ is the continuum solution of the quantity f. If $g_1 = 0$ the value of f is considered second order. If two grids, h_1 and h_2, are used to find the same quantity, f_1 and f_2, then Eq. (4.15) can be used to generate two series, solving for $f_{h=0}$ give:

$$f_{h=0} \cong f_1 + \frac{f_1 - f_2}{r_g^{p_c} - 1} + \text{higher order terms} \tag{4.16}$$

where r_g is the grid refinement ratio, $r_g = h_2/h_1$, and p is the order of the solution found in Eq. (4.14). The value $f_{h=0}$ is now used to assess the discretisation error of the grids. We must not presume that $f_{h=0}$ is the exact solution, it only purports to be the continuous grid solution and the Richardson extrapolation is used to assess the grid discretisation error, not the error that results from boundary conditions or solution of the governing equations. The extrapolation will magnify machine rounding errors and incomplete iteration errors and assumes 'monotone truncation error in the mesh spacing h' [159].

The error can be estimated for f_1 with:

$$A_1 = E_1 + \mathcal{O}\left(h^{p_c+1}, E_1^2\right) \tag{4.17}$$

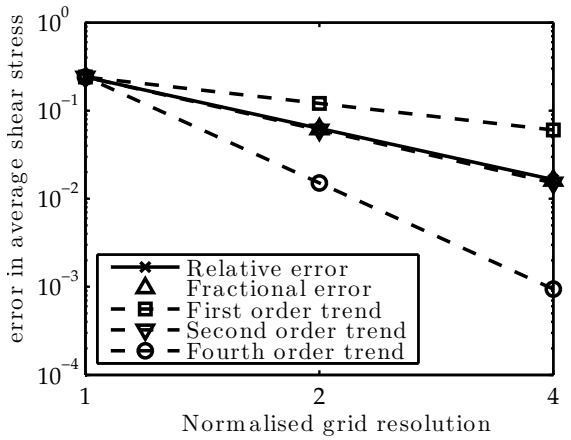

Figure 4.8: The relative error % of the tip vortex width for 3 different resolution grids.

where A_1 is the actual fractional error:

$$A_1 = \frac{f_1 - f_{h=0}}{f_{h=0}} \tag{4.18}$$

and the estimated fractional error E_1 is:

$$E_1 = \epsilon / \left(r_g^{p_c} - 1 \right) \tag{4.19}$$

$$\epsilon = \left(f_2 - f_1 \right) / f_1 \tag{4.20}$$

E_1 is a labelled as an ordered error estimator by Roache [159], that is "'an ordered approximation to the actual fractional error of the fine grid solution"'. Further a good approximation of the error is achieved by E_1 when $E_1 \ll 1$. In this work the middle resolution grid is used for the main analysis, to estimate the error of the h_2 grid we first present the Richardson extrapolation:

$$f_{h=0} \cong f_2 + \frac{\left(f_1 - f_2 \right) r_g^{p_c}}{r_g^{p_c} - 1} \tag{4.21}$$

and the error estimator for the middle resolution grid, E_2, is then expressed as:

$$E_2 = \frac{\epsilon r_g^{p_c}}{r_g^{p_c} - 1} \tag{4.22}$$

Given the average of the tip vortex width for each grid, $f_{1,2,3} = r_{c\,1,2,3}$, the estimated fractional error was found to be $E_1 = 1.7\%$ and $E_2 = 6.2\%$. The relative error, E_{abs}, was found for each grid size n using the Richardson estimated continuum solution $r_{c,h=0}$, $E_{\text{abs},n} = (r_{c,n} - r_{c,h=0})/r_{c,h=0}$ and plotted in Fig. 4.8. The relative and fractional error are reported in Fig. 4.8 and it can be seen that they differ only very slightly. The order of convergence was found to be $p_c = 1.94$ very close to the 2^{nd} order we expect.

Summary of the spatial discretisation assessment

In this section the Richardson extrapolation method was used to assess the discretisation error of the finite volume grids used in this rotor flow field. The middle grid resolution was used for the analysis in the remainder of this chapter; it has been shown that the results of this flow field, in the near rotor region, suffer from a 7% error due to spatial discretisation. In the remainder of this flow analysis we wish to understand the dynamics of the tip vortices. These large flow features

are explored in the next section.

4.4 Validation

In this section the flow field is visually compared with an experimental flow, the near wall mesh resolution is quantified and several different quantities are validated against experimental data from the literature.

4.4.1 Flow visualisation: a qualitative comparison

The flow field of the OGE case was visualised by plotting contours of vorticity and compared with the smoke visualisation of Lee *et al*. [27] in Fig. 4.9, stream lines were added to the numerical plot to show were fluid is entrained. A vorticity contour plot will not produce the same image as smoke visualisation but the vortex structures are highlighted by both methods. Figure 4.9 is a 2D slice through the 3D structure shown in Fig. 4.1b, but Fig. 4.1b is an iso-surface and only shows a single value of vorticity - Fig. 4.9 shows a range of vorticity values.

Figure 4.9 shows the same large structures exist in the simulation as in the experiment: a series of tip vortices define the wake boundary which necks beneath the rotor, vortex pairing is evident, fluid entrainment causes vortex growth and the coherence structures have largely dissipated beyond $3R$ below the disk. Differences in structure can be attributed to the differences in rotor configuration. The vortices in the experiment are further apart because of a larger ratio of induced velocity to angular velocity of the blade. Uniform blade loading on the numerical rotor causes the vortex sheet to stay more aligned with the rotor disk, the experimental rotor has a tip—heavy blade loading which causes the vortex sheet to angle downward at the tip. The comparison in Fig. 4.9 shows the smallest scales are not resolved by the simulation.

4.4.2 Near wall mesh resolution

The quality of the near wall mesh resolution was assessed by calculating the non-dimensional wall normal distance, y^+, for the first cell Eq. (3.20). For a fully developed turbulent boundary layer the mesh should be fine enough for $y^+ \simeq 1$ at the first cell, this enables the viscous sublayer to be resolved. In this flow field the boundary layer is not fully turbulent so it is difficult to assess how close the first cell should be. Nevertheless the first cell y^+ is reported in Fig. 4.10, averaged over time. The peak y^+ occurs at the peak wall shear stress, $1 < r/R < 2$, in this region the first wall cell is positioned between 20 and 50 y^+, the beginning of the log-law layer. This spatial resolution is insufficient to correctly resolve the near wall turbulent scales, however, the purpose of this analysis is to understand the dynamics of the large scale vortices.

4.4.3 Comparisons with experimental data

Before analysing the numerical flow results in the context of brownout three comparisons are conducted between these results and experimental results in the literature:

- the variation in power required for the rotor at different heights IGE.
- tip vortex trajectory.
- radial velocity profile.

To compare the data a number of parameters need to be defined. The rotor thrust coefficient, C_T, is defined as:

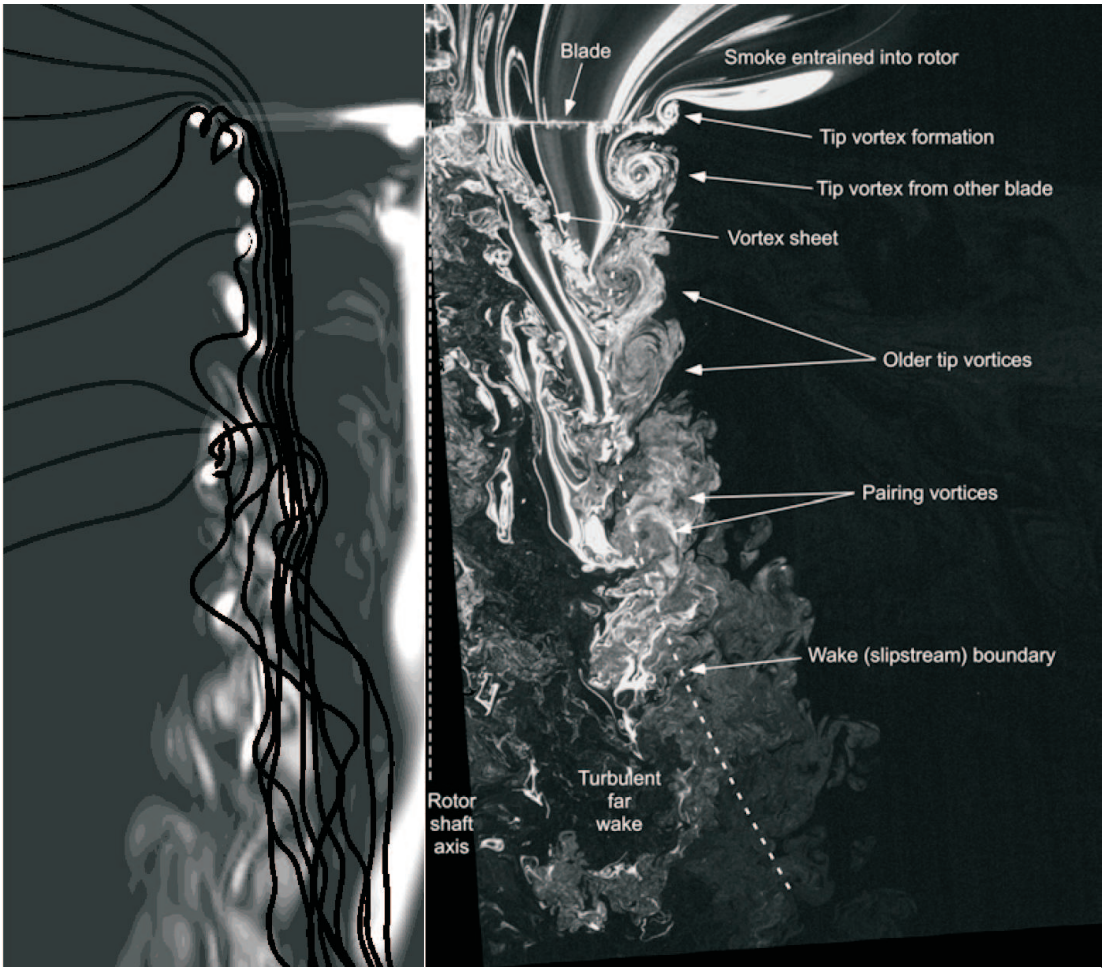

Figure 4.9: Left: contours of vorticity of a slice through the axis from the OGE case with streamlines, Fig. 4.1b shows a 3D image of this flow field. Right: smoke visualisations produced by Lee *et al*. [27] reproduced here with permission. The streamlines show entrainment, this is seen as smoke free air drawn into the vortices in particular the 'older tip vortices' indicated.

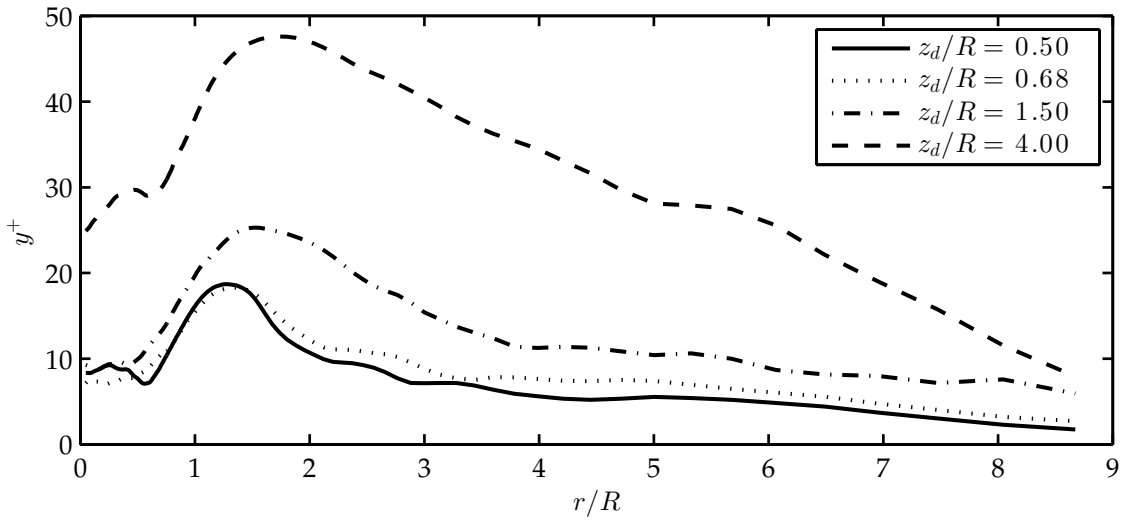

Figure 4.10: First near wall cell y^+ with r for each case.

$$C_T = \frac{T}{\frac{1}{2}\rho A(\Omega R)^2} \tag{4.23}$$

where T is the thrust, A is the disk area and Ω is the angular velocity of the rotor. The thrust is calculated as the sum of the vertical thrust in each fluid cell. The thrust coefficient, C_T is often normalised by the disk solidity, $\sigma = \frac{N_b c R}{\pi R^2}$, the ratio of blade area to disk area. If Eq. (4.13) is substituted into the expression for the thrust coefficient, Eq. (4.23), it becomes the ratio of the induced velocity, v_{ind}, to the tip velocity, ωR. This is the effective pitch in the vortex helix and should define the spacing between vortices, however, the blade loading changes the velocity distribution across the wake which can change the vortex spacing. The power coefficient is defined in a similar manner to C_T:

$$C_P = \frac{P}{\frac{1}{2}\rho A(\Omega R)^3} \tag{4.24}$$

where P is the power, calculated as shaft power and is found by summing the power contribution from each fluid cell:

$$P = \sum_{c=1}^{n_c} (r_{c,i} S_{c,i}) \bullet \Omega_i \tag{4.25}$$

Where $S_{c,i}$ is the force vector applied at cell c at radial position $r_{c,i}$, Eq. (4.6). It should be noted here that the nominally American system does not include the factor of a half in the denominator of Eq. (4.23) and 4.24 but the British system does, the latter is employed throughout this work - data from other works is converted to the British system.

Power required in IGE

It is a well known phenomena that power required to hover with constant thrust in ground effect is less than out of ground effect. The proximity of the ground heavily influences the wake. Figure 4.11 shows the power required to maintain constant thrust at different heights IGE as a ratio to power required to hover OGE, power is calculated using Eq. (4.23). The proximity of the ground acts to inhibit the incident velocity at the blade this effect is more pronounced the closer the rotor is to the ground.

The implementation of the ALM, described in Section 4.3.1, is designed to produce constant vertical thrust. As the ALM implemented here has no explicit drag the power measured is induced power, but Hayden [161] surmises that ground effect primarily alters the induced power rather than profile power. Figure 4.11 presents the power reduction at different heights IGE alongside the experimental results of Lee *et al*. [27] and the analytical expressions of Cheeseman and Bennett [160], Eq. (4.26), and Hayden [161], Eq. (4.27).

$$\frac{P_{\text{IGE}}}{P_{\text{OGE}}} = 1 - \frac{1}{16}\left(\frac{R}{z_d}\right)^2 \tag{4.26}$$

$$\frac{P_{\text{IGE}}}{P_{\text{OGE}}} = \frac{1}{0.9926 + 0.0379\,(2R/z_d)^2} \tag{4.27}$$

The rotor modelled using the ALM method does not appear to have such a dramatic power reduction as found by Lee *et al*. but more so than that predicted by Cheeseman and Bennett; once below $z_d/R = 1.5$ the behaviour of this rotor is similar to both. The rotor used by Lee *et al*. had a non-uniform blade loading, this is apparent in smoke visualisations [27] as non-horizontal vortex sheets. The blade is uniformly loaded in this simulation, there is some evidence that blade loading can alter the IGE performance [162, Ch. 5] and Lee *et al*. [27] conducted tests with a

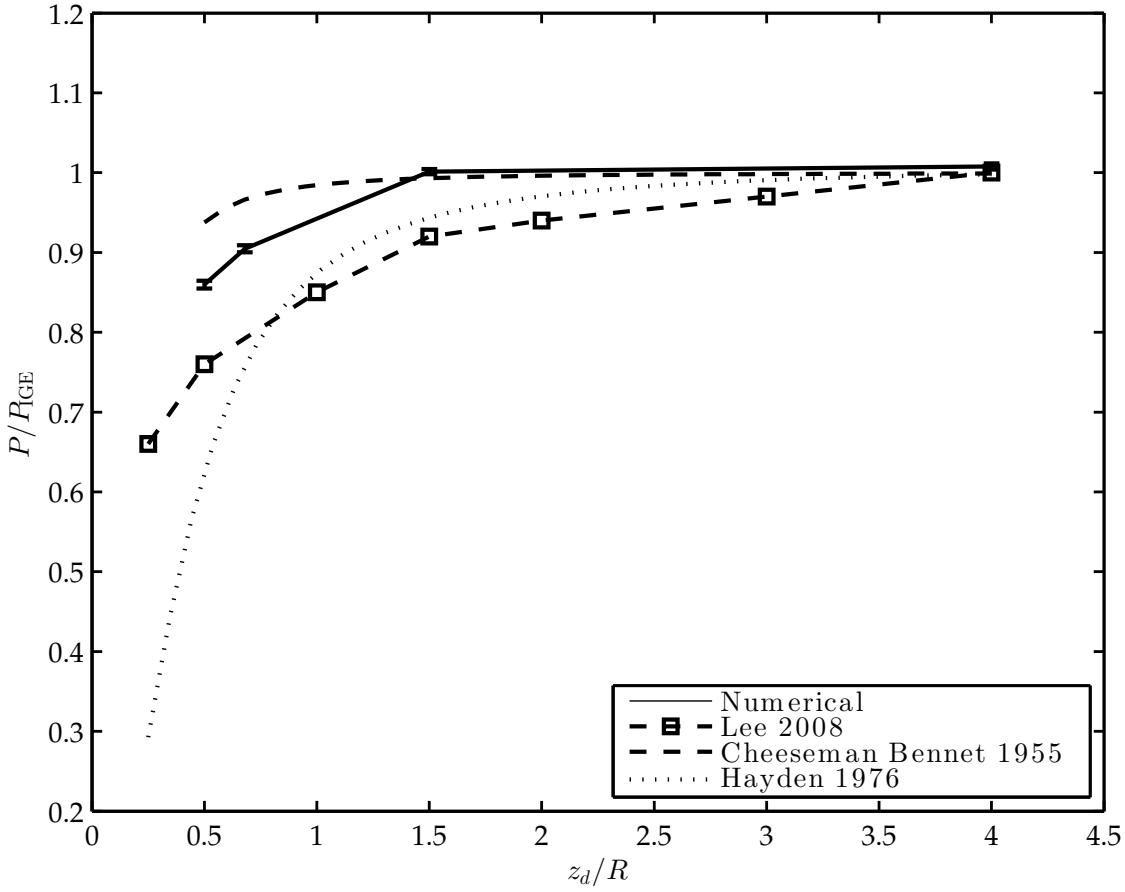

Figure 4.11: Power required to hover IGE: experimental results of Lee *et al*. [27], analytical prediction of Cheeseman and Bennett [160], Hayden [161] and numerical results from this work.

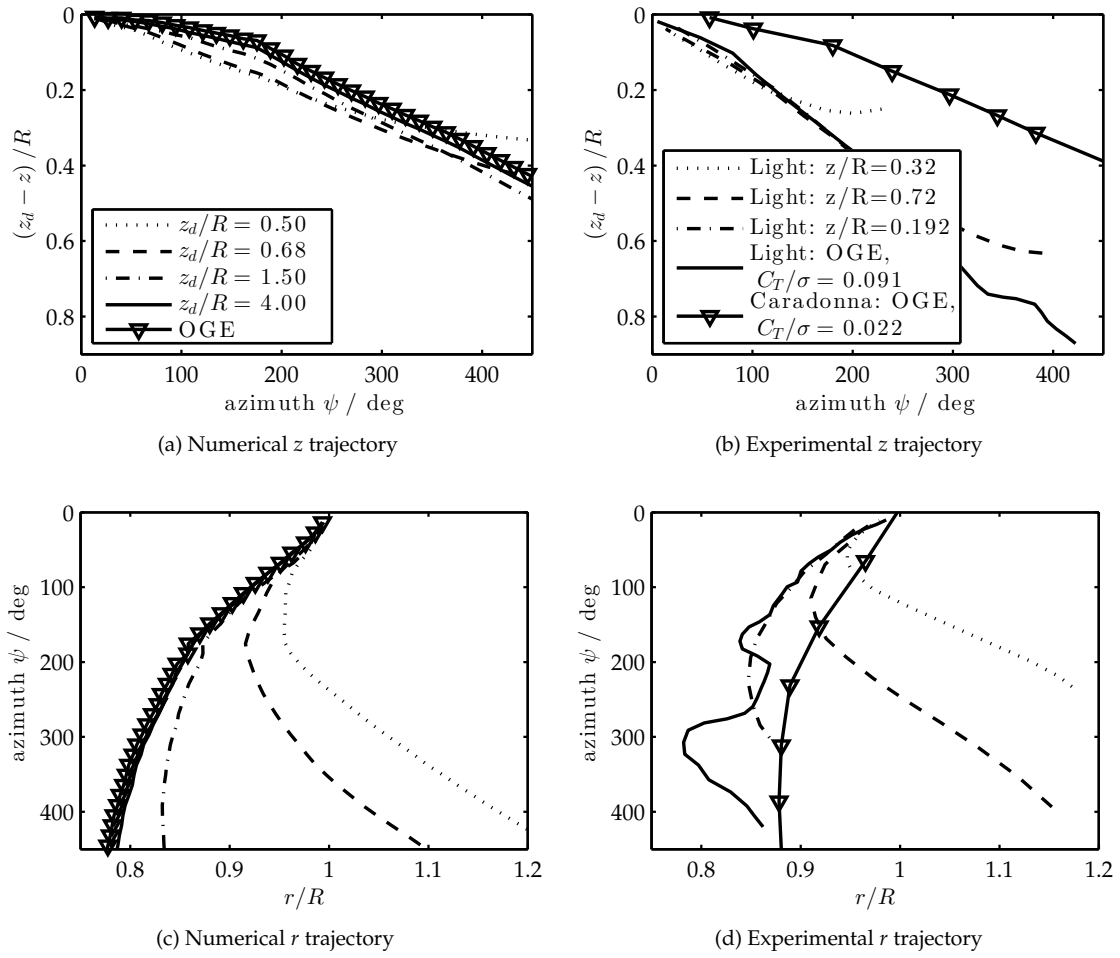

(a) Numerical z trajectory

(b) Experimental z trajectory

(c) Numerical r trajectory

(d) Experimental r trajectory

Figure 4.12: Vortex trajectories, experimental results of Caradonna and Tung [136] and Light [135] compared to numerical results from this work. Azimuth is a measure of vortex age measured by blade rotation since generation, see Fig. 4.1.

range of C_T/σ and found higher thrust loadings gave a greater power reduction.

Vortex trajectories

The wake shape and evolution can be compared by considering the position of the tip vortices over time, non-dimensionalised to azimuthal angle. Figure 4.12a and 4.12c present the position of the blade tip vortices from this work, Fig. 4.12b and 4.12d present data from Caradonna and Tung [136] and Light [135]. It is first obvious that the two experimental data sets do not align — the vortices from the Light rotor descend quicker. This maybe due to the different values of thrust coefficient, Caradonna and Tung [136] used $C_T/\sigma = 0.022$ while Light [135] used $C_T/\sigma = 0.091$, however, the trends of the two experimental results agree. The experimental results of Light [135] were not performed at the same rotor heights as the numerical studies but the trends are comparable. The numerical results do not diverge as early, the gradient indicates they are descending slower implying that the change in trajectory occurs with a certain proximity to the ground. A lack of disturbance in the experimental trajectories of Light [135] at $\psi = 180°$deg, the moment when the second blade passes indicates the vortex is outside the influence of the blade after half a revolution, a disturbance is clearly visible in the results of this work, Fig. 4.12a, and in the results of Caradonna and Tung [136], Fig. 4.12a.

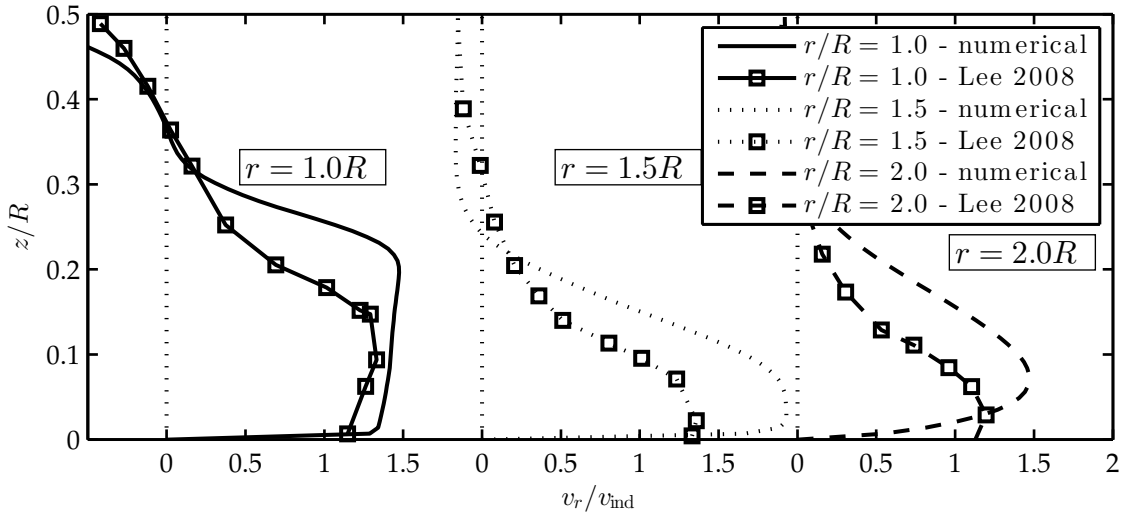

(a) $z_d/r = 0.5$

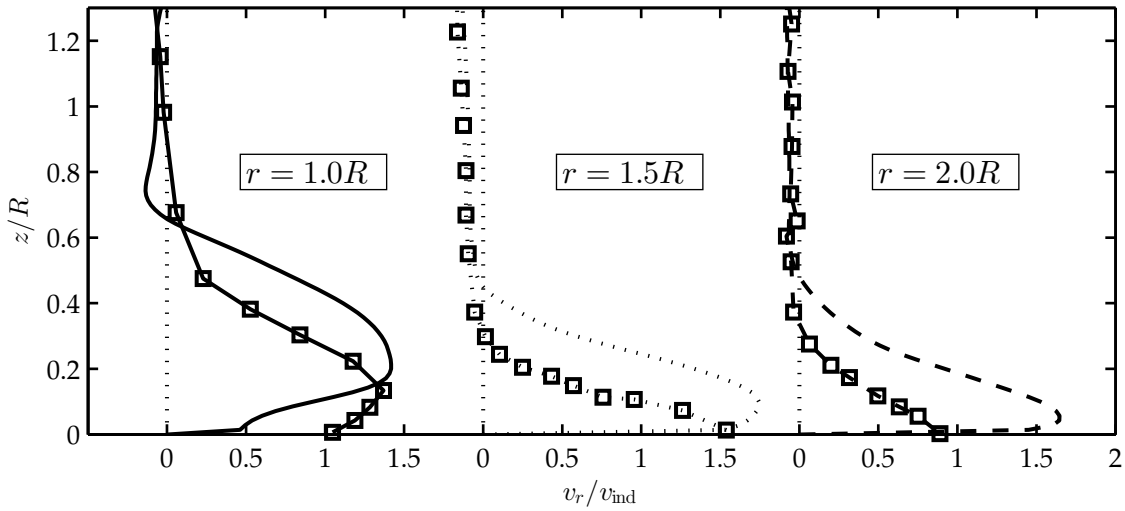

(b) $z_d/r = 1.5$

Figure 4.13: Radial velocity profiles comparing experimental results of Lee *et al*. [27] with numerical results of this work.

Radial velocity profile

Lee *et al*. [27] report time averaged radial velocity profiles, $u_r(r, z)$, at 3 radial positions for IGE heights of $z_d/r = 0.5, 1.5$ from their rotor experiments. The velocity is non-dimensionalised using the induced velocity Eq. (4.13). The radial velocity from these simulations is presented with results of Lee *et al*. [27] in Fig. 4.13. It is seen that the numerical flow is a different shape: the peak radial velocity is further from the ground plane throughout and the peak velocity is larger for the more distant radial positions. This again maybe due to the blade loading profile, the experimental profile shows that necking of the wake boundary extends closer to the ground than the numerical profile. The trends are repeated in both experimental and numerical profiles: the velocity is greatest at $r = 1.5R$, at $r = 1.0R$ the radial profiles are thick and then become thinner. It can be seen that the numerical results have overestimated the boundary layer thickness and underestimated the wall shear stress. These results are intended to gives us qualitative understanding of the unsteady flow behaviour and specifically the intermittency generated by the vortices.

4.5 Results

In this section the mean flow field results are presented, the shape of the velocity field helps consider the effect of the boundary conditions and the change in blade loading as the disk approaches the ground. The turbulent kinetic energy, k, and enstrophy, ω^2, help visualise where the flow is highly turbulent and indicate where dissipation is active. The wall shear stress is shown with the mean, standard deviation and skewness to give some indication of non-Gaussian nature of the wall shear stress fluctuations. Mean quantities depicted in this section are calculated for each point in space and averaged over the sample time given in Section 4.3.7, as in Eq. (4.28):

$$\overline{\phi}\left(x_i\right) = \int_{t=50t_{\text{rev}}}^{t=90t_{\text{rev}}} \phi(x_i, t)\mathrm{d}t \tag{4.28}$$

4.5.1 Mean velocity field

The mean flow field is given in Fig. 4.14. For clarity the figures have been cropped to the region of interest, additionally for context Fig. 4.15 gives the full extent of the domain for each case.

The full extent of the domain is given in Fig. 4.15, streamlines have been included in these plots to show pressure changes. Some boundary effects are visible: in Fig. 4.15b a contour above the disk has a small kink not present in Fig. 4.15a, likewise in Fig. 4.15c and 4.15d. The contours closer to the disk, however, are smooth and the streamlines smoothly change shape as they move away from the boundary indicating no dramatic pressure change. At the eastern edge the streamlines are parallel in all but the $z_d/R = 4.0$ case where they smoothly spread apart suggesting the pressure is forced to increase at the boundary. The pressure increase only occurs after $r = 7R$ giving confidence that the region of interest, typically $< 4R$, is not affected by the pressure boundary. The pressure plot in Fig. 4.5 gives another look at how the pressure boundary might effect the flow.

4.5.2 Turbulent kinetic energy

Turbulent kinetic energy is calculated as the kinetic energy due to the flow fluctuations per unit mass:

$$k = \frac{1}{2} < v_i' v_i' > \tag{4.29}$$

where v_i' is the fluctuation component of velocity. Figure 4.16 shows the mean turbulent kinetic energy (TKE) for each case. For all cases the peaks are at the blade root and at the rotor tip both places of strong vorticity. The path of the tip vortex has strong k and it can be seen that this kinetic energy spreads out similarly to the vortex paths seen in Fig. 5.14a. There is also strong TKE around the path of the root vortex; the rotor positions closer to the ground, Fig. 4.16a and 4.16b, have a incoherent region of high TKE beneath the rotor but in Fig. 4.16c the TKE of the root vortex is very coherent. For the heights of $z_d/R = 1.5$ and 4.0, Fig. 4.16c and 4.16d, the TKE associated with the root vortex seems to be more present near the ground than the TKE associated with the tip vortex. In all 4 cases with ground there is a significant amount of TKE in the boundary layer around $1.5R < r < 3R$, in this region the fluid in the boundary layer contains high energy fluctuations and this will be seen by the particles.

4.5.3 Enstrophy

Enstrophy is the square of vorticity , ω_f^2, and it is an indicator of the rotational kinetic energy. The global average of enstrophy and dissipation are related by the kinematic viscosity as: $< \epsilon >= \nu < \omega^2 >$.

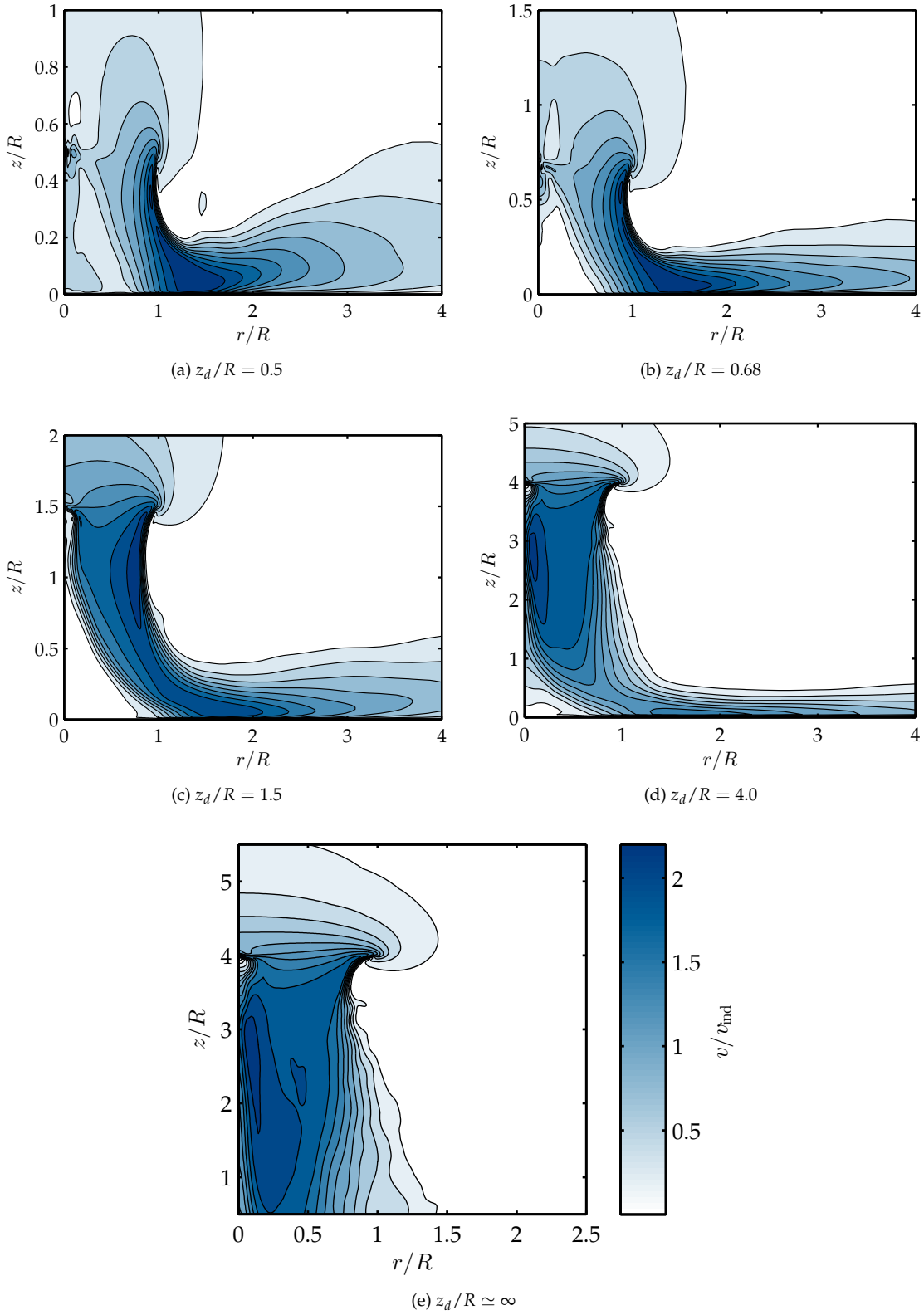

(a) $z_d/R = 0.5$

(b) $z_d/R = 0.68$

(c) $z_d/R = 1.5$

(d) $z_d/R = 4.0$

(e) $z_d/R \simeq \infty$

Figure 4.14: The mean flow field, velocities non-dimensionalised with v_{ind}. Slice in $z - r$ plane.

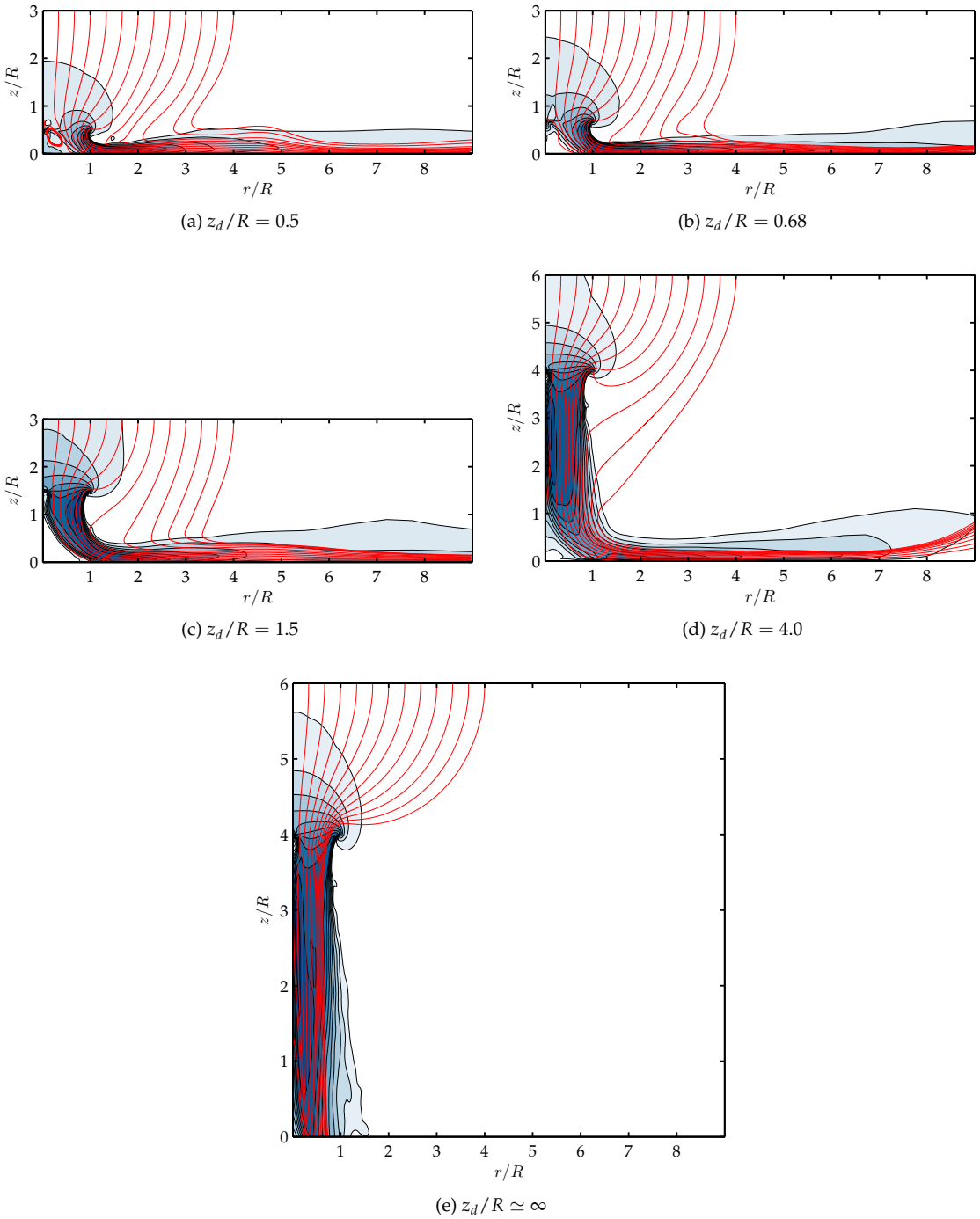

(a) $z_d/R = 0.5$

(b) $z_d/R = 0.68$

(c) $z_d/R = 1.5$

(d) $z_d/R = 4.0$

(e) $z_d/R \simeq \infty$

Figure 4.15: The mean flow field of the complete slice for each case. The contour levels of velocity magnitudes are the same as in Fig. 4.14.

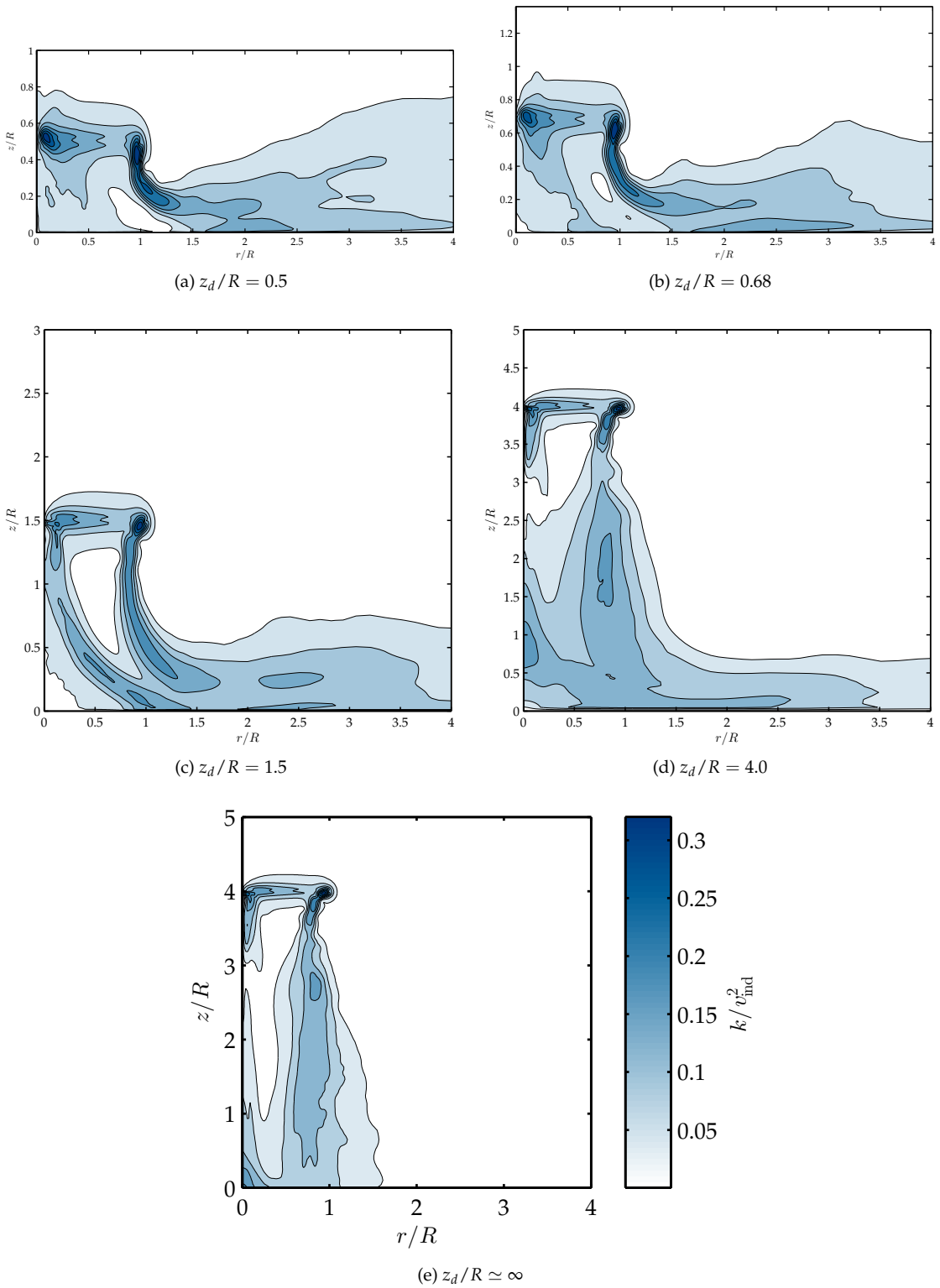

(a) $z_d/R = 0.5$

(b) $z_d/R = 0.68$

(c) $z_d/R = 1.5$

(d) $z_d/R = 4.0$

(e) $z_d/R \simeq \infty$

Figure 4.16: The mean turbulent kinetic energy field, k, of the complete slice for each case nondimensionalised by v_{ind}^2.

Mean enstrophy for the slice through each case is given in Fig. 4.17. It is clear that enstrophy is highest where the tip and root vortices are strongest, there is also strong enstrophy in the boundary layer at $r \simeq 2R$. It is expected that dissipation and therefore enstrophy will be present where there is large k, comparing Fig, 4.16 with 4.17 we find this to be true, enstrophy is found at the regions of highest k. The regions of high rotational energy are regions where the flow can throw particles upwards as will be seen in Section 5.8.

4.5.4 Wall shear stress

Shields [163] described a simple method of determining the onset of sediment transport. The Shields parameter, τ_{sh}, is a non-dimensional shear stress, Eq. (4.30), if the Shields number exceeds a threshold of $\tau^*_{\text{sh}} = 0.06$, for uniform grains or $\tau^*_{\text{sh}} = 0.03$ for non-uniform grain sizes, then sediment transport begins. The wall shear stress was non-dimensionalised by the critical Shields stress for non-uniform grain sizes for $D_p = 10\mu$m: $\tau_{\text{ref}} = 0.03\rho_p g D_p$.

$$\tau_{\text{sh}} = \frac{\tau_w}{\rho_p g D_p} \tag{4.30}$$

The wall shear stress was analysed statistically; the mean, standard deviation and skewness are presented in Fig. 4.18. The quantities are found for each point on the wall measured over time. It can be seen that the mean wall shear stress peaks at $r \approx 1.3R$ but the standard deviation peaks later at $r \approx 1.6R$ indicating that the extreme events are most likely to occur in this region. The skewness shows that the distribution varies dramatically along the wall, and that it can be both strongly positively or negatively skewed. To model the wall shear stress using a simple Gaussian distribution would be incorrect. Looking at the Fig. 4.18a it is seen that at $4.5 < r/R < 6$ the distribution is skewed negatively by rare low or negative wall shear stresses most likely a result of ground vortex interaction seen in more detail in Section 5.8. At $r = 0.3R$ the distribution is positively skewed indicating a few very high wall shear stress events occur here. When the skewness appears to be zero, e.g. at $r \simeq 1.5R$, there is a balance between flow stagnation events and close vortex proximity causing both rare, and very large, negative and positive stresses, this is re-enforced by high standard deviation at that location. With increasing rotor height the $\bar{\tau_w}$ peak reduces, widens and moves further away from the axis. The rare peak stress events are capable of picking up the largest particles, the location of these events are where there is high values of all three statistics reported in this analysis, i.e. $r \simeq 1.6R$.

The change in strength and location of the peak wall shear stress with the rotor height is given in Fig. 4.19. The peak wall shear is observed to move from $r \approx 1.3R$ towards the limit of $r \approx 1.8R$ as the rotor height increases in height from 0.5 to $4z_d/R$. Likewise the shear stress decreases as the rotor gains height, but we would expect the shear stress to continue to reduce to zero. This has interesting implications for the pilot as the source of dust inception moves closer to the helicopter as it approaches the ground as well as more dust being entrained.

4.6 Conclusions

A 3D unsteady rotor wake model has been implemented using the actuator line method. The rotor was simulated both in ground effect and out of ground effect and assessment was made on the validity of the results.

Spatial discretisation was assessed using the Richardson extrapolation, for the young tip vortices the error was found to be 7% when compared to the grid free solution. The first cell was found to have a $20 < y^+ < 50$, near the base of the boundary layer. A very low frequency perturbation was found across the sample period but its magnitude was very low and the flow

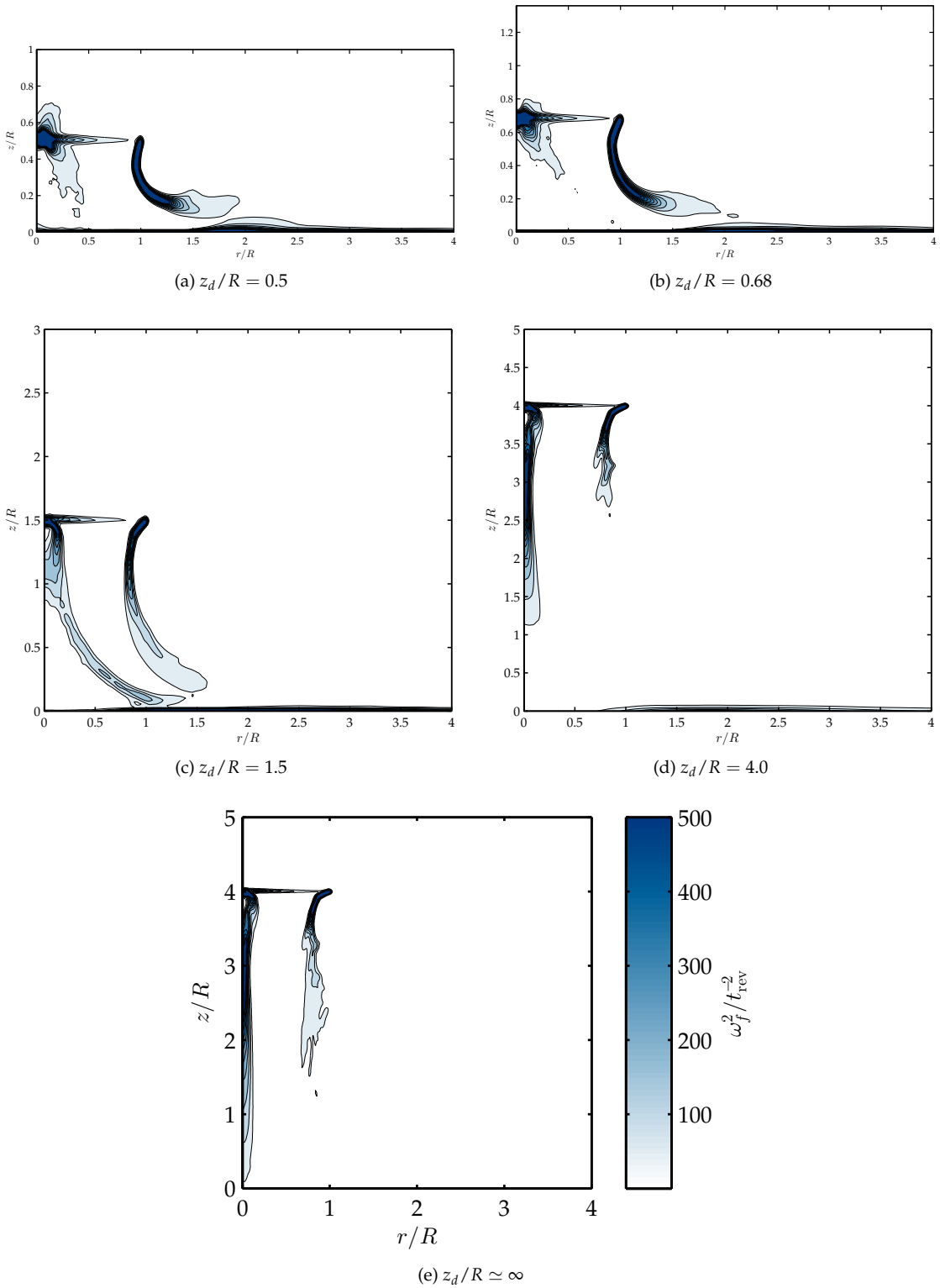

(a) $z_d/R = 0.5$

(b) $z_d/R = 0.68$

(c) $z_d/R = 1.5$

(d) $z_d/R = 4.0$

(e) $z_d/R \simeq \infty$

Figure 4.17: The mean enstrophy field, ω_f^2, of the complete slice for each case nondimensionalised by t_{rev}^{-2}. The peak value is artificially limited to show greater contrast.

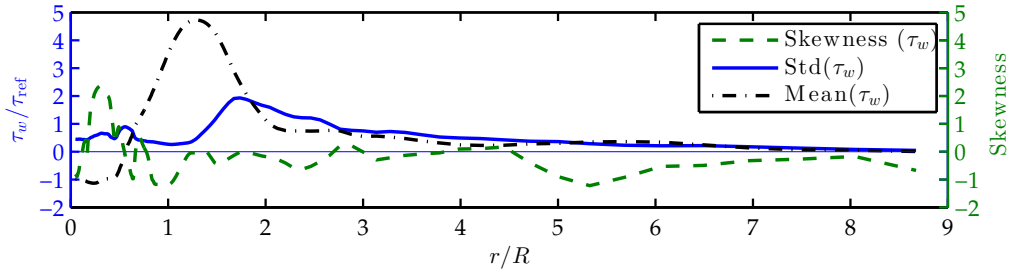

(a) $z_d/R = 0.5$

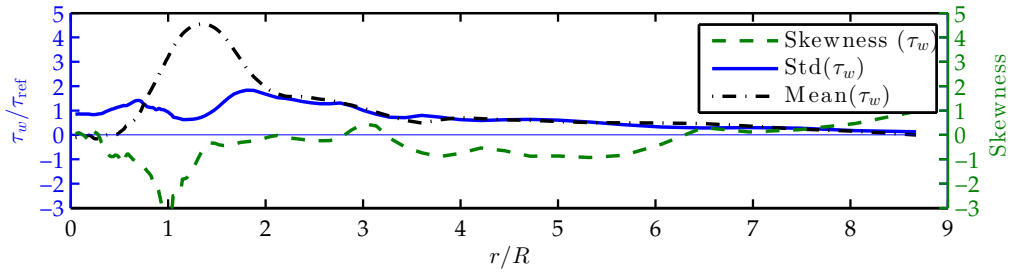

(b) $z_d/R = 0.68$

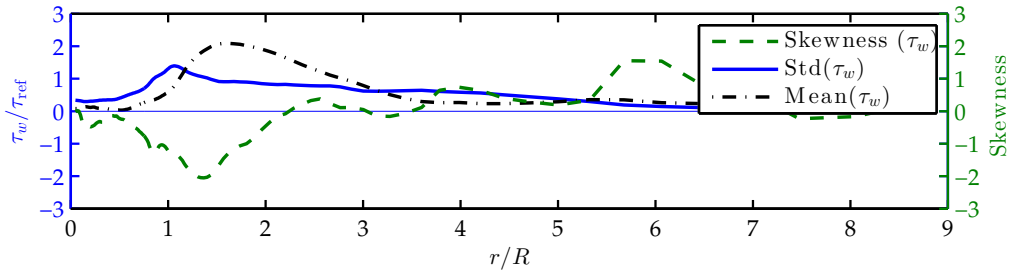

(c) $z_d/R = 1.5$

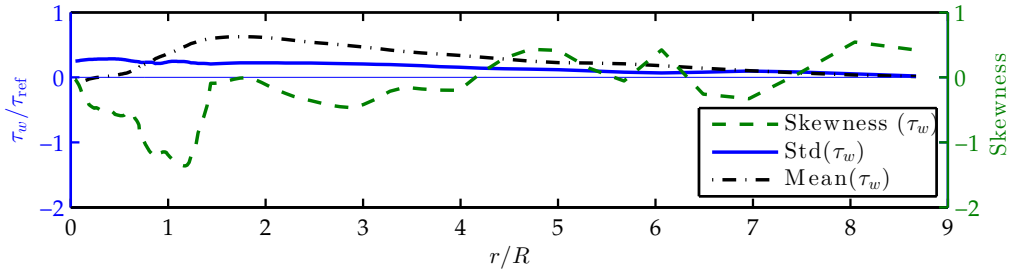

(d) $z_d/R = 4.0$

Figure 4.18: The wall shear stress statistics for each case, nondimensionalised by τ_{ref}.

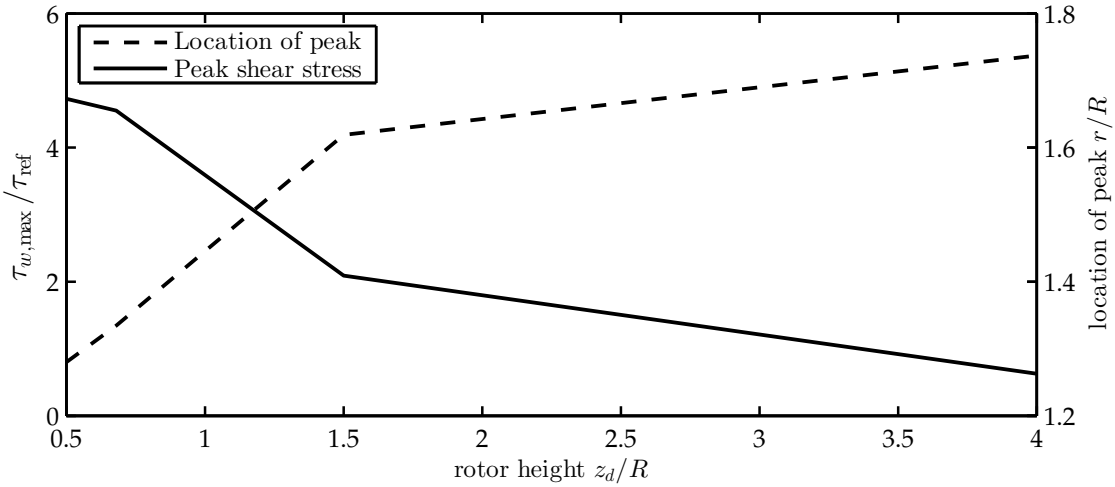

Figure 4.19: The value and location of the peak wall shear stress with rotor height, z_d/R.

period was considered to be statistically stationary. Boundary conditions and extents were examined and shown to be adequate to resolve the large scale activity.

The power required for constant thrust IGE reduced with proximity to the ground as in the literature, the result was not as dramatic as the change in the experiments but the trend was similar and the result was a close match for an analytical relationship from the literature.

The radial velocity profile and vortex trajectories were compared quantitatively and smoke visualisations from the literature were used in a qualitative comparison of the structure of the flow. The numerical results were found to follow the same trends as the experiments and were a good match for vortex trajectory.

The aim of this chapter was to validate the results of an unsteady 3D rotor wake simulation that is later used to understand and predict particle entrainment mechanisms. The tip vortices are the primary feature in this flow and they are the large scale disturbance that is responsible for particle entrainment. The validation in this chapter shows that the flow behaves reasonably compared with experimental evidence and that the tip vortex evolution is adequately resolved.

Chapter 5

Model Scale Rotor Wake Simulation: Flow Structure and Particle-Flow Interaction

---

The previous chapter concentrated on time averaged and statistical quantities in the rotor flow to validate and understand the anatomy of the flow. The subjects of this chapter are the unsteady events of the rotor wake, and how those features may influence particle pick-up and trajectory. The flow structure is dominated by vortices generated at the rotor tips that advect toward the ground and expand radially. The vortex development is explored through autocorrelation. The vortices cause peaks in the wall shear stress, vortex pairing and ground interaction causes rare events of high shear stress. The intermittency of the near wall flow and wall shear stress is identified and explored with respect to particle entrainment.

The flow is scaled to that of a full-scale helicopter and particle motion simulated by releasing particles into the flow and applying the particle-fluid forces from Chapter 3. It is shown that the particles are entrained between the tip-vortex and a separation bubble made from induced counter rotating fluid at the wall. A region of fast upward fluid is created between these two features that carry particles upwards. The particle paths are traced and show consistency with experimental and full scale observations.

5.1 Introduction

This chapter examines the unsteady vortical nature of the flow and how it pertains to entrainment. The chapter is structured to first look at the vortex features qualitatively and then makes several quantitative analyses. Section 5.2 is an overview of the vortical structures in the 3D flow and how they change. Section 5.3 examines the trajectory of the blade tip vortices and statistically summarises the distribution of vortex proximity to the wall. Autocorrelation is used to quantify periodicity of the flow in Section 5.4, probe points are placed along the wake boundary to look at how the vortical flow change with distances from the rotor. The final sections look at particle forces within the flow field, to do this the flow field is scaled to that of a full scale helicopter using parameters in Section 5.5. Section 5.6 looks at the wall shear stress, the driving quantity in aeolian sand transport models, and Section 5.7 looks at the forces seen by a particle on the wall. Section 5.8 releases particles into the flow to see where they are blown, this reveals the mechanism that allows particles to be blown upwards, seen experimentally by Johnson *et al*. [39].

5.2 Anatomy of the IGE rotor flow

Figure 5.1 shows an iso-surface of the 3D rotor wake structure for Case $z_d/R = 1.5$, defined by Table 4.2 in Chapter 4. Here we see a typical hovering rotor wake structure with all the usual components: the tip vortex helix is very stable near the rotor, the wake contracts and then expands as it approaches the wall, then the vortices start to interact with each other by twisting and pairing. Compare Fig. 5.1 with the OGE structures seen in Fig. 4.1b; the wake necks beneath the rotor in both cases and the coherent structures breakdown in a similar fashion but the wall causes the vortex helix in the the IGE case to expand radially. Near the wall the vortices are less coherent and the twisting has moved some structures closer and others further away from the wall. The vortices that are pulled near to the wall create large shear stresses, this occurs irregularly and gives rise to rare high shear stress events much more capable of entraining particles than vortices travelling along the wake boundary.

5.3 Vortex trajectories

The vortices do not follow a consistent route through the flow due to the twisting and pairing seen in Fig. 5.1, since the proximity of the vortices to the ground directly influences particle entrainment the paths of all the tip vortices have been mapped here. The paths of each tip vortex were recorded using an algorithm that followed local peaks in vorticity magnitude over time in the 2D slice. The trajectory of the tip vortices over time were compared with experiments from the literature in Section 4.4.3 and found to behave well and match the experimental data. The tip vortices move downwards along the wake boundary, for a hovering rotor their speed is typically half the induced velocity. The path of each vortex over time for case $z_d/R = 1.5$ was recorded in the 2D slice presented in Fig. 5.2. If any given vortex position over time is $\zeta_i\left(t_{\text{vort}}\right)$, where t_{vort} is the time since that vortex was generated, then the mean vortex path is the ensemble average $\bar{\zeta}_i\left(t_{\text{vort}}\right) = \langle \zeta_i\left(t_{\text{vort}}\right) \rangle$ and the standard deviation and skewness are $\text{std}(\zeta_i)$ and $\gamma_1(\zeta_i)$.

The vortices begin to diverge from the mean below the necking region at $z \approx 1.2R$, however, the paths of each vortex are all very similar. The average tip vortex moves horizontally after $r = 1.5R$ at a height of approximately $R/4$, standard deviation in z was approximately $R/10$. The centre of the tip vortices tend to not approach the wall closer than $R/8$. At this distance the vortex tracking method struggles to distinguish between unique vorticity peaks and vorticity at

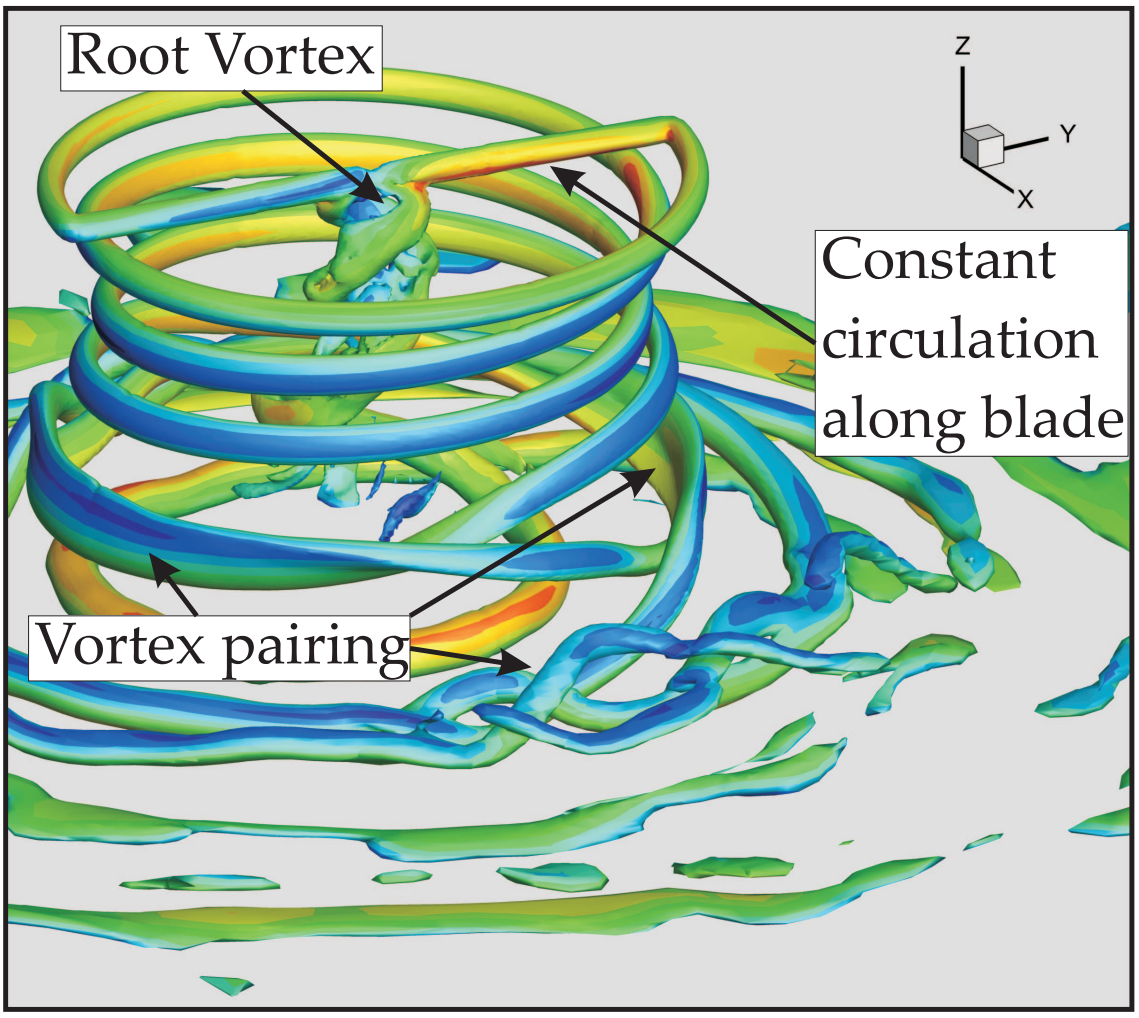

Figure 5.1: An iso-surface of vorticity magnitude at $|\omega_f| = 80\text{s}^{-1}$ coloured by velocity magnitude, Case $z_d/R = 1.5$ at $t = 89t_{\text{rev}}$.

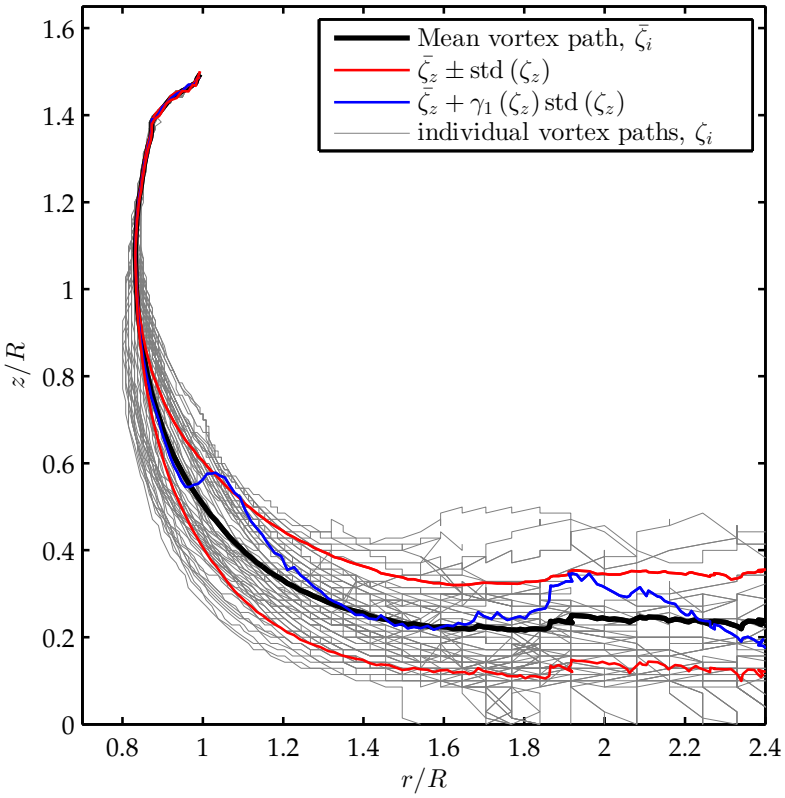

Figure 5.2: The trajectories of each vortex and ensemble statistics for the $z_d/R = 1.5$ case. The vertical standard deviation of the vortex path is presented as the mean path $\pm\text{std}(\zeta_z)$; the skewness, $\gamma_1(\zeta_z)$, is presented as the sum of the mean and the product of the standard deviation and skewness.

the wall but the mean distance from the ground of $R/4$ is observable in plots of vorticity, such as Fig. 5.13a.

The statistical properties of the distribution of vortex paths at $r = 2R$ are presented in Table 5.1 to compare the deviation in position and proximity of the vortices to the wall for the different rotor heights. It is seen that the mean distance of the vortex from the wall is loosely dependent on z_d; if the rotor is too close, as for $z_d/R = 0.5$, the vortex path lifts away from the wall a little. The standard deviation shows that it is not uncommon for vortices to move considerably closer to the wall, these vortices will produce the highest shear stresses at the wall and therefore have the biggest impact on entrainment, this is explored in Section 5.6. Skewness is mild, $\gamma_1 \approx \pm 0.5$ at $r = 2R$, but positive in most cases; this would suggest there are rare events of a vortex being far from the wall - this is common in distributions that have a physical limitation in one direction, *i.e.* vortices cannot penetrate the wall. The skewness value varies with r in Fig. 5.2 becoming positive and negative but never greater than ± 1, the mean and standard deviation are more consistent.

5.4 Temporal flow development along the wake boundary

The development of the tip vortices through the rest of the flow can be assessed by probing specific locations in the flow and observing how the flow changes over time. The autocorrelation, one-point two-time correlation, indicates how well the flow is correlated with itself over time. The autocorrelation function is given by Eq. (5.1), and the normalised autocorrelation is given in Eq. (5.2). Nine locations were chosen in the flow, highlighted in Fig. 5.3, these locations were placed along the mean path of the vortices, found in Section 5.3,

z_d/R	$\bar{\zeta_z}$	std(ζ_z)	$\gamma_1(\zeta_z)$
0.5	$0.19R$	$0.06R$	-0.58
0.68	$0.16R$	$0.06R$	0.32
1.5	$0.24R$	$0.10R$	0.49
4.0	$0.28R$	$0.12R$	0.53

Table 5.1: Statistics of vortex positions in z at $r = 2R$ for each rotor height. $\bar{\zeta_z}$ is the ensemble average vertical position, std(ζ_z) is the standard deviation of vertical position and $\gamma_1(\zeta_z)$ is the skewness of the vertical position distribution.

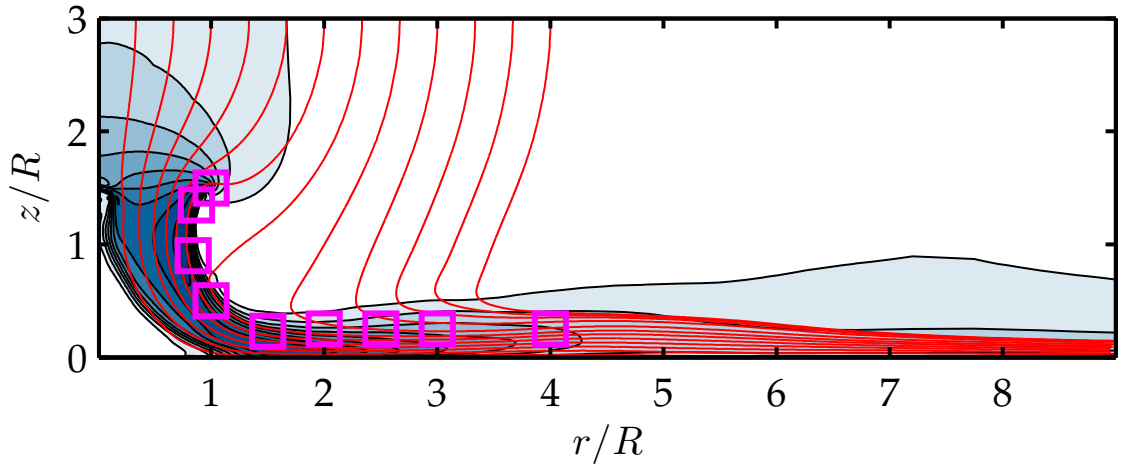

Figure 5.3: The locations of the points analysed with autocorrelation, superimposed on the mean flow field, for $z_{\text{disk}}/R = 1.5$.

this is also the mean wake boundary. The velocity signal for each location was processed using the normalised autocorrelation, Eq. (5.2), and plotted in Fig. 5.5. In this analysis the vertical velocity fluctuations were considered to analyse the rotational and vertical velocity changes.

$$R_{ij}(r,z,\tau) = < u_i'(r,z,t)u_j'(r,z,t+\tau) > \tag{5.1}$$

$$f(r,z,\tau) = \frac{R_{ij}(r,z,\tau)}{R_{ij}(r,z,0)} \tag{5.2}$$

Whilst the mean flow field is shown in Fig. 5.3 it is pertinent to show an instantaneous image of the velocity field to portray the typical structures that will be analysed by the autocorrelation approach, such a typical flow field is show in Fig. 5.4. In Fig. 5.4 several vortices are visible, it is also clear that the vortices are not positioned in an orderly pattern along the wake boundary, reflected in Fig. 5.2.

The autocorrelation shows the breakdown of flow structures that start with coherence near the rotor and become more disorganised with r. Figure 5.5a indicates that while every vortex effects the same velocity change at the blade, $r = R$, at down stream positions every other vortex must have been displaced as the correlation is weaker, the consistency of this second mode implies a stable oscillation in the wake. At $r = 1.5$ the correlation shows a doubling in periodicity, further positions, Fig. 5.5b show the vortices are travelling slower and are likely to be combining as the periods becomes very large, $> 10t_{\text{rev}}$, and more complex modes in the signal emerge and decay with r.

Conducting the FFT of the autocorrelation gives the temporal energy spectrum, a reflection of the energy contained in each time scale. Figure 5.6 portrays the product of Y and the complex conjugate, $|Y|$, where $Y = \text{FFT}(R_{zz})$. The energy spectra show that energy is located in the large

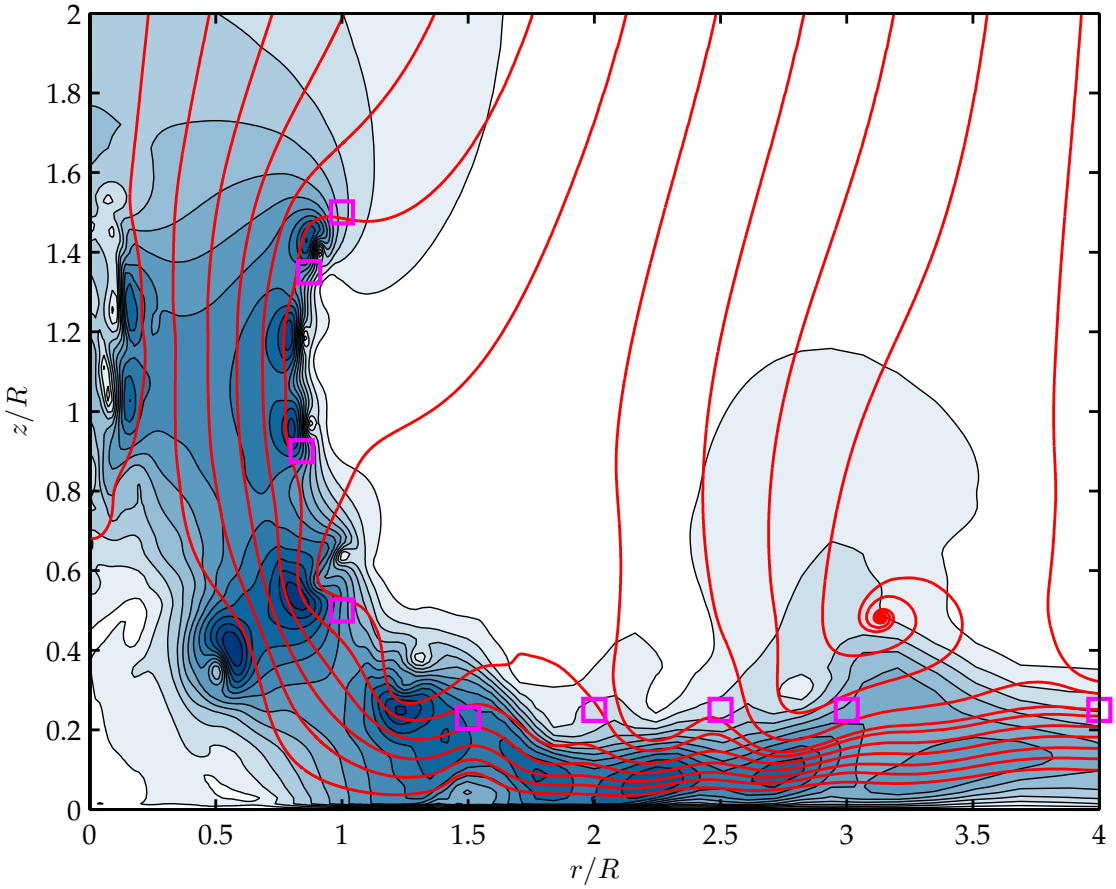

Figure 5.4: An instantaneous image of the velocity magnitude field with streamlines and the probe locations. Case $z_d/R = 1.5$ at $t = 50$ revolutions. Fluid entrainment and vortex pairing are visible.

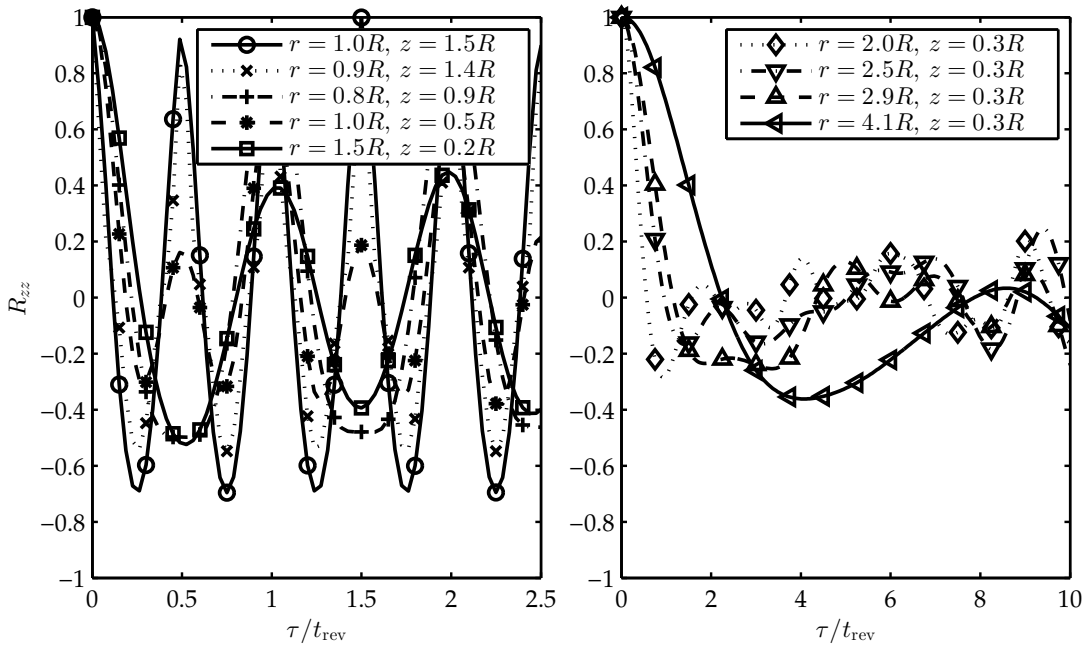

(a) Near the rotor the autocorrelations have short wavelengths.

(b) Further from the rotor the autocorrelations have increasing wavelengths

Figure 5.5: The autocorrelations of the velocity signals, $v_z(t)$, at given locations in the flow.

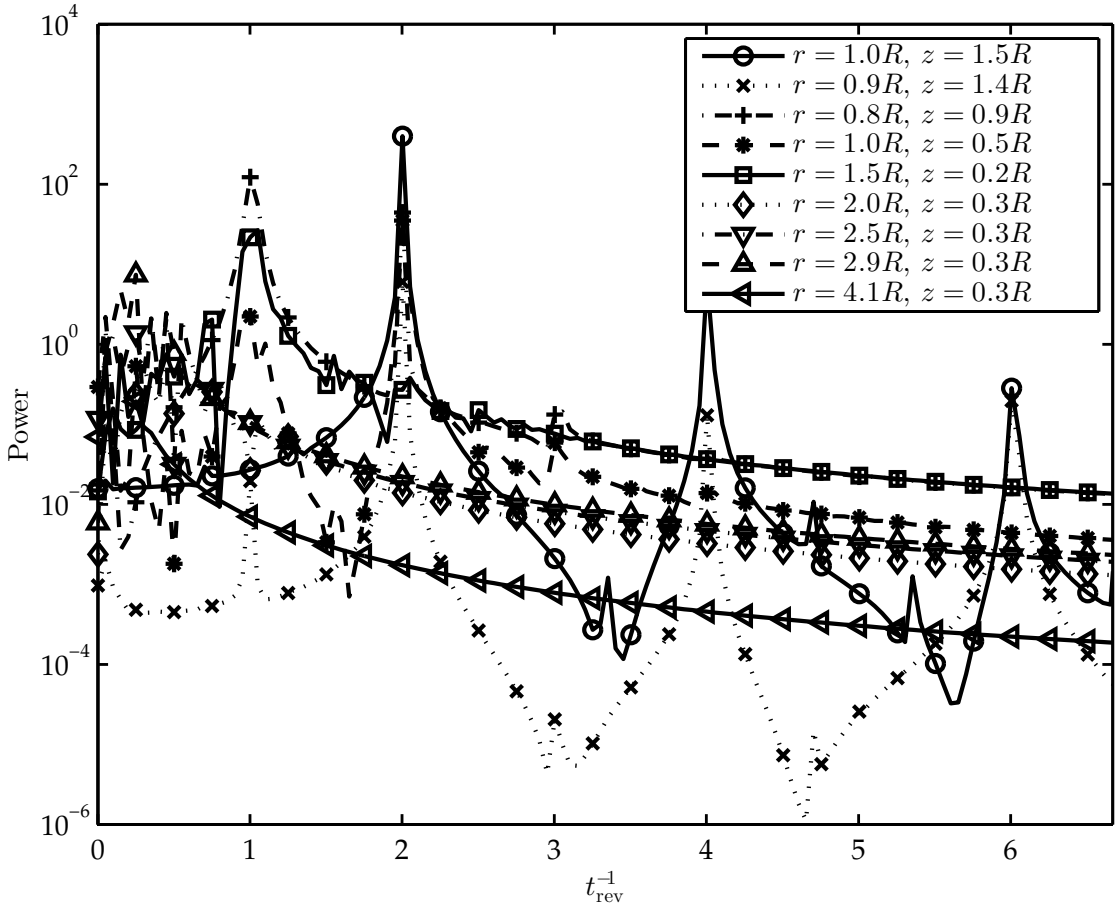

Figure 5.6: The temporal energy spectra at the probe locations of Fig. 5.3.

.

scales, and there are the expected peaks at 2 t_{rev}^{-1} for the near rotor probe positions. The peak energy frequency decreases with increasing r showing that the structures have slowed because of radial expansion and fluid entrainment. At $r = 1.5R$ the dominant frequency becomes 1 t_{rev}^{-1}, at this location vortex-vortex interaction or pairing must be a regular occurrence.

The region of particular interest is near the ground at $1 < r/R < 3$, this is the region where the flow is fastest and where the vortices first approach the ground. In this region the vortices go through the most changes, the autocorrelations in Fig. 5.5a show that the vortices enter the region with strong periodicity but by $r = 2R$, Fig. 5.5b, many more modes are visible due to vortex-ground and vortex-vortex interactions. At $r = 3R$ the vortices have slowed with the entrainment of more mass, and in many cases vortices have combined again this is revealed in the autocorrelation as a complex but much lower frequency signal in Fig. 5.5b.

5.5 From model scales to helicopter scales

To be able to describe the forces on sand particles from a full scale helicopter the flow described in this chapter and Chapter 4 needs to be scaled. To scale this flow correctly the thrust coefficient, C_T Eq. (4.23), is held constant and the parameters of a nominally small and large helicopter are used as scaling parameters, v_{ind} and R. The small helicopter was modelled around the Bell 47, used in Chapter 6, and the large helicopter was modelled on the Augusta Westland AW101 Merlin, Fig. 2.2. Table 5.2 provides the details of the aircraft, the values for weight and rotor radius are aircraft parameters, the remaining quantities were derived using the thrust coefficient from the model scale simulation defined in Chapter 4.

parameter	Small Helicopter	Large Helicopter	Model
Weight, W	$900g$N	$12500g$N	$0.6g$N
Rotor radius, R	5.66m	9.30m	0.5m
1D induced velocity,v_{ind}	6.0ms^{-1}	13.2ms^{-1}	1.8ms^{-1}
Rotor angular velocity, Ω	14.2 rads^{-1}	19.65 rads^{-1}	47.1 rads^{-1}
time scale, $t_{rev} = 2\pi/\Omega$	0.44s	0.32s	0.13s
Modelled thrust coefficient, C_T	0.0023	0.0023	0.0023

Table 5.2: Scaling parameters used for full scale analysis.

The near wall flow presents a problem: the boundary layer is not a fully developed turbulent boundary layer so it cannot be scaled using analytical methods such as those described by Schlichting *et al*. [60]. The wall lift force is based on the particle position in the boundary layer, it is greatly underestimated if the flow field is simply scaled upwards. This is true of shear stress and all near wall flow properties, however, examining properties like shear stress statistically allows us to explore the transient nature of the particle forces in time and space. In the following analysis the wall shear stress and near wall flow has been scaled linearly though it is acknowledged here that this is an underestimate.

The sections that follow make use of scaled helicopter flow fields to provide full scale shear stresses and particle forces in the flow. Whilst is is acknowledged that the wall shear stress is not sufficiently resolved, the wall shear stress analysis adds value to this study through the intermittency analysis — the availability of particle entrainment in the flow.

5.6 The wall shear stress

The wall shear stress is the dependent quantity in the Bagnold entrainment flux expressions. In this section it is demonstrated that the wall shear stress, Eq. (3.22), is highly dependent on the vortices. Equation (3.22) described in Chapter 3 is suitable for the linear sublayer when v_r at $y^+ = 1$ is known. Here the near wall cell is outside of this region, $y^+ > 10$, using Eq. 3.22 will underestimate the wall shear stress but the qualitative results born from analysing the intermittency and large scale features are still valuable. The flow simulated here used a no-slip but smooth wall, if a rough wall had been applied the boundary layer would have been thicker due to momentum lost to the roughness elements in the wall and increased mixing.

The time-average wall shear stress for case $z_d/R = 0.5$ is presented with the standard deviation and skewness in Fig. 4.18a. The standard deviation peak is not aligned with the mean peak suggesting that the near wall flow structure changes from a steadier fast flow, at $r \approx 1.2R$, to become a more intermittent flow as the vortices approach the wall, at $r \approx 1.6R$.

The wall shear stress over time at $r = 1.6R$ is shown in Fig. 5.7. The location $r = 1.6R$ was chosen because the largest fluctuations occurs there, Fig. 4.18. The skewness in Fig. 5.7 is indicated by the modal average, generally if the mean is more positive than the mode the distribution is positively skewed, here we see a slightly negative skewed distribution. Figure 5.7 shows that the peak stresses are up to 100% larger than the mean and typical peaks are 50% larger than the mean, as suggested by Fig. 4.18. Several peaks in the stress are very close together showing vortices interacting or in the process of pairing. The wall shear stress frequently reduces to zero and there is also some flow reversal and negative wall shear stress indicating that at this position the entrainment is governed by the immediate local vortex or vortices. The changing statistics, in r, shown in Fig. 4.18 and the fluctuations in Fig. 5.7 show that the fluctuations in shear stress are highly non-Gaussian, and the distribution structure changes

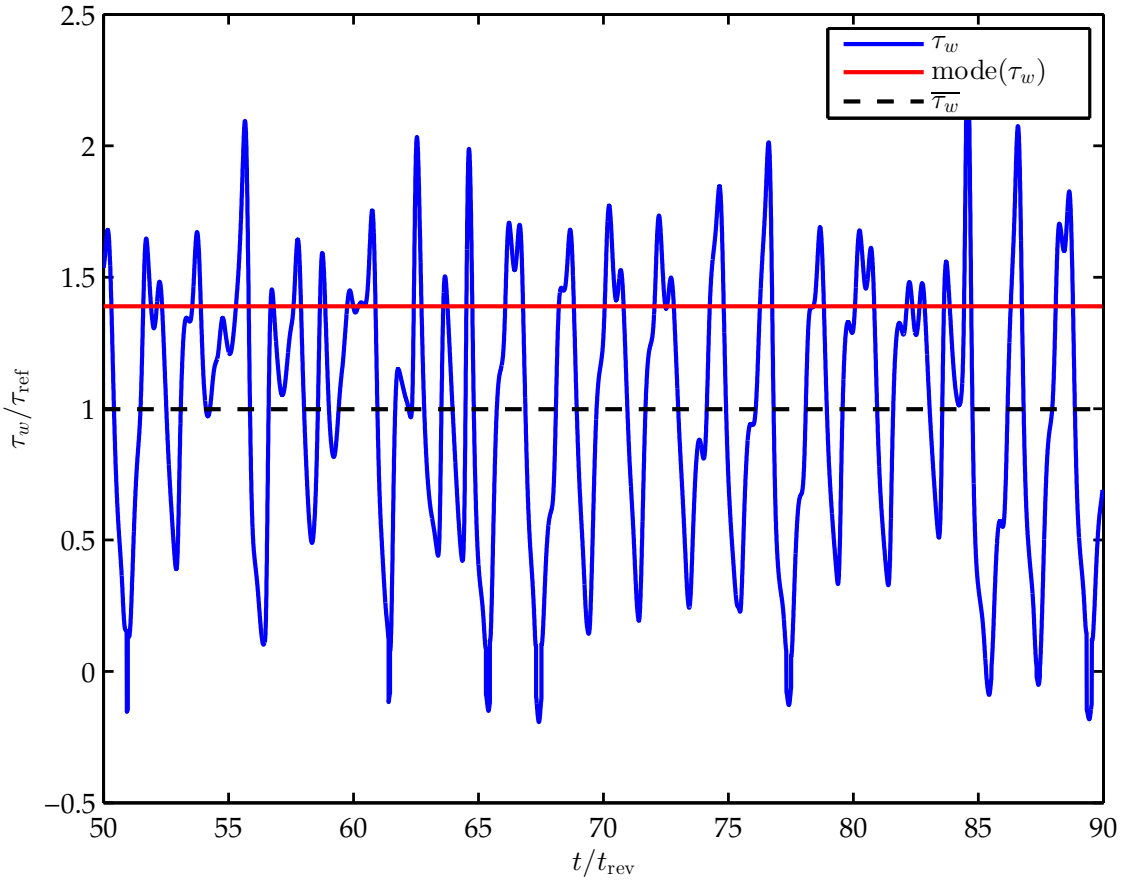

Figure 5.7: Wall shear stress at $r = 1.6R$ with mean and mode indicated for case $z_d = 0.5R$. The mode is presented to show that the distribution is heavily positively skewed. Scaled to a small helicopter from Table 5.2.

with r and with z_d making it very difficult to state *apriori*.

The Shields number, Eq. (4.30), is indicated on Fig. 5.7; the Bagnold expression [17] described in Section 2.6 models entrainment flux as a function of $\tau_w - \tau_w^*$. Figure 5.7 shows us that the peaks in shear stress are sudden and of relatively short duration. The particles will respond to the vortices if the duration of the wall shear stress peaks are larger than the particle response time, τ_p. The particle response time is given by Eq. (3.30), it is a characteristic time for a given particle to respond to changes in the flow. In order for the particles to be entrained into the flow the duration of the flow features should match or exceed the particle response time. The duration of the peaks in wall shear stress that exceeded the Shields threshold were measured and are presented as a PDF in Fig. 5.8. Small particles have a very small response time, for $D_p = 10\mu$m we have $\tau_p = 5 \times 10^{-3} t_{\text{rev}}$ while larger particles such as $D_p = 100\mu$m have a response time of $\tau_p = 0.5 t_{\text{rev}}$. Larger particles encounter fewer occasions when the wall stress is larger than the threshold and the duration of those events is shorter.

The analysis in this section has been made on the time history at $r = 1.6R$ for the case $z_d = 0.5R$, the location was chosen because of the large fluctuations. Figure 5.9 shows the fraction of time the wall shear exceeds the threshold for each radial location and for each case. For lower rotor heights the shear stress almost continuously exceed the Shields threshold in the region $r \approx 1.2R$; as the rotors increase in height the fraction decreases, the peak region moves away from the root and the pick-up region broadens.

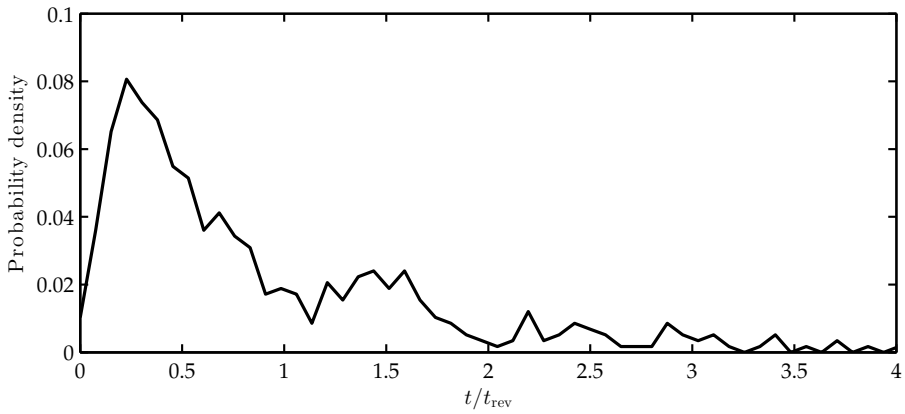

Figure 5.8: A PDF of the duration of the wall shear stress peaks that exceed the Shields threshold for $D_p = 10\mu$m, in a small helicopter flow field.

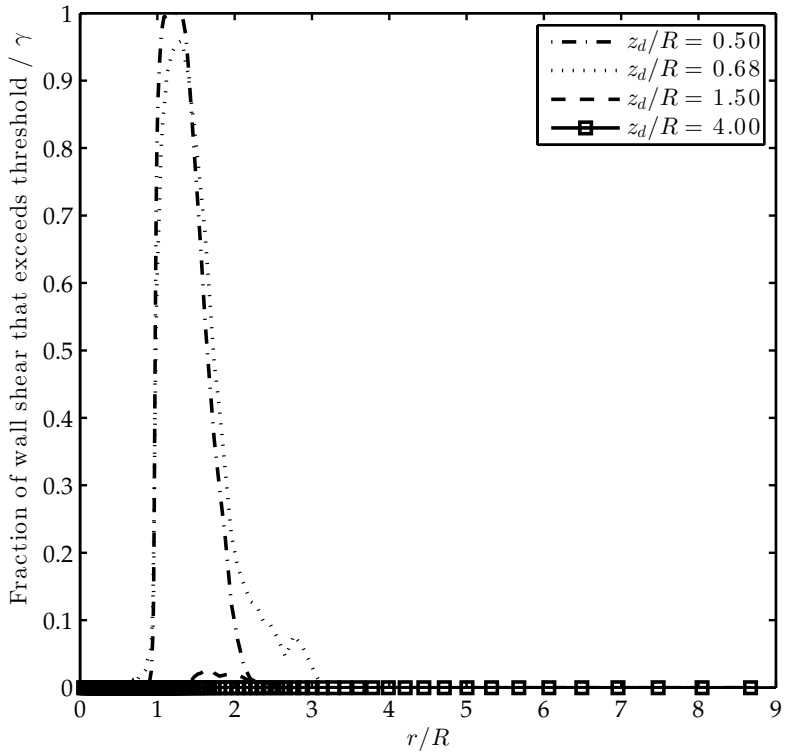

Figure 5.9: Wall shear stress that exceeds the Shields threshold for $D_p = 10\mu$m, for each rotor height, scaled for a small helicopter.

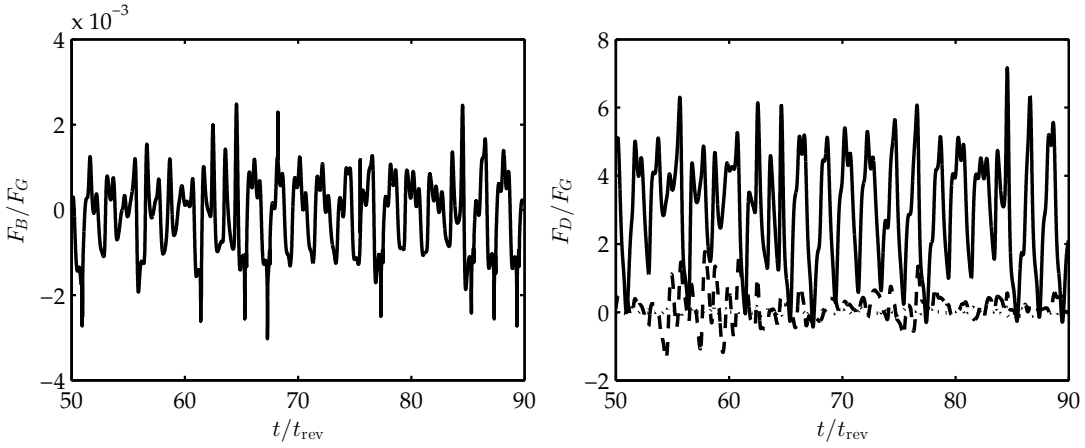

(a) Basset force

(b) Drag force

Figure 5.10: The Basset and Drag force for a fixed position at $r = 1.5R$, $z = 0.01R$ in a *small* helicopter scaled unsteady flow field with $r_p = 5\mu$m.

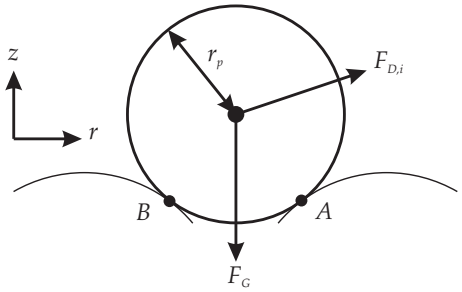

Figure 5.11: The simplified scenario of a particle resting on 2 particle asperities.

5.7 Particle fluid forces in the unsteady flow

The particle forces from Chapter 3 will be calculated in the next Section and used to progress the particle position through time and space. Before doing so the Basset force and the drag force are reported at a fixed location at $r = 1.6R$, $z = r_p$. The Basset force is dependent on acceleration history, Eq. (3.35), here only the radial acceleration is considered for clarity. Figure 5.10a gives the Basset history for the small scaled helicopter flow field, normalized by particle weight F_G, the fluctuation force is generally 3 orders weaker than the weight. Figure 5.10b shows the drag and is three orders of magnitude greater than the Basset force and larger but of the same order as the particle weight, F_G.

5.7.1 Particle rocking probability

Consider the simple arrangement of a particle resting on two particles of the same size, Fig. 5.11. If a large simplification is made and only the forces of drag and gravity act on this particle. The simplification does not give us the true moments, as forces such as cohesion and wall lift are omitted, but it does give an indicator to the availability of entrainment potential near the wall. Taking moments about the down wind asperity 'A' gives:

$$F_{D,r} r_p \cos(\pi/6) - \frac{1}{2}\left(F_G - F_{D,z}\right) r_p = M_\theta \tag{5.3}$$

Now we find the probability that at any time the drag force will be sufficient to pivot the particle, $P(M_\theta > 0)$, but also that the duration of any pivot event is longer than the particle relaxation time, $\tau\left(M_\theta > 0\right) > \tau_p$. Figure 5.12 shows $P\left(\tau\left(M_\theta > 0\right) > \tau_p\right)$ with r. It is interesting

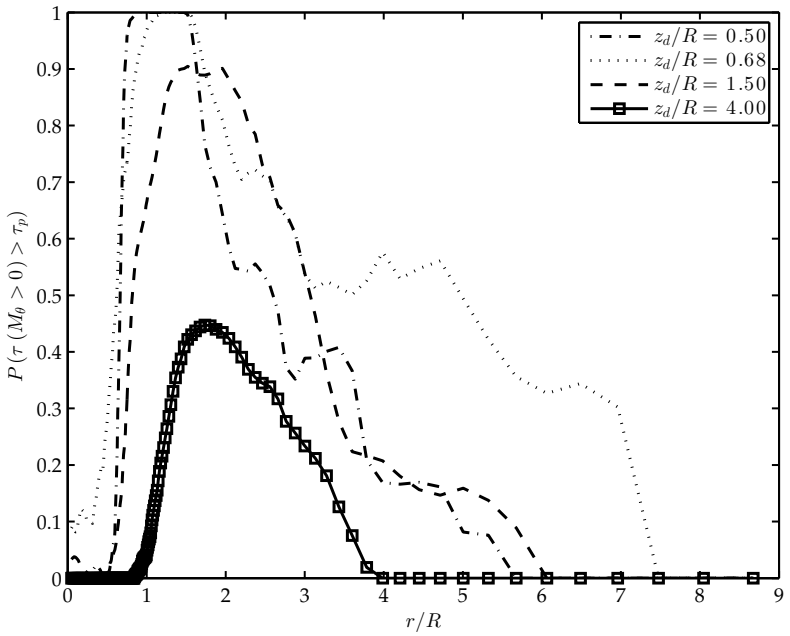

Figure 5.12: The probability of near wall velocities rocking a particle in a small helicopter scaled flow, Table 5.2.

to compare this with Fig. 5.9, the peak is centred around the same location in both analyses but via the rocking mechanism the threshold is relatively much lower than for the shear stress analysis.

Near wall particle forces are analysed further in Chapter 6, the flow is steady but full scale and more appropriately resolved at the wall.

5.8 Particle trajectories

The presence of vortices in the flow has been shown to increase the wall shear stress dramatically, however, the vortices contribute toward entrainment and brownout cloud development in a further way: carrying the particles upwards. The mean flow is downward from the rotor and parallel to the ground in the radial wall jet, but, in the unsteady flow the vortices produce large regions of positive vertical fluid flow, these can be capable of carrying the particle upwards. In this section the capacity for the IGE rotor flow to carry particles upwards is demonstrated.

To model the particle trajectories particle-fluid forces from Chapter 3 were found at point locations in the flow field in time and space, the forces were then integrated over time to evolve the states of the particles. The particle motion simulation was entirely 1-way coupled: the fluid is unaffected by the particles. The 3D rotor flow field in Chapter 4 was simulated in model scale and the results presented in non-dimensional terms, for this analysis we use the full scale flow field found using the reference parameters in Table 5.2. Whilst the particle-forces can be calculated non-dimensionally, the near wall lift forces depend on boundary layer position - this is not linearly scalable and, as the boundary layer is not a steady full developed zero pressure gradient boundary layer, using approximations for the full scale boundary layer was not appropriate. To continue the analysis particles were released from a series of fixed near ground positions, $\theta = 0$, $1 < r/R < 4$, $z = 0.005R$. The release time was after $t = 50t_{\text{rev}}$ but also conditional upon a time when the flow would accelerate the particle upwards. A basic Euler integration scheme is used to evolve the particle position, the time step was $\Delta t = 4 \times 10^{-3} t_{\text{rev}}$ an order of magnitude smaller than the particle response time, Eq. (3.30), for $r_p = 5\mu$m the particle relaxation time is $\tau_p = 5 \times 10^{-3} t_{\text{rev}}$. The flow was scaled using the small helicopter, Table 5.2, in

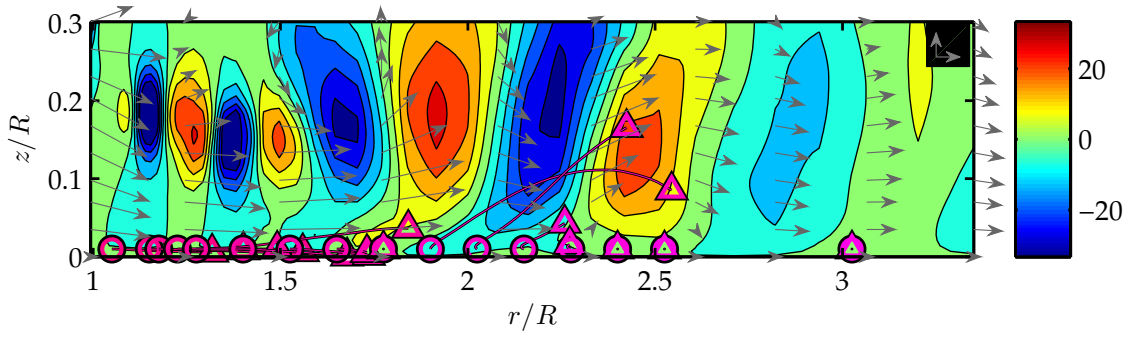

(a) $t = 51.2t_{\text{revs}}$

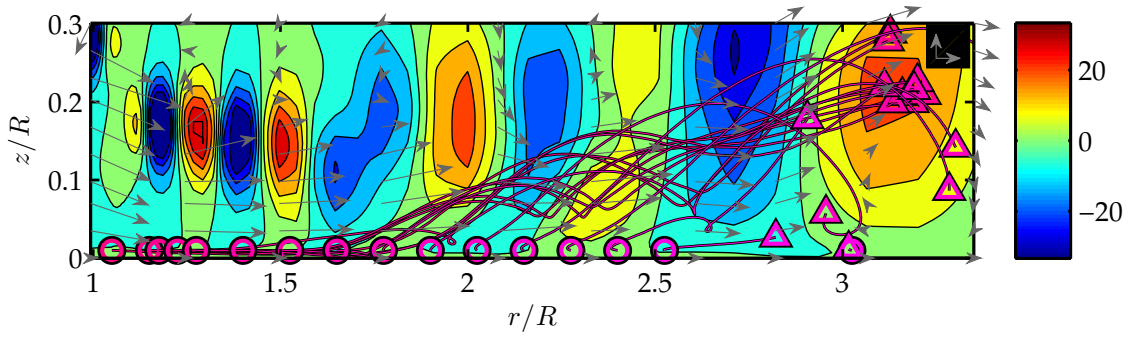

(b) $t = 54.8t_{\text{revs}}$

Figure 5.13: Particle trajectories over time with vorticity contours and velocity vector arrows for case $z_d/R = 0.5$. Particle release point shown by ◯ and current position by △. Vorticity range is limited for clarity and nondimensionalised by t_{rev}^{-1}. Velocity magnitude is normalized by v_{ind} and shown by arrow length, where $1v_{\text{ind}}$ in both r and z directions is defined in the top right of the figure. The spatial aspect ratio is *not* 1:1.

the first analysis — the effect of larger particles and a heavier helicopter are considered later in this section.

The trajectories are shown against contours of vorticity about theta, $\omega_{f,\theta}$, and arrows indicating velocity vector. Vorticity about theta is positive for clockwise vortices and negative for anti-clockwise in Figures 5.13a - 5.15. Tip vortices are negative from this perspective and contribute positively to the radial velocity near the ground, between negative and positive vorticity features are regions of strong vertical velocity. Each figure shows the velocity field and vorticity field at a specific time, the particle position and path up to that time is overlayed.

Figures 5.13a and 5.13b indicate that the particles are stimulated into horizontal motion by vortices passing over them increasing the local radial velocity. The *entrainment* of particles, that is their movement away from the surface into the main flow structures, occurs during a combination of events. The primary tip vortices approach the ground in the vicinity of $r \approx 2R$, this generates stagnation or separation at the wall, this is seen at $r = 2.5R$ in Fig. 5.13a and $r = 3R$ in Fig. 5.13b as stagnation or flow reversal near the wall. Particles are stimulated into horizontal motion by the tip vortex, but they are thrown upwards by the vertical velocity jet that is generated between the primary vortex and the secondary vortex at the wall. Figure 5.14a shows the region of the flow in detail, a strong velocity region is generated between the positive and negative vortex structures causing particles caught in this region to be elevated upwards.

Figures 5.13a and 5.13b also show that the particles stay close to the wall for a considerable distance, $1 < r/R < 2$ in Fig. 5.13b until the vortices are close enough to the wall to generate the vertical flow regions. The particles positioned at $r \approx 2.5R$ only begin to move when a vortex moves past as is occurring in Fig. 5.13b.

The time scale of the vortices was measured to be $2\pi r_{\text{vort}}/v_{\text{vort},\theta} = \tau_{\text{vort}} = 0.75t_{\text{rev}}$, the

particle relaxation time for $r_p = 5\mu$m is $\tau_p = 5 \times 10^{-3} t_{\text{rev}}$, this results in a very low Stokes number of $\text{St} = 7 \times 10^{-3}$, Eq. (3.29). In this flow with these small Stokes numbers the particles react quickly to changes in the flow. Consider the locations of the particles in Fig. 5.13b, marked by $\triangle$, the particles can be seen to move with and around the positive vortex associated with their entrainment in Fig. 5.13a.

Consider the settling velocity, or terminal velocity, this is found simply by equating the drag force to the weight force, resulting in;

$$u_{\text{term}} = \sqrt{\frac{8\rho_p g r_p}{3\rho_f C_D}} \tag{5.4}$$

For a small particle in free fall the drag coefficient is simply $\text{Re}_\text{p}/24$, Eq. (3.33), for $r_p = 5\mu$m the terminal velocity is $u_{\text{term}} = v_{\text{ind}}/800$; the vertical flow around the vortices presented is easily sufficient to keep the particles aloft as demonstrated in Fig. 5.13b.

A closer look at the fast flow between counter rotating vortices is given in Fig. 5.14 presented with the wall shear stress and radial velocity for that space and time. A separation bubble forms on the ground under the positive vortex, $r = 2.3R$, the positive radial flow is forced to go over the obstruction. The particles that were initially moved radially by the high radial velocity caused by the nearby negative vortex are now in a body of air that is moving upward as well as radially. The separation bubble and other flow features develop in time and space, the separation region was previously near $r = 2.1R$ seen by the reversal in the particle path at that point. High shear stress can be seen in Fig. 5.14b beneath the tip vortex and negative shear stress indicates flow reversal beneath the separation bubble. The movement of the entrainment-responsible flow feature is clearly visible in the photo shown in Fig. 2.2, dust entrainment is clearly occurring in spiral patterns as the vortices advance radially away from the helicopter. It is important to stress that not every blade tip vortex results in a favourable pairing with a positive vortex or separation bubble, evident when comparing vorticity in Figs. 5.13a and 5.13b.

For the rotor cases with higher rotors the entrainment mechanisms are the same, however, the point of inception can be considerably further away from the root of the rotor, $2.5R \leq r \leq 4R$. The speed of the flow is considerably reduced at this distance where the particles are entrained but the small particles have a relatively low terminal velocity so even slow upward flow features can carry the particles upwards. The particles are less inclined to be trapped by vortices for the higher rotors.

The helicopter used in Chapter 6 is the Bell 47 designated as 'small' in Table 5.2, it was chosen because experimental data is available for the near ground flow in hover, however, it is a lightweight aircraft and has a low disk loading and as such the entrainment potential is less. The AW101 or Merlin helicopter, designated as 'large', is approximately ten times heavier, it is used frequently in desert theatres at this time. The Merlin is known to produce a doughnut shaped dust cloud surrounding the aircraft but the aircraft itself is relatively dust free. Scaling the flow to the size and weight of the Merlin does not change the trajectories of the particles considerably because the Stokes number is low for both flows, Fig. 5.15. Increasing the weight of the helicopter seems to entrain more heavy particles and they seem to spread further out radially.

The experiments by Nathan and Green [164] used high speed photography to capture wave like bursts of sediment entrainment from a model scale IGE rotor. The wave like nature of the burst was attributed to the near ground vortices. The experiments by Nathan and Green [164] used a rotor with different forward velocities, a landing helicopter will approach the landing zone with forward velocity, noting that this changed the sediment cloud size and formation. The sediment entrainment experiment performed by Johnson *et al*. [39] produced very similar results, the position where particles leave the surface and the height they are transported to are

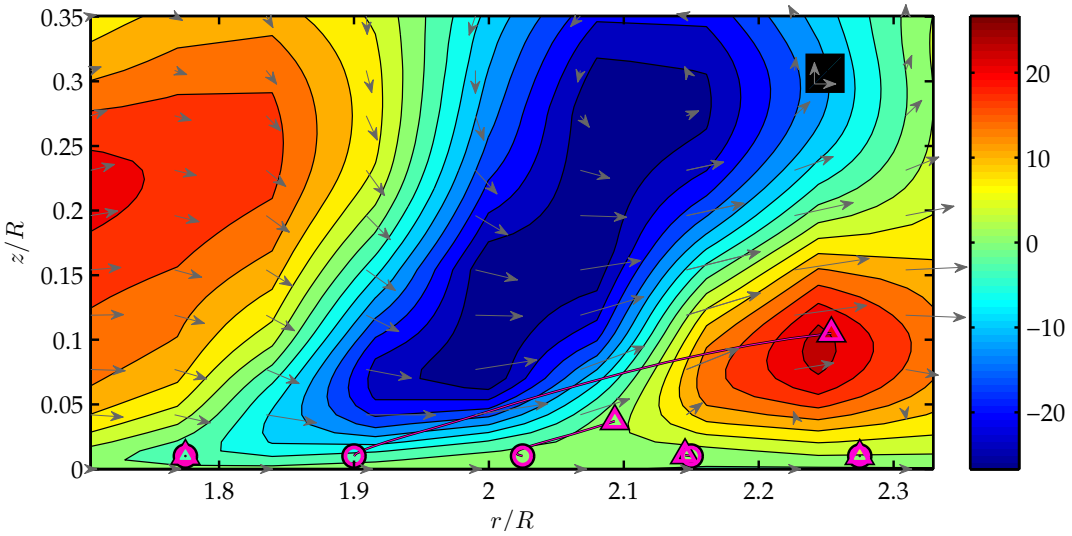

(a) Particle trajectories over time with vorticity contours and velocity vector arrows for case $z_d/R = 0.5$ at $t = 50.8$. Particle release point shown by ◯ and current position by △. Vorticity range is limited for clarity and nondimensionalised by t_{rev}^{-1}. Velocity magnitude is normalized by v_{ind} and shown by arrow length, where $1v_{\text{ind}}$ in both r and z directions is defined in the top right of the figure. Spatial aspect ratio is 1:1.

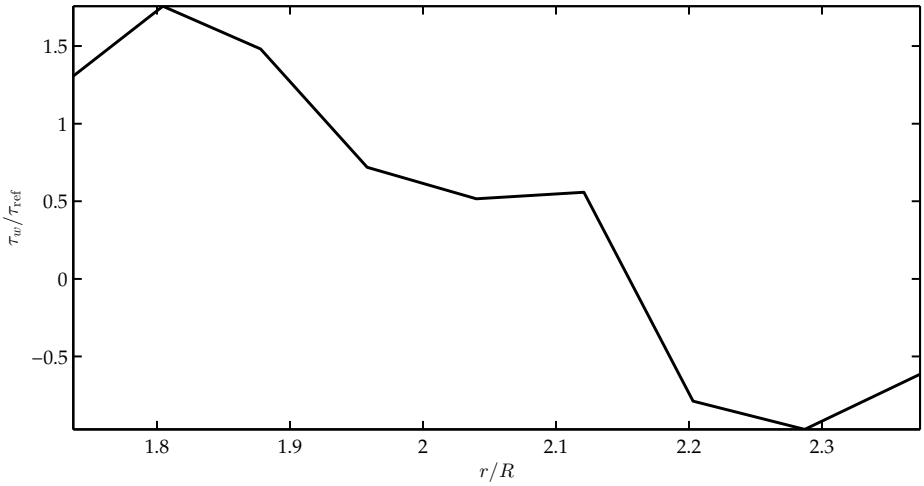

(b) Wall shear stress at the same place and time as Fig. 5.14a.

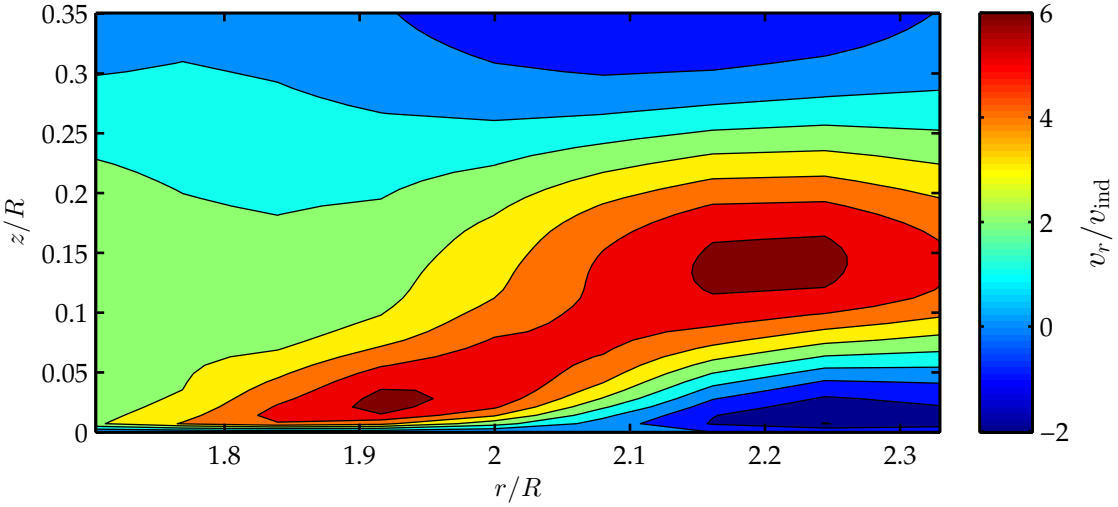

(c) The radial velocity field for the same location and time as depicted in Fig. 5.14a.

Figure 5.14: Particle trajectories over time with vorticity contours, velocity vector arrows and wall shear stress for case $z_d/R = 0.5$ at $t = 50.8$.

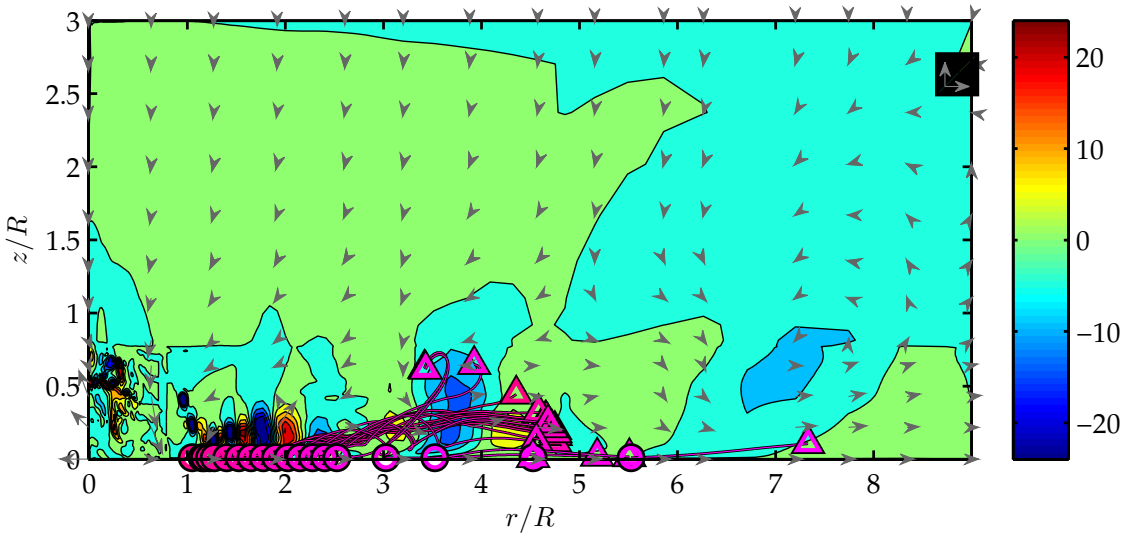

Figure 5.15: Particle paths in the flow scaled for the heavy helicopter, Table 5.2. Legend is the same as Fig. 5.13.

both a good match with the results presented here. Johnson *et al*. noted the aperiodicity of the vortices makes analysis and modelling difficult and undermines the justification for using the traditional aeolian entrainment functions. The results found here agree with those conclusions, the aperiodicity could be quantified stochastically based on the data presented in Fig. 5.7 but the vortex-vortex interaction that creates the vertical thrust, Fig. 5.14a, is not as easily identified but was found here to aperiodic also. The path of the sediment in the experiments of Johnson *et al*. showed the particles to be blown outwards and upwards with a only a very few particles showing recirculation.

The brownout condition brings to mind a helicopter lost in a cloud of dust, as it should, but photographs of the sediment movement early in the development of the brownout cloud show that the sand follows the trajectories found in this study and in the experimental work by Johnson *et al*. [39] quite well. Doughnut shaped dust clouds were reported by Rodgers [23] and are seen with the AW101 in Fig. 2.2, taking the trajectories of the dust entrained here and revolving around the axis would produce a doughnut structure giving further support to the qualitative results found here and elsewhere in the literature.

5.9 Discussion

Can Lagrangian particle simulations be used to predict brownout? The Lagrangian calculated particle path has been demonstrated here to produce good results. The viscous flow field modelled here produced the required flow features that were also observed by Johnson *et al*. [39] as the cause of particle transport from the near ground flow to elevated positions. An inviscid flow calculation could provide the aperiodic peaks in shear stress but would not provide the juxtaposition of negative tip vortex with induced positive vortex at the ground. Entraining particles from the ground bed into the flow remains a difficulty, the difficulty is predominantly a scaling issue in the near wall flow because a model scale unsteady boundary layer is not linearly scalable. The particle bed needs to be simulated to include the effects of saltation bombardment, occlusion and to have an appropriate method of knowing how many particles are entrained from a certain area.

Reingestion of dust back through the rotor blades is seen in many photos and videos of brownout. However, it can be seen from stream line plots, Fig. 5.4, that no fluid appears to be

reingested through the rotor, this indicates that the rotor configuration maybe a deciding parameter for dust reingestion and therefore the difference between the doughnut shaped dust clouds and complete helicopter immersion. The unsteady simulation is model scaled as are the experiments of Johnson *et al*. [39] and Lee *et al*. [27], and fluid reingestion does not appear to happen in any significant quantity in those works either. The work of Nathan and Green [164] indicates that forward velocity, as opposed to static hover as tested here and by Johnson *et al*. [39] and Lee *et al*. [27], causes the required recirculation to induce the envelopment of helicopter, since this is also more akin to the approach used by helicopter pilots it is an important factor for future work. The additional factors of the fuselage and tail rotor — which were not included here or in the studies of Johnson *et al*. [39] and Lee *et al*. [27] — may also have more significance than was first thought. Further work, both experimental and numerical, is needed to include these components.

5.10 Conclusions

The 3D unsteady rotor flow developed in Chapter 4 was explored to better understand the mechanisms behind particle entrainment and trajectory. The development of the tip vortex through space and time showed that the vortex path is irregular with significant variance in proximity to the ground. Autocorrelations were conducted along the mean vortex path, they showed that the vortices combine and slow down quickly over the region of interest, $1 < r/R < 3$.

The wall shear stress was analysed and found the following conclusions:

- The vortices passing close to the wall increased the local wall shear stress by as much as two times the mean.
- The distribution of wall shear stress over time at a given point was highly non-Gaussian and each location had a different distribution shape.
- The passage of vortices enables the Shields threshold to be exceeded to some extent for the 3 lowest rotor heights.
- As the rotor height increased shear stresses were less frequently large enough to exceed the Shields threshold.
- The duration of the vortices was larger than the response time of the particles, particles that are entrained into the flow will be carried by the flow.

The unsteady flow field from Chapter 4 and particle forces from Chapter 3 were used to find the paths of particles released into the flow from near ground positions. The particle trajectory analysis allowed a more direct understanding of how particles behave at the early stages of their entrainment and beyond. The flow was scaled linearly to a full scale helicopter flow and particles were released near to the ground, the fluid forces on each particle were calculated and integrated to evolve the position of the particles in time.

It was found that on some occasions a tip vortex positively induced a near ground vortex: effectively a separation bubble caused at the ground by the tip vortex. The results indicated that this arrangement of tip vortex and separation bubble are required to elevate the particles upwards. The flow is constantly changing and aperiodic such that not every vortex that passes interacts with the ground in this way and is capable of causing particles to be entrained. The particles considered had a very small Stokes number and consequently the entrained particles maintained association with the vortices that entrained them, often orbiting the positive vortex.

The particles were entrained into the main flow but propagated away from the rotor radially, they were not recirculated back through the rotor in the fashion of a typical brownout cloud but behaved more like the doughnut cloud associated with the Merlin helicopter. It is likely this is possible to the static hover scenario modelled, introducing a more realistic approach trajectory for the rotor would be a good future study as would the inclusion of the tail rotor and fuselage. These trajectories were a good match with those seen in the experimental results of Johnson *et al*. [39], performed at a smaller scale and the photographic evidence such as Fig. 2.2.

Chapter 6

Full Scale RANS Simulation of Near Wall Helicopter Flow

Particle inception is a critical stage in the development of the brownout dust cloud. In this chapter near wall Lagrangian particle forces are considered through analysing an approximate time averaged full-scale rotor flow. This simplified flow does not attempt to predict brownout, instead it provides scales and velocity data in the near wall region, compares the role of particle-fluid forces and provides a foundation for Lagrangian entrainment models. The analysis shows three characteristic particle sizes are exposed to different physics in different boundary layer zones, a function of the distance from the helicopter. Drag is the dominant aerodynamic force, cohesion is large for small particles but wall-bounded lift is sufficient to entrain medium sized particles. A complementary analytical prediction of tip vortices found that both large scale inviscid features and small scale viscous features of the boundary layer are significant. The results of the unsteady model scale simulation from Chapter 5 are brought into the discussion to combine the knowledge from both investigations.

The analysis and results of this chapter are published in the *Journal of the American Helicopter Society* [2].

6.1 Introduction

This chapter aims to highlight the key aerodynamic forces that act on the particles on the ground beneath a hovering helicopter and contribute to a multi-scale entrainment model suitable for simulating the phenomena of brownout. This chapter presents a nondimensional analysis of particle-fluid forces to assess the significance of each contributing force and then compares those findings with the forces a particle experiences in a time averaged helicopter downwash flowfield calibrated against results of Leese [22].

Leese [22] conducted an experiment using full scale hovering helicopters. Leese measured the near ground radial velocity at several radial locations for a hovering H13 helicopter. The H13 is a small helicopter used by the US military also known as the Bell 47, it was made famous by the film and television series M*A*S*H.

The simplest Eulerian wake modelling is performed using the 1D actuator disk as in this chapter. McAlpine *et al*. [165] performed a steady state full-scale numerical model attempting to characterize dust emissions for a helicopter travelling forward IGE, they used a steady Computational Fluid Dynamics (CFD) simulation to find upwash regions associated with dust entrainment. The flow results recreated measured detachment points of the ground jet but the simulated vortex deviated from the measured values. The flow field is simulated for the purpose of understanding the generation of the brownout cloud but with no dust simulated.

The nondimensional analysis starts with the nondimensional particle force expressions defined in Section 3.6. Scaling values from the H13 helicopter used in the experiments of Leese [22] are applied to the nondimensional expressions to find the relative importance of each force.

The flow fields in the works by Phillips and Brown [166] and Wachspress *et al*. [19] are full scale but are calculated using inviscid methods. In this work we wish to find the aerodynamic particle forces at the point of inception very close to the ground in the boundary layer, a viscous feature of the flow. An unsteady rotor flow is modelled with a rotor radius of $R = 0.5$m in Chapter 4, but modelling a full scale unsteady rotor flow is extremely computationally demanding if the flow is modelled down to the particle scales. Instead a full scale axisymmetric RANS simulation is conducted with a turbulence model and a near wall grid spacing of $y^+ \approx 1$ to resolve the viscous sublayer of the boundary layer.

The forces are calculated on 3 different particle sizes in the near wall region to discover how each particle size is stimulated by the flow.

The blade tip vortex contribution is assessed analytically and the impact they have on the mean flow results is discussed. The vortices in the unsteady simulation performed in Chapter 5 and the analytical calculations are compared.

6.2 The helicopter flow field

The flow field analysis has been split into two parts; the viscous mean flow with turbulent fluctuations and an inviscid tip vortex analysis. The bulk of the analysis in this study is carried out using the mean flow results. The tip vortex analysis uses the mean flow field to estimate the vortex path, lift from the rotor to estimate circulation and an analytical method to calculate the induced velocity profile around the vortex.

6.2.1 Reynolds Averaged Navier Stokes (RANS) flow field

A full-scale experiment of a helicopter hovering above the ground, performed by Leese [22], was simulated with Fluent (version 12.0.16) using the Axisymmetric RANS equations from Section 3.1. The horizontal velocities measured by Leese up to 0.1m from the ground at different radial

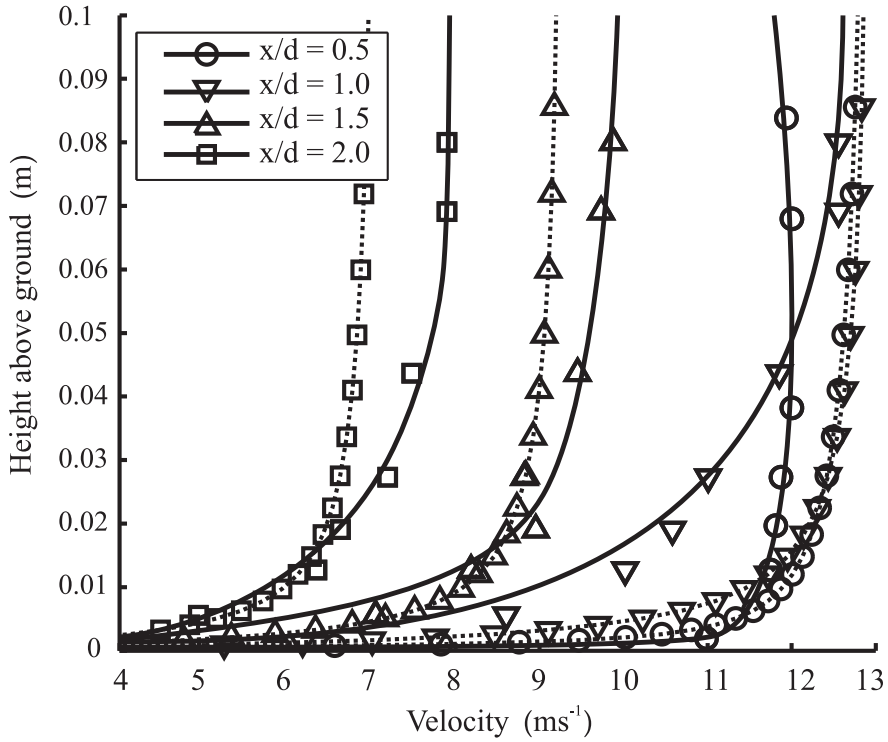

Figure 6.1: Experimental data [22] (solid line) compared with the RANS results (dotted line).

distances from the rotor hub are reported in Fig. 6.1. Since the flow field was measured with a real full size hovering helicopter above an outdoor dusty landing zone the ground was likely to be rough, however, since landing zone preparation was unknown it was chosen to model the wall smoothly and use a mesh with good near wall resolution, $y^+ \simeq 1$, rather than making assumptions, though it is understood that modelling the wall smoothly is also an uncertain assumption. The simple steady 2D axisymmetric domain consisted of a rotor of radius $R = 5.66$m hovering at height $z_d/R = 0.68$ above the ground.

Figure 6.2 shows the domain configuration. The axis cut vertically through the rotor hub and was the west boundary. The south boundary was the ground and had a non-slip wall condition. The north and east boundaries were modelled as constant gauge pressure boundaries and were positioned $5R$ and $9R$ from the ground and axis boundary respectively, Section 4.3.3. The rotor was modelled as a momentum source in Eq. (3.13) injected into cells at the rotor position, a region 0.1m thick. The momentum was applied uniformly across the disk with a linear transition region reducing the momentum source to 0 at $4.66 \leq r \leq 6.66$m, the transition region avoided the discontinuity present at the blade tip.

The mesh contained 400x200 nodes, concentrated near the axis and the wall with the first node at $y^+ \simeq 1$ to capture the viscous sublayer. In addition we ensured that the first node resolved the flow to the scale of the particles. A realizable $k - \epsilon$ turbulence model [62] was used because of its favourable performance in axisymmetric jets and a two layer non-equilibrium wall model [64] was chosen because of the strong pressure gradients. In essence it was chosen to resolve the full range of length scales at the expense of unsteady flow structures.

To find the air velocity through the rotor a 1D momentum balance was conducted for the hovering helicopter IGE. Assuming the flow to be incompressible, inviscid and steady a simple momentum balance [28] provides Eq. (6.1):

$$T = \dot{m}(v_\infty - v_0) \tag{6.1}$$

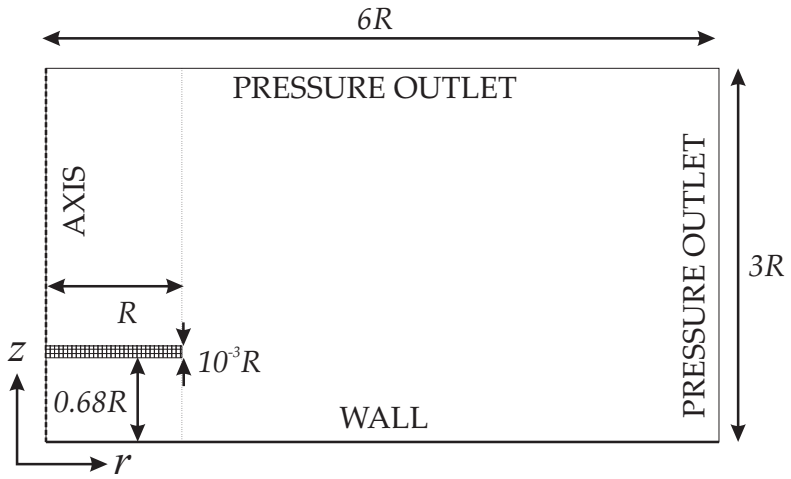

Figure 6.2: The 2D axisymmetric domain dimensions and boundary conditions.

where T is the thrust the disk exerts on the fluid, $\dot{m}$ is the mass flux through the disk, v_∞ is the velocity far downstream and v_0 is the velocity far upstream. A control volume is applied around the disk and the volume of air above the rotor to where the velocity $v = v_0 = 0$ and below the disk where the velocity is $v = v_\infty$. Applying the momentum and energy equations yields Eq. (6.2):

$$T v_{\text{ind}} = \frac{1}{2}\dot{m} v_\infty^2 \tag{6.2}$$

with $\dot{m}$ given in Eq. (6.3):

$$\dot{m} = \rho v_{\text{ind}} A_{\text{disk}} \tag{6.3}$$

where v_{ind} is the induced velocity through the disk and A_{disk} is the area of the rotor disk. The Bell H13 helicopter empty mass is 858kg and has a maximum take off mass of 1350kg, the craft is estimated to weigh 8.8kN. The blade radius is $R = 5.66$m which gives a disk area of 100m^2. These parameters result in an induced disk velocity of $v_{\text{ind}} = -6\text{ms}^{-1}$ and a mass flux of $\dot{m} = 725\text{kgs}^{-1}$.

6.2.2 Flow field results

The RANS flow field results obtained were accurate to within 20% of the full scale experimental results of Leese [22], however, the experimental flow at the further radial stations is more detached from the wall than the simulated results — this is likely due to the vortices in the experimental flow promoting mixing in the boundary layer and in doing so thickening it, the results of Chapter 4 which included vortices show a thick boundary layer. The general trend and magnitudes were consistent for the scaling analysis performed in this work. Fig. 6.1 shows the RANS results directly compared with Leese [22]. Additionally the radial flow field compares well with the small scale experimental results of Lee *et al*. [27], scaled with the induced velocity, v_{ind}, at the disk.

It is commonly accepted that the peak velocity not the average is responsible for inception [26, 52]. The near wall region velocity field and the RMS velocity fluctuations, v', are shown in Fig. 6.3 to give indication of the fluid velocity fluctuations the particles will be exposed to. The fluctuations are approximately 10-20% of the local mean and both the flow speed and turbulent intensity have a maximum at $r/D_{\text{disk}} \simeq 1$. Compared with the results of Chapter 5 it is seen that not including the vortices results in an underestimate of fluctuations, the near-wall RMS

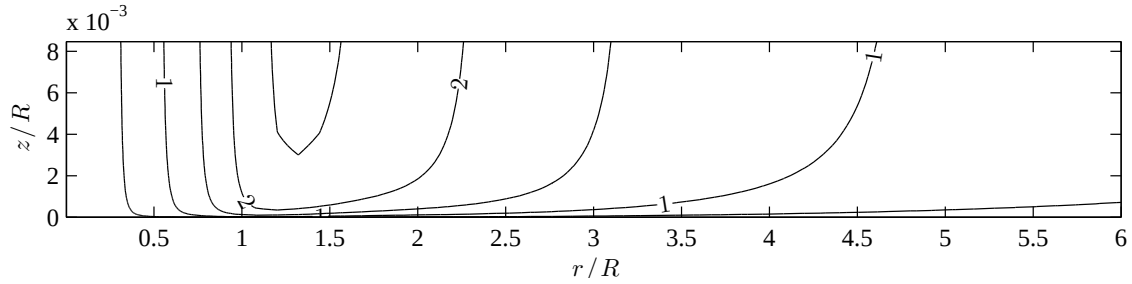

(a) Mean velocity magnitude

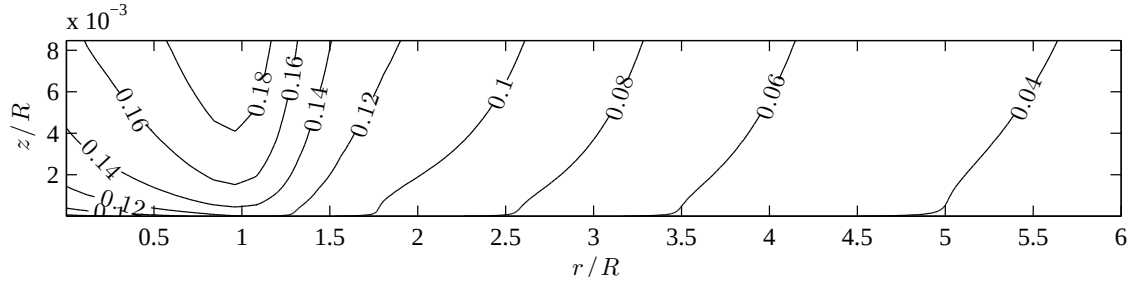

(b) RMS turbulent fluctuations

Figure 6.3: RANS results for near wall fluid velocity magnitude field and the RMS turbulent fluctuations, normalised with v_{ind}.

Property	Sand (glass)	Air	units
density	2480	1.19	kg/m^3
dynamic viscosity	N/A	1.82×10^{-5}	Ns/m^2
surface energy	2×10^{-4}	N/A	N/m

Table 6.1: Physical properties of sand and air (20°C, 1 bar)[a] [167, 106].

fluctuations from the unsteady simulation were as much as 300%, Fig. 6.4, we also see that simulating at model scale and insufficient grid resolution increases the relative thickness of the boundary layer.

6.3 Sand

Three sand grain sizes were chosen using a sand grain particle distribution function (PDF) generated from data collected by Rodgers [23] of particles found on the desert floor, recreated here in Fig. 6.5. It was found that the sand diameter PDF closely followed a Gaussian distribution with mean 300μm and standard deviation 120μm. The distribution was calculated as percentage by weight and the maximum and minimum sieve size was 500 and 10μm respectively. For the following analysis the force expressions for three particle sizes are evaluated; $D_p = 10$, 300 and 500 μm diameter, representing a small, medium and large particles encountered on the surface of the desert. Whilst the smaller particles contribute most to visual obscuration, as there are more of them and they remain airborne for longer, the other sizes are investigated here for their role in the entrainment process via saltation.

A summary of the material properties of sand and air are given in Table 6.1. The values have been used in subsequent analysis.

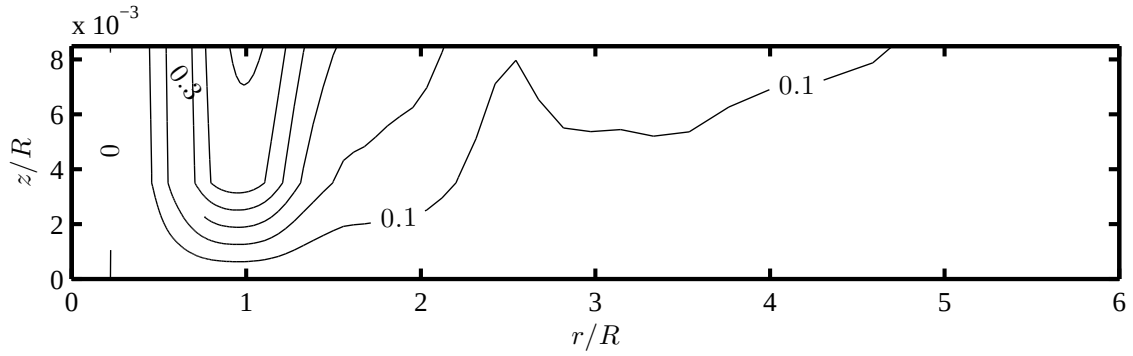

(a) Mean velocity magnitude

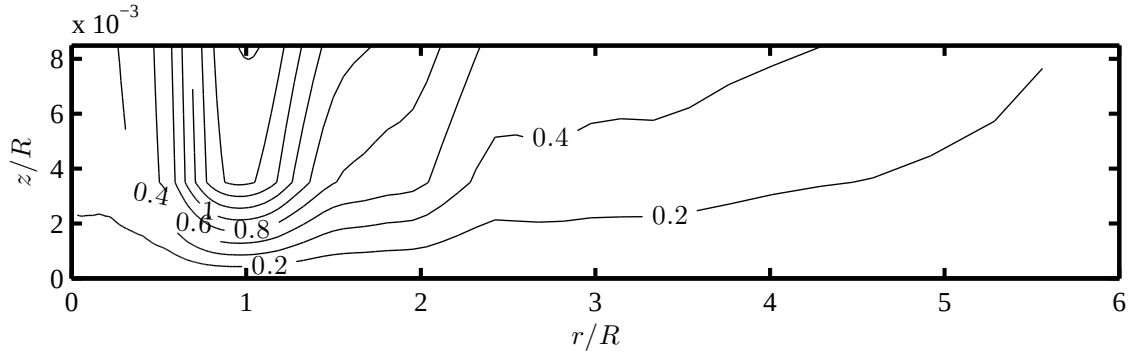

(b) RMS turbulent fluctuations

Figure 6.4: Unsteady results from Chapter 4. Near wall fluid velocity magnitude field and the RMS turbulent fluctuations, normalised with v_{ind}.

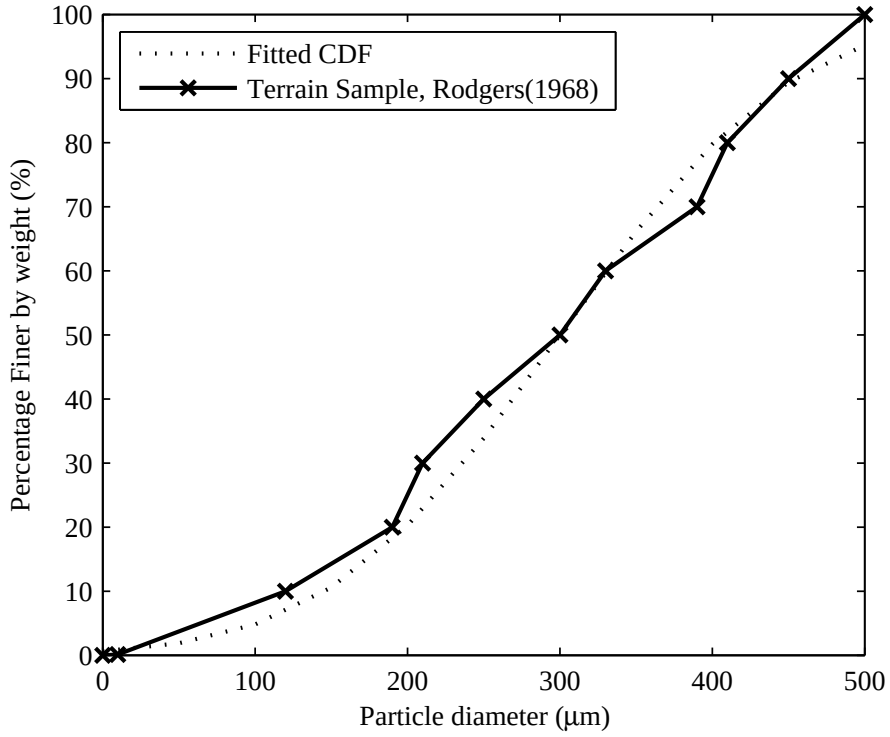

Figure 6.5: Sand distribution from the study of Rodgers [23].

6.4 Nondimensional particle-fluid forces

The particle-fluid forces consist of drag and the Basset force, from the traditional Basset — Boussinesq equation, and the transverse forces: Magnus and Saffman, Section 3.3. The particle is also subject to gravity and, when in contact with other particles, friction and cohesion.

The particle-fluid forces were defined in Section 3.3 and nondimensionalised in Section 3.6. The nondimensionalised equation of motion is expressed in terms of reference forces and nondimensional forces in Eq. (6.4) in order that each force can be compared for relative importance.

$$\frac{\mathrm{d}u_i^*}{\mathrm{d}t^*} = \left[F_{D0}F_{D,i}^* + F_{B0}F_{B,i}^* + F_{M0}F_{M,i}^* + F_{L0}F_{L,i}^* + F_{G0}F_{G,i}^* + F_{P0}F_{P,i}^* + F_{Fr0}F_{Fr,i}^*\right] \tag{6.4}$$

where the forces are: F_D = drag, F_B = Basset, F_M = Magnus, F_L = Saffman, F_G = gravity, F_P = cohesion and F_{Fr} = friction; note each force reference term, $F_{\phi 0}$, has units of N/kg.

Table 6.2 lists the non dimensional reference values and derivations. The velocity scale was chosen to be the induced disk velocity, v_{ind}, and the length scales are the three particle diameters, D_p, the remaining scales are material properties or derivatives.

The nondimensionalised force expressions are given in Table 6.3. Twice the turbulent velocity fluctuation from the $k-\epsilon$ turbulence model, $2u'$, was added to the mean flow field to give a peak velocity field [60] and is used in all the force calculations. Cohesion was calculated between particles in a bed of equal size. Friction is calculated as the product of the friction coefficient and the normal reaction component.

In addition to the forces in Table 6.3 there is the lift experienced by a particle at rest on a wall in a flow, described in Section 3.3.8.

6.4.1 nondimensional particle force analysis

The reference values from Table 6.2 were applied to the force expressions in Table 6.3 to find the relative importance of the forces for the typical scenario. The nondimensional variables, F_ϕ^*, are typically of order 0. The reference terms, $F_{\phi 0}$, have been evaluated and are given in Table 6.4 with the direction of action of the force. These results present only a general overview due to the highly inhomogeneous flow, demonstrated by the range of v seen in Fig. 6.3. However, the nondimensional procedure shows which forces dominate and which forces are completely negligible.

In the nondimensional analysis the drag force is most significant for smaller particles and reasonably insignificant for the larger particles when compared with the particle weight. The Basset force appears to be significant across all particle ranges. Magnus force has some presence for all particle ranges, as it is a transverse force it is competing with gravity and pull-off forces, for small particles pull-off is larger but for the large particles Magnus is comparable. The Saffman force is always very small and can be considered negligible as $F_M^* \gg F_S^*$. The particle weight is a significant force throughout, the pull off force is stronger than gravity for the smallest particles, but reduces to similar order for the largest particles. The strength of the Basset force and the lower value of drag support the notion that the peak fluctuations cause inception, [49]. Among the vertical forces the retarding forces are strongest for the smallest particles but the Magnus lift force is sufficient to allow larger particles to entrain more readily, this supports the concept of the initial entrainment of larger particles evidenced by Ibrahim *et al*. [58]. Friction is proportional to the normal force, for the smaller particles the lift is small but with increased particle size the lift exceeds the cohesive and gravitational forces as indicated by negative friction, the values are still very small therefore fluctuations will be important.

	description	symbol	ND	Value		
length scale	particle diameter	D_0	$D_0^* = \frac{x}{D_0}$	10μm	300μm	500μm
velocity scale	bulk rotor flow speed	u_0	$u^* = \frac{u_i}{u_0}$	6.0m/s	-	-
fluid density scale	air density	ρ_{f0}	$\rho_f^* = \frac{\rho_f}{\rho_{f0}}$	1.19kg/m^3	-	-
particle density scale	sand density	ρ_{p0}	$\rho_p^* = \frac{\rho_p}{\rho_{p0}}$	2480kg/m^3	-	-
viscosity scale	viscosity of air	μ_0	$\mu^* = \frac{\mu}{\mu_0}$	1.82×10^{-5}kg/ms	-	-
time scale	*derived*	$\frac{D_0}{u_0}$	$t^* = t\frac{u_0}{D_0}$	1.56×10^{-6}s	46.9×10^{-6}	78.1×10^{-6}
surface energy scale	surface energy of glass	σ_0	$\sigma^* = \frac{\sigma}{\sigma_0}$	2×10^{-4}Jm^{-2}	-	-
Reynolds number	*derived*	$\frac{\rho_{f0} D_0 u_0}{\mu_{f0}}$	Re_0	4.31	1.29×10^2	2.15×10^2
gravity scale	magnitude of gravity	g_0	$g = g_0 g^*$	9.81m/s^2	-	-
Froude number	*derived*	$\sqrt{\frac{u_0^2}{g_0 D_0}}$	Fr_0	646	118	91.4
density ratio	fluid to solid density	$\frac{\rho_{f_0}}{\rho_{p_0}}$	$\frac{\rho_{f_0}}{\rho_{p_0}}$	5.57×10^{-4}	-	-

Table 6.2: Nondimensional parameter definition.

Force		F_ϕ	C_ϕ or f_ϕ
Drag	F_{D0}	$\left[18 f_D \frac{\rho_{f0}}{\rho_{p0}} \frac{1}{\mathrm{Re}_0}\right]$	$f_D = \begin{cases} 1 & \mathrm{Re_p} \ll 1 \\ 1 + 0.15\mathrm{Re_p}^{0.687} & \mathrm{Re_p} < 800 \end{cases}$
[70, ch:6], [71, 72]	F_D^*	$\left[\frac{\mu_f^*}{\rho_p^* D_p^{*2}} \left(u_i^* - v_i^*\right)\right]$	
Basset	F_{B0}	$\left[\frac{9 C_B}{\sqrt{\pi}} \left(\frac{\rho_{f0}}{\rho_{p0}} \frac{1}{\mathrm{Re}_0}\right)^{\frac{1}{2}}\right]$	$C_B = 2.88 + \frac{3.12}{(0.12+A_c)^3}$ $A_c = \frac{\lvert u_{rel}\rvert^2}{2 r_p \frac{d\lvert u_i - v_i\rvert}{dt}}$
[70, ch:6],[73]	F_B^*	$\left[\left(\frac{1}{\mathrm{Re}^* t^*}\right)^{\frac{1}{2}} \left(\int_0^t \frac{1}{\sqrt{(t^* - \tau^*)}} \frac{\mathrm{d}\left(u_i^* - v_i^*\right)}{\mathrm{d}\tau^*} \mathrm{d}\tau^* + \frac{\left(u_i^* - v_i^*\right)_0}{\sqrt{t^*}}\right)\right]$	
Magnus	F_{M0}	$\left[\frac{3}{4} C_M \frac{\rho_{f0}}{\rho_{p0}}\right]$	$C_{L,M} = 0.45 + \left(\frac{\mathrm{Re}_{rot}}{\mathrm{Re}_p} - 0.45\right) \exp\left(-0.05684 \mathrm{Re}_{rot}^{0.4} \mathrm{Re}_p^{0.3}\right)$
[70, ch:6], [66, 48]	F_M^*	$\left[e_{ijk} \Omega_j^* \left(u_k^* - v_k^*\right)\right]$	$\mathrm{Re}_{rot} < 140$
Saffman	F_{S0}	$\left[3.07 f_S \frac{\mu_0}{\left(u_0^2 \rho_{p0}\right)} \left(\mathrm{Re}_0\right)^{\frac{1}{2}}\right]$	$C_{L,S} = \begin{cases} \left(1 - 0.3314\sqrt{\beta_L}\right) \exp\left(-\frac{\mathrm{Re_p}}{10}\right) + 0.3314\sqrt{\beta_L} & \mathrm{Re_p} \leq 40 \\ 0.0524\sqrt{\beta_L \mathrm{Re_p}} & \mathrm{Re_p} > 40 \end{cases}$
[70, ch:6], [84]	F_S^*	$\left[\left(\frac{\mu^*}{D^{*2} \rho_p^*}\right)^{\frac{1}{2}} \left(\frac{e_{ijk}\left(u_j^* - v_j^*\right) \omega_{f,k}^*}{\lvert\omega_{f,i}^*\rvert^{\frac{1}{2}}}\right)\right]$	$\beta_L = \mathrm{Re_p} \frac{\lvert\omega_{rel}\rvert}{\lvert u_{rel}\rvert}, \quad 0.005 < \beta_L < 0.4$
Gravity	F_{G0}	$\left[\frac{1}{\mathrm{Fr}_0^2}\right]$	
	F_G^*	g_i^*	
Cohesion	F_{P0}	$\left[6 f_p \frac{\sigma_0}{D_0 u_0 \rho_{p0}}\right]$	$f_p = \begin{cases} 1.5 & \mathrm{JKR} \\ 2 & \mathrm{DMT} \end{cases}$
[97, 98, 57, 105]	F_P^*	$\left[\frac{\sigma^*}{D^{*2} \rho_p^*} r_i^*\right]$	
Friction	$F_{fr0} F_{fr}^*$	$C_{Fr}\left(F_{P0} F_{p,i}^* + F_{g0} F_{g,i}^* - F_{S0} F_{S,i}^* - F_{M0} F_{M,i}^*\right)$	

Table 6.3: Forces and nondimensionalisation.

Force reference	Direction	Particle diameter, D_p		
		10μm	300μm	500μm
F_{D0}	$\rightarrow$	$2.20 \times 10^{-3} f_D^*$	$7.34 \times 10^{-5} f_D^*$	$4.40 \times 10^{-5} f_D^*$
F_{B0}	$\rightarrow$	$5.62 \times 10^{-2} C_B^*$	$1.03 \times 10^{-2} C_B^*$	$7.94 \times 10^{-3} C_B^*$
F_{M0}	$\uparrow$	$3.60 \times 10^{-4} C_M^*$	$3.60 \times 10^{-4} C_M^*$	$3.60 \times 10^{-4} C_M^*$
F_{S0}	$\uparrow$	$1.24 \times 10^{-9} f_S^*$	$6.79 \times 10^{-9} f_S^*$	$8.77 \times 10^{-9} f_S^*$
F_{G0}	$\downarrow$	2.73×10^{-6}	8.18×10^{-5}	1.36×10^{-4}
F_{P0}	$\downarrow$	$8.06 \times^{-3} f_P^*$	$2.69 \times 10^{-4} f_P^*$	$1.61 \times 10^{-4} f_P^*$
F_{Fr0}	$\leftarrow$	$7.71 \times 10^{-3} C_{Fr}^*$	$-9.31 \times 10^{-6} C_{Fr}^*$	$-6.23 \times 10^{-5} C_{Fr}^*$

Table 6.4: Force reference values for 3 particle sizes.

6.4.2 Analysis of nondimensional forces for inception about an asperity

Inception occurs when the fluid forces acting on the particle are sufficient to exceed the resistive forces of gravity and cohesion. A sand particle on a bed of sand can be modelled as a sphere resting on two or more asperities which are themselves spheres, as in Fig. 3.2. This approach, adopted by Ibrahim *et al*. [58] and ZFG [57], uses the moments to liberate the particle, ZFG includes a full analysis of particle detachment from a flat plate as well as rocking about an asperity, here only the latter will be considered as the dusty ground is composed of particles upon particles not smooth surfaces. The analysis is as follows; moments are calculated about the downwind asperity, A, the horizontal fluid force, F_H, acts at distance $0.74r_p$ above the centre of the particle as suggested by Ibrahim *et al*. [58] due to the shear $\frac{du}{dy}$. The lift and weight act at the centre, cohesion acts at the contacts. The distance between asperities A and B is a. Resolving the moments about asperity A gives Eq. (6.5):

$$F_H r_p \left(0.74 + \left(r_p^2 - \frac{a^2}{4}\right)^{\frac{1}{2}}\right) - aF_P - (F_g - F_L) r_p \frac{a}{2} = 0 \tag{6.5}$$

such that the horizontal streamwise force required for motion becomes Eq. (6.6):

$$F_{H_{crit}} = \frac{aF_P + (F_g - F_L)\frac{r_p a}{2}}{r_p \left(0.74 + \left(r_p^2 - \frac{a^2}{4}\right)^{\frac{1}{2}}\right)} \tag{6.6}$$

Once the particle is freed from this stable position it is still reliant on the lift forces to overcome gravity. As particles tend to occupy stable positions it is the motion of larger particles, more exposed to the flow and with smaller asperity bases, that precede the suspension of the finer colloidal particles.

Nondimensionalising Eq. (6.6) results in Eq. (6.7):

$$F_{H_{crit}} = \frac{F_{p0} a^* F_P^* + a^* D^* \left(F_{g0} \frac{D_0}{4} F_g^* - F_{S0} \frac{D_0}{4} F_S^* - F_{M0} \frac{D_0}{4} F_M^*\right)}{\frac{0.74}{2} D^* + \frac{D_0}{4} D^* \left(D^{*2} - a^{*2}\right)^{\frac{1}{2}}} \tag{6.7}$$

substituting values from Table 6.4 into Eq. (6.7) and ignoring the insignificant terms, $F_{g0} D_0$, $F_{S0} D_0$ and $F_{M0} D_0$, gives Eq. (6.8):

$$F_{H_{crit}} = \left[A_H \frac{a^* F_P^*}{D^*}\right] \tag{6.8}$$

where $A_{H,D=10} = 2.18 \times 10^{-2}$, $A_{H,D=300} = 7.27 \times 10^{-4}$ and $A_{H,D=500} = 4.36 \times 10^{-4}$.

F_H is the sum of all the fluid forces acting in the direction of the flow, the common force in

this case is drag, but as seen in the previous analysis the Basset force is also potentially significant. Substituting the nondimensionalised drag force and the reference term from Table 6.4 gives Eq. (6.9):

$$F^*_{D_{crit}} = \left[9.90\frac{a^*}{f_D D^*}F^*_P\right]_{10\mu\text{m}} = \left[9.90\frac{a^*}{f_D D^*}F^*_P\right]_{300\mu\text{m}} = \left[9.90\frac{a^*}{f_D D^*}F^*_P\right]_{500\mu\text{m}} \tag{6.9}$$

From this analysis it is clear that the moment required by the drag force scales with the pull off force. For the drag force to be capable of rocking the particle there will need to be fluctuations to increase drag and a relatively small asperity base. Larger particles are more likely to be resting on smaller particles, will have a smaller a^*/D^* and will be easier to rock.

Repeating the above substitution for the Basset force yields Eq. (6.10):

$$F^*_{B_{crit},i} = \left[A_B\frac{a^*}{C_B D^*}F^*_P\right] \tag{6.10}$$

where $A_{B,D=10} = 0.388$, $A_{B,D=300} = 7.09 \times 10^{-2} \times 10^{-4}$ and $A_{B,D=500} = 5.49 \times 10^{-2}$.

This indicates that the Basset force is much more capable of causing inception than the drag force; this indirectly supports the rock'n'roll model, described by Reeks and Hall [168], based on the premise that a particle will oscillate by pivoting backwards and forwards around one of the asperities. The analysis in both cases agrees with the notion of Ibrahim *et al*. [58] that larger particles are suspended more readily than fine particles.

6.5 RANS flow-particle analysis

In this section the RANS flow field is applied to the particles; first their location in the boundary layer is considered, second the particle-fluid force expressions described earlier are applied to the near ground region of the flow field and results discussed.

6.5.1 Boundary layer analysis

To see where the particles rest in the turbulent boundary layer Fig. 6.6 shows D_p/y^+, where y^+ is the nondimensional distance from the wall, Eq. (3.20). The regions of the boundary layer are defined by their y^+ those regions are described in Section 3.2.1. It can be seen that the smallest particles are well within the viscous sublayer and so are subject to the physics and lift forces given by Saffman [95], Leighton and Acrivos [96]. Where as the larger particles protrude into the buffer zone and are subject to the wall lift forces described by Mollinger and Nieuwstadt [91], and Hall [55]; for these particles inertial effects are significant and the assumption of a linear shear layer [61] is not entirely valid. The Phillips and Brown [166] model assumes a single threshold velocity without consideration of where the particle exists in the boundary layer and the Wachspress *et al*. [19] model makes no allowances for the change of physics involved between particles in the viscous and those in the inertial layers.

The Stokes number is the ratio of particle relaxation time to fluid time scales, Eq. (3.29), it is an indicator of the particles reaction to unsteady flow features such as turbulent eddies. The time-scales of the larger eddies was found using turbulent kinetic energy and dissipation rate $\tau_f = \frac{k}{\epsilon}$. In this flow we find $\text{St}_{10} > 1$ for $y^+/D_p < 1$ indicating that a particle on the surface will not resonate in response to turbulent eddies close to the wall. The larger particles also show they are unlikely to be stimulated by the near wall fluctuations as $\text{St}_{300} \gg 1$ and $\text{St}_{500} \gg 1$. However, the time scale of the turbulent fluctuations is much smaller than the time scales indicated by the unsteady simulation in Chapter 5. The unsteady analysis indicated the time scale of the large scales is of the same order as the rotor frequency, and the particle relaxation time is much smaller

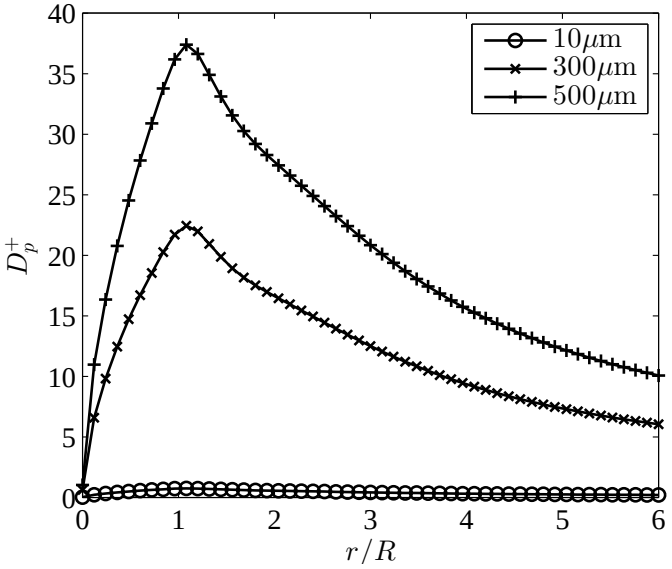

Figure 6.6: The particle diameter D_P^+, nondimensionalised by the viscous length scale $\delta_\nu = \nu\sqrt{\frac{\rho_f}{\tau_w}}$, for three particle diameters computed across the radial extent of the domain.

than that resulting in St < 1 for the smaller particles and St $\rightarrow 1$ for $D_p \Rightarrow 500\mu$m. It must be iterated, however, that only the large scales were appropriately resolved in the unsteady analysis of Chapter 5, the scales of this flow are appropriate to a steady full scale flow and are a good approximation of the scales of a full scale unsteady flow.

It has been suggested in the literature, [100, 14], that the flow can cause particles to resonate in situ before being ejected. The resonance entrainment model [14] assumes energy from the turbulent fluctuations causes the particle to resonate within the adhesive potential well, the particle detaches from the surface when it has acquired enough energy to escape from the well. The evidence here suggests the drag force is not capable of this concept as St $\gg 1$.

6.5.2 Particle forces

The particle forces were calculated for the 3 diameters of $D_p = 10, 300$ and 500μm in the near wall region $y < 3D_p$ and nondimensionalised by the sum of cohesion and gravity; $F_\phi/(F_g + F_p)$. In all cases the particle is assumed stationary relative to the ground and not rotating. The value at a height of $y \simeq 0.5D_p$ is of particular interest as that is the location of the resting particles centre of mass. For the regions where $y > D_p$ the particle is unlikely to be stationary so forces in this region are overestimated, however, it is useful to have an indication of the fluid forces a particle is likely to encounter should it leave the ground.

The drag forces, Fig. 6.7, are significant for all but the smallest particle sizes, the region $1 < r/R < 3$ is of most significance, here the forces are strongest. The horizontal region where the drag is significant is very large providing a large surface for potential inception. The trends here agree with those indicated by the nondimensional analysis; for the smallest particles the drag is very large - but cohesion holds the particles back, for the medium and large particles the drag is of similar order to the retarding forces.

The Basset force requires relative acceleration history over time. To simulate this from the RANS results the larger eddy time scale, $\tau_f = \frac{k}{\epsilon}$ is used as the period and twice the RMS fluctuation, $2u'$, is used as the amplitude. The relative acceleration is; $\dot{u} = u'\frac{2\pi}{\tau_f}\cos(t\frac{2\pi}{\tau_f})$, where t is time. These forces were all insignificant compared to the sum of cohesion and gravity for this flow field. However, the fluctuations in this flow will not be the same as those in flow with ground vortex interaction. Recall Fig. 5.5 that showed autocorrelation of velocity over time at a

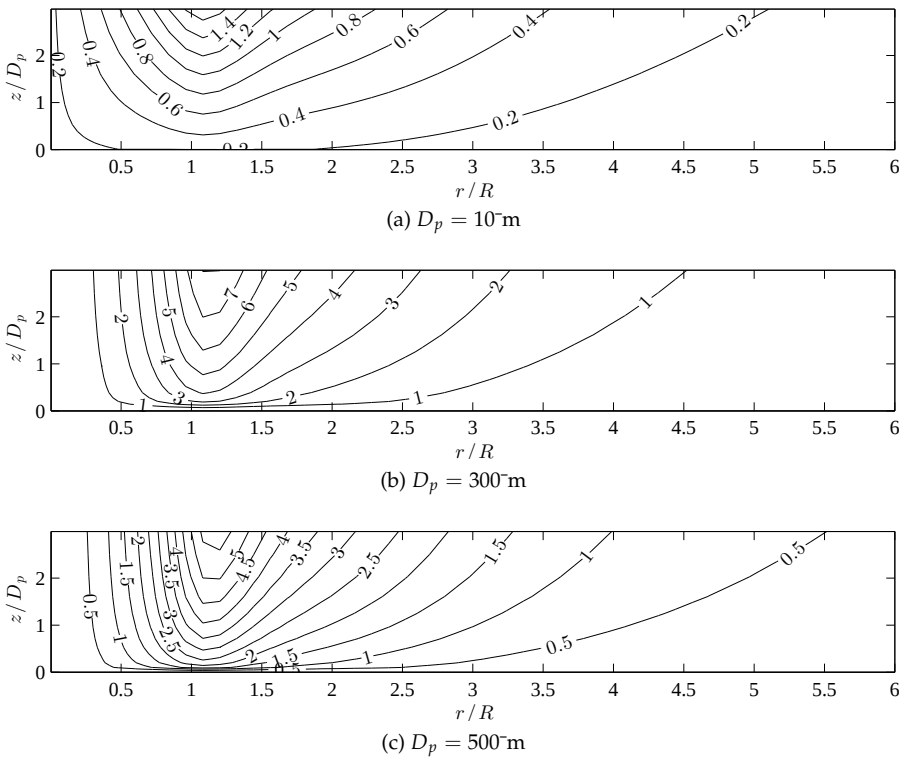

(a) $D_p = 10^{-}$m

(b) $D_p = 300^{-}$m

(c) $D_p = 500^{-}$m

Figure 6.7: Drag force field for three particle sizes, nondimensionalised by weight and cohesion. Plot of the near ground region, $y < 3D_p$, and radially from hub to $r = 6R$.

specific location: the velocity was near sinusoidal, however, the frequency of velocity oscillation was linked to the frequency of the rotor and grew less frequent with increasing r.

The Basset force was calculated for the scaled unsteady flow field in Section 5.7, it was insignificant compared with the drag force and weight of the particle.

The wall induced lift force is quantified in Fig. 6.8 for the 3 particle diameters. The peak is in the region of $r \simeq R$. The smaller particles are subject to strong lift forces but are dominated by the cohesive forces; the medium sized particles are capable of being entrained by these flow conditions but the largest particles are too heavy.

Summing the forces acting on the particle gives a resultant force vector, these have been plotted for six radial particle locations in Fig. 6.9, a vector length of one radius indicates a resultant force equal in magnitude to $F_G + F_P$. It is clear that the medium particles are the most likely to be incepted, the region $0.5 < r/R < 2.5$ showing the strongest resultant forces.

6.6 Effects of blade tip vortices

It is clear from both the literature noted above and the unsteady simulations performed in Chapter 4 that the tip vortices present in the rotor wake are a significant factor in the entrainment process. In this section we follow the approach of Ananthan *et al*. [156] to estimate the initial location and strength of tip vortices produced by the rotor IGE and the transport of these vortices toward and across the ground plane.

The wake boundary is found by following a streamline from the rotor tip, the tip vortices are known to travel along this streamline [27] and the vortex paths from the unsteady results confirm this, presented in Fig. 6.11b. As the tip vortices convect downwards two processes act upon them; diffusion and strain. Diffusion acts to increase the radius of the vortex core whilst positive strain, stretching the vortex filament, decreases the vortex core radius and conservation of circulation causes the filament to spin up. As in Ananthan *et al*. [156] the radius of the vortex

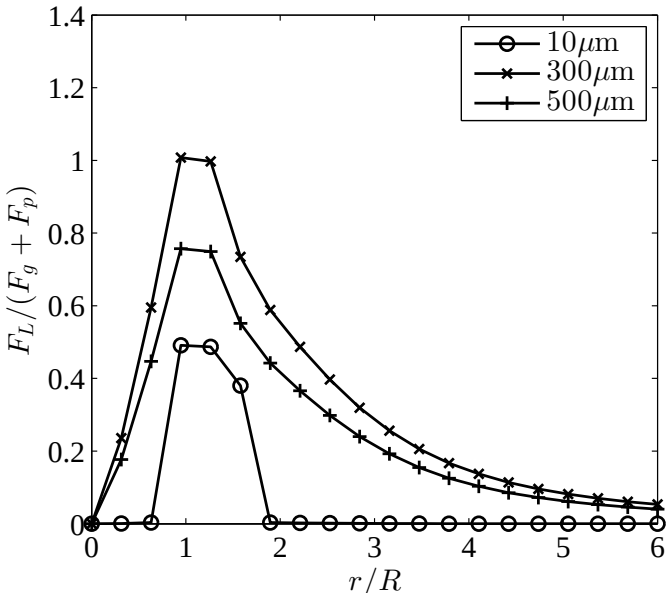

Figure 6.8: Induced lift force for wall bound particles. Three diameters plotted.

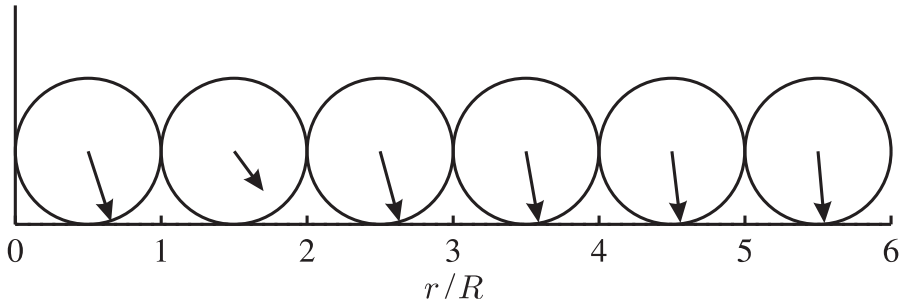

(a) $D_p = 10\mu$m

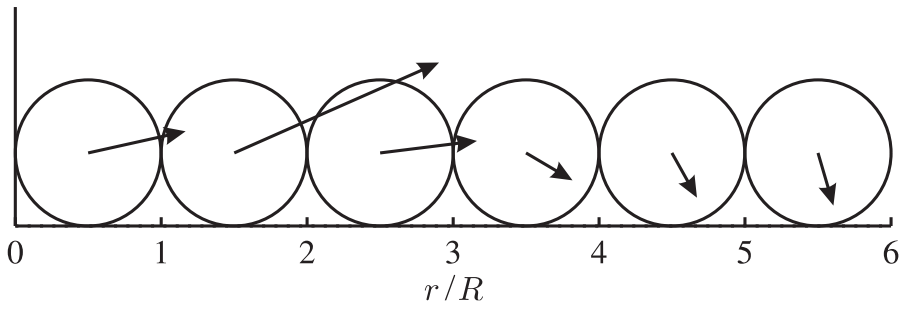

(b) $D_p = 300\mu$m

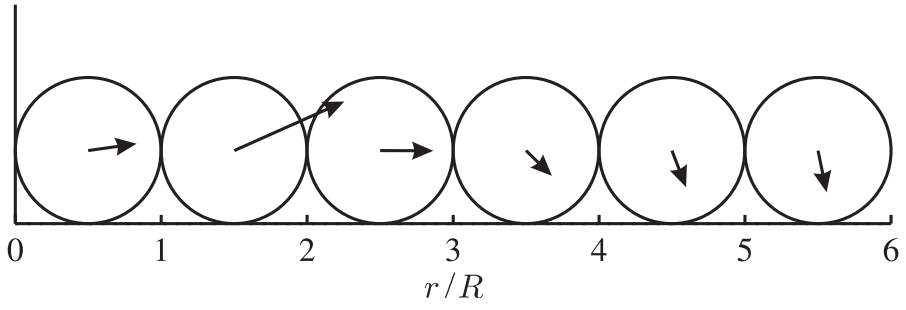

(c) $D_p = 500\mu$m

Figure 6.9: Resultant force vectors for wall bounded particles at varying radial positions. Arrow length of 1 radius indicates $F_{Total} = F_G + F_P$.

is defined as the radial distance from zero to the peak swirl velocity. A third process also occurs due to the influence of other nearby vortices, the induced velocity of one vortex will influence the position of those around it and vice versa resulting in filaments twisting around each other and even joining up [39], this was seen in the unsteady results such as in Fig. 5.1 and in the many other vortex paths shown in Fig. 6.11b. For a near ground vortex the induced velocity would lower the pressure between the vortex and the ground and suck the vortex downwards. The first two of these processes are considered in this analysis.

The tip vortices of a helicopter are helical, for the purposes of calculation they are considered to be discrete rings in this axisymmetric simulation. The vortices follow the wake boundary therefore the strain at any time can be given as the relative change in the circumference of the vortex ring, that is $\epsilon(\psi) = \frac{r_v(\psi) - r_{v0}}{r_{v0}}$ where $r_v(\psi)$ is the radius of the vortex ring at wake age $\psi = \Omega t$ and r_{v0} is the radius of the rotor blade. The vortex core radius, r_c, following a given strain can be found using Eq. (6.11) from Ananthan *et al*. [156]:

$$r_c(\psi) = r_{c0} \frac{1}{\sqrt{1 + \epsilon(\psi)}} \tag{6.11}$$

where r_{c0} is the vortex core radius at $\psi = 0$. Diffusion acts to increase the vortex radius as described by Lamb [169] and modified by Squires [170], defined by Eq. (6.12):

$$r_c(\psi) = \sqrt{r_{c0}^2 + \frac{4\alpha\delta_\nu \nu\psi}{\Omega}} \tag{6.12}$$

where α is a constant found to be 1.25643 [169], δ_ν is an eddy viscosity parameter $\delta_\nu = 1 + a_1 (\Gamma_v/\nu)$ with $a_1 = 2 \times 10^{-4}$ from Ananthan and Γ_v is the tip vortex circulation. The tip vortex circulation can be estimated from the lift, given 2 blades then $\Gamma_v = L/(R^2\Omega\rho)$ where Ω is the blade angular velocity. Combining the effects of diffusion, Eq. (6.12), and filament strain, Eq. (6.11), gives Eq. (6.13):

$$r_c(\psi) = \sqrt{r_{c0}^2 + \frac{4\alpha\delta_\nu \nu\psi}{\Omega}} \frac{1}{\sqrt{1 + \epsilon(\psi)}} \tag{6.13}$$

Using the previously defined lift value, $L = 8800$kN, using a typical blade rotational speed of $\Omega = 340$rpm $= 35.6$rads^{-1} and estimating the initial vortex core radius using the PIV results of Johnson *et al*. [39] to be $r_{c0} = 0.03R$ we can quantify the vortex initialisation. The inset in Fig. 6.10 compares the size of the vortex radius over time using the diffusion model with the combined diffusion-strain model. In the combined model r_c is larger where negative strain caused by the contraction of the rotor wake is present and similarly when strain is positive as the wake expands across the ground r_c decreases more rapidly than the expanding process of diffusion.

The mean vortex size in the unsteady simulations performed in Chapter 5 was captured and is presented in Fig. 6.11a. Clearly the vortices in the unsteady simulation diffuse much more rapidly than the analytical model, probably due to insufficient grid resolution. The path of the vortices from Chapter 5, however, is a very close match to the RANS results in this chapter.

Having found r_c the swirl velocity around the vortex can be described using the Lamb-Oseen model [169] in Eq. (6.14):

$$V_\theta(\bar{r}) = \frac{\Gamma_v}{2\pi r_c} \frac{1 - e^{-\alpha\bar{r}^2}}{\bar{r}} \tag{6.14}$$

where $\bar{r} = r_v/r_c$ is the relative radial distance from the vortex core and r_v is the radial distance from the vortex core. This model is for the laminar diffusion, the vortices are large and fast causing the flow in and around the vortex to become turbulent. Weigand and Gharib [171] explains that the turbulence will cause the vortices to diffuse more rapidly, and will cause them

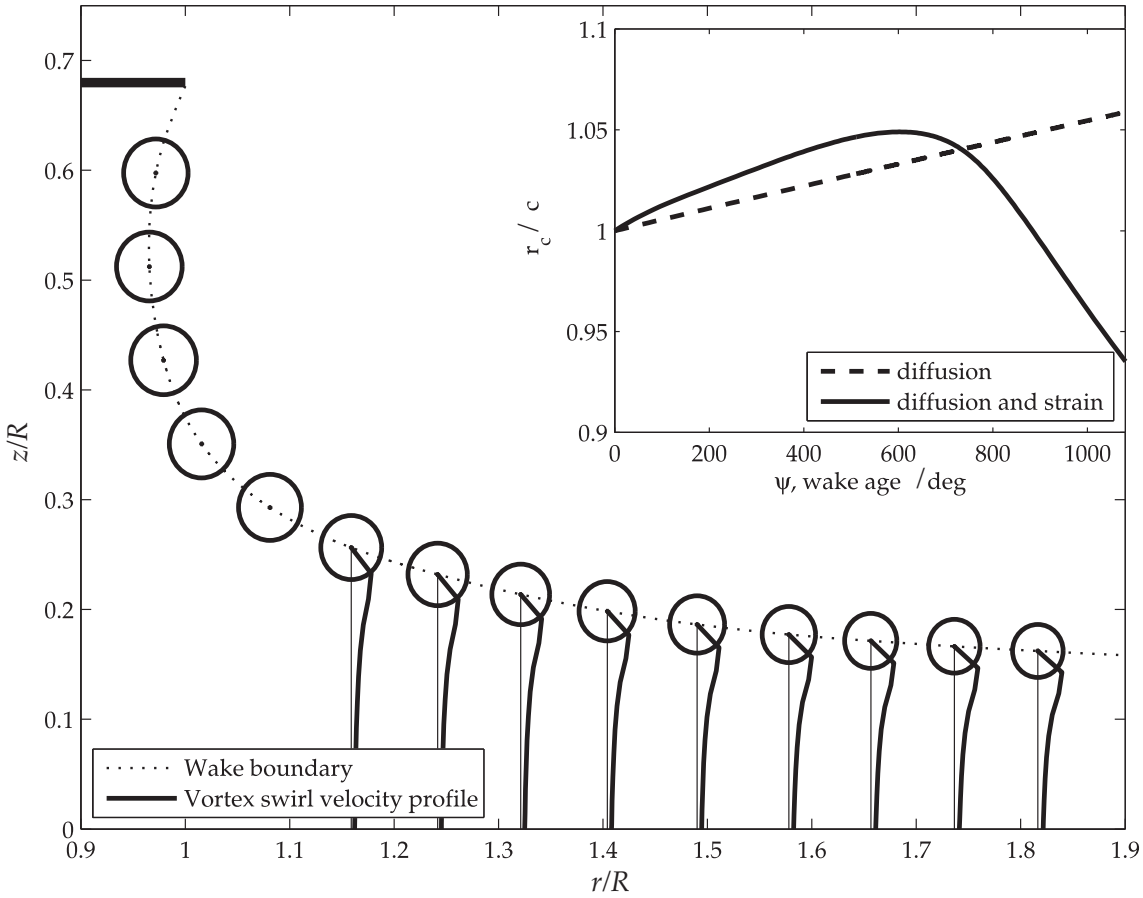

Figure 6.10: Vortex core progression in the axisymmetric flow field. Inset figure compares vortex core growth with and without strain effects.

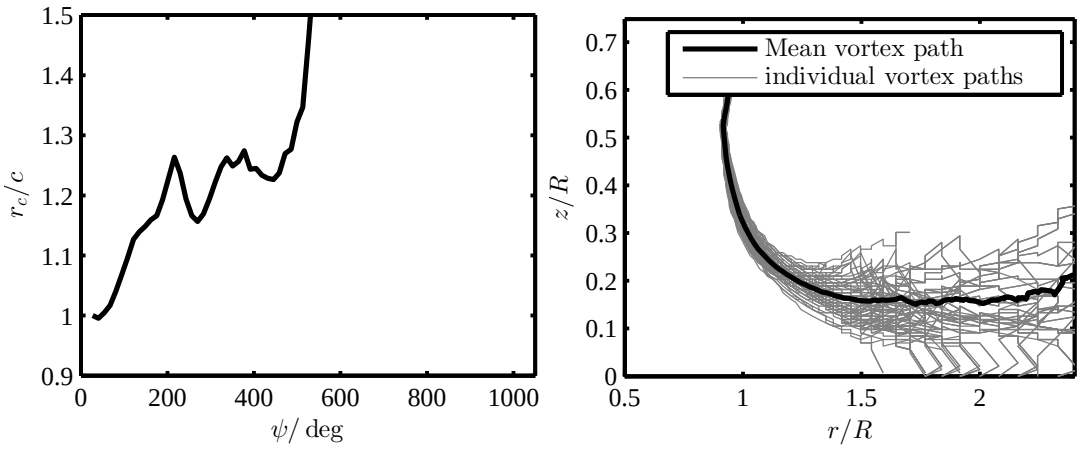

(a) Vortex width.

(b) Vortex path.

Figure 6.11: Vortex width and path results from unsteady simulations for case $z_d/R = 0.68$ in Chapter 5.

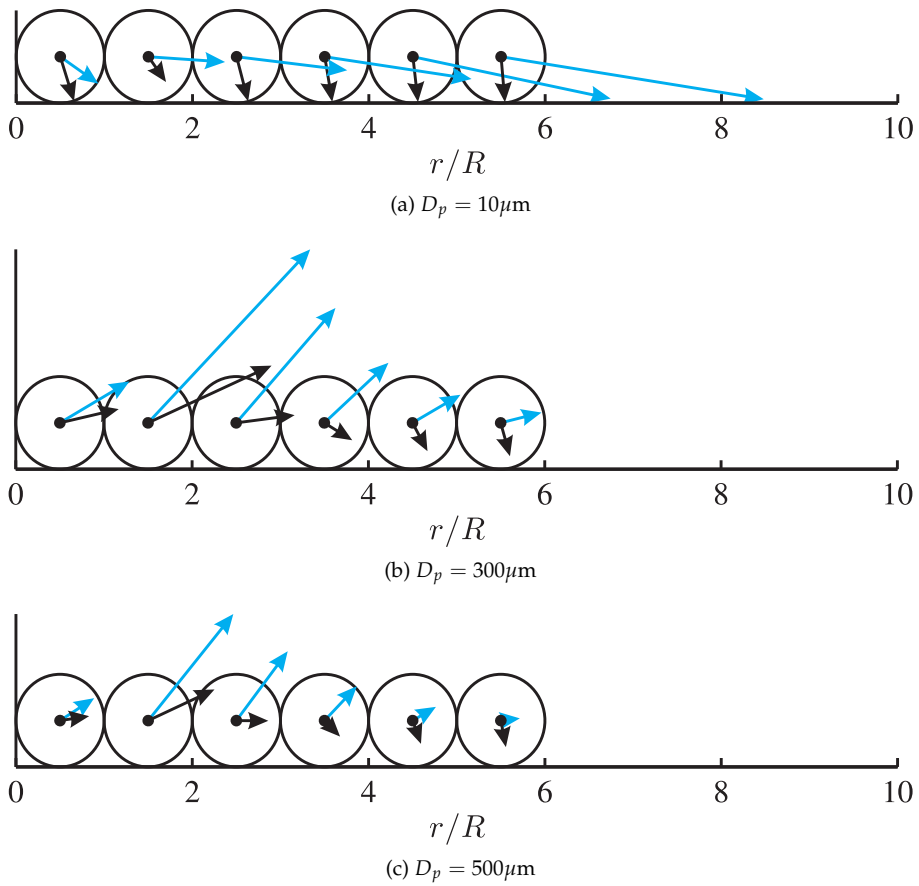

(a) $D_p = 10\mu$m

(b) $D_p = 300\mu$m

(c) $D_p = 500\mu$m

Figure 6.12: Resultant force vectors for wall bounded particles at varying radial positions, the blue arrow indicates the force vector including the effect of the analytical tip vortices and the black arrow is from the RANS flow field. Arrow length of 1 radius indicates $F_{Total} = F_G + F_P$.

to lose circulation and propagation speed.

Figure 6.10 indicates the swirl velocity profile for a series of vortex positions, these are reasonable when compared with the predictions of Ananthan *et al*. [156] and Ramasamy and Leishman [36] and compare qualitatively with the smoke visualisations of Lee *et al*. [27]. The swirl velocity seen at the ground has a value of $V_{\theta,\text{ground}} \simeq 1\text{ms}^{-1}$ and is fairly invariant to radial position in contrast with the average flow field. The fluctuations reported by the RANS results were of the order of 10-20% of the mean flow with the peak beneath the rotor tip. The vortices, however, represent higher fluctuations as much as 100% of the mean flow for the near ground distances, this still falls short of the potential 300% RMS values seen in the unsteady results in Fig. 6.4. The effect of the tip vortices has been included in a resultant force vector analysis in Fig. 6.12, the calculation assumes an analytical vortex is directly above each particle position on the path indicated in Fig. 6.10. We can see that the radial force is greatly increased for the smallest particles but the medium sized particles are still the most lifted, the large particles are now capable of being lifted in the pick up region $1 < r/R < 3$.

The vortex is a highly 2 dimensional flow feature; as the vortex passes a fixed point on the ground the vortex swirl velocity is first an upwash, then a horizontal flow as the vortex is directly above and finally when the vortex has passed the flow is directed toward the ground. The velocity magnitude peaks when the vortex is directly overhead. The increase in horizontal flow velocity and velocity gradient from the passing vortex will increase the range of particle sizes stimulated and increase the spatial entrainment region. The vortices also provide the vertical flow that pulls particles up and away from the ground. In Chapter 5 the process of vortices lifting particles upwards was found to relate to the interaction between vortices and

separation bubbles induced at the wall by those vortices. Standard inviscid models of rotor flows would not generate those separation bubbles. To capture this effect either an advanced ground model would need to be introduced to go with the inviscid methods, or a method like the VTM of Phillips and Brown [166] could be extended to include viscosity.

6.7 Discussion

The aim of the analysis is to discover which forces are capable of causing or contributing to particle inception within the downwash of a full scale helicopter flow. The nondimensional analysis gave some indication as to the influence of the different forces acting on the particle but the influence of the nondimensional term, the deviation from reference values, was not quantified. There are some differences between the behaviour indicated by the nondimensional analysis and the forces from the RANS model, this is due to the highly inhomogeneous flow. The results prove that the flow field cannot be characterized with a single set of scales, and similarly the RANS results show that the entrainment cannot be characterized by one set of scales either given that each particle size behaves differently.

The RANS results indicate that of the fluid forces presented only drag and wall-induced lift contribute significantly. Looking at Fig. 6.9 the drag force would easily be sufficient to induce movement through rocking about an asperity as proposed by ZFG (Ziskind *et al*. [57]). There is experimental evidence that the larger particles are the first to be incepted in parallel flows [58], correlating here in Fig. 6.9, emphasizing the varying significance of the cohesion force across particle sizes as the key factor.

Given the boundary layer is spatially developing and a range of particle sizes exist no one force is dominant but the lift-drag combination are the driving inception forces. For a Lagrangian entrainment model the cohesion, drag and wall induced lift are critical for understanding the location and size of the incipient particles. In this flow field the incipient motion is of the middle sized particles in the region $0.5 < r/R < 1.5$, although the vortices in Chapter 5 show they are able to expand that and the horizontal velocity that the analytical vortices induce near the ground does not decay as rapidly as the mean flow. The lift and drag both peak in this region and the force is enough for direct lift off or to initiate motion along the surface. The larger particles would rush along the surface knocking smaller particles breaking the cohesive forces enough that they can be entrained. These particles would continue in the wall jet until they met an upwash, the smaller particles would be taken up but the larger particles would not be as influenced. The larger particles would continue to saltate along the ground and cause subsequent fine particle entrainment, if these particles meet an upwash they will be carried upwards as well. A pattern of particle entrainment peaking around radially expanding vortices is visible in photographs of brownout and experimental observations of Lee *et al*. [27], Johnson *et al*. [39]. The paths of entraining particles in Fig. 5.13b also indicate the behaviour of particles being carried radially outward by a vortex and some particles travelling far along the ground before being blown upward.

The analytical tip vortex assessment looks at what is essentially a large scale inviscid feature; the turbulent fluctuations discussed in the mean flow field results are a result of the near wall boundary layer, a viscous flow feature with much smaller scales. Both the near wall boundary layer and the tip vortices are present in the real-world rotor wake, the vortices provide increase in horizontal velocity near the wall and upwash in the near wall region and the boundary layer is where all the particles lie before inception. The location of the particle in the boundary layer is shown by the RANS results to effect the aerodynamic forces on the particle, the passing vortex will alter the boundary layer structure. Combining the results of the RANS analysis with the

analytical tip vortex assessment and the unsteady simulations of Chapter 4 leads to the idea that the interaction of these two processes, inviscid large scale tip vortices and viscous small scale fluctuating boundary layer structures, are the key to the deterministic Lagrangian entrainment model.

Of the entrainment models reviewed it is difficult to say which best corroborate. The wall induced lift force is based on the friction velocity as are the aeolian mass flux models, this will give them similar behaviour if the aeolian parameters are tuned appropriately. Only the small particles are accounted for in the particle tracking models, assuming that saltation is confined to a near ground region is appropriate as the wall induced lift diminishes as the particle moves away from the wall so larger particles will not lift very high. However, the flow is highly inhomogeneous and the size of particles that can be entrained will change with radial position, this will subsequently change the saltation characteristics as well. The vortex ground interaction demonstrated in Chapter 5 and the experimental PIV work by Johnson *et al*. [39] are shown to be crucial to how the near wall animated particles are carried into the bulk flow.

A higher order unsteady analysis is required to study the evolution of the particle forces spatially and temporally and to determine how they contribute to entrainment as a whole.

6.8 Conclusion

The aim was to discover which particle forces are crucial to a physics based Lagrangian entrainment model for use with rotorcraft simulations. Presented here is a scaling analysis for the common fluid-particle forces with typical particle sizes using nondimensional analysis and time averaged flow field velocities. The nondimensional analysis indicated that the Saffman force could be ignored. Comparing the RANS results with the nondimensional analysis demonstrated that the flow is highly inhomogeneous and that using nondimensional analysis to find relative importance was difficult to interpret. The flow field showed that the smallest particles, and those primarily responsible for the visual obscuration, sit within the viscous boundary layer whereas large particles are well outside it. This analysis has reinforced the notion that larger particles are excited before small particles, it has highlighted the importance of wall bounded lift, but dismissed the shear based Saffman lift. Cohesion controls the particle dynamics at the smallest scale and weight controls them at the largest scale, the medium sized particles are the ones of most interest as these are the ones that will be first stimulated into motion and it is speculated that these will drive saltation. The analytical tip vortex assessment revealed that the vortices will likely increase the entrainment area through the increase in horizontal flow speed. The vortices will alter the structure of the boundary layer and in doing so change the aerodynamic forces on the particles, the vortices also provide the vital upwash that blows the liberated particles upward into the large clouds that cause brownout.

The complexity of the problem is not easily captured, the complex arrangement of the particle bed, the powerful vortex-ground interaction and the particle saltation are all potentially significant factors. The union of the Lagrangian forces, inviscid tip vortices and the viscous boundary layer development on the ground could be the solution to this problem if it could also capture the separation bubble effect shown to be vital in Chapter 5.

Chapter 7

Towards Enhanced Bed Modelling

Of vital importance to a deterministic entrainment model is appropriate modelling of the particle bed. The previous chapters have explored how the flow of a rotorcraft can carry particles up into the bulk flow but the position of particles on the bed and how the particles on the bed respond to the flow are both very important. This chapter briefly explores the current literature on modelling particle beds in flows and methods used. The chapter continues by considering the eligibility of the Discrete Element Method to model the particle bed in an aeolian flow scenario. The results of two studies using the Discrete Element Method (DEM), Appendix A and C, show that the DEM can recreate dynamics appropriately and is recommended as a method to describe the particle bed.

7.1 Introduction

A deterministic entrainment model requires that specific flow events cause a corresponding degree of particle entrainment. But the particle state must not be considered digitally as entrained or not-entrained, rather that particles must be free to be moved by the flow, to this end large particles may remain unmoved or creep gently while other particles may roll along the tops of other particles before being carried away. Particles free to behave in this way will exhibit the full range of aeolian transport phenomena.

The position of particles in the has been shown to be significant, with regards to entrainment, by XU *et al*. [172]. XU *et al*. [172] examined the particles in a 2D bed and considered variation in size, shape and protrusion from the bed surface. It is demonstrated that large particles in a bed of non-uniform particles require a lower incipient velocity and smaller grains in that bed require a higher incipient velocity and are also dependent on exposure to the flow. The results show that the arrangement of particles on the mesh and the particle size distribution have an impact on inception.

A combined fluid and particle simulation was conducted by Yang *et al*. [173] to attempt to simulate aeolian saltation. The fluid was simulated using a finite volume method similar to that used in Chapters 6 and 4 and the particles were simulated using the Discrete Element Method (DEM) described in Chapter 3 and used in Appendix A. A shear flow was passed over a bed of particles and the particles were subjected to a drag force from that flow, the flow received the same drag force distributed over the appropriate fluid cell; the simulation was 2-way coupled. The mass flux results, and the lift off velocity is a good match for experimental results by Kang *et al*. [174]. Similar simulations were performed by Kang and Zou [175] combining so called 2D and 2.5D fluid methods with 2D and 3D DEM methods. Heald *et al*. [176] also had success using 3D DEM and a 2.5D uniform flow model. These works are highlighted here because they show that the combination of computational fluid and particle methods is capable of recreating experimental results of aeolian saltation. Rotor induced entrainment, on the other hand, is unsteady - the presence of discrete vortices near the ground means the flow field changes constantly. In the unsteady scenario it is therefore important to know the time scale of the flow changes, the time between vortices, and the response time of particle ejection. These concepts were explored in an unsteady rotor flow simulation in Chapter 5.

DEM has been used to simulate particle entrainment in other industries with success. Sakai and Koshizuka [177] use a more advanced DEM model to simulate pneumatic conveying. This DEM method uses a clustering concept to reduce the computation required, very applicable to the modelling of a particle bed on the helicopter scale.

The DEM is also readily expandable in terms of including more complex features such as non spherical particles, [117], and different force models [118].

To examine the finer motions of the fluid around each particle a more detailed approach is required. A fully resolved method will enforce the no-slip wall condition on the surface of each particle and allow those particles to move will allow a validation of the Lagrangian fluid forces that are to be applied to the DEM. Furthermore they will allow a validation to the behaviour of the particle between its initial excitation, when the particle first begins to move, and inception into the flow. Derksen and Larsen [178] considered layers of fully resolved particles on a surface in a low Reynolds number flow, the flow was fully resolved and the particles were modelled using the immersed boundary method. Derksen and Larsen found that from one particle to the next the forces on the particle changed considerably due to the flow interaction. In multiple layers Derksen and Larsen found that there was some fluid force on the particles but it decayed rapidly with depth into the bed. This method is very computationally expensive but gives very good results. The challenge is to scale the processes upwards to involve more particles and yet

retain the features that are resolved in the most detailed models.

7.2 Towards an enhanced bed model

The DEM model has been used in other studies to simulate a particle bed in a horizontal flow.

Mathematically the DEM has an interesting characteristic compared with other numerical models, because particle interactions are modelled the initiation of contacts causes discontinuous forces to be a regular feature of the system. A separate study was conducted to assess the impact of these discontinuities on performance of the system, Jasion *et al*. [1], this study is included in Appendix A. A single particle collision is carefully modelled so that the exact point of collision can be controlled between time steps. The study performed here examines the tangential forces and follows from a similar study that looks at the normal force model. It was found that the all numerical schemes were reduced to first order behaviour if they encountered discontinuities at different points during the time step.

It is proposed here that the DEM be used to model the particle bed in this unsteady and vortically dominated flow. It has been established in literature that the position of particles in the bed is significant. To be successful the DEM must be capable of recreating the dynamics of changes in the bed structure, to this end a probe indentation experiment was modelled using the DEM to see if the DEM was capable of recreating the bed dynamics, Jasion *et al*. [3]. The probe indentation experiment consisted of a probe with a ruby sphere tip driven into a die containing a powder of glass spheres, the largest sample had $\overline{r_p} = 250\mu$m. The probe was driven at constant velocity and the force on the probe was recorded over time and depth. The study is included in full in Appendix C, the study concluded that while the forces on the probe were not the same as the experiments the trends were recreated and the dynamics were also recreated. If the force dynamics of the DEM are recreated then the particles are rearranging themselves appropriately, this indicates that the DEM could be used to model the particles in the bed as they are perturbed by the flow.

The next step is to compare the simplified approaches of [175] or Drake and Calantoni [179] with a fully resolved method that has dynamic particles. Following this unsteady flows need to be considered, perhaps the simplest to recreate maybe the parallel but accelerating flow that [58] used in the wind tunnel. Beyond this the vortex ground interactions seen in Chapter 5 can be recreated and compared with the experimental results of Johnson *et al*. [39].

Chapter 8

Conclusions and Further Work

The entrainment of sand and dust into the rotor wash can result in the degraded visual environment known as brownout. Attempting to land a helicopter during a brownout can be very hazardous. The aim of this thesis was to gain a better understanding of the physics involved in the entrainment of sand into a near ground helicopter flow in order that a physics based model of particle entrainment and helicopter brownout could be developed.

The literature, Chapter 2, highlighted several strong complete brownout simulations and experimental investigations of the flow field and entrainment. The brownout simulations used entrainment models based on the aeolian expression derived by Bagnold. The empirical expressions by Bagnold are derived for steady aeolian environments rather than the unsteady, vortically dominated flows seen in the wake of a helicopter; a shortcoming highlighted by an experimentalist in the literature [39]. This thesis aimed to advance the modelling of particle entrainment by looking to overcome this shortcoming.

A summary of the work conducted and the key findings is provided here:

- An Eulerian finite volume unsteady flow simulation was performed and validated in Chapter 4 and explored from an entrainment context in Chapter 5. The simulation was validated against experimental results. It was found that the vortex path varied considerably and that over the region of interest, $1 < r/R < 3$, the vortices undergo considerable changes due to twisting, pairing and expanding. The vortices created strong near wall shear stress events which were found to be larger than the relaxation time of typical sand particles. It was found that an arrangement of a tip vortex and separation bubble at the wall caused entrained particles to be carried upwards, the particles were found to follow trajectories similar to those observed in the literature.

- A full scale but steady helicopter IGE flow field simulation was conducted, Chapter 6. The forces were found for particles at rest on the ground in the flow. The particles were found to sit in different regions of the boundary layer depending on their size; which strongly affects the flow physics they are subjected to. The simulation revealed that smaller particles are bound by cohesion to other particles in the bed, larger particles are bound by their weight but medium sized particles receive sufficient lift to be entrained. Including an analytical model of the tip vortices and comparing the results with the unsteady flow field of Chapters 4 and 5 showed that the boundary layer structure would be greatly altered by the tip vortices. The analysis and results of this chapter have been published [2].

- The Discrete Element Method, introduced in Chapter 3, was assessed for its numerical performance in Appendix A. The discontinuities in forces that occur at the start and end of every particle collision in a DEM simulation were found to reduce the order of the schemes

tested, it was found that no scheme could maintain above 1st order performance across a range of scenarios; the recommended scheme is the Simplectic Euler scheme. The work in Appendix A examines the effect of the discontinuities in the tangential direction, it builds upon the work of Tuley *et al*. [4] which assessed the normal direction, the former has been published [1].

- A large system of particles was simulated using the DEM in Appendix C. A simulation of a probe indentation experiment was conducted with several different combinations of DEM parameters. It was found that using higher stiffnesses and including friction came closest to recreating the trends seen in the experiment. The magnitudes of the force recorded were much lower than those seen in the experiment for all configurations but the frequency profiles of the forces were well matched indicating that the dynamics were recreated by the simulation. The chapter concludes that because the particle rearrangements are well represented by the simulation the method would be suitable for modelling the sand bed in a sand entrainment model. The work of this chapter has been accepted for publication pending acceptance of corrections [3].

The problem of particle entrainment into a rotor flow spans many scales. This thesis has considered the constituent parts of the problem at several different scales and found that: the tip vortices and their viscous interaction with the ground is crucial, the Lagrangian fluid-particle forces are a satisfactory means towards an entrainment model, and the DEM is a good choice to model a dynamic particle bed. This thesis has built a foundation for the creation of a physics based entrainment model for helicopter brownout simulations.

8.1 Future work

Application of a vortex dominated flow field to a particle bed would test the DEM and the Lagrangian fluid-particle forces in a dynamic flow field scenario. The flow would need to include the ground vortex interaction features described in Chapter 5. A study of this nature would help test the capability of the DEM during the entrainment phase.

An interesting observation is that the IGE rotor flow fields produced in both this work and the experimental and numerical work in the literature do not have flow recirculating back through the blade yet this can be seen in footage of helicopters in the desert. Including the fuselage, blade loading or control of the helicopter are all parameters that can be explored. An interesting avenue of investigation would be to see how different fuselage shapes and configurations alter the paths of the vortices and so the forces seen by the particles and the trajectories they follow. Literature [164] suggests that simulating the approach of a helicopter to the landing site would provide the recirculation characteristics more familiar with footage seen of helicopters in the desert. The viscous evolution of the near ground vortices has been shown to be crucial to the uplift of particles, simulating a helicopter with forward speed and discovering how the vortices behave near the moving ground could lead to some very interesting results.

The simulations performed here used a smooth wall; in reality the desert floor is not smooth therefore advancing the simulations here to consider rough walls would be a fruitful study.

This thesis worked with point particle fluid forces, however, a bed of particles could be modelled using fully resolved methods by employing Fictitious Boundary or Immersed Boundary methods. These methods allow for a two way coupled solution, modelling a fluid-particle bed would give a more detailed explanation of entrainment mechanisms.

The range of scales in this problem will always make solutions difficult, however, if particle entrainment can be related to large scale flow features, such as the vortices, then a deterministic solution can be found.

Appendix A

Performance of Numerical Integrators in the Discrete Element Method

---

The Discrete Element Method (DEM), first present in Chapter 3, is a numerical method that can be used to simulate a large number of Lagrangian particles. The DEM is considered in this thesis as a means to model the particles on the ground during inception into the rotor flow. Before that recommendation can be made the method must be assessed to see if it recreates the physics and behaviour seen in the laboratory, this assessment is performed in Appendix C. An important step in any DEM implementation is the integration of forces to update the particle position, however, unlike other physical simulations the forces acting on the particles are often discontinuous due to particle collisions. In this chapter the performance of various numerical integration schemes is quantified in a controlled DEM collision. It was found that all schemes were limited to 1st order by at least one of the conditions tested. The Symplectic Euler integration scheme is recommended as it is found to be of generally higher accuracy than other 1st order schemes in these tests. This chapter combines the results of the *normal* impact performed by Tuley *et al*. [4] with a *tangential* study performed for this chapter. The analysis and results of the tangential collision study are published in the journal *Computers & Chemical Engineering* [1].

A.1 Introduction

In the process of entrainment that precedes brownout the particle system on the ground must be understood. The Discrete Element Method (DEM) is a numerical model designed to simulating granular assemblies by evolving the motion of discrete elements, or particles, in time by means of a force model in the Lagrangian frame.

This chapter concentrates on the performance of numerical integrators applied to DEM simulations considering the force discontinuity that occurs during a particle collision. The process and assumptions of the Discrete Element Method were introduced in Section 3.4.4. There are numerous numerical integration schemes, in continuous scenarios high order methods offer more error reduction than low order methods for a given reduction in time step. However, the force a particle sees in a DEM simulation will contain many discontinuities due to particle collisions. The study performed in this chapter looks at how those discontinuities affect the performance of the integration schemes.

In this Chapter two simple collision scenarios are simulated: a normal impact between a fixed sphere and a free sphere and a sliding impact - a particle collides obliquely with a plane and continues to slide along it. For these simple scenarios analytical solutions of the DEM equations of motion exist. Several different numerical integrators are used to integrate the force expressions. The numerical and analytical solutions are compared to find the error for each scheme.

This chapter starts with a review of assessments of numerical integrators from the literature. Following this is a brief summary on the work of Tuley *et al*. [4] assessing the performance of the numerical integrators during a normal collision. The chapter follows the work of Tuley *et al*. [4] with a simulation to assess the performance of integrators on the tangential component of an oblique impact, the results of which are published in the journal *Computers & Chemical Engineering* [1].

A.2 Review of assessments of numerical integrators in particle simulations

Rougier *et al*. [180] conducted a thorough study of accuracy and stability of integration schemes used in DEM, molecular dynamics and similar systems. The analytical solution for comparison was a continuous one degree of freedom oscillating mass-spring system. The integration schemes were compared against the analytical solution for stability and accuracy, a study of CPU time required to achieve a given error was also performed. They concluded that no scheme is conditionally stable, and higher order schemes are not necessarily faster in terms of achieving a certain level of accuracy. Fraige and Langston [181] performed an assessment of the Leap Frog Verlet (LFV) integration scheme with the Velocity Modified Euler scheme for a normal collision of a particle with a wall with linear and non-linear damping and a larger simulation of 300 particles in a hopper. They concluded that the LFV scheme was more accurate for the single collision, and more stable for the hopper simulation. The effect of the discontinuity is only mentioned with regards to the damping parameter. Kruggel-Emden *et al*. [114] performed a thorough analysis of a number of integration schemes used for DEM explicitly looking at oblique impacts, they compare both the analytical restitution coefficient with the resulting numerical restitution coefficient and the rebound angle to assess error. Kruggel-Emden *et al*. [114] also considers the time grid accuracy, the accuracy associated with identifying the contact when it occurs.

In situations where there is free normal or tangential motion between contacts, the system

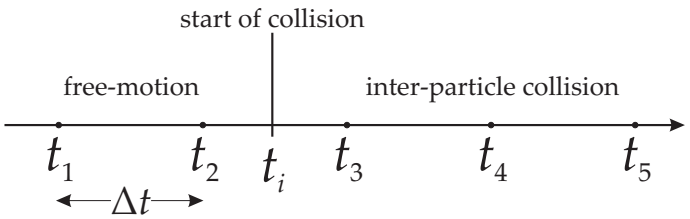

Figure A.1: Time discretisation leads to late collision detection.

has a force discontinuity at the time of impact. This study is a continuation of work by Tuley *et al*. [4] that explored the performance of typical integration methods for continuous systems used to integrate the linear *normal* forces. A short account of the method and analysis performed by Tuley *et al*. is included here for context.

The original work in this chapter aims to discover the effect on global scheme order over the discontinuity with the *tangential* forces, which schemes provide the least error across both normal and tangential motions and therefore which scheme is the best choice for a DEM simulation.

A.3 Assessing the discontinuity through temporal discretisation

In a numerical particle simulation the exact impact time is likely to be between time steps, as illustrated in Fig. A.1. The fraction N_{FM} defines the fraction of the time step difference between the true collision time and the closest time step in a numerical simulation. In the normal collision there is only one discontinuity and the time step fraction associated with that is N_{FM}, for the tangential study there are two events and the time step fraction for those are N_{FM1} and N_{FM2} defined below. N_{FM} is defined as:

$$N_{FM} = \frac{t_{impact} - t_{nearest}}{\Delta t} \tag{A.1}$$

In the tangential study the collision is detected when the particle is overlapping the plane at the beginning of a time step. Figure A.3 shows how time discretisation can lead to impact not being detected at the exact collision point. In Fig. A.3 τ_1 is $t_{impact} - t_{nearest}$ as in Eq. (A.1). In the tangential study N_{FM1} is the fraction of a time step that occurs after impact before the model applies any force to that particle, it is equivalent to N_{FM} in the normal impact study.

The normal collision test encounters only one discontinuity and that is at impact. For the tangential collision there are two key times when a force discontinuity occurs, the first is the impact the second is a transition time. For the elastic-frictional force regime there is a fraction of time step that occurs before transition, $N_{FM2} \propto \tau_2$ in Figure A.3, this is calculated in the same way as Eq. (A.1).

The different tests in this study use varying values of N_{FM} to explore the effect on error. Given the initial free motion speed, u_0, the required N_{FM} can be achieved by initially positioning the particle a distance, x_0, away from the plane such that $x_0 = u_0(1 + N_{FM1})\Delta t$. This chapter starts with a summary of the effect of the impact discontinuity on the performance of integrators in the normal impact, from the work of Tuley *et al*. [4]. The chapter then reports in detail the effect discontinuities in the tangential forces have on the performance on the same numerical integration schemes.

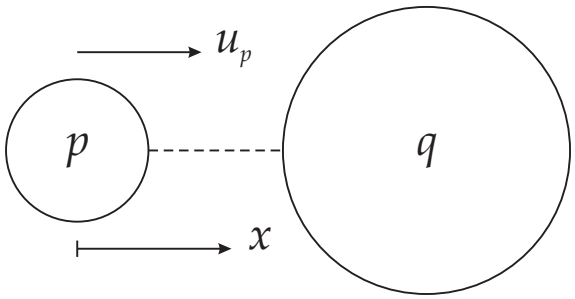

Figure A.2: The particle configuration in the normal integration tests performed by Tuley *et al*. [4]. Particle p has some initial velocity and is travelling toward fixed particle q.

A.4 Time discretisation for normal collision assessments

Tuley *et al*. [4] assessed the effect of the temporal discretisation around the impact point of two particles with and without damping and considered the effect of changing the damping parameters, here only the results of the temporal discretisation are reported. The results present the change in error based on N_{FM} and the error with varying time step at $N_{FM} = 0$ and 0.5 to gauge the scheme order.

The normal collision assessment was performed by Tuley *et al*. [4]. Two particles were used in the test, particle p is positioned a set distance from fixed particle q as in Fig. A.2. Particle p has velocity and is moving towards the centre of stationary particle q resulting in an exclusively normal collision. The force expression to be integrated and the analytical derivation can be found in Tuley *et al*. [4] they are also included in Appendix B.

The schemes evaluated by Tuley *et al*. [4] are given in Table A.1, these same schemes are later evaluated in the tangential integration assessment in this chapter.

A.4.1 Test configurations and results of the normal collision assessment

Tuley *et al*. [4] conducted several tests, two of which will be reported here, the change in error resulting from changing N_{FM} and the scheme order for $N_{FM} = 0$ and 0.5 found by calculating the error produced for different time step sizes. The results are reported along side the results of the tangential case for comparison in Section A.6.1 and A.6.2.

A.4.2 Summary of the normal spatial discretisation assessment

Tuley *et al*. [4] used a linear force model and investigated both elastic and damped normal impacts. It was found that all of the multi-point integrator algorithms tested were limited to 2nd order accuracy with respect to time step size. Furthermore the single-point RK4 scheme only achieved 4th order accuracy when an elastic collision began at the start of a time step. When the time step did not coincide, the 4th order Runge-Kutta scheme also provided 2nd order accuracy. For integration into a flow solver Tuley *et al*. recommend the Symplectic Euler method as it provides best absolute accuracy and can provide global 2nd order accuracy under elastic conditions, Tuley *et al*. also claim "For poorly resolved collision events, accuracy is preserved or *improved*.".

The impact of discontinuities on the performance of the integration methods solving the normal forces is understood. Given that the tangential force has two discontinuities how do the numerical integrators perform when solving the tangential force? What differences are seen between sliding and elastic tangential regimes? Do the same schemes that perform well when solving the normal force also perform well when solving the tangential force?

Scheme	Type	Force Evaluations (per time step)	Time history stored	Existing literature Usage	line style in plots
Forward Euler (FE)	explicit	1	1	Taguchi [182], Sadd *et al.* [183], Tsuji *et al.* [74]	(· · · × · · ·)
Symplectic Euler (SE)	explicit	1	1		(- - - ◇ - - -)
2nd order Runge-Kutta (RK2)	explicit	2	1		(—×—)
4th order Runge-Kutta (RK4)	explicit	4	1	Ovesen *et al.* [184]	(- - - ✳ - - -)
2nd order Adams - Bashforth (AB2)	explicit	1	2	Marshall [110], Sundaram and Collins [185]	(—◯—)
4th order Adams - Bashforth (AB4)	explicit	1	4		(- - - ◯ - - -)
4th order Adams - Bashforth - Moulton (ABM)	explicit	2	3		(- - - ▽ - - -)
1st order back - differenced (BD1)	implicit	number of iterations	1		(- - - △ - - -)
2nd order back - differenced (BD2)	implicit	number of iterations	2		(—△—)
4th order back - differenced (BD4)	implicit	number of iterations	4		(· · · △ · · ·)

Table A.1: Numerical integration schemes [4].

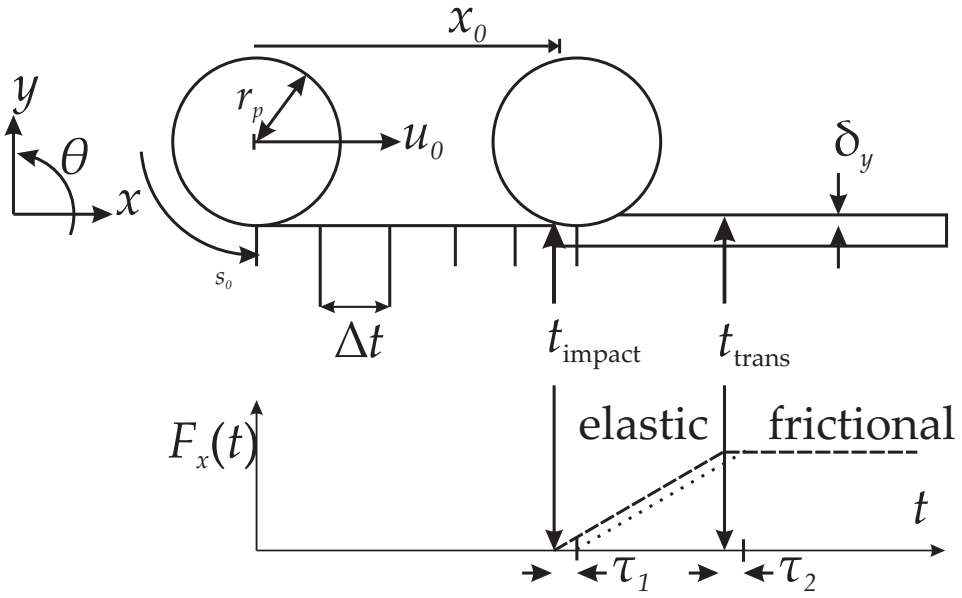

Figure A.3: The numerical system, shown on the plot as (· · · · ·), the particle experiences free motion for a number of time steps then, upon first contact, enters the elastic region until the elastic force exceeds the friction force at which point it transitions to frictional motion. The exact analytical force, shown on the plot as (- - -), starts at t_{impact} and transitions at t_{trans}. The time step, Δt, the time difference between the numerical and analytical collision time, τ_1, the time difference between the numerical and analytical transition time, τ_2, and the normal overlap, δ_y, are shown.

A.5 Performance of numerical integrators on tangential motion in DEM

This study examines the behaviour of continuous time integration schemes over discontinuities in the tangential forces typical in an oblique impact within a DEM simulation. High order schemes are associated with low error and efficient computation, however, for DEM this is not always the case - as seen in Section A.4. To investigate only the tangential motion this simulation consists of a particle impacting tangentially with a plane and sliding along it, this makes the numerical integration independent of errors from the normal force integration. Three possible force regimes that occur in the tangential motion of an oblique impact are explored; frictional, elastic and elastic-to-frictional. Tests are conducted to explore the effects of the location of the discontinuity within the time step and to examine scheme order through varying time step resolution. For certain scenarios the tangential motion contains elastic and then frictional forces, this presents a second discontinuity between these force regimes. The effects of this second discontinuity are also presented.

The physical scenario and the mathematical models both numeric and analytic are described and explained in this section. In this study only the tangential motion is explored numerically, it can be likened to a 1D oblique impact with the normal repulsive motion ignored.

The problem is shown in Fig. A.3, a particle is placed a distance away from a plane with initial velocity toward that plane, the plane is parallel to the motion of the particle but offset from its centre such that when the particle reaches the plane only a fraction of the particle will overlap with the plane. Using the soft-sphere force approach this overlap is used to calculate the force opposing particle motion. The particle experiences zero force during free motion and elastic and then tangential frictional forces when in contact with the plane. No other forces are present. The simulation finishes after a characteristic time defined in Section A.5.1. The position of the particle at this time is compared with the analytical solution to calculate the error. The analytic solution for the elastic region is presented elsewhere [186, 114], the frictional region

impact criteria, ψ_0	outcome
$\psi_0 \leq 1$; small	Tangential forces are elastic at first, then transition to frictional toward the end of the impact.
$1 < \psi_0 \leq 2r^*\kappa - 1$; intermediate	Frictional mechanism at first, then elastic and frictional again toward the end.
$\psi_0 > 2r^*\kappa - 1$; large	Frictional motion is observed throughout the collision.

Table A.2: Summary of the tangential mechanisms for different oblique impact angles [186].

analytic solution is straightforward and was derived for this test. This situation is a 1D equivalent of an oblique impact with elastic-frictional mechanisms. The free-motion to frictional-motion will occur for specific impact angles, in DEM simulations this force would increase with the normal force and then decrease as the particle is repelled. In this work the normal force has been fixed to make the results independent of the normal impact errors, therefore we make the frictional force constant also.

A criteria exists [186] to predict which mechanism will occur during contact in oblique 2D impacts based on the impact angle of the contact point, $\alpha = \arctan(\frac{u_{s0}}{u_{y0}})$, s being the surface point coordinate defined in Section A.5.1, and the ratio of normal to tangential stiffness, $\kappa = k_x/k_y$. The criteria, ψ_0 in Eq. (A.3), is used in the analytical solution [186] to determine which equations to use. Here it illustrates the different mechanisms that can occur and hence justify testing the different force regimes. The regimes are summarised in Table A.2, where:

$$r^* = 1 + (r_p/R_g)^2 \tag{A.2}$$

is the non-dimensional radius, r_p is the particle radius and R_g is the radius of gyration and the criteria, ψ_0, is defined as:

$$\psi_0 = \frac{\kappa}{\mu}\frac{u_{s0}}{u_{y0}} = \frac{\kappa}{\mu}\tan(\alpha) \tag{A.3}$$

This investigation is primarily concerned with the effect of force discontinuities on the behaviour of continuous integration schemes for tangential impacts. For the purposes of this numerical investigation three scenarios are considered. The first two scenarios, purely frictional and purely elastic contain one force discontinuity whilst the elastic-frictional contains two force discontinuities. Figure A.3 describes the 2-discontinuity model; a period of free motion, elastic motion occurring after impact then transition into pure frictional motion. The three scenarios will be evaluated to explore the effect of the discontinuities on global scheme order and the effect on accuracy when the discontinuity is at different locations within the time step. The intermediate angle force mechanism described in Table A.2 is not evaluated here as there is no strict analytical solution for the transition time from frictional to elastic motion. The analytical solutions provided in the literature all use a numerical method to solve the intermediate mechanism, [186, 114].

A.5.1 Governing equations

In this study we are isolating the effects of the tangential force by fixing the normal overlap to a constant fraction of the particle radius, shown in Fig. A.3. In linear DEM the tangential force acting on a particle during contact is composed of elastic forces from particle deformation and a

frictional force from sliding. Recent studies, such as [115, 186], tend not to include tangential dissipative phenomena beyond friction but the seminal paper by Cundall and Strack [107] includes options for global damping and visco-elastic damping during particle deformation. Tangential damping is not included in these tests as it is not often used in DEM simulations.

Figure A.3 explains the coordinate system and mathematical setup. The tangential force acting on a particle in contact with the plane in an entirely elastic collision will be:

$$F_x = k_x(x + r_p\theta) \tag{A.4}$$

where k_x is the material stiffness in the x direction. The particle centre of mass is governed by two second order coupled ordinary differential equations (ODEs):

$$x: \; m\ddot{x} + k_x(x + r_p\theta) = 0 \tag{A.5}$$

$$\theta: \; I\ddot{\theta} + r_p k_x(x + r_p\theta) = 0 \tag{A.6}$$

Introducing $s = x + r_p\theta$ as the surface coordinate and combining with the non-dimensional radius, r^* Eq. (A.2), this generates one equation to be solved for x and θ [186]:

$$s: \; m\ddot{s} + r^* k_x s = 0 \tag{A.7}$$

These equations are only valid when the tangential force does not exceed the Coulomb limit:

$$k_x|s| > \mu k_y|\delta_y| \tag{A.8}$$

Once this occurs the elastic force, Eq. A.4, in the above ODEs, Eq. (A.5) and A.6, is replaced by the frictional force $\mu k_y|\delta_y|$. The ODEs for s and x become:

$$s: \; m\ddot{s} + r^* k_y \mu \delta_y = 0 \tag{A.9}$$

$$x: \; m\ddot{x} + k_y \mu \delta_y = 0 \tag{A.10}$$

A.5.2 Analytical model

The analytical equations for the elastic case are the exact solutions to Eqs. A.5 and A.7. For the elastic region the analytic solutions [186] are shown here in Eqs. A.11 and A.12. The initial conditions for Eqs. A.5 and A.7 to be integrated are:

$$t = 0: \; s(0) = 0, \; u_s(0) = \dot{s}(0) = u_{s0}$$

$$t = 0: \; x(0) = 0, \; u(0) = \dot{x}(0) = u_0$$

yielding the analytical solutions for the elastic equations;

$$s(t) = \frac{u_{s0}}{\omega_s} \sin(\omega_s t) \tag{A.11}$$

$$x(t) = \frac{u_0}{r^*\omega_s} \sin(\omega_s t) + u_0(1 - \frac{1}{r^*})t \tag{A.12}$$

and the analytical solutions for the frictional case;

$$t = t_1: \; s(t_1) = s_1, \; u_s(t_1) = \dot{s}(t_1) = u_{s1}$$

$$t = t_1 : \; x(t_1) = x_1, \; u(t_1) = \dot{x}(t_1) = u_1$$

$$s(t) = u_{s1}(t - t_1) + s_1 - \frac{k_y r^* \mu \delta_y (t - t_1)^2}{2m} \tag{A.13}$$

$$x(t) = u_{x1}(t - t_1) + x_1 - \frac{k_y \mu \delta_y (t - t_1)^2}{2m} \tag{A.14}$$

where $\omega_s = \sqrt{r^* k_x / m}$ is the natural frequency of the system, u_0 is the initial velocity in x, t is the simulation time and r^* is the non-dimensional radius described above. During the frictional region the analytic solutions are simply quadratic equations in time since the force is constant and independent of tangential state. Eqs. A.13 and A.14 describe the particle position during the frictional regime, where the subscript 1 denotes the initial condition for these equations based on either the transition time if transitioning from elastic mode, or simply the initial condition at the impact time.

The analytic solution is a multi-part solution involving a period of free motion and then either 1 or 2 in-contact solutions depending on the test configuration. The time at which the solution changes from one regime to another is decided by analytically calculated times. The first of these is the impact time, t_1, and is trivial to calculate; simply the initial distance from particle to plane divided by the initial velocity. The second time is the transition time between the elastic and frictional mechanisms found using the Coulomb condition, Eq. A.8, and the analytical solution for s during the elastic mechanism, Eq. A.11. The transition time is given in Eq. A.15.

$$t_{\text{trans}} = \frac{1}{\omega_s} \sin^{-1} \frac{\mu k_y |\delta_y| \omega_s}{k_x u_0} \tag{A.15}$$

Combining the equations for the different regimes gives a single analytic solution for x. The complete solution for s is not given here, but can be found by combining the s equations in a similar manner. For elastic-frictional scenarios Eq. A.16 is the complete analytic solution, for purely frictional Eq. A.17 is the complete analytic solution. A purely elastic solution can be obtained by evaluating Eq. A.16 for $t_{total} < t_{trans}$.

$$x_{\text{elast-fric}} = \begin{cases} u_0 t + x_0 & t \leq t_1 \\ \frac{u_1}{r^* \omega_s} \sin\left(\omega_s (t - t_1)\right) + & \\ \quad u_1 (1 - \frac{1}{r})(t - t_1) + x_1 & t_1 < t \leq t_{\text{trans}} \\ u_{x\,\text{trans}} (t - t_{\text{trans}}) + & \\ \quad x_{\text{trans}} - \frac{k_y \mu \delta_y (t - t_{\text{trans}})^2}{2m} & t_{\text{trans}} < t \end{cases} \tag{A.16}$$

$$x_{\text{frictional}} = \begin{cases} u_0 t + x_0 & t \leq t_1 \\ u_{x1}(t - t_1) + x_1 - \frac{k_y \mu \delta_y (t - t_1)^2}{2m} & t_1 < t \end{cases} \tag{A.17}$$

A.5.3 Numerical schemes

The numerical schemes calculate the tangential position, x, by integrating Eq. (A.5), however, F_x is dependent on s, Eq. (A.18), thus both Eq. (A.19) and A.20 are integrated by the schemes. The schemes are validated by running a control test described in the section A.6 to ensure they produce the order they claim when they integrate without a discontinuity.

$$F_s = r^* k_x s = r^* F_x \tag{A.18}$$

$$\ddot{x}m + k_x \left(x + r_p\theta\right) = \ddot{x}m + k_x s = 0 \tag{A.19}$$

$$\ddot{s}m + r^* k_x s = 0 \tag{A.20}$$

At each time step the elastic force is compared with the friction force using the Coulomb condition, Eq. (A.8). When the Coulomb limit is reached the frictional force is used instead, Eq. (A.21) and A.22, and the numerical schemes integrate in Eqs. A.9 and A.10.

$$F_x = k_y \mu \delta y \tag{A.21}$$

$$F_s = r^* k_y \mu \delta y \tag{A.22}$$

The numerical time integration schemes used are either 1st, 2nd or 4th order and are summarised in Table A.1. These schemes contain a variety of features including implicit and explicit, multi-point and single-point, locally 1st, 2nd and 4th order as discussed by Tuley *et al*. [4].

A.5.4 Error quantification

The error for each scheme is calculated by comparing the prediction with the exact analytical solution at a specific time. The specific time chosen is a characteristic of the system: in the purely frictional case it is the time taken for the particle to come to a stop; the frictional force is constant $F_{fr} = \left|\delta_y\right| K_y \mu$ therefore the time taken to stop is calculated as $v_0 - t_c \frac{m}{F_{fr}} = 0$, as in Eq. (A.24). In the elastic case the period of the oscillation is the characteristic time, it is defined as $t = \pi/\omega_s$. For the elastic-frictional case, the comparison time is different, a characteristic time that involves both elastic and frictional mechanisms must be used; the transition time from the elastic to frictional mechanism is based on the analytic solution for elastic displacement Eq. (A.16) and the Coulomb limit Eq. (A.8). The transition time, Eq. (A.15), is doubled giving both mechanisms the same number of time steps in the simulation, and then added to the time set aside for the free motion before impact. The characteristic time for the elastic case was chosen to be $t_c = 0.8 t_{trans}$. This was sufficiently short to prevent interference from the discontinuity for the lower resolution tests. These characteristic times maybe summarised as:

$$t_c = 0.8 t_{trans} \qquad \text{, elastic} \tag{A.23}$$

$$t_c = v_0 \frac{m}{|\delta_y| K_y \mu} \qquad \text{, frictional} \tag{A.24}$$

$$t_c = 2 t_{trans} \qquad \text{, elastic} - \text{frictional} \tag{A.25}$$

The analytical position of the particle is compared with the numerical position at the comparison time, Eq. (A.26), where t_c is the time of comparison. The comparison time, t_c, is divided by the number of time steps to give the time step size, as such the numerical solution has a result for exactly that time step. The analytical solution is calculate for t_c; no interpolation is needed. The error is thus defined:

$$\varepsilon^{x}_{amp}(\%) = \frac{\left| x\left(t_c\right)_{\text{numeric}} - x\left(t_c\right)_{\text{analytic}} \right|}{x\left(t_c\right)_{\text{analytic}}} \times 100 \tag{A.26}$$

A.6 Test configurations and results

The 1st, 2nd and 4th order numerical integration schemes listed in Table A.1 were validated using a control test with no discontinuity. Separate tests were conducted for both elastic and frictional force regimes. The particle was initialised in contact with the plane with an initial velocity, any time histories required were populated using a self starting scheme run to a very high accuracy to limit start-up error. The particle spent the entire simulation in only one tangential force regime and so there was no force discontinuity of any kind, either from impact or transition. The results proved the scheme order obtained is consistent with the nominal order of the scheme listed in Table A.1, note: the Symplectic Euler scheme exhibits second order behaviour in this test. This finding is in complete agreement with a similar test for normal impacts considered previously [4].

The numerical schemes were then explored using three different tests.

A.6.1 Test 1: variation of time step fraction prior to impact: N_{FM1}

The first test explores the sensitivity to time step discretisation about the point of initial contact. There are three possible impact configurations for this test; free motion to frictional motion, free motion to elastic motion and free motion to elastic and then frictional motion. For each configuration the numerical schemes are tasked to evaluate the particle motion using the equations and method described in section A.5.1. Each configuration uses the comparison times defined in Eqs. A.24, A.23 and A.25, respectively. Before impact the numerical solution is exact as no forces are applied, therefore N_{FM1} at impact ($\propto \tau_1$ in Fig. A.3) can be controlled exactly for the numerical schemes. The tests are run with a time step of $\Delta t = 1 \times 10^{-4}$. The results of the normal collision study by Tuley *et al*. [4] are presented and compared at the end of this section.

Free motion to frictional motion (solution of Eq. A.10)

Figure A.4a shows the performance of the first order schemes. All the schemes are fairly insensitive to N_{FM1} and there is little performance difference between schemes.

Considering the second order schemes, in Fig. A.4b, the 2nd order Runge Kutta (RK2) scheme produces lowest error at $N_{FM1} = 0$, the error at this point is five orders below the error for other values of N_{FM1}. The 2nd order Backward Differenced (BD2) and 2nd order Adams Bahsforth (AB2) schemes give very similar error and are only weakly dependent on N_{FM1}, for non-zero values of N_{FM1} the error produced is similar to that of the RK2 scheme.

The 4th order Runge Kutta (RK4) scheme very sensitive to N_{FM1}, Fig. A.4c, with the lowest error at $N_{FM1} = 0$ while across all other values of N_{FM1} the error is steady. The other 3 schemes produce identical results that again are only weakly dependent on N_{FM1}. The RK4 scheme produces the lowest error of any of the ten schemes tested, however, the extremely low error only occurs at $N_{FM1} = 0$, for all other values the error is very similar to all other schemes even the 1st and 2nd order schemes.

Free motion to elastic motion (solution of Eq. (A.19))

Amongst the first order schemes, Fig. A.5a, the SE method is noted for having a consistently smaller error than any of the other 1st order schemes but also more sensitive to N_{FM1}. Error

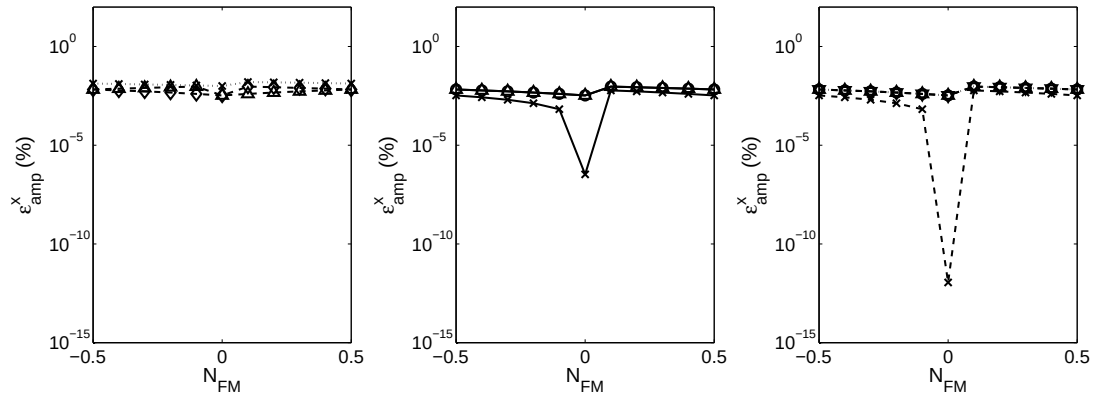

(a) 1st order schemes: FE ($\cdots\times\cdots$), SE ($--\diamond--$), BD1 ($--\triangle--$)

(b) 2nd order schemes: RK2 ($—\times—$), AB2 ($—\bigcirc—$), BD2 ($—\triangle—$)

(c) 4th order schemes: RK4 ($--\times--$), AB4 ($--\bigcirc--$), ABM ($--\triangledown--$), BD4 ($\cdots\triangle\cdots$)

Figure A.4: Frictional motion with variation in N_{FM1}, $\Delta t = 1 \times 10^{-4}$.

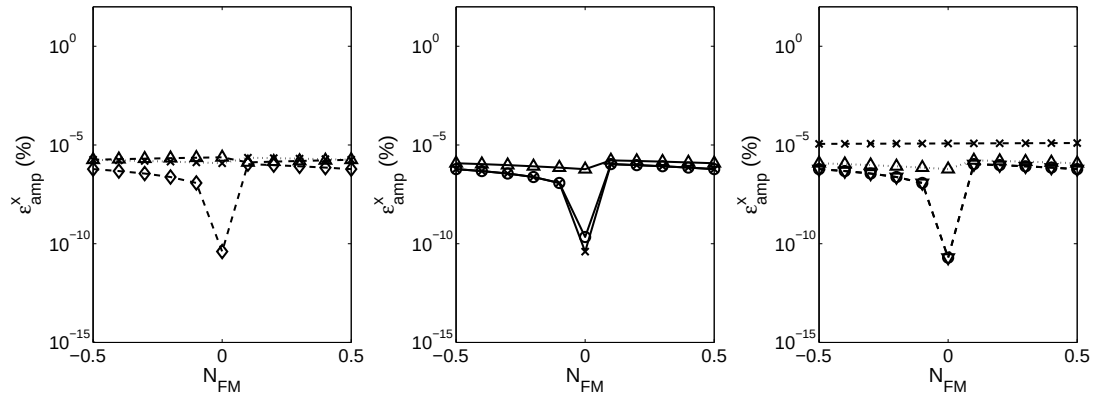

(a) 1st order schemes: FE ($\cdots\times\cdots$), SE ($--\diamond--$), BD1 ($--\triangle--$)

(b) 2nd order schemes: RK2 ($—\times—$), AB2 ($—\bigcirc—$), BD2 ($—\triangle—$)

(c) 4th order schemes: RK4 ($--\times--$), AB4 ($--\bigcirc--$), ABM ($--\triangledown--$), BD4 ($\cdots\triangle\cdots$)

Figure A.5: Elastic motion with variation in N_{FM1}, $\Delta t = 1 \times 10^{-4}$

decreases by 5 orders at $N_{FM1} = 0$. The BD1 and FE schemes are largely invariant to N_{FM1}.

The two explicit second order schemes, Fig. A.5b, are very similar, the RK2 and AB2 schemes show large sensitivity with a reduction in error of 3 orders at $N_{FM1} = 0$. They provide a smaller error throughout than the BD2 scheme which has only a slight variation with N_{FM1}. For this time step resolution the SE scheme would produce results with the same error as either the RK2 or AB2 despite being nominally first order and computationally less demanding.

Amongst the 4th order schemes, Fig. A.5c, the ABM and AB4 scheme behave identically and provide the lowest error. Curiously RK4 scheme, however, appears to be independent of N_{FM1} and the BD4 scheme behaves much like the BD2 scheme with relatively little sensitivity. Whilst the low error presented by the ABM and AB4 scheme is very low the same low error can be achieved by the 1st order SE scheme, results for non zero values of N_{FM1} are very similar for all schemes.

In both the frictional and elastic case it is clear that only a small region of the N_{FM1} range produces very low error for certain schemes, for a large simulation, where N_{FM1} will be indeterminable, theses schemes cannot achieve the high accuracies that may occur for specific N_{FM1} values, such as $N_{FM1} = 0$, throughout the whole simulation.

Free motion to elastic and then transition to frictional motion (Solving Eq. (A.10) **& A.19)**

There is very little difference between the results with the transition and the results presented in Fig. A.5, for solely elastic motion. The results show the same asymmetric tendency and the same sensitivities. This indicates that the second discontinuity has no great effect on the error. The second discontinuity is examined in more detail in Test 3.

Effect of temporal discretisation at impact in the normal direction: N_{FM} [4]

In this section we present results from Tuley *et al*. [4] for each scheme, elastic and damped, with a fixed time step of $\Delta t^* = 3 \times 10^{-3}$ with varying N_{FM}.

Except for the SE scheme, Fig. A.6a - A.6d, the first order schemes for both damped and elastic cases are only weakly dependent on N_{FM}. The error of the SE scheme is much lower than the other first order schemes for all N_{FM} but the error spans several orders of magnitude. The SE scheme was relatively inert in the tangential frictional case, but in the tangential elastic case produced much lower errors than in the normal collision. The lowest error in the tangential case was always at $N_{FM} = 1$.

The second order schemes, Fig. A.6b - A.6e, show more dependence to N_{FM} in the damped case than in the elastic. The RK2 scheme proving the lowest error in the elastic case throughout, but in the damped case the BD2 and AB2 schemes produce a lower error at $N_{FM} = \pm 0.5$. The RK2 scheme behaved similarly in the tangential study as in the normal study, but in the tangential study the BD2 scheme showed a weak dependence to N_{FM} and no scheme produced lowest error at $N_{FM} = \pm 0.5$.

The fourth order schemes, Fig. A.6a - A.6d, show a mixture of behaviours; the RK4 scheme produces significant error reduction for the elastic case with $N_{FM} = 0$ but in the damped case is comparatively less sensitive. The other schemes produce the lowest error when $N_{FM} = \pm 0.5$ in the damped case, and are relatively insensitive to N_{FM} in the elastic case. The elastic tangential and normal damped cases proved the worse for the RK4 scheme, but the RK4 produced the lowest error of any scheme in the frictional tangential case.

Overall there does not appear to be a parallel between the normal and tangential behaviours for any scheme, but the Runge-Kutta family seem to perform well in many cases.

A.6.2 Test 2: variation of time step and scheme order obtained

The test simulates an impact with a number of different time steps sizes in order to determine if the reduction in error is consistent with the expected scheme order of the numerical integration scheme. This test is conducted only with the two extremes of N_{FM1}, 0 and 0.5 as shown in test 1. The test is conducted for frictional, elastic and elastic-frictional cases. The time-step size varies from the low resolution, 10^{-1} (i.e. 10 time steps per simulation), to the high resolution 10^{-4} (i.e. 10000 per simulation). The expected 1st, 2nd or 4th order gradient will be linear when plotted on a log axis, the results are plotted with the expected gradients to aid the eye. In these tests the particle moves toward the plane with initial free motion and then after impact moves tangentially along the surface, three different tangential force regimes are applied to the particle after it is in contact with the plane. The reduction in scheme order for each tangential force model will give insight to the obtainable scheme order for the tangential motion of the different modes of an oblique impact.

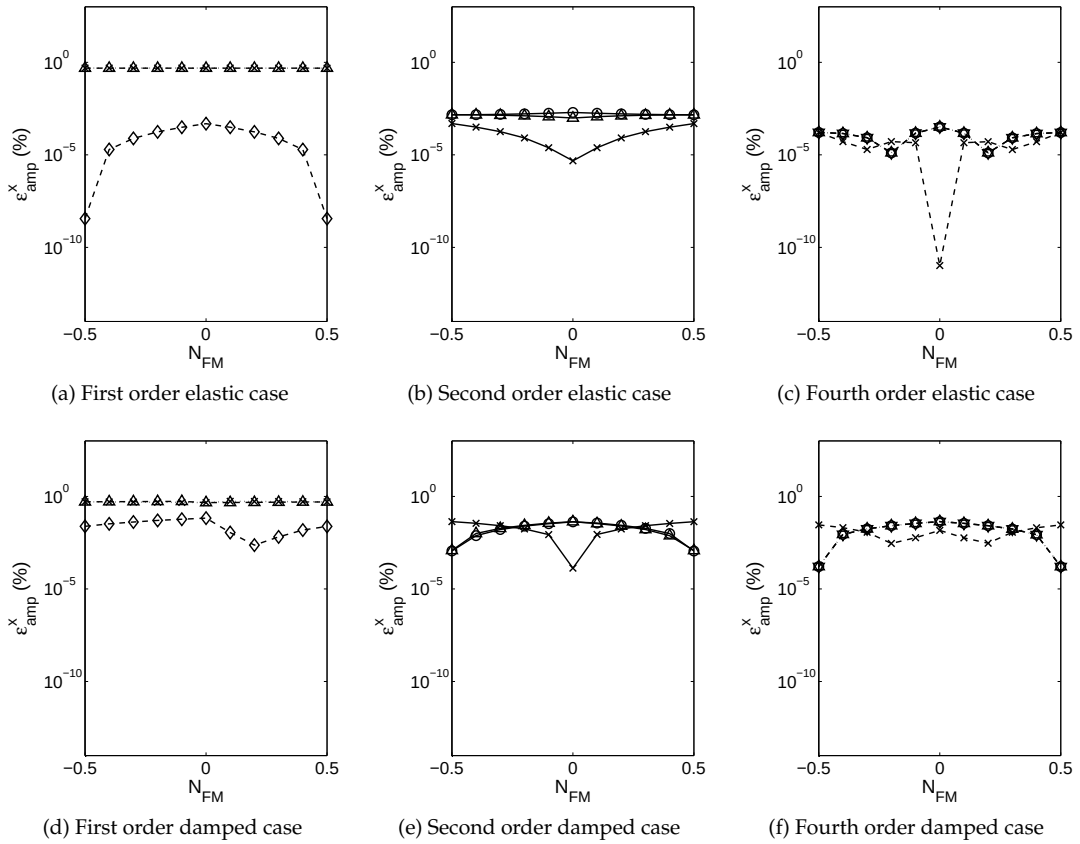

(a) First order elastic case (b) Second order elastic case (c) Fourth order elastic case

(d) First order damped case (e) Second order damped case (f) Fourth order damped case

Figure A.6: Error dependent on N_{FM} in normal collision [4], reproduced with permission. Scheme line styles are given in Table A.1.

Results of test 2: variation of time step and scheme order obtained

Frictional motion (solution of Eq. (A.10)**)**

In Figures A.7, A.8 and A.9, linear trends are visible indicating reduction in error with a reduction in time step size as is to be expected. The 1st order models can all be expected to behave globally as 1st order. The results show the SE and BD1 schemes produce near identical results while the FE scheme produces slightly more error.

Amongst the 2nd order models, Figure A.8, there are none that hold 2nd order behaviour throughout all circumstances. The BD2 & AB2 schemes give 1st order behaviour for $N_{FM1} = 0$ and $N_{FM1} = 0.5$, the RK2 on the other hand, gives 1st order behaviour when $N_{FM1} = 0.5$, but 2nd order with $N_{FM1} = 0$. This is reflected in the results from test 1 in Fig. A.4.

The fourth order schemes, Figure A.9, all provide 1st order performance except the RK4 scheme which provides 2nd order for $N_{FM1} = 0$. Considering the performance of the 4th order schemes over all values of N_{FM1} shows that no scheme can provide higher than 1st order in all cases. The RK family of schemes is the only scheme that performed above first order, a result reflected by Fig. A.4. None of the ten schemes tested could perform above first order for all values of N_{FM1} and only the RK2 and RK4 schemes could provide above first order but only for the exact value of $N_{FM1} = 0$.

Elastic motion (solution of Eq. A.19)

Test 1 showed the error some schemes is sensitive to N_{FM1}. As seen in Fig. A.5b the SE scheme is capable of reduced error during the elastic regime at $N_{FM1} = 0.0$, in Fig. A.10a we see the SE scheme has provided second order performance. The SE scheme produces less error than either

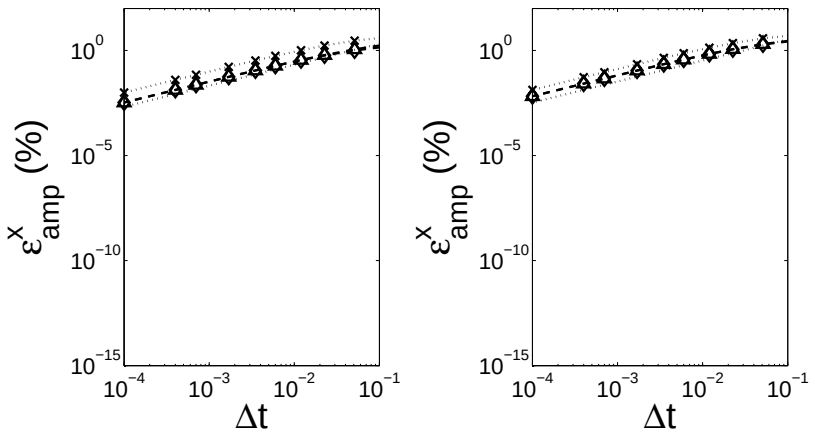

(a) $N_{FM1} = 0$, FE ($\cdots \times \cdots$), SE ($- - \diamondsuit - -$), BD1 ($- - \triangle - -$)

(b) $N_{FM1} = 0.5$, FE ($\cdots \times \cdots$), SE ($- - \diamondsuit - -$), BD1 ($- - \triangle - -$)

Figure A.7: Scheme order analysis, frictional motion: 1st order schemes

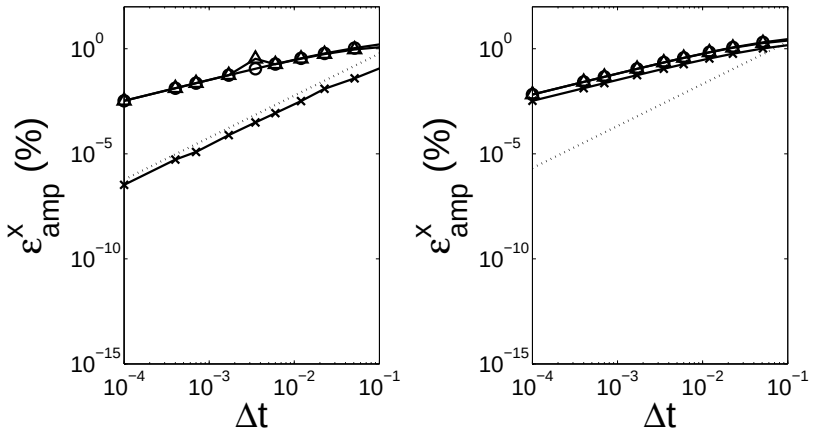

(a) $N_{FM1} = 0$, RK2 (—×—), AB2 (—◯—), BD2 (—△—)

(b) $N_{FM1} = 0.5$, RK2 (—×—), AB2 (—◯—), BD2 (—△—)

Figure A.8: Scheme order analysis, frictional motion: 2nd order schemes

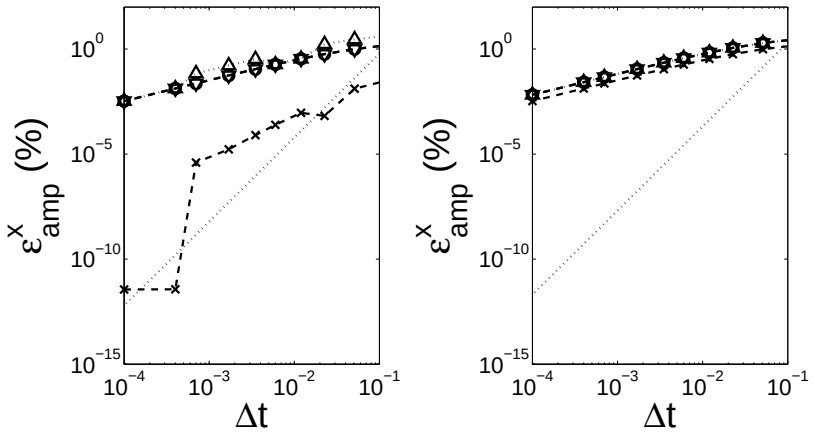

(a) $N_{FM1} = 0$, RK4 ($- - \times - -$), AB4 ($- - \bigcirc - -$), ABM ($- - \triangledown - -$), BD4 ($\cdots \triangle \cdots$)

(b) $N_{FM1} = 0.5$, RK4 ($- - \times - -$), AB4 ($- - \bigcirc - -$), ABM ($- - \triangledown - -$), BD4 ($\cdots \triangle \cdots$)

Figure A.9: Scheme order analysis, frictional motion: 4th order schemes

the BD1 or FE schemes, Fig. A.10, and the latter both show little dependence on N_{FM1}, as was seen in Fig. A.5.

The BD2 scheme, Fig. A.11, is the only second order scheme not to achieve 2nd order behaviour with $N_{FM1} = 0$, both the AB2 and RK2 schemes give second order behaviour for that pre-collision fraction. Interestingly they can only *match* the error of the 1st order SE scheme. The RK2 scheme performs best overall, but like the other second order schemes is reduced to 1st order for $N_{FM} = 0.5$.

The RK4 scheme produces 1st order behaviour at $N_{FM1} = 0$, Fig. A.12a, and identical result for $N_{FM1} = 0.5$ as we expected from Fig. A.5. The BD4 scheme is first order like the other Backward Differenced schemes previously. The AB2 and ABM schemes manage a second order performance for $N_{FM1} = 0$. In Fig. A.12b however all the schemes provide a 1st order performance, with the BD4 scheme giving a slightly greater error.

Clearly N_{FM1} makes a large difference to scheme order, looking at the results from the N_{FM1} tests, Fig. A.5, it can be seen that the "high performance" region of the N_{FM1} range is very small, maybe 5% about $N_{FM1} = 0$ for the SE RK2 AB2 AB4 and ABM schemes only. Therefore there is little justification to use anything other than a first order scheme when using these tangential force models in general problems. The SE scheme is the obvious choice since it surpasses or matches the other schemes in all circumstances.

Elastic and transition to frictional motion (Solving Eq. (A.10) **& A.19)**

The results produced by this test are similar to those in the section above, all scheme orders are the same for $N_{FM1} = 0$, all schemes are still limited to first order when $N_{FM1} = 0.5$.

Assessment of scheme order for the normal collision

The scheme order over the discontinuity was found for both elastic and damped collisions at $N_{FM} = 0$ and $N_{FM} = 0.5$ by running the simulation with different time steps. The results are reproduced from Tuley *et al*. [4] in Figs. A.13-A.15. The first order schemes presented in Fig. A.13 show that all the schemes maintain first order performance except the Symplectic Euler scheme that produces second order performance for both $N_{FM} = 0$ and 0.5 in the elastic case, but first order for the damped case though it produces a consistently lower error than the other tested schemes across all four plots.

Among the second order schemes, Fig. A.14, not one could maintain second order behaviour across all tests. The RK2 scheme produced third order behaviour for elastic conditions at $N_{FM} = 0$ but first order behaviour in damped collisions at $N_{FM} = 0.5$. The RK2 scheme was the only scheme to maintain second order with damped conditions and $N_{FM} = 0$.

The fourth order schemes mostly achieve first or second order behaviour, Fig. A.15, the RK4 scheme being the only scheme to achieve fourth order and only for the elastic case at $N_{FM} = 0$, second or first order is all that can be expected for any of the schemes away from that condition. The second order schemes produce similar error but with less computational expense.

In the elastic case the discontinuity had some impact, but did not reduce any scheme below second order. In the damping case no scheme could maintain above first order behaviour for both values of N_{FM} tested. Tuley *et al*. [4] confirmed the nominal order of each of the schemes in a simulation with no discontinuity during in collision motion.

Comparing the normal collision results, Fig. A.13 - A.15, with the tangential results, Fig. A.7 - A.12, we see the damped results behave similarly to the tangential frictional results with the majority of the schemes limited to first order. The conclusion that no scheme can maintain greater than first order performance across all N_{FM} values stands for damped normal collisions and all tangential collisions.

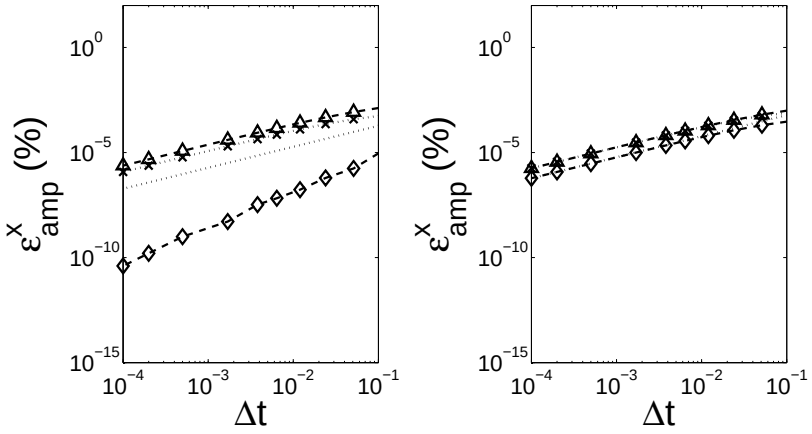

(a) $N_{FM1} = 0$, FE ($\cdots\times\cdots$), SE ($--\diamondsuit--$), BD1 ($--\triangle--$)

(b) $N_{FM1} = 0.5$, FE ($\cdots\times\cdots$), SE ($--\diamondsuit--$), BD1 ($--\triangle--$)

Figure A.10: Scheme order analysis, elastic motion: 1st order scheme behaviour

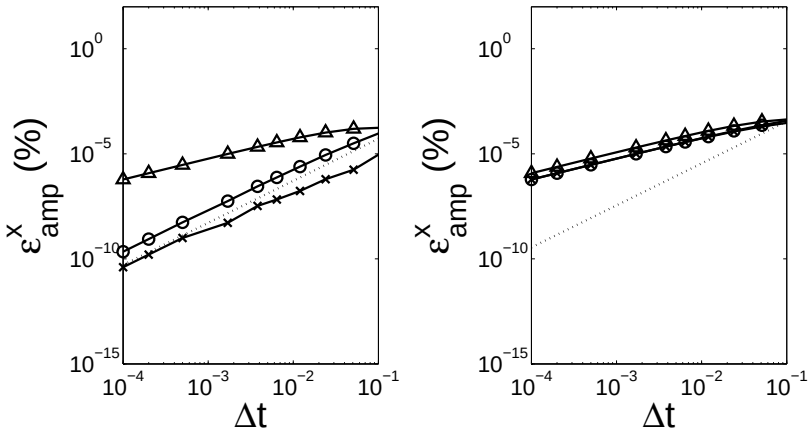

(a) $N_{FM1} = 0$, RK2 (—×—), AB2 (—◯—), BD2 (—△—)

(b) $N_{FM1} = 0.5$, RK2 (—×—), AB2 (—◯—),BD2 (—△—)

Figure A.11: Scheme order analysis, elastic motion: 2nd order scheme behaviour

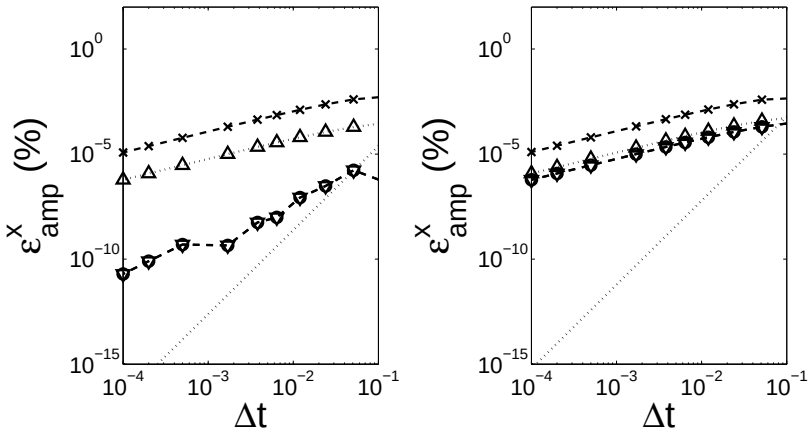

(a) $N_{FM1} = 0$, RK4 ($--\times--$), AB4 ($--\bigcirc--$), ABM ($--\triangledown--$), BD4 ($\cdots\triangle\cdots$)

(b) $N_{FM1} = 0.5$, RK4 ($--\times--$), AB4 ($--\bigcirc--$), ABM ($--\triangledown--$), BD4 ($\cdots\triangle\cdots$)

Figure A.12: Scheme order analysis, elastic motion: 4th order scheme behaviour

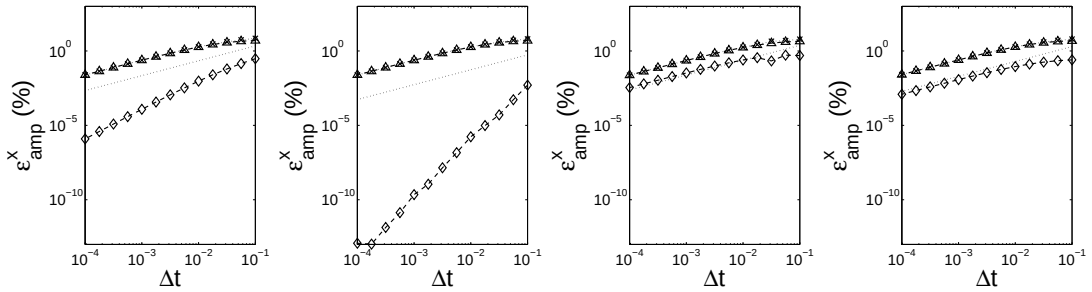

(a) Elastic, $N_{FM} = 0$ (b) Elastic, $N_{FM} = 0.5$ (c) Damped, $N_{FM} = 0$ (d) Damped, $N_{FM} = 0.5$

Figure A.13: Assessment of scheme order for first order schemes [4], reproduced with permission. Scheme line styles are from Table A.1. Dotted line indicates first order gradient as a guide to the eye.

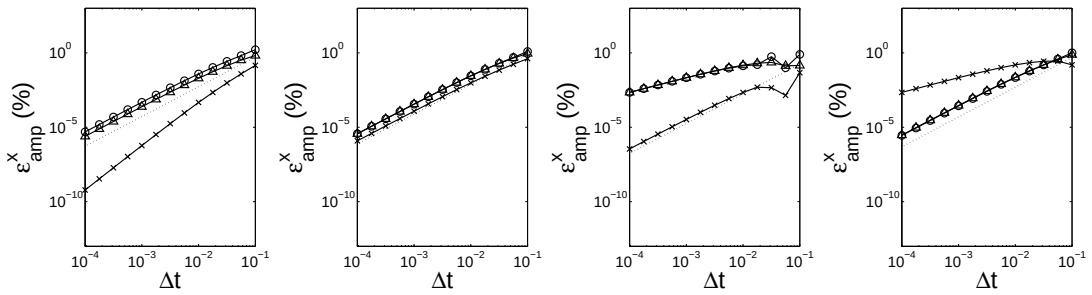

(a) Elastic, $N_{FM} = 0$ (b) Elastic, $N_{FM} = 0.5$ (c) Damped, $N_{FM} = 0$ (d) Damped, $N_{FM} = 0.5$

Figure A.14: Assessment of scheme order for second order schemes [4], reproduced with permission. Scheme line styles are from Table A.1. Dotted line indicates second order gradient as a guide to the eye.

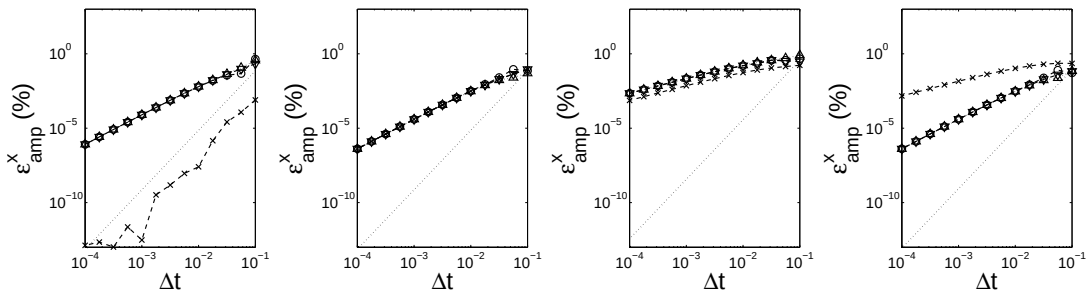

(a) Elastic, $N_{FM} = 0$ (b) Elastic, $N_{FM} = 0.5$ (c) Damped, $N_{FM} = 0$ (d) Damped, $N_{FM} = 0.5$

Figure A.15: Assessment of scheme order for fourth order schemes [4], reproduced with permission. Scheme line styles are from Table A.1. Dotted line indicates fourth order gradient as a guide to the eye.

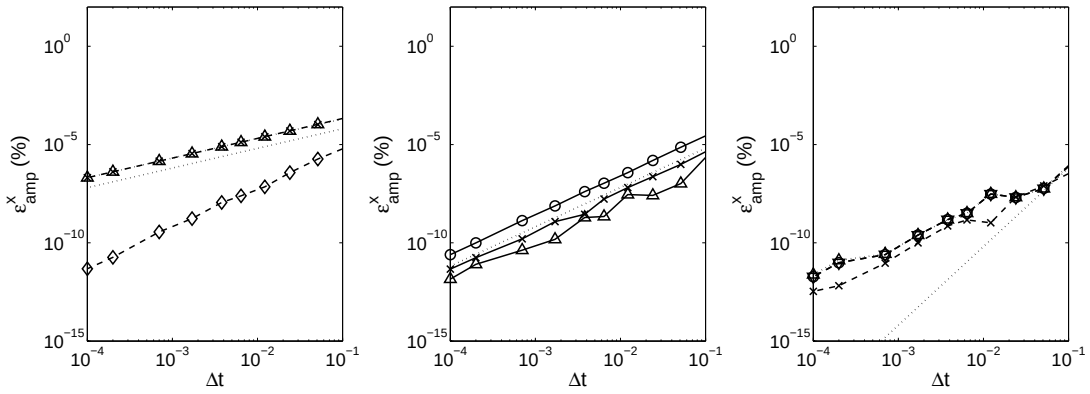

(a) 1st order schemes: FE ($\cdots\times\cdots$), SE ($--\diamond--$), BD1 ($--\triangle--$)

(b) 2nd order schemes: RK2 ($—\times—$), AB2 ($—\bigcirc—$), BD2 ($—\triangle—$)

(c) 4th order schemes: RK4 ($--\times--$), AB4 ($--\bigcirc--$), ABM ($--\bigtriangledown--$), BD4 ($\cdots\triangle\cdots$)

Figure A.16: Global scheme order for a continuous elastic then transition to frictional

A.6.3 Test 3: variation of time step fraction prior to transition: N_{FM2}

The third test uses the elastic-frictional model to explore the effect of the transition discontinuity on scheme order. The simulation is initiated within the elastic motion much like the initial control test to avoid the impact discontinuity, however, the particle is allowed to transition into frictional motion. The comparison time is $t_c = 2t_{trans}$, and the only discontinuity is the transition from elastic to frictional. Any loss of scheme order in this test can be attributed to the transition discontinuity.

Before the impact discontinuity the numerical schemes have no force to integrate and therefore produce exact results, this enables the time step fraction prior to impact, N_{FM1}, to be prescribed to the system. The transition discontinuity, however, takes place after a period of elastic motion during which error will be introduced to the system. For this reason the time step fraction prior to transition, N_{FM2}, cannot be accurately prescribed to the system. A variety of different time step offsets were implemented to probe the effect of varying N_{FM2} but the differences were negligible with no new information obtained.

The results presented in Fig. A.16 are revealing; the first order schemes seem unaffected, with the SE scheme maintaining 2nd order. The 2nd order schemes all produce second order, the BD2 scheme was unable to produce 2nd order through the impact discontinuity. Among the 4th order schemes not one could produce 4th order behaviour, although they all provide 2nd order behaviour and all produce a smaller error than the second order schemes.

The transition discontinuity limits all schemes to 2nd order. For the free motion to frictional motion case, section A.6.2, all schemes were limited to second order also. Table 1 describes three different tangential force mechanisms that could occur in an oblique impact; in each of these scenarios there is either a transition discontinuity or free motion to frictional motion, therefore the numerical method used will always be limited to second order.

A note on other schemes

Ten common integration schemes were tested here, however, there are many other integration schemes used in DEM and granular modelling such as Verlet leap frog or velocity method and Gear's predictor corrector method. The Verlet and leap-frog Verlet scheme finds velocities between time steps but acceleration and position on the time step. The Simplectic-Euler scheme is the most similar to the Verlet scheme in its structure as the SE scheme applies forward

integration for the velocity and the position is calculated from this updated velocity. Typically the Verlet method is poor at handling a velocity dependent force but as the force models here are only dependent on the position it is likely that the Verlet and Simplectic-Euler schemes will have similar results. Gear's method was designed to be stable both through choice of coefficients and the corrector stage will dampen potential instabilities. The Adams Moulton method tested here is a predictor corrector of sorts, but uses polynomial fitting instead of Taylor series.

A.7 Conclusions

Ten continuous integration schemes were used to solve the motion of a particle during impact in the soft sphere linear DEM model. The results of the *normal* impact were included from the work of Tuley *et al*. [4] and the *tangential* study was performed here.

Three tangential force scenarios were identified; free motion to frictional motion, free motion to elastic motion and free motion to elastic with transition to frictional. The effect on error of the time step fraction prior to impact, N_{FM1}, was presented. The order of each scheme was assessed over the force discontinuity at impact and transition and the results discussed.

In the tangential study the extreme variation across the N_{FM1} range is visible in all schemes except the Forward Euler scheme and the Backward Differenced family of schemes, as was also the case in the damped normal study. For a large scale system with many collisions all with varying values of N_{FM1} a robust scheme is advantageous. However, the Backward Differenced schemes, all of which produce first order behaviour, also produce the highest error in most scenarios. The benefits of an implicit scheme, with no stability constraints on time step size, coupled with a robust and predictable scheme order should be carefully weighed against those of a potentially quicker and higher accuracy first order explicit scheme such as the Symplectic Euler scheme.

It is clear, for the majority of schemes, that controlling N_{FM1} would greatly help in lowering the error in predictions of most numerical schemes. Controlling N_{FM1} in a single particle system would be trivial but in a many-particle system, e.g. Yu and Xu [187], there would need to be routines that dynamically alter the time step. With many simultaneous or non-binary collisions it would not be feasible, or take vast computational effort, to have every collision impact exactly with $N_{FM1} = 0$. For lowest error the alternative to controlling N_{FM1} is to be aware of the worst error produced by the chosen scheme, and mitigate that through increased time resolution.

The case of a single particle collision has been assessed here because there are analytical expressions that can be compared with the numerical results. The conclusions of this work can be utilised for the case of many particles by considering that higher order schemes are, overall, reduced to 1st order due to uncontrollable N_{FM}. These schemes demand considerably more computation without providing lower error therefore a scheme higher than first order is unnecessary. For a simulation with thousands of particles the computation time is a limiting factor in simulation size so it is important to be efficient. To measure the accuracy of a large system bulk quantities, such as flow rate, need to be measured and compared to experimental data.

The best 1st order scheme is clearly the SE scheme. It produces either 1st or 2nd order results and the error is always lower than the other 1st order schemes when a discontinuity is involved. The SE scheme is also the recommended scheme of choice for the *normal* collision tests by Tuley *et al*. [4].

The conclusions of the work by Tuley *et al*. [4] are not dissimilar to those found here. The following conclusions are true of normal collision models and tangential collision models:

- Time discretisation about the impact, illustrated in these tests as N_{FM1} or the pre collision

time step fraction, causes a change in scheme order.

- Multi-point integrators are limited to 2nd order behaviour, the single-point 4th order Runge Kutta scheme achieves 4th order results only when the time step starts on the collision boundary, and in the tangential case only for the free-to-elastic motion force regime.

The following conclusions are drawn specifically from this work, the results from Tuley et al. indicate similar effects though not as distinct as the results presented here.

- None of the integrator schemes tested here was able to maintain higher than 1st order performance for all values of N_{FM1}.
- The transition discontinuity limits 4th order schemes to 2nd order, lower order schemes appear unaffected.
- The optimum value of N_{FM1} is such a small portion of the total range that the large benefits that occur within this range cannot be globally attainable for large systems of particles. The Backward Differenced family of schemes demonstrate the least sensitivity to N_{FM1}, although they also produce the largest error.

The recommended solver for any large scale system would be the Symplectic Euler scheme due to its ability to produce near second order results, its general high accuracy, simple implementation and low storage requirements.

Appendix B

Derivation of the Analytical Normal Collision for Appendix A

The force model for a normal collision was given in Section 3.4.4, it can be split into the elastic, F_e, and viscous, F_v, terms as:

$$\begin{aligned} F_e &= -k_e \delta_n \\ F_v &= -cu \end{aligned} \tag{B.1}$$

where k_e is the elastic stiffness, δ_n is the overlap between particles given by Eq. 3.61, c is the damping coefficient and u is the velocity of particle p.

The analytical solution during impact is based on simple harmonic motion, given that at the start, $t = 0$, the force on the particle is 0 and the velocity is defined as $u(0) = u_0 \neq 0$, the analytical solution is given as:

$$x(t) = \begin{cases} u_0 t & t < t_i \\ \frac{u_0}{\omega_d} \exp\left(-\xi \omega_n (\, t - t_i \,)\right) \sin\left(\omega_d \left(t - t_i\right)\right) + x - \left(r_p + r_q\right) & t \geq t_i \end{cases} \tag{B.2}$$

where t_i is the impact time given by:

$$t_i = \frac{x(0) - \left(r_p + r_q\right)}{u_0} \tag{B.3}$$

and the damping ratio, ξ, natural frequency, ω_n, and damped frequency, ω_d, are given as:

$$\xi = \frac{c}{2\sqrt{k_e m}}, \qquad \omega_n = \sqrt{\frac{k_e}{m}}, \qquad \omega_d = \omega_n \sqrt{1 - \xi^2} \tag{B.4}$$

The coefficient of restitution, e, is the ratio of the final velocity after impact, $u(\infty)$, to the initial velocity, $e = |u(\infty)/u(0)|$. The coefficient of restitution is used to find the damping coefficient, c, given by Eq. 3.64.

The numerical schemes from Table A.1 were used to calculate the position of the sphere p over time. The error between the analytical and numerical results were found by comparing the maximum displacement:

$$\epsilon^x_{\text{amp}} = \frac{\hat{x}_{\text{numerical}} - \hat{x}_{\text{analytical}}}{\hat{\delta}_{n,\text{analytical}}} \tag{B.5}$$

The analytical maximum overlap can be found by equating the analytical velocity expression to zero and finding the displacement at that time, given by Tuley *et al*. [4] as:

$$\begin{aligned} \hat{\delta}_{n,\text{analytical}} &= \frac{Au(0)}{\omega_d\sqrt{1+A^2}} \exp\left(-\frac{\arctan(A)}{A}\right) \\ A &= \frac{\omega_d}{\zeta\omega_n} \end{aligned} \tag{B.6}$$

Tuley *et al*. explain that using the maximum displacement during the collision is a good choice as it represents a 'worse case' value, it requires the force to be integrated twice - once for velocity and again for position, and is easy to evaluate analytically.

Appendix C

Numerical Probe Indentation as a Means of Validating Discrete Element Method Simulations

---

Dusty ground that is prone to brownout is made of sand particles. To be able to model particle inception from a bed of particles interaction of particles in the particle bed must first be simulated.

The Discrete Element Method (DEM), introduced in Section 3.4, is widely used to model particulate systems, however, compromises are made in terms of physics and resolved length and time scales. Model implementations and simulation parameters chosen by researchers are often based on precedence or computational capacity. The aim of this work is to validate DEM model parameters by simulating a mesoscale mechanical process that is heavily dependent on particle interactions. Mesoscale processes bridge the gap between the single particle Atomic Force Microscopy (AFM) and bulk measurements such as shear cell tests [6].

This chapter describes the experimental process of dry powder penetrometry as performed by Danby [6], summarises a first attempt by Danby to model the experiment using a 2D DEM simulation and compares the results with the experiments. Following this the development of a new 3D code for this work is described and these results are compared with the experiments to identify which DEM parameters and models yield the most realistic behaviour.

The 2D code produced quantitatively different results to the experiments but the trends shed insight into the process and the length scales identified by the 2D spectral results were a good match with the experimental data. It was envisaged that the 3D system developed here would more closely follow the experimental observations and go further to calibrate DEM models using mesoscale penetrometry.

The expansion to 3 dimensions required approximately 20 times the number of particles to occupy the simulated volume; as such significant algorithm enhancements to reduce the memory footprint and reduce computational cost were required, these improvements enabled the code to approach $\mathcal{O}(n)$ scalability with particle number. The increased number of particles required in the 3D simulation lengthened the run-time, despite the improvements to the algorithm the run time required was estimated to be several months. In order that simulations could be completed in a more practical time several faster probe speeds were used.

Building on the conclusions of the 2D simulations conducted by Danby several variations of force model and parameters were simulated in the 3D system: linear and Hertzian normal

forces, 4 different particle stiffness values and a basic friction force. The force magnitudes were still significantly lower than the experimental results but all the frequency responses gave good match to the experiments. The frictional model was the best match for the force profile.

C.1 Outline of the chapter

In this chapter the experimental procedure of Danby [6] is explained and the original data is replotted in Section C.4. Section C.5 explains the method and parameters of the numerical simulations. The general simulation process including the necessary enhancements required by the 3D simulation is outlined in Section C.5.1. The parameters used by Danby in the 2D simulations are explained and the pertinent results are reproduced from that work [6] in Section C.5.2 and C.5.3. The results from the 2D simulations are used to define the parameters of the 3D cases in Section C.5.4. Following this Section C.5.5 presents the 3D results, these are and compared with the 2D simulations and the experiments. The final discussion in Section C.6 reviews the results and assesses the capability of the DEM to represent systems at the mesoscale.

C.2 Introduction

Calibration of a DEM through assessment of inter-particle behaviour in a large bed is necessary to accurately model the saltation inception from a particle bed at the root of a brownout simulation. Inception from non-uniform beds requires a different modelling approach to that of uniform beds; XU *et al*. [172] show that larger particles have a lower inception velocity when in a non-uniform bed compared with a uniform bed, conversely the smaller particles have a higher inception velocity. Particle protrusion into the flow is identified as a factor by XU *et al*. [172], it can be assumed therefore that the arrangement of particles in the bed and the way in which they rearrange under load will also be significant. The penetrometry experiments help assess the suitability of the DEM to reproduce particle interaction dynamics.

Typical methods of assessing suitability of granular simulation methods to accurately predict dynamic powder behaviour concentrate on recreating the results of characterisation experiments that are used regularly in industry. Granular materials can be tested at three scales:

- Microscopic, would typically involve Atomic Force Microscopy (AFM) to establish particle stiffness or cohesion for an individual particle [106].
- Macroscopic, testing properties of a large amount of particles together such as the stiffness using a confined compression test [188], shear using a shear cell [189] or flowability by measuring the angle of repose, [190].
- Mesoscopic: this test range attempts to capture particle-particle interactions and rearrangements in a large system of particles that is experimentally represented but small enough to be modelled directly with DEM.

To bridge the gap between macroscopic and microscopic testing Danby performed mesoscopic penetrometry experiments with a small probe capturing the inter-particle rearrangements that occur as a probe pushes through a particle bed. The force recorded by the probe over time captures each rearrangement as a change in force, the probe moves slowly to capture quasi-static forces rather than dynamic forces associated with moving particles.

C.3 Literature review – use of DEM to simulate powder characterising experiments

The DEM was developed to model large systems of particles; of continuing interest are assessments of the ability of the method to model real world processes such as: hopper flows [108], powder conveying [109], aerosol flows [110], filtration and separation processes [111] and

many other scenarios. To model these systems *physical* and *model* parameters must be chosen, physical parameters are those for which there is a direct parallel in the experimental case, such as material density or particle diameter, *model* parameters are used in the simulation and do not have an experimental equivalent, such as time step. *Physical* parameters are often chosen to match those of the materials used in the simulation and *model* parameters are chosen either from practicality or experience.

Several authors have simulated the powder testing processes enumerated in Section C.2 using DEM and compared the results with experiments. A macroscopic method of testing bulk shear properties is performed using the Jenike shear cell [189]. A cylindrical pot that contains the test powder is compressed with a defined load. The cylinder has upper and lower halves, the lower half is fixed whilst the top half is driven horizontally at a fixed speed shearing the confined powder within, the load resistance is recorded. Härtl and Ooi [189] conducted Jenike style shear cell testing both physically and numerically and found that DEM predicts the shear stress very well. It was also found that increasing the friction coefficient between particles had only a small effect on the bulk friction coefficient since the friction caused a decreased number of contacts between particles in the bed. Hartl also found that bulk friction reached an asymptote as particle friction was increased.

Zhou *et al*. [190] used a modified DEM to simulate angle of repose experiments. The simulated powder is held in a long narrow container, the floor at each end is then removed to allow the powder to pour leaving a pile in the middle. The angle of slope of the powder is the angle of repose. Zhou *et al*. [190] modified the DEM to include a rolling friction model and found friction parameters to have a dramatic effect on the angle produced. With appropriate parameters chosen the modified DEM was able to reproduce the experimental results.

The mesoscale range explores particle interactions in a large bed of particles undergoing some dynamic loading. Albert *et al*. [191] experimentally investigated granular drag, the drag experienced by an object moving through a granular material, using 0.4 - 0.3 mm diameter particles. The apparatus consisted of a cylindrical die of particles that rotated at a fixed speed, a portion of a cylindrical rod was immersed in the particle bed and fixed such that particles were continuously pushing past it as the die turned. The rod was mounted on a load cell to measure the drag. The experiment was continuous and could be run for an extended time to give average results. Albert did not provide spectral results of the drag but the fluctuations reported show distinctive sawtooth stick-slip particle reorganisation behaviour, linear increases in force followed by sudden drops. Albert found the drag to be independent of grain size and velocity in the low velocity regime, < 1.5 mm s^{-1} , it was however dependent on rod diameter and immersion depth. A proposed drag expression, Eq.C.1, was developed:

$$F_d = \eta g \rho H^2 d_c \tag{C.1}$$

where η is a shape parameter, g is gravitational acceleration, ρ is the density of the individual particles, H is the depth of the cylindrical rod and d_c is the diameter of the rod.

Frenning *et al*. [192] conducted powder penetration experiments: a conical probe was slowly driven at a fixed speed into a die containing powders between $1 - 20\mu$m in diameter and the force on the probe was recorded. Lactose powders were tested with varying amounts of the additive Tween to control cohesion. Frenning *et al*. [192] looked at the spectral results of the force fluctuations on the probe; as in the study by Albert these fluctuations are associated with particle rearrangement. Frenning *et al*. found that the fluctuations were independent of die geometry and probe shape, but the dynamics of small cohesive powders are dominated by agglomerate style behaviour and are very similar to the dynamics of larger cohesionless particles. The power spectral density was also presented and showed that the peak fluctuations had characteristic

lengths of $0.2 - 1$ mm, Frenning *et al*. associated this with the formation of agglomerate clusters. The fluctuations Frenning *et al*. recorded had the same distinct sawtooth pattern seen by Albert and would appear to be a characteristic of low-speed granular flow.

C.4 Experimental probe indentation

C.4.1 Experimental process

The penetrometry experiment was performed by Danby and has been reported in full detail in [6], a summary is included here.

Five soda-lime glass powder samples were tested, the size ranges were; 0-50μm, 70-110μm, 100-200μm, 300-400μm, 400-600μm. An HR Texture Analyzer was used to drive a probe and measure the indentation force. The probe was a 2mm diameter rod tipped with a ruby sphere of diameter $D_{\text{probe}} = 3$mm fitted to a 5kg load cell mounted on the Texture Analyzer. Manufacturers claim the equipment position measurement was accurate to within ± 1 μm and the force measurement accurate to within ± 1 mN. The sampling rate was 500Hz.

A 'blank run' indentation was performed without powder between runs to measure the machine noise.

Each powder sample was carefully poured into a cylindrical die, 22.5mm deep and 12 mm in diameter. A spatula was used to remove any excess powder such that a flat surface of powder, level with the die, remained. Efforts were made to remove static charge build up using an anti-static gun, the die was also earthed. To prevent significant changes in packing arrangement the powder was poured carefully and the die was not agitated, as an additional precaution the die was weighed to find differences in powder density that would occur if the packing arrangement was significantly altered.

Each sample was tested 5 times, each at three different probe speeds of 0.5, 0.1 and 0.05 mms^{-1} all of which are below the fluidisation velocity $u_{\text{probe}} < \sqrt{2gD_p}$.

C.4.2 Experimental results

Danby tested several particle sizes and found that the rate of change of force with depth was dependent on the particle size. The schematic in Fig. C.1, [6], summarises the typical profile shape of the probe force for particle beds of varying particle diameter. In a particle bed composed of small particles, $< 50\mu$m, the resistance on the probe increases rapidly at first and then begins to asymptote. The medium sized particle sample, $70 - 110\mu$m, produced a linearly increasing force on the probe. The large particles, $400 - 600\mu$m, provided a constantly increasing rate of probe resistance approximately proportional to y^2.

The experimental results of Danby [6] for particle size 400-600μm were reprocessed from the original data and are shown in Fig. C.2, 5 repeated runs are plotted with the results of the blank run – the plots are offset for clarity. Each run gave the same qualitative behaviour: the resistance increased with depth following a near quadratic profile and the magnitude of fluctuations increased with depth.

Following Frenning *et al*. [192] each force trace can be considered to have the form $F = \bar{F} + F'$, where $\bar{F}$ is the mean and F' is the fluctuating component. A least squares curve fitting routine was used to fit the mean force with the exponential function:

$$\bar{F} = ay^p \tag{C.2}$$

where y is the probe depth and a and p are constants found for each case. As the bed surface is of

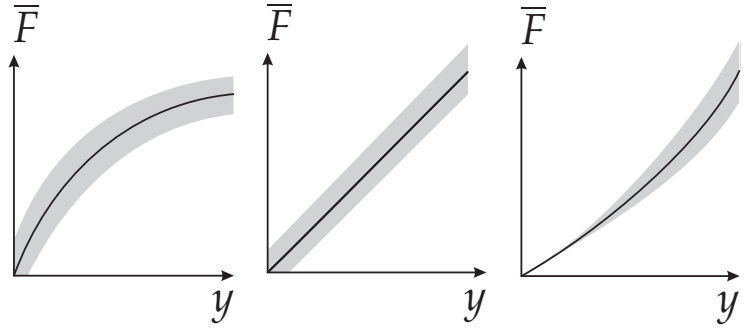

(a) $0 - 50\mu$m (b) $70 - 110\mu$m (c) $400 - 600\mu$m

Figure C.1: Typical behaviour profiles of probe force during penetration into beds of different particle sizes, reproduced from Danby [6]. Solid line represents mean profile, shaded region represents fluctuation magnitudes.

varying shape the profiles are only considered once the probe is completely immersed. The average of the five runs gave $a = 0.173$ and $p = 2.06$, a near quadratic behaviour as previously considered. The other particle sizes behaved similarly to the schematic in Fig. C.1: the medium sized particles provided a value of $p \simeq 1$ and the smallest particles gave $p \simeq 0.5$.

Danby [6] speculated that for the smaller particles the mean force becomes almost independent of depth, that is the mean force is approaching an equilibrium state, perhaps if the particle container was deeper and the probe was driven further the mean force would approach a steady value as is the case for Albert *et al*. [191]. However, Albert also showed the dependence on depth due to a pressure force, we might expect therefore to see a steady linear trend once the granular drag had reached a constant. The packing density for the different particle sizes was reported by Danby and are used to explain this behaviour. Fine powders can be strongly affected by a cohesive force called the van der Waals forces, Danby showed that the particle size for which the van der Waals force exceeds particle weight is $D_p < 20\mu$m. The smallest particles have the lowest packing densities and therefore the largest void fraction because the van der Waals forces are stronger than gravity, this causes the particles to adhere to each other rather than occupying the voids to minimise gravitational potential as is the case for larger particles. Danby explains that the smaller particles can accommodate the intrusion of the probe by moving into these voids, so called *local rearrangement*. The larger particles, however, are already closely packed so any rearrangement requires further reaching particle motion, this is termed *whole-scale rearrangement*. For the smaller particles only the local particles are affected by the probe and we see the mean force approach some steady state. Large particles, however, have a larger force network which if it extends to the container walls would cause the force to increase with depth. The parabolic increase might be explained by densification, a region of the stress-strain curve in the compression of foam or cellular materials [193, Ch. 5], which occurs once the cells have collapsed and the cell walls are in contact; this is analogous to the particles rearranging to occupy the voids, as these are filled the load is more directly transferred to the particles.

Effect of changing probe speed

For the larger particles Danby conducted probe penetration experiments at 3 speeds: 0.05, 0.1 and 0.5 mm s^{-1}. The results of Albert *et al*. [191] state that for slow speeds, well below the fluidisation speed, the granular drag is independent of speed. The results presented by Danby showed similar results, the probe force was independent of speed for the experimental runs.

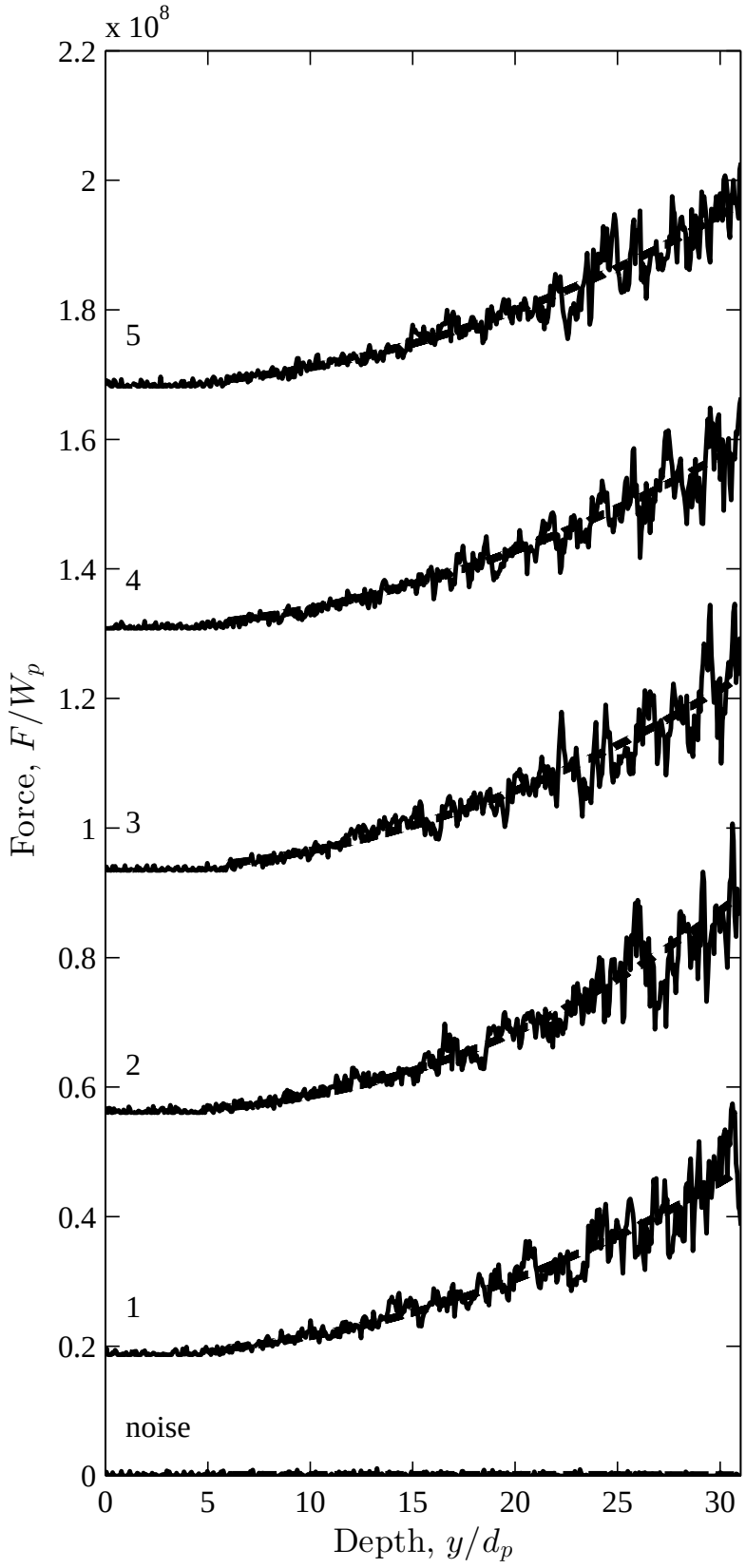

Figure C.2: Probe force during indentation – 5 Identical Experimental runs with powder diameter 400-600μm and the machine noise. Run 1 is offset by $+30/W_p$ subsequent results are incrementally offset by $+60/W_p$. Reproduced using raw data from [6].

Length scale	Length mm	Length D_p
D_{probe}	3	6
r_{probe}	1.5	3
$d_{p-\max}$	0.6	1.2
$\overline{D_p}$	0.5	1
$d_{p-\min}$	0.4	0.8

Table C.1: Length scales corresponding to physical bodies in the indentation process.

Spectral results of the experimental force profile

The force recorded by Danby for the $400-600\mu$m experimental indentations has been reprocessed here to examine the spectral content as performed by Danby. The force trace was passed through a Fast Fourier Transform (FFT) the exact process is explained in section C.5.5. Probe depth, y, was used as the independent variable instead of time providing results in terms of spatial frequency or wavenumber and therefore independent of probe speed. The wavenumber was inverted to allow the fluctuations to be directly related to length scales present in the simulation. Figure C.3 shows the Power Spectral Density (PSD),Φ, against length scale, l, for the experimental results on log axes. PSD has been nondimensionalised with $W_p^2 D_p^{-1}$, where W_p is average particle weight; length scale, l, is nondimensionalised with average particle diameter, D_p. Curves are offset and every 30^{th} point is plotted for clarity.

Here the approach of Danby is expanded on: looking more closely at the large length scales and using linear scales Fig. C.4 identifies a concentration of peaks associated with lengths from $1-10D_p$. The physical bodies associated with length scales in the experiment are given in Table C.1, it is seen that the peaks in the experimental results correspond to $l \simeq D_p$ and $l \simeq D_{\text{probe}}$; Runs 1, 3 and 4 favour the former Run 2 the latter but Run 5 shows peaks corresponding to both scales. Logically these peaks must correspond to the distance the probe travels between force fluctuations and therefore the distance the probe travels to build up the force before it slips. From this we can presume that the particle contacts of most influence slip after a probe motion of approximately D_p or D_{probe}, quicker force changes are weaker seen by the low power in the low length scales. Run 5 shows significant power distributed across all the large length scales the greatest of which is the length of the probes path through the particle bed.

In Fig. C.3 for $l < 0.5D_p$ as the length scale decreases the PSD decays steadily, this is highlighted in Fig. C.5 with two fitted lines. Danby conducted experiments with several different powder sizes and found a logarithmic relationship between the decay rate, γ, and the particle size, D_p. The larger particles produced $\gamma = -1.4$, similar to behaviour seen by Frenning *et al*. [192] who noted $\gamma = -2$, but as the powder size reduced γ increased to $\gamma = -0.4$ for $D_p = 0-50\mu$m. Danby speculated that *local* and *whole-scale* rearrangements were responsible for the different behaviours, for small particles *local* rearrangements would have a relatively low PSD for the large length scales but the large particles would have a wider reaching effect and therefore the PSD of those rearrangements would be shifted toward the larger length scales.

The machine noise or 'blank run' is included in Fig. C.3 as the lowest result. The contribution of the noise can be seen in the other runs: where the power reduces in the smallest length scales the steady decay gradient changes to become horizontal, this horizontal region as $l \to 10^{-2}$ is noise.

The results show the same behaviour seen by Frenning *et al*. [192], the majority of power is in the low frequencies, large l, but there are peaks in the high frequencies, small l. Frenning *et al*. also observed there is a near linear decay trend as length scale decreases, the decay trend has an

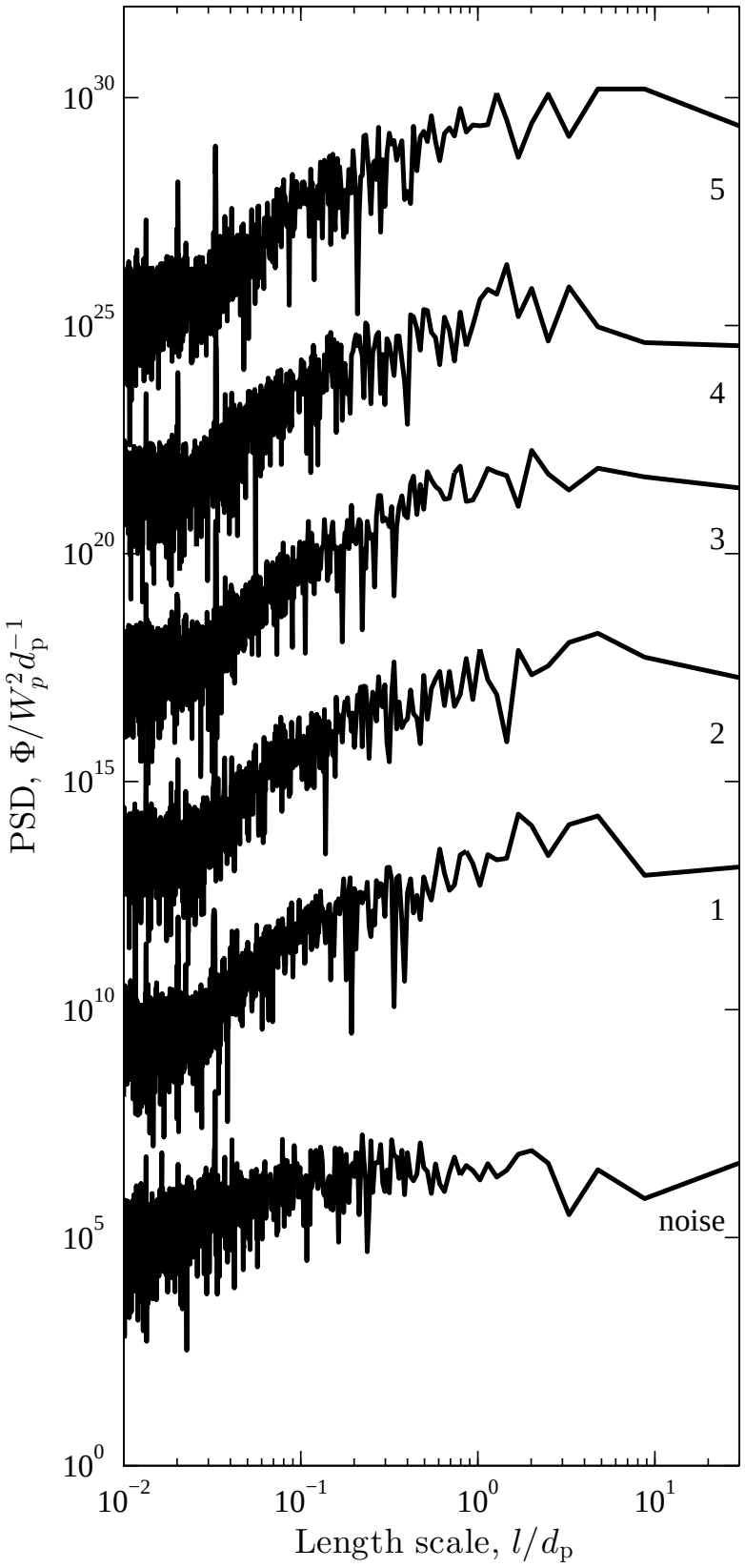

Figure C.3: Spectral power results of 5 experimental indentations by Danby [6] with powder size $400 - 600\mu$m. Results are offset incrementally by $\times 10^4$ and every 30^{th} point is plotted for clarity. Reproduced using raw data from [6].

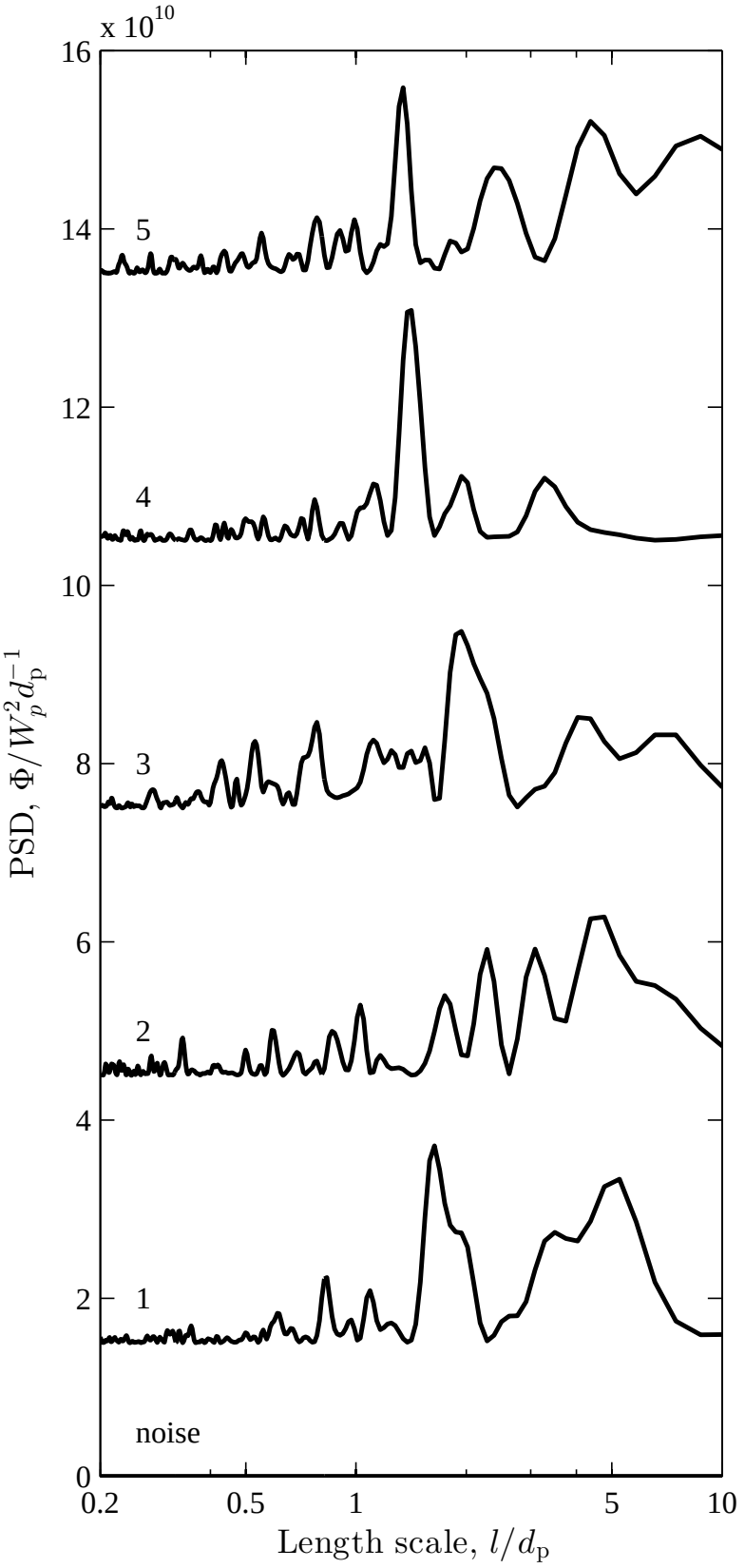

Figure C.4: Spectral power plotted of 5 experimental indentations by Danby [6] with powder size $400 - 600\mu$m. Linear vertical axes are used to highlight the large length scale peaks, the horizontal axis is logarithmic. The magnitudes of the noise results are too low to be seen. Run 1 is offset by $+1.5 \times 10^9$, subsequent results are offset by $+3 \times 10^9$.

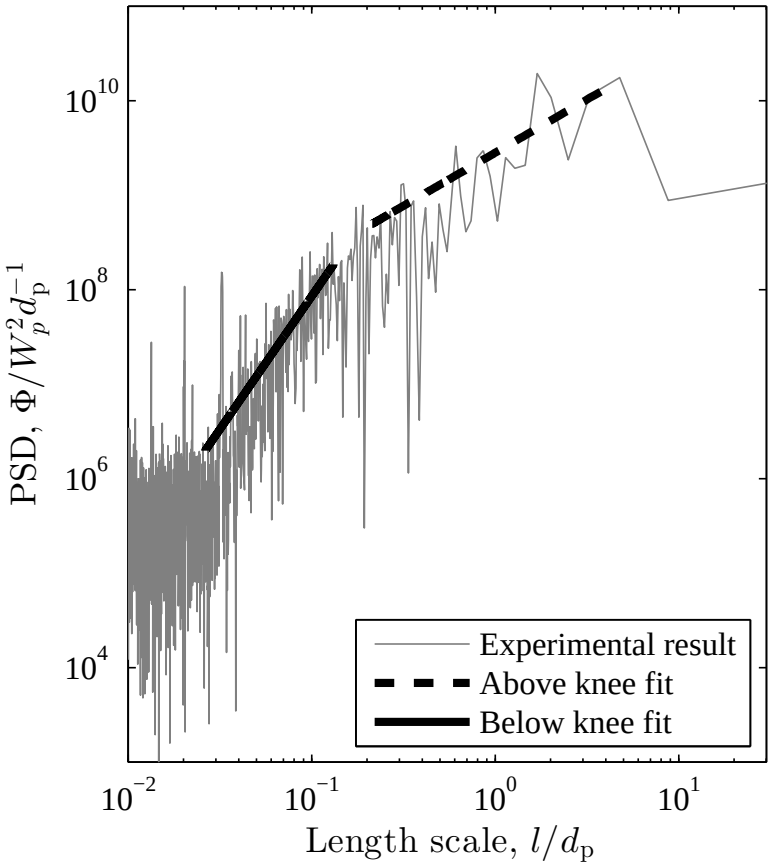

Figure C.5: Spectral results of a single experimental run from Danby [6] indicating the decay gradient γ and the 'knee' where γ changes.

exponent of < -1. Figure C.5 shows one of the spectral results of experimental runs by Danby and also indicates the two decay gradients, the first is mentioned by Frenning *et al*.. The two gradients are separated by a 'knee' where the gradient changes, this knee appears to be at $l \simeq 10^{-1}$.

C.5 Simulated probe indentation

The 3D simulation presented in this chapter is based on a 2D simulation developed by Danby [6], the original simulation has been much adapted to accommodate the third dimension and larger number of particles simulated. This section outlines the processes in the simulation and how they were adapted from the 2D to the 3D. The results of the 2D simulation are summarised with respect to the experimental results. Several cases for the 2D results were simulated with different model parameters, the effects of these parameters are discussed and used to design the parameter choices for the 3D simulations. Finally the results of the 3D simulations are discussed and an assessment of the suitability of the DEM to simulate the powder penetration experiment is made.

C.5.1 The simulation process

The numerical simulation is divided into a number of processes enumerated below:

1. Initialisation of variables and arrays. The physical domain is defined, Fig. C.6, the 3D simulations use the 2D domain from Danby and set depth equal to width. Material and

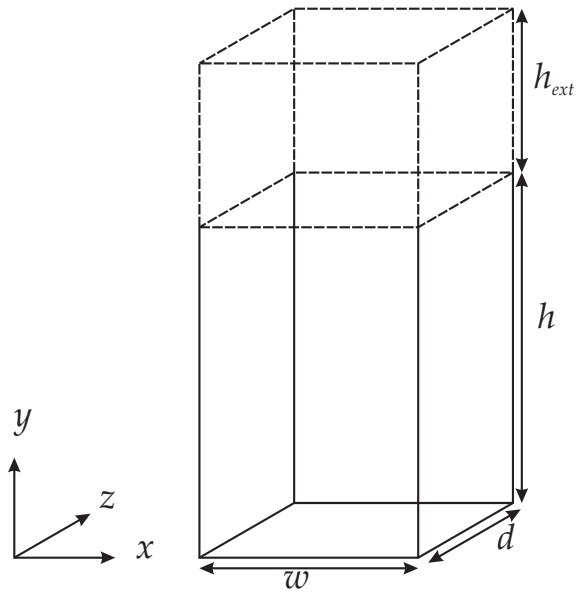

Figure C.6: The coordinate system and domain dimensions.

simulation parameters such as time step size are set. The particle diameters are log-normally distributed, as the powder in the experiments was found to be, using Eq. (C.3);

$$D_p = \frac{1}{2} e^{\mu + \sigma N} \tag{C.3}$$

where μ and σ are the mean and standard deviation and N is a randomly chosen variable from a Gaussian distribution also with mean and standard deviation of μ and σ.

2. Injection of new particles or advancement of the probe. The simulation has two parts: filling the container and probe indentation once the container is full;

   (a) The injection routine injects a number of particles according to a predefined injection rate. The rate is chosen to give a sparse 'sprinkling effect' as seen in Fig. C.9. Each particle is placed using a uniform random position in x and z across the domain and a uniform random height between 1 and 4 r_p above the highest previously existing particle. Each particle is checked to ensure it does not interact with another particle that has just been injected. This method was used in the 3D simulation developed in this work.

   (b) Probe advancement: after the fill the simulation of the probe indentation begins. The probe is modelled as another particle in the system in terms of particle interaction calculations, however, the velocity of the probe is fixed and the position is updated from this fixed velocity.

3. Neighbour finding. DEM systems with many particles are in simple terms an N-body problem, that is every particle could be potentially interacting with every other particle. However, because the particles have a maximum radius of influence, the particle's physical radius, the system need only consider particles that are near each other: so called 'neighbours'. These neighbours can be found using a grid system; the domain is broken into a uniform orthogonal grid of cell width equal to the largest particle radius, $r_{p,\max}$. A list of neighbours for each particle is made from all the other particles present in the grid cell and the 26 cells that surround it. If cohesion is enabled the larger value of r_{coh}, in Eq. (3.68), is used as the cell width.

4. Force calculation. There are three types of forces that act on the particles:

(a) independent forces, such as gravity and drag.

(b) particle-particle forces: elastic repulsion, damping, cohesion.

(c) particle-wall forces: elastic repulsion, damping, cohesion.

The particle-particle forces are calculated by processing the neighbour lists. If we designate any single contact to be between particle a and b then for each a particle there is a list consisting of many b particles. Each particle pair is tested for contact, $\delta_n > 0$ in Eq. (3.61) then Eq. (3.60) or 3.63 is solved to find the force on a, the force on b is identical but the sign is reversed, $F_{n,i,b} = -F_{n,i,a}$. To find the total particle-particle force the forces are summed over all the lists as particles will appear on many lists. The independent forces are applied without need to consider particle location or neighbours, gravity is found using Eq. (3.48) and drag is found using Eq. (3.82). Particle-wall forces are calculated for those particles in a boundary grid cell using Eq. (3.71) or 3.72 where $\delta_{n,\text{wall}} > 0$. The domain is bound on all sides by walls.

5. Evolution of particle positions. The total force vector on each particle is now known. Here the Simplectic Euler integration scheme [4] is used to find the velocity and positions of the particles for the next time step. Danby used the nominally second order backward difference scheme for stability, no stability issues were encountered as a result of solver choice in the 3D simulation.

6. Iteration complete. The total time is incremented by Δt, Eq. (3.67), and the process returns to step 2 until either the fill condition, having the highest particle remain above a certain height for a given number of time steps, or the probe having reached the maximum descent point, $<$ 15mm above the container base.

During probe indentation the neighbour grid methodology explained in stage 3 would require a very coarse grid with cell width equal to the probe size. This would reduce the number of cells in the domain and increase the number of neighbours in each neighbour list. This would result in many more interaction checks and a significantly slower solution speed. The 2D code used a hybrid grid system that contained larger cells around the probe, however, the grid itself needed to be regenerated every time step. It was found during the 3D development that a more efficient method than either the coarse or hybrid grid methods was to use the original grid and deliberately include the probe on every neighbour list.

The two most demanding processes in the enumerated algorithm above are the neighbour finding routine and the force calculation. There is a balance between these two processes in that a finer grid takes longer to process and produces more lists but the total number of collisions considered is smaller whereas for a coarse grid the neighbour lists are much quicker to generate but leads to more processing in the force calculation. Through profiling the code and trial and error an increase in grid cell width to $1.2r_{p,\max}$ gave a small improvement in iteration time.

C.5.2 2D test cases

The model parameters of the 2D particle simulations carried out by Danby are summarised in table C.2, where k_n and k_{coh} are the elastic and cohesive normal stiffness in Eq. (3.60) and 3.68 respectively, r_{coh} is the cohesive radius in Eq. (3.68) and N_p is the number of particles in the simulation.

Danby chose to simulate the experimental test cases with the two largest particle sizes because of the increase in time step and the reduction in the number of particles in the simulation, both reducing the cost of computation. The stiffness values were chosen to be

Case	Diameter D_p μm	Particle-particle k_n Nm^{-1}	k_{coh} Nm^{-1}	Particle-wall k_n Nm^{-1}	k_{coh} Nm^{-1}	r_{coh} r	Friction Forces	N_P	Restitution coefficient e
1	400–600	0.5	0	1.0	0	n/a	No	1590	0.2
2	400–600	1.0	0	2.0	0	n/a	No	1380	0.2
3	400–600	0.5	-0.05	1.0	-0.1	1.1	No	1590	0.2
4	400–600	1.0	-0.1	2.0	-0.2	1.1	No	1425	0.2
5	300–400	0.5	0	1.0	0	n/a	No	2961	0.2
6	300–400	1.0	0	2.0	0	n/a	No	2688	0.2
7	400–600	0.5	0	1.0	0	n/a	Yes	1545	0.2
8	400–600	1.0	0	2.0	0	n/a	Yes	1380	0.2

Table C.2: DEM parameters used by Danby and Shrimpton [7].

artificially low as is common practice in DEM in order to reduce the time step to feasible computation times, it was shown by Langston *et al*. [194] that altering the stiffness could still produce acceptable results. Damping was chosen to be artificially high to reduce rebound and speed up particle settling with the justification that the damping force contributed only slightly in the quasi-static force regime for the probe indentation. The other parameters were chosen for comparison to consider the effects of including cohesion or friction models on the indentation profiles.

Danby used a friction model and resolved the particle angular velocity and angular momentum in the 2D simulations. Danby solved the friction force described in Eq. (3.66) and resolved the particle rotation using the angular momentum expression, Eq. (3.75). Danby used a friction coefficient of $\mu = 0.7$ and a tangential to normal stiffness coefficient of $k_t/k_n = 1/5$, these same values have been used in the frictional cases of the 3D simulations performed here. In 2 of the cases in the 3D simulations performed in this work friction was used but only in addition to the rectilinear forces, no rotation was solved due to encounters with stability issues when expanding the rotational calculations to 3D.

Danby conducted extensive validations including particle-wall and particle-particle collisions and the effect of changing time-step resolution. The collisions provided satisfactory results. The change in time step resolution gave a curious result: for a small system of particles the final positions were compared for varying time resolutions, it was found that no consistent convergence was achieved for the final positions of particles by increasing the time resolution.

C.5.3 2D results

The force on the probe in the 2D simulations performed by Danby is presented in Fig. C.7 comparable with Fig. C.2. Danby highlights several differences between his experiments and his 2D simulations:

1. The magnitude of the forces in the 2D simulations are 2 orders of magnitude less than those in the experiments.
2. The exponent of the mean force curve, p, for all the 2D cases was $p \simeq 0.7$ but the equivalent experimental cases for this particle size gave values of $1.4 < p < 2.0$. The 2D numerical cases used sizes of $400 - 600\mu$m but p was similar to the experimental cases with particle sizes of $0 - 50\mu$m.
3. The smaller particles in Cases 5 and 6 result in a slightly reduced value of p but the reduction is less significant than seen in the experimental results for the same particle sizes.

Each model choice used 2 stiffness values; comparing Case 1 with 2, 3 with 4 etc. it is clear that increasing the stiffness increased the amplitude of the fluctuations. The smaller particles in

Cases 5 and 6 produced very small fluctuations compared with the larger particles in Cases 1 and 2. Cases 7 and 8 were identical to cases 1 and 2 but included a friction model, Eq. (3.66), however there was large scale change in behaviour. The addition of rotation added an extra degree of freedom to the particles, Danby expected this to effect the way particles rearranged but there was no evidence of this in the results.

Spectral results

The 2D simulated force traces from Danby were reprocessed here to find the spectral profile, Fig. C.8. The method used was identical to that used to process the experimental spectral results presented in Fig. C.3 in Section C.4.2. All of the cases behave in a similar manner. The power is concentrated in the larger length scales and all profiles have a decay rate, γ, similar to each other. There is a distinctive sawtooth wave throughout the results in Fig. C.7 but most noticeable in case 4, sawtooth curves are observed in the experimental results, Fig. C.2 but not as distinctive. A 'kink' in the spectral curves is obvious in all the 2D results, Fig. C.8, corresponding to a distance of $0.05 - 0.1D_p$. Danby expected the smaller particles, in Cases 5 and 6, to have more power located in the small length scales compared the other cases but this did not occur, even the length scale of the 'kink' was unaffected in the results with the smaller particles. Stiffness, however, seems to have a consistent effect on the 'kink' across all cases, the larger stiffness of Cases 2, 4, 6 & 8 shifted the 'kink' to slightly smaller lengths.

The frictional cases, 7 and 8, had an increased response amongst the the smallest length scales compared to the smooth cases, Danby speculates this is a result of a numerical instability related to the friction force calculation, Eq. (3.66) and the angular momentum calculation, Eq. (3.75).

Danby speculated that the restricted motion of a 2D system and the dramatically reduced particle stiffness are the main cause of discrepancy between the results. The trends of the experimental results were, however, recreated in the 2D model. Danby was able to draw the following conclusions from the 2D probe work:

- The number of degrees of freedom in the 2D simulation makes it less easy for a particle to slip past its neighbour when under stress.
- The number of *critical contacts* is likely to be responsible for reducing the force exponent of Eq. (C.2), p. *Critical contacts* are contacts between particles that will slip if they are loaded any more. Adding cohesion slightly reduces the value of p, whilst not changing the packing structure it is speculated that it encourages *critical contacts* in the force network.
- The spectral results of the simulations are similar to the experiments showing the clear dominance of high length scales and similar rates of decay, γ as the length scale decreases.
- The peaks in the spectral curves are in the vicinity of $l \simeq D_p$ indicating that the probe slipping past particles dominates the force trace. Danby suggests that the dominant frequencies are not caused simply by particles sliding past the probe but rather a more complex scenario involving extended force networks of multiple particles. Given that the numerical simulation is free of machine noise this explanation accounts for the presence of power in other length scales.

C.5.4 3D test cases

The findings of the 2D study along with the computational restrictions were considered when choosing which 3D cases to model:

- 2D Cases 1 and 2, Table C.2, were chosen to be modelled as base cases as they were in the 2D simulations, the equivalent 3D cases are designated 'A' and 'B'.

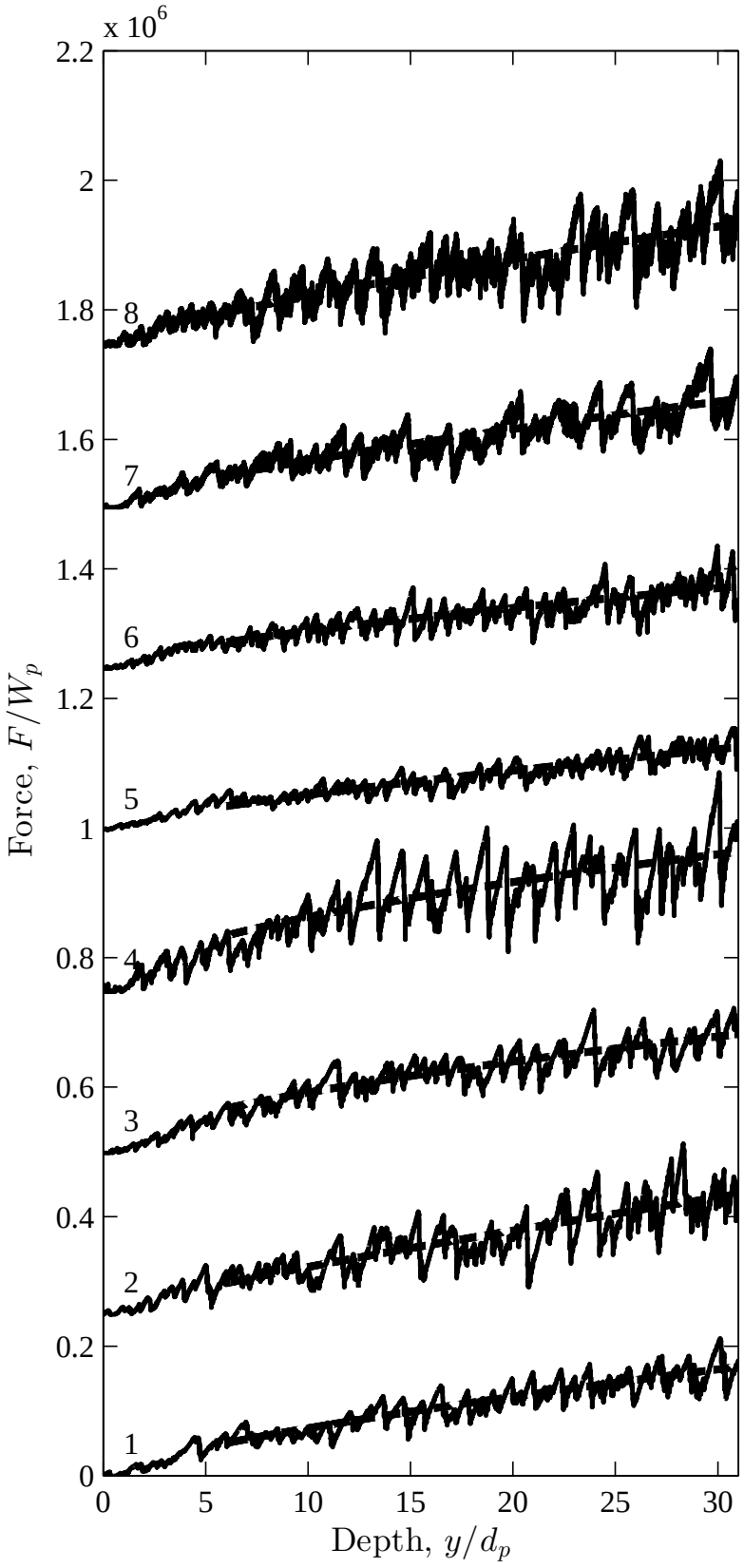

Figure C.7: The resistive force on the probe during indentation for the 2D simulations performed by Danby [6]. Results are incrementally offset by $+0.4/W_p$ and labelled with case numbers from Table C.2.

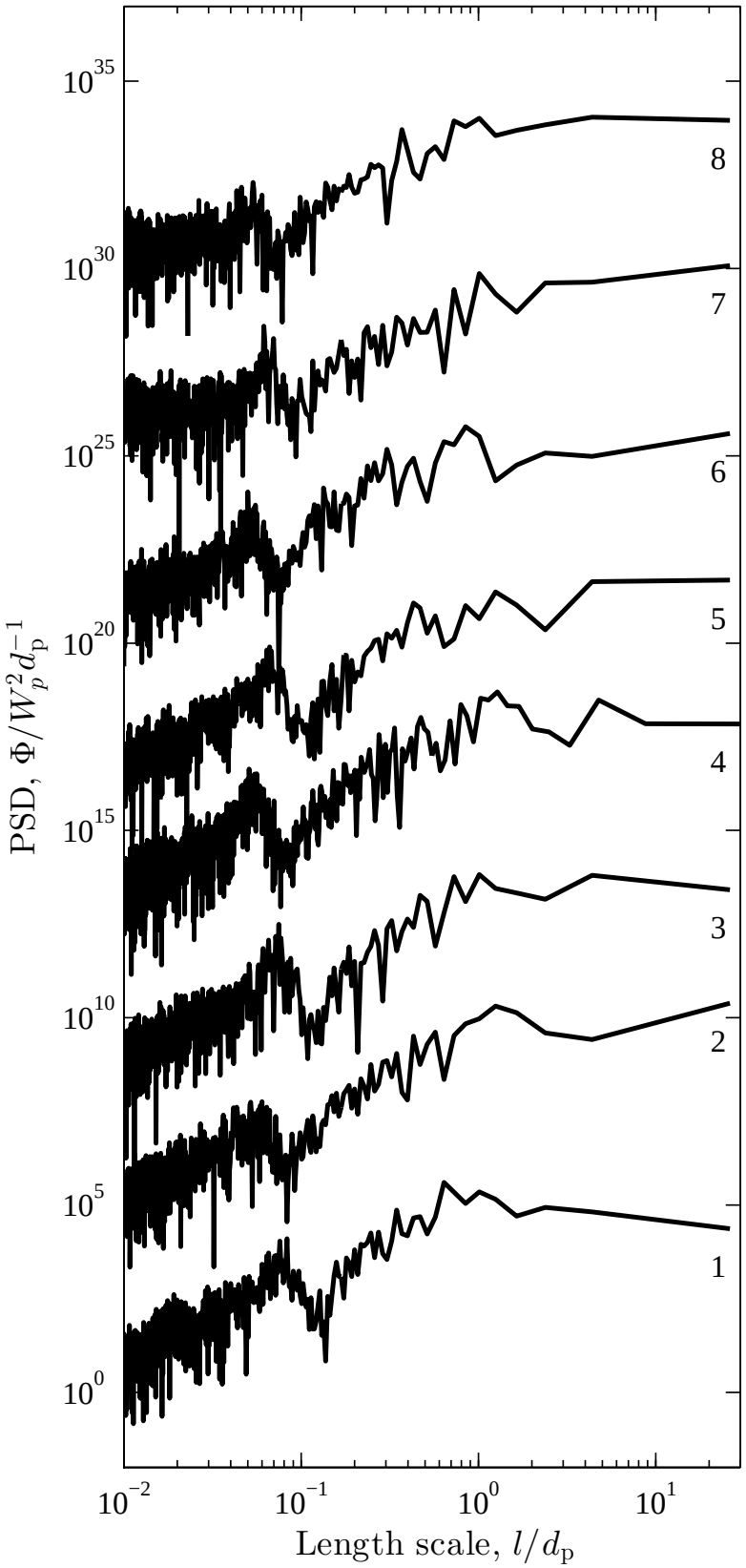

Figure C.8: Spectral power of the 2D results by Danby [6]. Results are incrementally offset by $\times 10^4$ and labelled with case numbers from Table C.2. Reproduced using raw data from [6].

- Smaller particles of Cases 5 and 6, Table C.2, require a smaller time step and also many more particles are required to fill the container, this would increase the runtime past feasibility in 3D. Danby noted no significant differences in the results with smaller particles. Cases 5 and 6 will not be modelled in 3D.

- Danby speculated that cohesion would reduce packing density by inhibiting the natural tendency of particles to minimise their gravitational potential, in the experimental work Danby associated the packing density with the *local* and *whole-scale* rearrangement behaviours. Friction should have a similar effect and so reduce packing density. Danby noticed that the numerical cases with tangential forces, Cases 7 and 8, exhibited different behaviour in the low length scale range, though the source may have been numerical instability. Danby included rotation in Cases 7 and 8 but found change as a result. In the 2D cases friction did not alter the exponent but with the additional degree of freedom offered in the 3D simulations the behaviour may change. Tangential forces will be included in the 3D study by solving Eq. (3.66), but in the 3D cases no rotation was included as Danby observed no effect of including rotation. Cases with friction are prefixed with the letter 'F', smooth cases have no tangential forces and are prefixed with 'S'.

- Danby concluded that the cohesive forces have a small effect on the particle packing structure and slightly reduce the mean force exponent, p, discussed further in section C.5.5, but overall cohesion had little effect on the results. For these reasons cohesive cases were not modelled in the 3D simulations.

- As observed in Fig. C.7 all of the simulations by Danby resulted in mean force trends with an exponent $p < 1$, Eq. (C.2), contrasting the experimental data, Fig. C.2, showing $p \simeq 2$. The linear force model was used in all of Danby's simulations to model the repulsion force between interacting particles, Eq. (3.60). The Hertzian model is an alternative non-linear force model, the rate of force increases with overlap, Eq. (3.63). The Hertzian model was considered in half the 3D cases, 'H' designates a case that used the Hertzian model and 'L' indicates the linear model was used.

Initial findings from Cases A and B showed a clear increase in the exponent value, p, when the stiffness increased. Danby discusses the reduction of stiffness as a possible source of discrepancy in the DEM, to test this a further 2 stiffness values $k = 2.0$ and $k = 4.0$ designated 'C' and 'D'. The wall stiffnesses had to be greatly increased to handle the weight of the particles especially during the injection process, the wall stiffness was scaled with the particle stiffness consistently in each case. A new test matrix was designed with 4 stiffness values, 2 frictional cases using the lower stiffnesses and all replicated with the Hertzian force model, the exact parameters are given in Table C.3. The restitution coefficient was greatly reduced for the 3D simulations as this aided convergence during the filling process.

C.5.5 3D Results

Filling process

The particles were injected into the top of the domain at a constant rate, of particles per second, with a uniform random position but constrained to ensure they were not initiated in contact with other particles. The particles fell under gravity and settled at the bottom of the container. Fluidic drag was also introduced to the simulation, for the injection process only, to provide a terminal velocity to the falling particles, using drag reduced rebound occurrences and aided

Case	Diameter D_p μm	Particle-particle k_n Nm^{-1}	Particle-wall k_n Nm^{-1}	Normal model Eq. (3.60) 3.63	Tangential Forces Eq. (3.66)	N_P	Restitution coefficient e	Packing density ρ_{pack}
SLA	400–600	0.5	12.0	Linear	No	42762	0.0001	86%
SLB	400–600	1.0	24.0	Linear	No	36813	0.0001	74%
SLC	400–600	2.0	48.0	Linear	No	32667	0.0001	66%
SLD	400–600	4.0	96.0	Linear	No	31582	0.0001	64%
FLA	400–600	0.5	12.0	Linear	Yes	40490	0.0001	82%
FLB	400–600	1.0	24.0	Linear	Yes	34184	0.0001	69%
SHA	400–600	0.5	12.0	Hertzian	No	39438	0.0001	80%
SHB	400–600	1.0	24.0	Hertzian	No	35926	0.0001	73%
SHC	400–600	2.0	48.0	Hertzian	No	32707	0.0001	66%
SHD	400–600	4.0	96.0	Hertzian	No	31221	0.0001	63%
FHA	400–600	0.5	12.0	Hertzian	Yes	36118	0.0001	73%
FHB	400–600	1.0	24.0	Hertzian	Yes	31294	0.0001	63%

Table C.3: DEM parameter matrix for 3D simulations.

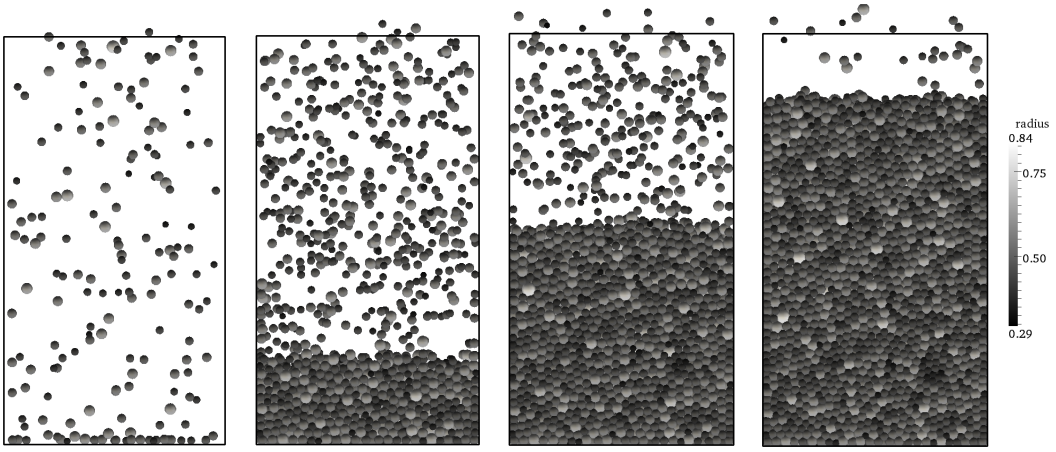

(a) 3% (b) 20% (c) 60% (d) 90%

Figure C.9: Particle filling process for Case A. Particles coloured by radius, r_p. Only 20% of particles are shown for clarity.

particle settling. The drag was calculated for a particle moving through a frozen air flow using Eq. (3.82) assuming $u_{\mathrm{rel}} = u_p$. This pouring process allowed structures that are dependent on the physical properties of the particles to develop freely. These structures may contain voids, force-chains or other arrangements that could be critical to the force experienced by the probe. The sparse pouring process also mimicked the experimental procedure.

The filling process is shown in Fig. C.9, this injection method avoids the vertical oscillation and instability that can occur if a large mass of particles all collide with the particle bed simultaneously. As more particles are introduced the compute time for each iteration increased, the filling process took several days of compute time, much longer for the stiffer frictional cases, FLB and FHB.

Table C.3 lists the packing density for each case, $\rho_{\mathrm{pack}} = \frac{4N_p\pi r_p^3}{3V_{\mathrm{box}}}$, where V_{box} is the total volume of the container. DEM is based on the soft sphere methodology, the repulsive forces between 2 particles in contact are based on the overlap, δ_n as in Eq. (3.61). As stiffness increased the overlap decreased and the packing density reduced. Friction reduced particle rearrangement and created more voids between particles evident in the reduced packing density. The experimental packing density was 61% indicating that using higher stiffnesses and the friction model causes the simulation to approach the experimental packing density.

Probe speed

The probe in the experiments by Danby moved at V_{exp} =0.05, 0.1 and 0.5mm s^{-1} and no dependence on speed was found. In the 2D simulations by Danby the probe speed was $V_{probe} = 0.5$mm s^{-1} but no other speeds were tested. Ideally this would have been the probe speed in the 3D cases, however, the run time required for the probe to complete the necessary number of time steps which that speed required was several months or even a year for the stiffer cases. Cases SLA and SLB were tested with several faster probe speeds, the slowest being $20V_{exp}$. Case SLB has twice the stiffness of Case SLA. The results of these different speeds are shown in Fig. C.10a and C.10b, it can be seen that the results all show similar behaviour with the magnitude of the curves reducing with speed. It is curious that the simulation should demonstrate a dependence on speed when the experiments did not. The speeds tested in Fig. C.10a are all very high, it is possible that at lower speeds the results are independent of speed but there is no indication of that from the results here.

Using the mean force fitting method, Eq. (C.2) in Section C.4.2, the exponent, p, and coefficient, a, of the force profiles in Fig. C.10a and C.10b was found. Figure C.11 shows how speed effected a and p. Both Case SLA and SLB approached the experimental result for a. The larger stiffness of Case SLB produced larger values of p than in Case SLA but both cases failed to reach experimental values of p at the lowest speeds and gave no indication of reaching it even at $V_{probe} = V_{exp}$. The speed of $V_{probe} = 20V_{exp}$ was chosen for the 3D simulation as it was both obtainable computationally and was closest to the presumed results at the experimental probe speed, V_{exp}. This speed is well below the fluidisation velocity.

Force-depth

The 3D numerical results of the Linear and Hertzian models are presented in Fig. C.12 and C.13, the results are offset for clarity but all start at zero force. There is a clear trend and strong fluctuations are present in the force profile, the dominant fluctuation being a sawtooth shaped signal present in all the numerical results. In all cases the amplitude of the fluctuations increases with depth, as in the experiments.

The same fitting method used in the experimental results, Eq. (C.2) in Section C.4.2, was used to find the mean force coefficient, a, and exponent, p, of the 3D force results. For each case the analytical expression for the mean force was found. As the bed surface is of varying configuration only the results from the probe completely immersed are considered. The values of a and p are given in Table C.4.

The purpose of running simulations in 3D was to better match the trends of the experimental results. Table C.4 demonstrates that moving from 2D to 3D increases the value of a by an order of magnitude but exponent, p, is unaffected; these effect minimal changes in the qualitative results. Using the Hertzian model instead of the linear model did not change p with any significance. Stiffness did not have a consistent effect on p or a but overall an increase in stiffness seemed to increase the force magnitude. Friction appeared to have a large influence and brought the exponent over the unity threshold such that the rate of probe resistance was increasing with depth, the values of a and p were still smaller than those found in the experiments but the behaviour of the frictional cases now shares several qualitative characteristics with the experimental results.

Spectral response

In the unsteady simulation of a physical process, such as the one presented in this chapter, the frequency of fluctuations can be attributed to the time scales of events in the simulation. In this

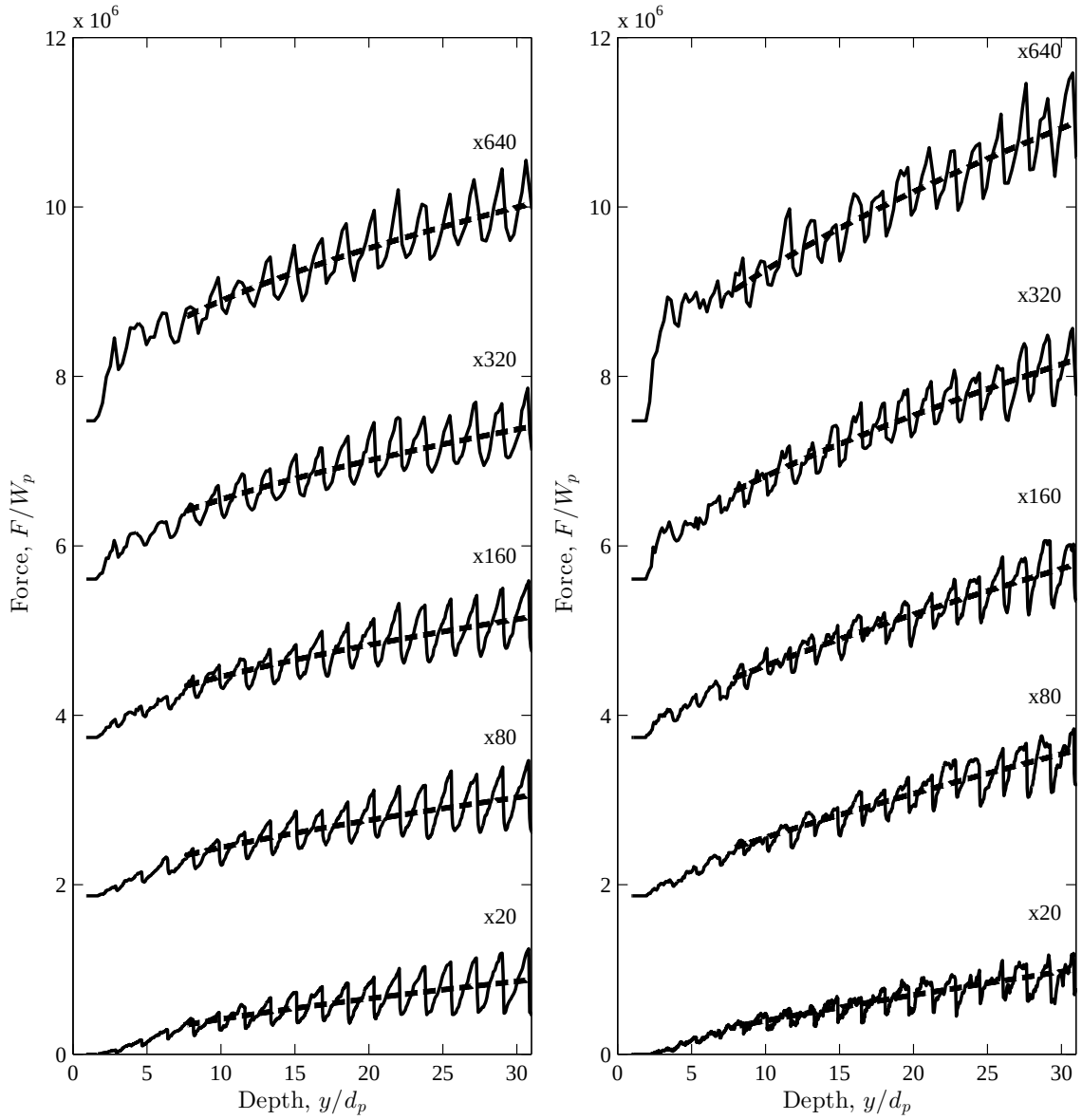

(a) Case A

(b) Case B

Figure C.10: Force profile results for 3D Cases SLA and SLB, Table C.3, labelled by multiples of experimental probe speed, V_{exp}. Case B has double the stiffness of Case A, both cases are smooth and use the linear force model.

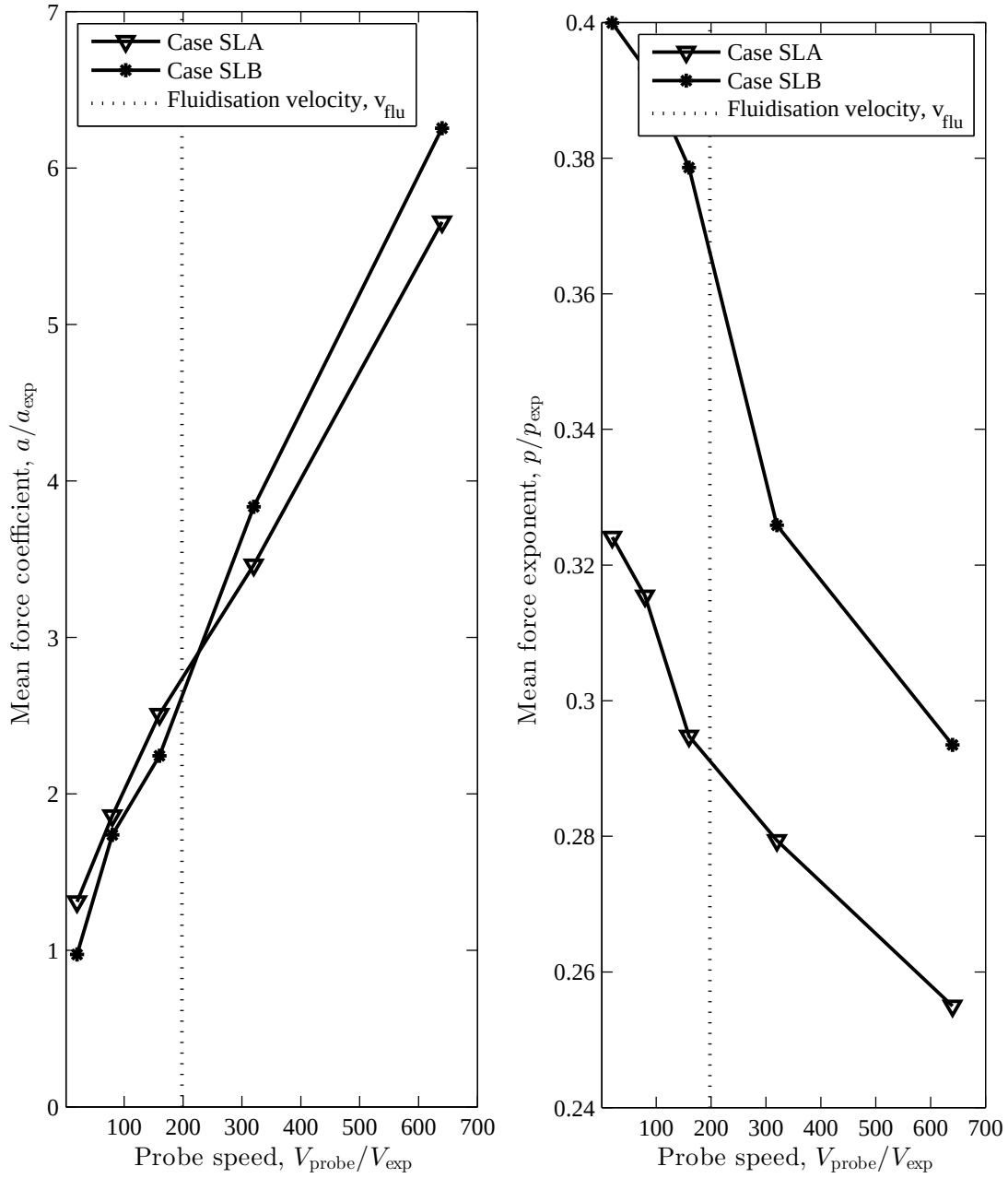

(a) Variation of coefficient a with simulated probe speed (b) Variation of exponent p with simulated probe speed.

Figure C.11: 3D cases A and B, Table C.3. Variation of mean force coefficient, a, and exponent, p of Eq. (C.2), with simulated probe speed nondimensionalised by the experimental values. Case B has double the stiffness of Case A.

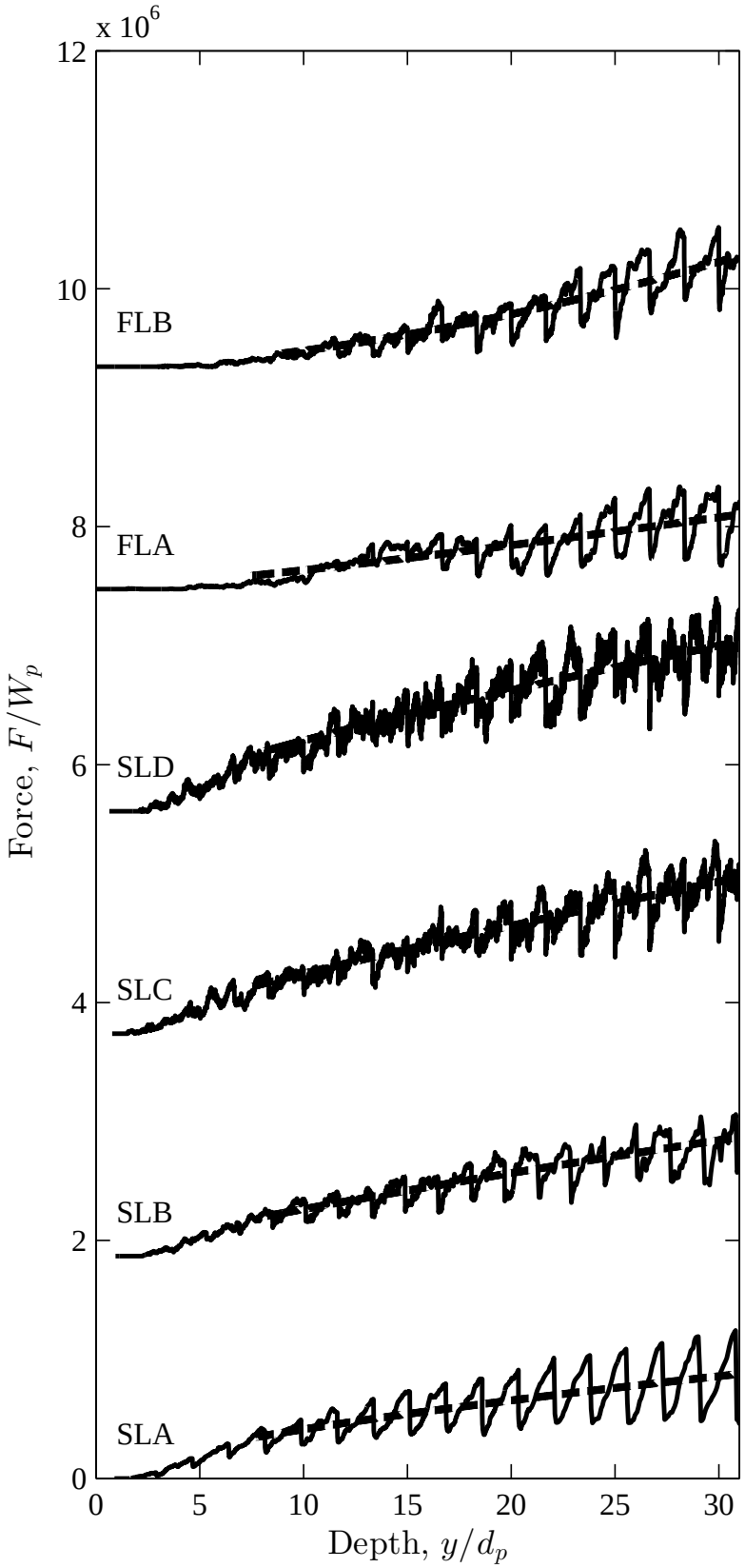

Figure C.12: Probe force during indentation – 3D Linear cases. Results labelled from Table C.3 and offset for clarity.

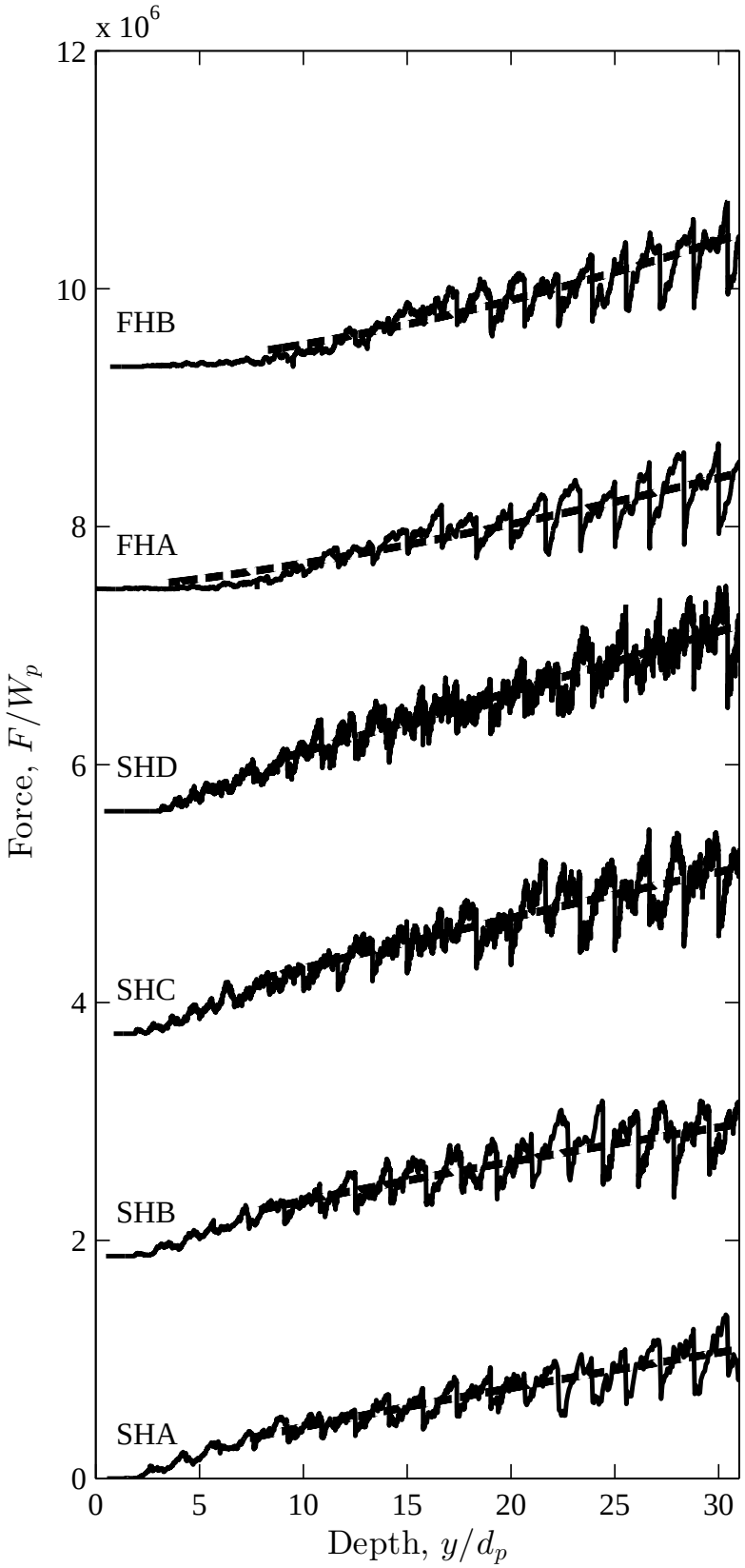

Figure C.13: Probe force during indentation – 3D Hertzian cases. Results labelled from Table C.3 and offset for clarity.

case	a	p	V_{probe}
SLA	0.226	0.667	$20V_{\text{exp}}$
SLB	0.195	0.868	$20V_{\text{exp}}$
SLC	0.207	0.847	$20V_{\text{exp}}$
SLD	0.274	0.776	$20V_{\text{exp}}$
FLA	0.0359	1.22	$20V_{\text{exp}}$
FLB	0.0138	1.71	$20V_{\text{exp}}$
SHA	0.186	0.816	$20V_{\text{exp}}$
SHB	0.216	0.770	$20V_{\text{exp}}$
SHC	0.234	0.825	$20V_{\text{exp}}$
SHD	0.157	1.01	$20V_{\text{exp}}$
FHA	0.0404	1.33	$20V_{\text{exp}}$
FHB	0.0312	1.47	$20V_{\text{exp}}$
Experimental (average of 5 runs)	0.0420	2.06	V_{exp}
2D (case 1: equivalent to SLA)	0.0361	0.734	V_{exp}
2D (case 2: equivalent to SLB)	0.0312	0.823	V_{exp}

Table C.4: Coefficient and exponent of the mean force expression, Eq. (C.2), and the probe speed.

case a probe diameter of $D_{\text{probe}} = 3$mm is being driven through a bed of particles of $D_p = 400 - 600\mu$m at a fixed velocity, V_{probe}.

Danby ran the 2D simulations with $V_{\text{probe}} = V_{\text{exp}}$ therefore the spectral results could be acquired in the frequency domain using time as the independent variable and then directly compared with the experimental results. Danby first separated the fluctuating signal from the mean by subtracting the mean force expression from the force recorded, Eq. (C.2), using values of a and p found from curve fitting. Danby applied a Hanning window to cut down on periodic anomalies and then processed the signal with a Fast Fourier Transform (FFT) to convert the signal into spectral space, using Matlab (2009). Danby performed the same procedure on the 2D simulations and the experimental results, frequency results were reported in units of Hz with PSD in units of N^2/Hz.

In this study we wish to compare the results of simulations and experiments with different probe speeds, time can not be used as the independent variable but the indentation depth is constant throughout simulation and experiment allowing depth, y, to be the independent variable. Using length instead of time results in wavenumber when converted to spectral space by the FFT process. Wavenumber has units of inverse length, the inverse of the wavenumber gives the length scale associated with that fluctuation. Table C.1 lists the physical length scales present in the simulations and experiments.

In similar manner to Danby, the dominant length scales in the force trace were found by separating the fluctuating signal, F', from the mean, $\bar{F}$. A Blackman-Harris window was applied to the signal before processing to reduce periodicity anomalies, as it has superior performance, [195], though no noticeable differences between the results of the Hanning and Blackman-Harris windows were seen. An FFT was used to convert the signal to spectral space using Matlab (2011a), the output of the FFT was multiplied by the complex conjugate of the output to produce the Power Spectral Density (PSD), Ψ. The PSD has units of N^2mm and wavenumber has units of mm^{-1}, the spectral plots were nondimensionalised using $W_p^2 D_p$, where W_p is average particle weight; wavenumber is nondimensionalised with particle diameter, d_p^{-1}. The wave number value was inverted to present results in terms of length scale, l, in units of D_p.

The spectral results of the 3D cases are given in Fig. C.14, curves are offset and every 5^{th} point is plotted for clarity. Figure C.14 can be directly compared with the earlier experimental

result shown in Fig. C.3 and the 2D results in Fig. C.8. The dominant peaks are all in the higher length scale region, results displayed are several orders below the Nyquist frequency.

Both linear, Fig. C.14a, and Hertzian, Fig. C.14b, models produce similar results. The majority of the power is located in the large length scales and the power decays rapidly as l decreases. The Hertzian cases show a 'knee' in the smaller values of l around which the gradient of the PSD profile changes, the length scale of the 'knee' that separates these two regions is $10^{-2} < l < 10^{-1}$ and can be seen to decrease with increasing stiffness. Linear cases SLB and FLA and FLB also display this behaviour. Danby found observed a 'knee' in the experimental results around which the gradient changed this has been highlighted here in Fig. C.5, the feature seen in these 3D results is very similar to the experimental results. Danby also found a very distinctive 'kink' in the 2D results which also shifted with stiffness, Fig. C.8, though there was no change in gradient the feature exists in the same range of length scales.

Expanding on the approach by Danby the spectral results are additionally presented with a linear vertical axis. Figure C.15 looks more closely at the dominant length scales around $l = D_p$. Here the results are comparable to the experimental results in Fig. C.4. The numerical results produce very similar spectral profiles to each other, indicating that the dominant rearrangement length scales are independent of stiffness, normal and frictional force models. In all these plots a family of peaks is clearly visible; this family are the harmonics associated with sawtooth shaped waves. A pure sawtooth wave in the spectral domain has its largest peak as the wave frequency and a set of harmonics identifiable as integer multiples of the principle frequency with amplitudes reducing exponentially with a decay value of $\gamma = -2$, spectral analysis of a pure sawtooth is illustrated in Appendix D for comparison. The pure sawtooth wave produces the same basic shape as the experimental – Fig. C.3, 2D – Fig. C.8 and 3D – Fig. C.14 spectral results. If a physical process, such as a particle slipping past the probe, creates a sawtooth wave then only the length that produces the principle peak carries meaning, the other peaks are produced by the FFT process as they build the triangular waveform but have no physical meaning. The length scale associated with the triangular signal appears to be invariant to the parameters chosen, consistently $l \simeq 1.5D_p$, the harmonic peaks are present as a series of smaller peaks as l decreases.

It would appear that in most cases the single sawtooth peak dominates the spectral response, in addition a closer look at Fig. C.12 and C.13 tells us that we should expect sub dominant length scales much smaller than the sawtooth length, however their amplitude is low and difficult to distinguish in Fig. C.14 but they may be related to the 'knee' feature. The peak values present in the 3D results, Fig. C.15, and the experimental, C.4, are similar to those predicted in Table C.1 more notably the middle range of particle-particle length scales. The sawtooth wave seems to have a length scale slightly larger than the particle diameter, this could be due to particles being carried by the probe before they slip and so extending the wavelength. This explanation would also account for the very large amplitude in the force fluctuations if the particles that are carried build up a lot of force before they slip.

The experimental results in Fig. C.4 indicate activity is concentrated across a narrow range of high length scales from $1 < l < 10D_p$ with several peaks at $\simeq 1.5$, $\simeq 2 \simeq 3.5$ and $4D_p$. The distinctive sign of a sawtooth family of peaks is not as clear as in Fig. C.15 but the peak length scale values match. These values, allowing some deviation, are what we expected based on the physical length scales in Table C.1 and the peak at $l \simeq 1.5D_p$ is the same value produced by the numerical simulations.

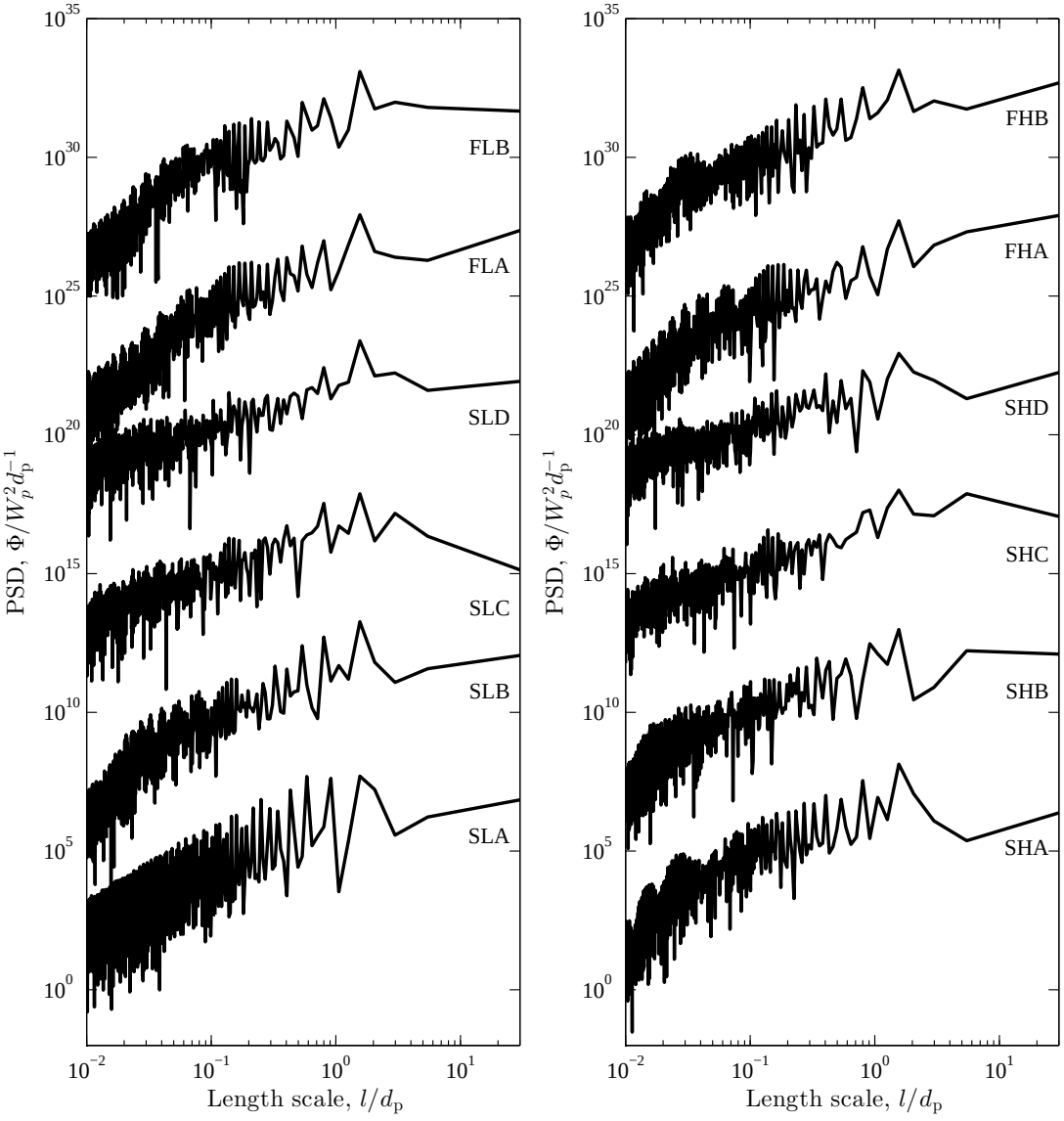

(a) Linear; curves are offset by 10^5

(b) Hertzian; curves are offset by 10^5

Figure C.14: Spectral profiles of the 3D numeric simulations. Length scale has been nondimensionalised by particle diameter, D_p, power has been nondimensionalised by $W_p^2 d_p^{-1}$. Every 5$^{\text{th}}$ point is plotted for clarity and curve offsets are indicated in their individual captions. Curves labelled by case as in Table C.3.

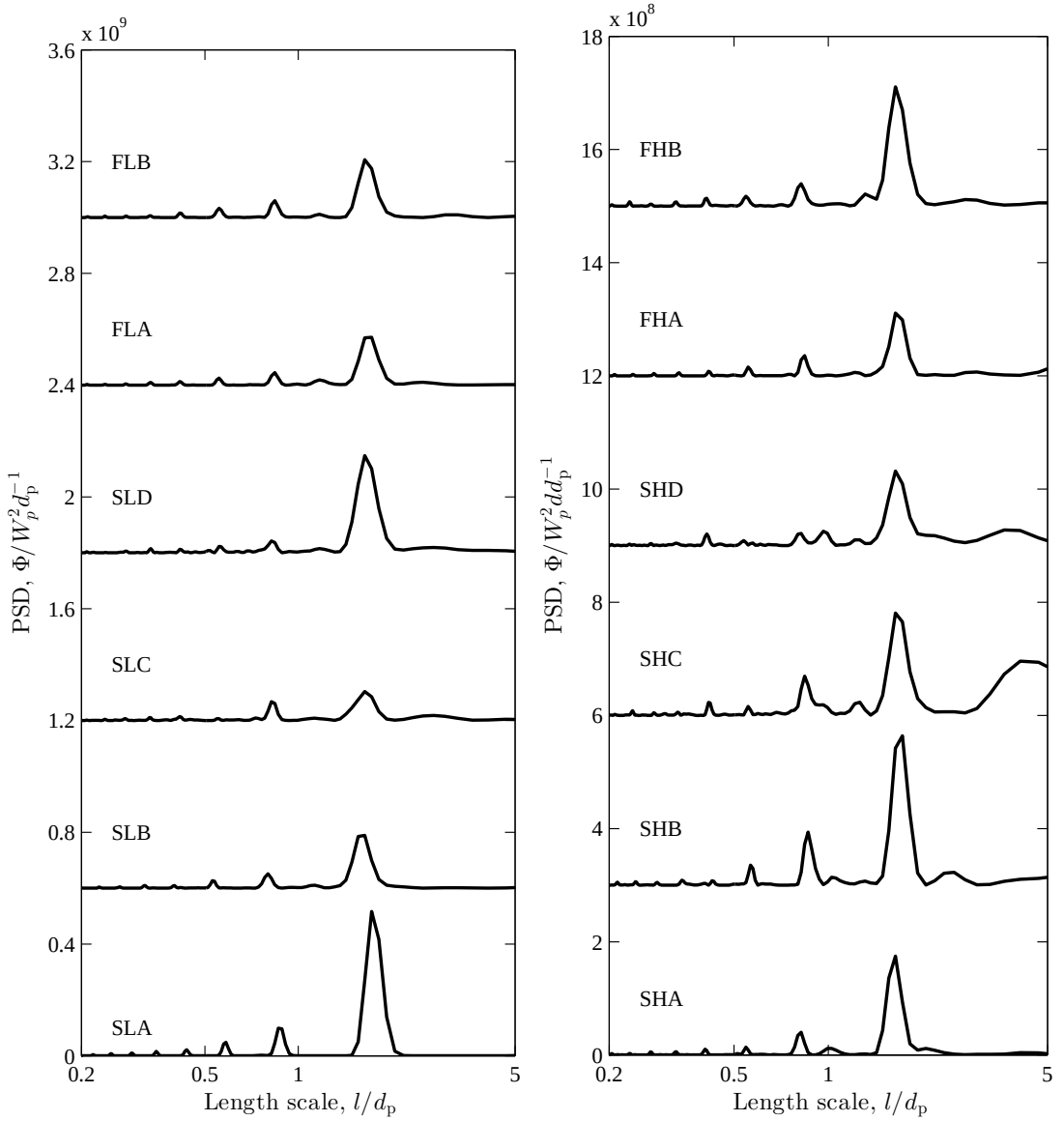

(a) Linear; curves are offset by 6×10^8

(b) Hertzian; curves are offset by 3×10^8

Figure C.15: Spectral profiles of the 3D numeric simulations plotted with linear Y-axis and log X-axis to indicate length scales associated with peak force fluctuations. Length scale, l has been nondimensionalised by particle diameter, D_p, power, Φ, has been nondimensionalised by $W_p^2 d_p^{-1}$. Every 5$^{\text{th}}$ point is plotted for clarity and curve offsets are indicated in their individual captions. Curves labelled by case as in Table C.3.

C.6 Discussion

C.6.1 *Whole-scale* and *local* rearrangements

The experimental results of Danby showed that the mean force for smaller particles exhibited an exponent value of $p < 1$, while larger particles have $p > 2$, Fig. C.1. Danby offered in explanation of the behaviour of small particles: they rearrange easily and the force chains are small because cohesion gives rise to a higher void fraction allowing the small particles to rearrange by moving into the those voids. Conversely *whole-scale* rearrangement involves a far reaching network of particles that are affected by the probe. A low exponent, $p < 1$, implies a localised rearrangement of particles who react to the probe by moving into voids in the packing structure. The 2D numeric results of Danby also offered a low exponent value with and without cohesion. Since the DEM uses the soft sphere methodology and the stiffnesses are low compared with reality the particles can pass each other easily and may accommodate the volume of the probe by simply overlapping more with neighbouring particles, increasing δ_n in Eq. (3.61), analogous to the void filling *local* rearrangement speculated by Danby. Increasing the stiffness should extend the range of particles that are required to rearrange and make it more difficult for particles to slip past each other, this is seen to some extent through increases in a and p in Table C.4 for the increase of stiffness in the 3D simulations.

Danby suspected sawtooth signals are associated with sudden stress releases present in a tightly packed bed within which rearrangements are difficult and this is typical of larger particles with low cohesion-weight ratio as these are shown to have a lower void fraction [6]. The 3D simulations performed here consisted of large particles, tightly packed in the smooth case as seen by the value of ρ_{pack} in Table C.3, and the sawtooth response behaviour was strongly present. However, the packing density, ρ_{pack}, reported in Table C.3 decreased while p, reported in Table C.4, increased. The soft particles will have a higher packing density because they overlap more, due to the ratio of weight to stiffness, $W_p/(k_n\delta_n)$, meaning the packing density in the simulations is not a reliable metric for predicting rearrangement behaviour. Above an explanation of the mean force exponent value, p, speculated that the extremely soft particles used in the simulations were capable of *local* rearrangements by overlapping in much the same way as a particles move to occupy voids in a powder with a high void content. It would appear then that ease of *local* rearrangement has a large influence over the value of p.

In all the numerical simulations, both the 2D Danby simulations and the 3D simulations performed here, the magnitudes of the forces on the probe were significantly smaller than the experiments, the reduced stiffness, k_n, is responsible. Spectral results showed that despite using different probe speeds the numerical results attribute the force fluctuations to similar peak length scales seen in the experimental data and a similar power distribution across the length scales is also seen. However, due to the reduced force magnitudes the PSD magnitudes are also several orders of magnitude too small to reproduce the exact results.

C.6.2 Particle force visualisation

Figures C.16 and C.17 show particle positions shaded by compressive force, $k_n\delta_n$, for 3D Cases SLC and FLB respectively, dark particles have a low stress and pale particles are highly stressed. The stress due to the weight of the particles is clearly shown by a multitude of dark particles toward the top and pale particles near the bottom. Many particles showing much less stress due to the packing configuration are seen as isolated dark coloured particles. No obvious structures are apparent in the bed and none develop during the probe descent, an immediate few particles in contact with the probe have a higher stress and this could be a clue to the distinctive sawtooth pattern. If only a very small number of particles are taking the majority of the force from the

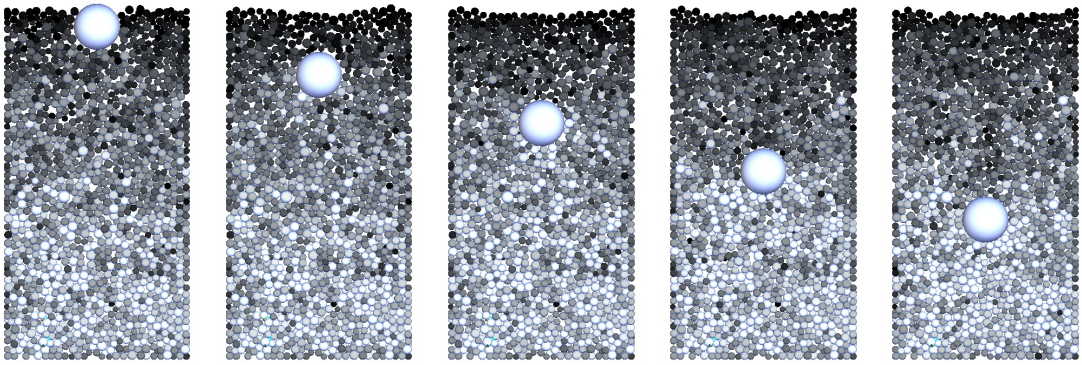

(a) 0% (b) 25% (c) 50% (d) 75% (e) 100%

Figure C.16: Probe progress during indentation case SLC. Particles shaded by normal force, $k_n\delta_n$, paler particles are experiencing greater force than dark particles.

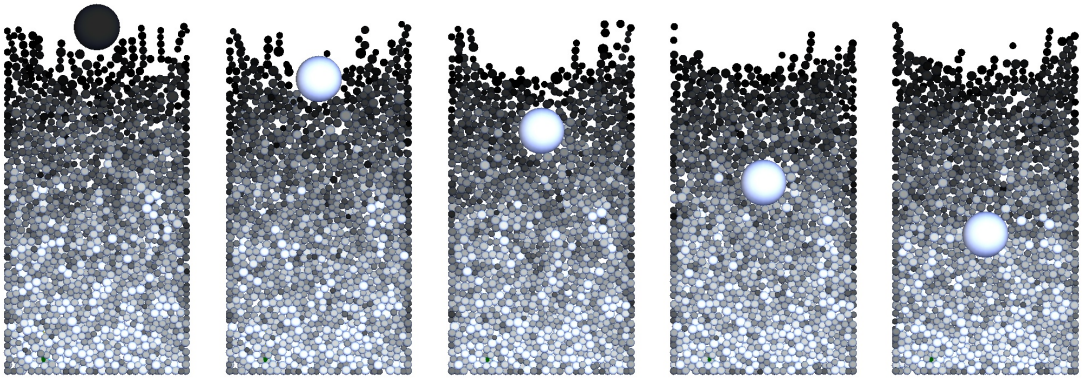

(a) 0% (b) 25% (c) 50% (d) 75% (e) 100%

Figure C.17: Probe progress during indentation case FLB. Particles shaded by normal force, $k_n\delta_n$, paler particles are experiencing greater force than dark particles.

probe then each rearrangement of those few particles would cause a large disruption in the force trace. In summary there are two behavioural features observed in Fig. C.16 and C.17: the probe resistance is caused by only a few particles and the force is distributed locally. The larger particle size would cause fewer particles to be in contact with the probe and so promote the sawtooth effect, this is visible in the experimental results of Danby discussed in Section C.4.2, where large particles give rise to large γ, indicating the the larger particles have a greater sawtooth influence on the spectral results.

The Figures of particle compression, Fig. C.16 and C.17, suggest that any near-probe particle has a small cluster of dependants and together these hold a lot of force, when a particle slips passed the probe the combined stress on the probe drops – but no large force chain was involved, though from the view point of probe the effect is the same. This explanation is corroborated by the spectral results that give a dominant length scale of slightly larger than D_p because the particles are transported a short distance while a large force builds up. Evidence of this concept would be visible as clusters or force chains of particles with similar compressive force but consisting of only a few particles rather than a structure spanning the whole bed. There appears to be a higher range of overlap present in the smooth case, C.16, this is to be expected as the friction should help share the load, but the cluster phenomenon is difficult to see.

The frictional cases showed a different behaviour, the exponent is large, $p > 1$, emulating the behaviour seen by the experiments. But if we look at Fig. C.17 there are no more force chains to be found than in the smooth case, Fig. C.16. Where does the higher exponent value come from then? If we recall the original explanation offered by Danby of *local* and *whole-scale* rearrangement we realise that strong force networks are not a necessity of this explanation. Instead the *whole-scale* structure could be simply be farther reaching interactions diffused amongst the whole bed. This is shown as a general increase in the magnitude of resistance in the force traces, Fig.C.12. In the particle visualisation Fig. C.17 the particle forces seems to be more uniform than in the smooth case of Fig. C.16 indicating a more widely distributed force in the friction case.

C.6.3 Spectral analysis

There are many peaks in the 3D spectral results from Section C.5.5, the strongest ones are easy to see on the linear scale, but the log scale exposes the many components of smaller amplitude. The experiments are subject to noise, but the numerical results which also look noisy are exact, where do these many small length scale results come from? These many low amplitude fluctuations over a large range of l are all a result of particle force changes carried through the bed to the probe. A sudden change in force in a particle results in a displacement causing force changes in all contacting particles, this force travels like a wave through contacting particles back to the probe. Damping in the fundamental equations, and indirect paths from the packing structure will inhibit this information from reaching the probe. Small length scales indicate short duration contacts, and the low power of these events indicate low stresses or distance from the probe. Looking at Figs. C.16 and C.17 the stress amongst particles seems to be unrelated to distance from the probe, therefore the fluctuations are likely to be small.

The most likely explanation of the slope of the spectral results, γ reported in Section C.4.2, is that the sawtooth shaped signal has a strong influence but is not the only contribution to the PSD. The experiments by Danby show that small particles produce a much shallower decay slope, $\gamma \simeq 0.4$, and the large particles have a much steeper decay slope, $\gamma \simeq 1.5$. We have already described that large particles having a more dominant sawtooth, therefore it follows that the sawtooth contribution is increased in the larger particle cases agreeing with the *whole scale* rearrangement notion. The other contributing signal could be a smoother interaction process with slow changes in forces between particles rather than the violent build up and slip behaviour, as seen in the small D_p cases of the experiments by Danby.

C.6.4 3D-2D comparison

The original aim of expanding the simulation to 3 dimensions was to attempt to recreate the behaviour seen in the experiments. Danby speculated that using only 2 dimensions was a key factor in the differences between his 2D simulations and his experimental results. However, the results of the 3D simulations performed here were remarkably similar to the 2D simulations in all but the frictional cases. The parameters of the 3D Cases SLA and SLB were identical to the 2D Cases 1 and 2 in all but the number of dimensions and the results are very similar: the exponents of the mean force are similar and the spectral results indicate similar length scales. It would appear that simply expanding the model to 3 dimensions had no impact. However, friction was modelled by Danby in the 2D Cases 7 and 8, Danby found that friction made no significant difference to the behaviour, as seen in Fig. C.7; but including friction in the 3D simulation, Cases FLA FLB FHA & FHB shown in Fig. C.12 C.12, had a large impact the exponent, p. The exponent was now greater than unity indicating behaviour similar to the experimental results of Danby.

C.7 Conclusions

DEM simulations can be significantly altered by choice of parameters and models. In this chapter a physical process operating in the mesoscale was simulated using a variety of parameters and models to find those that best match the experimental results in both spectral and absolute terms. The physical process investigated was a fixed velocity probe indentation into a particle bed. The work builds on the study by Danby [6] who produced the experimental results used here and created a 2D simulation code that was adapted to 3D in this work. Expanding on the knowledge acquired by Danby these new 3D simulations compared the Hertzian and Linear normal force models, the merits of including friction and the effect of different stiffness values. Computational restrictions prevented these simulations from running with the correct probe speed, instead several speeds were simulated. The results were found to be strongly dependent on speed – as speeds approached the experimental conditions the results moved closer to the experimental result but were not predicted to match entirely. A computationally affordable speed of $20V_{\text{probe}}$ was used. From the result presented above the following conclusions were drawn;

- The practice of reducing the stiffness of particles in DEM simulations prevents the force magnitudes from being matched and therefore the PSD in the spectral results.
- In the experimental results of Danby the force recorded gave a mean with exponent $p > 1$, Section C.4.2. The 2D results of Danby gave $p < 1$, Section C.5.3. Expanding the system to 3 dimensions did not change this, using a Hertzian force model did not change this, increasing the stiffness may have increased the exponent slightly but the use of a friction model gave a mean force exponent of $p > 1$ the closest match to the trend of the experimental data, Section C.5.5.
- The numerical results, 2D and 3D, contain a strong sawtooth signal that is less obvious in the experimental data though is argued to exist, Section C.5.5. This dynamic behaviour indicates the same length scales as in the experimental results. The length scales associated with the particle rearrangement are quantitatively reproduced and are very similar to the physical length scales in the experiments with $l \simeq D_p$. The distribution of power across other length scales in the simulated results qualitatively matches the experimental results indicating that broader particle rearrangements across the domain contribute to the probe force in a similar fashion to the experiments.

Is the DEM suitable for simulating the probe indentation method? The exact results could not be recreated using the DEM, however, the spectral results were a good match. The 3D frictional case matched the trends of the experiments but reproducing the force values will always be a challenge using the DEM due to the computational restrictions using standard hardware.

Is the DEM suitable for modelling the sand bed in a brownout inception model? The distribution of power in the 3D spectral results matches the experimental results of Danby. This indicates that the particle rearrangements across the particle population is reacting appropriately to the movement of the probe and therefore would be capable of reacting appropriately to the forced motion of surface particles in an entrainment simulation.

Appendix D

Frequency Analysis of Sawtooth Waves

Sawtooth waves contain multiple sine or cosine waves to make up their shape. The Fast Fourier Transform (FFT) finds those waves but since they are part of the same sawtooth it is desirable to be able to identify those components with are part of the single sawtooth wave and other unique frequencies that maybe present in the signal. Figure D.1 shows a sawtooth signal. It is good practice to use a window when processing FFTs to avoid the singularity of periodicity, fig. D.2, is the signal after a Blackman-Harris window has been applied. Applying the FFT and plotting the results on log axis gives the result in fig. D.3, the principle frequency is visible at 10 Hz but there is a large family of other responses decaying with the higher frequencies. If instead we plot the FFT result on linear axis the picture is suddenly very clear, fig. D.4 shows the principle frequency and a family of peaks decaying with increasing frequency. The family of peaks is easy to identify because each subsequent peak is an integer multiple of the principle frequency, these lesser peaks are called harmonics and help build up the triangular shape.

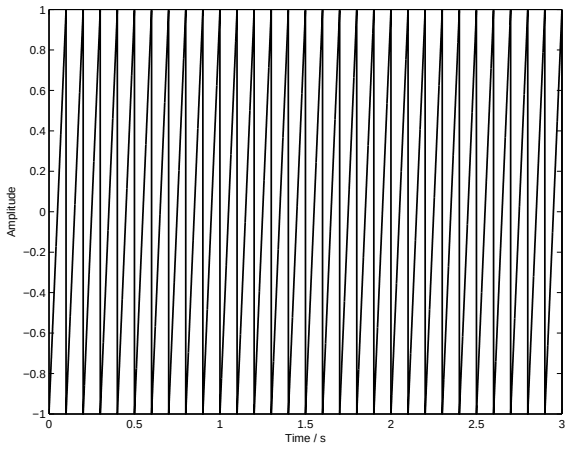

Figure D.1: A sawtooth signal

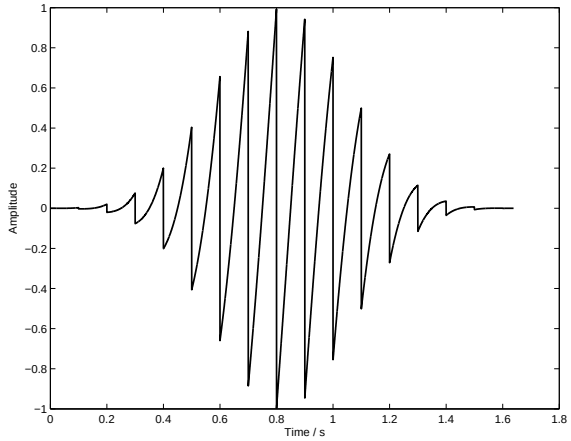

Figure D.2: A sawtooth signal with a BlackmanHarris window applied

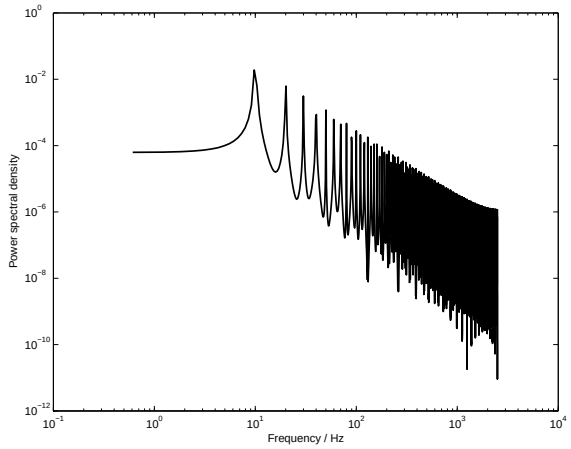

Figure D.3: The frequency response generated by an FFT on log-log axis

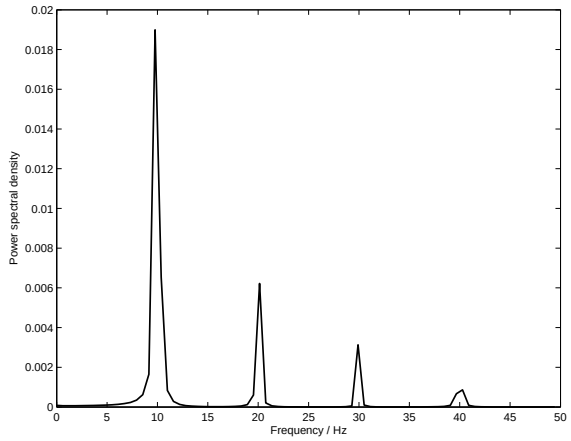

Figure D.4: The low frequency response generated by an FFT on linear axis

References

[1] G. Jasion, J.S. Shrimpton, M. Danby, and K. Takeda. Performance of numerical integrators on tangential motion of dem within implicit flow solvers. *Computers & Chemical Engineering*, 35(11):2218–2226, 2011.

[2] G. Jasion and J.S. Shrimpton. Prediction of brownout inception beneath a full-scale helicopter downwash. *Journal of the American Helicopter Society*, 57(4):1–13, 2012.

[3] G.T. Jasion, M. Danby, and J.S. Shrimpton. Suitability of parameters and models in the discrete element method for simulation of mesoscale powder indentation experiments. *Particle & Particle Systems Characterization*, accepted - pending reviewer corrections.

[4] R. Tuley, M. Danby, J.S. Shrimpton, and M. Palmer. On the optimal numerical time integration for lagrangian dem within implicit flow solvers. *Computers & Chemical Engineering*, 34(6):886–899, 2010.

[5] R.J. Tuley. *Modelling dry powder inhaler operation with the discrete element method*. PhD thesis, Imperial College London, UK, 2007.

[6] M. Danby. *Toward the Prediction of Agglomerate Behaviour in Dry Powder Inhaler Devices*. PhD thesis, University of Southampton, UK, 2010.

[7] M. Danby and J.S. Shrimpton. Probe indentation: A mesoscale approach to characterise powder systems: Experimental investigation of monomodel and bimodal diameter distributions of glass spheres. *Particle & Particle Systems Characterization*, 29(3):144–155, 2012.

[8] S. Colby. Military spin. *Aviation Today - Rotor & Wing*, 39, March 2005.

[9] L. Sabbagh. Flying blind in iraq: U.s. helicopters navigate real desert storms. *Popular Mechanics*, 3, October 2006.

[10] K. McNulty. Rotorcraft brownout science and technology update. *Air Force Research Laboratory*, 2008.

[11] R. Krantz. Concern network. *Air Medical Journal*, 21(6):6–6, 2002.

[12] Z. Cao. Turbulent bursting-based sediment entrainment function. *Journal of Hydraulic Engineering*, 123(3):233–236, 1997.

[13] M. Guingo and J. Minier. A new model for the simulation of particle resuspension by turbulent flows based on a stochastic description of wall roughness and adhesion forces. *Journal of Aerosol Science*, 39(11):957–973, 2008.

[14] M W Reeks, J Reed, and D Hall. On the resuspension of small particles by a turbulent flow. *Journal of Physics D: Applied Physics*, 21(4):574, 1988.

[15] H. T. Wang, Y. H. Zhou, Z. B. Dong, and M. Ayrault. Vertical dispersion of dust particles in a turbulent boundary layer. *Earth Surface Processes and Landforms*, 33(8):1210–1221, 2008.

[16] I. Eames and S. B. Dalziel. Dust resuspension by the flow around an impacting sphere. *J. Fluid Mechanics*, 403:305–328, 2000.

[17] R. A. Bagnold. *The Physics of blown sand and desert dunes. (2nd edition)*. London: Methuen & Company Limited, 1954.

[18] S. Kubota, K. Horikawa, and S. Hotta. Blown sand on beaches. In *Proceedings of the International Conference on Coastal Engineering*, volume 1, 2011.

[19] D. A. Wachspress, G. R. Whitehouse, J. D. Keller, K. Yu, P. Gilmore, M. Dorsett, and K. McClure. A high-fidelity brownout model for real-time flight simulations and trainers. In *American Helicopter Society 65th Annual Forum, Grapevine, TX*, May 2009.

[20] J. D. Iversen, J. B. Pollack, R. Greeley, and B. R. White. Saltation threshold on mars: the effect of interparticle force, surface roughness, and low atmospheric density. *Icarus*, 29(3): 381–393, 1976.

[21] D. A. Wachspress. Physics based modeling of helicopter brownout for piloted simulation applications. *The Interservice/Industry Training, Simulation & Education Conference (I/ITSEC)*, 2008.

[22] G. W. Leese. Helicopter downwash blast effects study. *Defence documentation center, Dept. of Defence, USA*, 1964.

[23] S. J. Rodgers. Evaluation of the dust cloud generated by helictopter rotor downwash. *U. S. Army Aviation Material Laboratories*, 1968.

[24] P. Bradshaw and E.M. Love. *The normal impingement of a circular air jet on a flat surface*. HM Stationery Office, 1961.

[25] A. Morse and H. Newhouse. Vtol downwash impingement study surface erosion tests. Technical report, DTIC Document, 1960.

[26] R. B. Haehnel. *Physics of particle Entrainment under the influence of an impinging jet*. Ft. Belvoir : Defense Technical Information Center, 2008.

[27] T. E. Lee, J. G. Leishman, and M. Ramasamy. Fluid dynamics of interacting blade tip vortices with a ground plane. *Journal of the American Helicopter Society*, 55(2):022005, 2010.

[28] A. T. Conlisk. Modern helicopter rotor aerodynamics. *Progress in Aerospace Sciences*, 37(5): 419–476, 2001.

[29] A. J. Wadcock, L. A. Ewing, E. Solis, M. Potsdam, and G. Rajagopalan. Rotorcraft downwash flow field study to understand the aerodynamics of helicopter brownout. Technologies for the Next Generation of Vertical Lift Aircraft, 2008. American Helicopter Society.

[30] D. McNew. Eh101 dust landing. online, May 2011. http://www.life.com/image/92776677.

[31] J. Kenny. Cfd to generalise flight simulation of rotorcraft-environment interactions. Master's thesis, University of Southampton, School of Engineering Sciences, 2008.

[32] M. C. Thompson, K. Hourigan, A. Cheung, and T. Leweke. Hydrodynamics of a particle impact on a wall. *Applied Mathematical Modelling*, 30(11):1356–1369, 2006. Selected papers from the Third International Conference on CFD in the Minerals and Process Industries - 3rd International Conference on CFD.

[33] M. Tsubokura, T. Kobayashi, N. Taniguchi, and W. P. Jones. A numerical study on the eddy structures of impinging jets excited at the inlet. *International Journal of Heat and Fluid Flow*, 24(4):500–511, 2003. Selected Papers from the Fifth International Conference on Engineering Turbulence Modelling and Measurements.

[34] T. Leweke, L. Schouveiler, M.C. Thompson, and K. Hourigan. Unsteady flow around impacting bluff bodies. *Journal of Fluids and Structures*, 24(8):1194–1203, 2008.

[35] N.D. Nathan and R.B. Green. The flow around a model helicopter main rotor in ground effect. *Experiments in Fluids*, 52:151–166, 2012. ISSN 0723-4864.

[36] M. Ramasamy and J.G. Leishman. The interdependence of straining and viscous diffusion effects on vorticity in rotor flow fields. In *Annual forum proceedings — American Helicopter Society*, volume 59, pages 1787–1801, 2003.

[37] S.E. Widnall. The stability of a helical vortex filament. *Journal of Fluid Mechanics*, 54(04): 641–663, 1972.

[38] J. N. Sørensen, I. V. Naumov, and V. L. Okulov. Multiple helical modes of vortex breakdown. *Journal of Fluid Mechanics*, 683:430, 2011.

[39] Bradley Johnson, J. Gordon Leishman, and Anish Sydney. Investigation of sediment entrainment in brownout using high-speed particle image velocimetry. In *65th Annual Forum of the American Helicopter Society*, Grapevine, TX, May 2009.

[40] J.A. Gillies, V. Etyemezian, H. Kuhns, J.D. McAlpine, J. King, S. Uppapalli, G. Nikolich, and J. Engelbrecht. Dust emissions created by low-level rotary-winged aircraft flight over desert surfaces. *Atmospheric Environment*, 44(8):1043–1053, 2010.

[41] C. Cowherd. Sandblaster 2 support of see-through technologies for particulate brownout. *DARPA Task 5 Technical Report*, MRI Project No. 110565, 2007.

[42] C. Phillips and R. E. Brown. Eulerian simulation of the fluid dynamics of helicopter brownout. *Journal of Aircraft*, 46(4):1416–1429, 2009.

[43] A. D'Andrea and F. Scorcelletti. Enhanced numerical simulations of helicopter landing maneuvers in brownout conditions. In *66th Annual Forum of the American Helicopter Society*, Phoenix, AZ, May 2010.

[44] M. Syal, B. Govindarajan, and J. G. Leishman. Mesoscale sediment tracking methodology to analyze brownout cloud developments. In *66th Annual Forum of the American Helicopter Society*, Phoenix, AZ, May 2010.

[45] Sebastian Thomas, Tarandeep Kalra, and James Baeder. A hybrid cfd methodology to model the two-phase flowfield beneath a hovering laboratory scale rotor. In *AIAA Summer Conference*, June 2012.

[46] Y. Shao and H. Lu. A simple expression for wind erosion threshold friction velocity. *Journal of Geophysical Research*, 105:22437–22444, September 2000.

[47] H. Lu and Y. Shao. Toward quantitative prediction of dust storms: an integrated wind erosion modelling system and its applications. *Environmental Modelling & Software*, 16(3): 233–249, 2001.

[48] B. R. White. Soil transport by winds on mars. *Journal of Geophysical Research*, 84:4643–4651, 1979.

[49] B. O. Bauer, J. Yi, S. L. Namikas, and D. J. Sherman. Event detection and conditional averaging in unsteady aeolian systems. *Journal of Arid Environments*, 39(3):345–375, 1998.

[50] G. R. Butterfield. Transitional behaviour of saltation: wind tunnel observations of unsteady winds. *Journal of Arid Environments*, 39:377–394, 1998.

[51] P. Spies and I. K. McEwan. Equilibration of saltation. *Earth Surface Processes and Landforms*, 25(4):437–453, 2000.

[52] G. Sterk, A. F. G. Jacobs, and J. H. Van Boxel. The effect of turbulent flow structures on saltation sand transport in the atmospheric boundary layer. *Earth Surface Processes and Landforms*, 23:877–887, 1998.

[53] N. Ardey and F. Mayinger. Aerosol resuspension by highly transient containment flow : insights by means of laser optical methods. *Kerntechnik*, 63:68–75, 1998.

[54] C. Marchioli, V. Armenio, M. Vittoria S., and A. Soldati. Mechanisms for deposition and resuspension of heavy particles in turbulent flow over wavy interfaces. *Physics of Fluids*, 18 (2):025102, 2006.

[55] D. Hall. Measurements of the mean force on a particle near a boundary in turbulent flow. *Journal of Fluid Mechanics*, 187:451–466, 1988.

[56] A. M. Mollinger, F. T. M. Nieuwstadt, and J. M. Bessem. A new device to measure the lift force on a particle in the viscous sublayer. *Measurement Science and Technology*, 6(2): 206–213, 1995.

[57] G. Ziskind, M. Fichman, and C. Gutfinger. Adhesion moment model for estimating particle detachment from a surface. *Journal of Aerosol Science*, 28(4):623–634, 1997.

[58] A.H. Ibrahim, P.F. Dunn, and M.F. Qazi. Experiments and validation of a model for microparticle detachment from a surface by turbulent air flow. *Journal of Aerosol Science*, 39 (8):645–656, 2008.

[59] M. Soltani and G. Ahmadi. Direct numerical simulation of particle entrainment in turbulent channel flow. *Physics of Fluids (1994)*, 7(3):647–657, 1995.

[60] H. Schlichting, K. Gersten, E. Krause, and H. Oertel Jr. *Boundary-layer theory*. Physics and astronomy online library. Springer,, Berlin ; London :, 8th rev.& enl.ed. edition, 2000. ISBN 3540662707. English translation of the 9th German completely revised edition.

[61] S. B. Pope. *Turbulent flows*. Cambridge University Press, Cambridge, 1st edition, 2000. ISBN ISBN: 0521591252 (cased).

[62] T. Shih, W. W. Liou, A. Shabbir, Z. Yang, and J. Zhu. A new k-[epsilon] eddy viscosity model for high reynolds number turbulent flows. *Computers & Fluids*, 24(3):227–238, 1995.

[63] Brian Edward Launder and DB Spalding. The numerical computation of turbulent flows. *Computer methods in applied mechanics and engineering*, 3(2):269–289, 1974.

[64] S. Kim and D. Choudhury. A near-wall treatment using wall functions sensitized to pressure gradient. In *Proceedings of the ASME/JSME Fluids Engineering and Laser Anemometry Conference and Exhibition, Hilton Head, SC; UNITED STATES*, Separated and complex flows, pages 273–280, August 13-18 1995.

[65] Fluent. *Fluent 6.2 User Guide*. Fluent Inc., Centerra Resource Park, 10 Cavendish Court, Lebanon, NH 03766, USA, 2005.

[66] C. T. Crowe, J. A. Roberson, and D. Elgar. *Engineering Fluid Mechanics - 7th Edition*. Wiley, 2001. ISBN 0471384828.

[67] J. Boussinesq. *Application des potentiels à l'éetude de l'équilibre et du mouvement des solides élastiques : principalement au calcul des déformations et des pressions que produisent, dans ces solides, des efforts quelconques exercés sur une petite partie de leur surface ou de leur intérieur : mémoire suivi de notes étendues sur divers points de physique, mathematique et d'analyse*. Gauthier-Villars, Paris, 1885.

[68] A B.. Basset. *A Treatise on hydrodynamics with numerous examples*. Deighton, Bell and Co ; G. Bell and Sons, Cambridge; London, 1888.

[69] S. Poisson and N. L. Rousseau. *Nouvelle théorie de l'action capillaire*. Bachelier père et fils, Libraires pour les mathématiques, la physique, etc., quai des Augustins, no 55.„ Paris :, 1831. Printer: Ïmprimerie de Alfred Courcier, Rue du Jardinet, no 12.÷- T.p. verso.

[70] E. Michaelides. *Particles, bubbles & drops : their motion, heat and mass transfer*. Hackensack, N.J. : World Scientific, 2006. ISBN 9789812566485.

[71] L. Schiller and A. Neumann. Uber die grundlegenden berechungen bei der schwerkraftaufbereitung. *Vereines Deutscher Ingenieure*, 77:318–320, 1933.

[72] P. Bagchi and S. Balachandar. Effect of free rotation on the motion of a solid sphere in linear shear flow at moderate re. *Physics of Fluids*, 14(8):2719–2737, 2002.

[73] F. Odar and W. S. Hamilton. Forces on a sphere accelerating in a viscous fluid. *Journal of Fluid Mechanics*, 18(02):302–314, 1964.

[74] Y. Tsuji, T. Kawaguchi, and T. Tanaka. Discrete particle simulation of two-dimensional fluidized bed. *Powder Technology*, 77(1):79–87, 1993.

[75] M. W. Reeks and S. McKee. The dispersive effects of basset history forces on particle motion in a turbulent flow. *Physics of Fluids*, 27(7):1573–1582, 1984.

[76] A.J. Dorgan and E. Loth. Efficient calculation of the history force at finite reynolds numbers. *International Journal Multiphase Flow*, 33:833–848, 2007.

[77] F. Armenio. The importance of the forces acting on particles in turbulent flows. *Physics of Fluids*, 13:2437–2440, 2001.

[78] R. W. Johnson. *The handbook of fluid dynamics*. CRC Press,, Boca Raton, Fla. :, 1998. ISBN 0849325099. Fluid dynamics.

[79] B. Oesterlé and T.B. Dinh. Experiments on the lift of a spinning sphere in a range of intermediate reynolds numbers. *Experiments in Fluids*, 25(1):16–22, 1998.

[80] S. I. Rubinow and J. B. Keller. The transverse force on a spinning sphere moving in a viscous fluid. *Journal of Fluid Mechanics*, 11(03):447–459, 1961.

[81] S. Laín, M. Sommerfeld, and J. Kussin. Experimental studies and modelling of four-way coupling in particle-laden horizontal channel flow. *International Journal of Heat and Fluid Flow*, 23(5):647–656, 2002.

[82] S. C. R. Dennis, S. N. Singh, and D. B. Ingham. The steady flow due to a rotating sphere at low and moderate reynolds numbers. *Journal of Fluid Mechanics*, 101(2):257–279, 1980.

[83] C. T. Crowe. *Multiphase flow handbook*. Taylor & Francis/CRC Press, Boca Raton, FL, 2006. ISBN 0849312809.

[84] X. Zou, H. Cheng, C. Zhang, and Y. Zhao. Effects of the magnus and saffman forces on the saltation trajectories of sand grain. *Geomorphology*, 90(1-2):11–22, 2007.

[85] G. Green. Researches on the vibration of pendulums in fluid media. *Transactions of the Royal Society of Edinburgh*, III:54–62, 1836. reprinted in Mathematical Papers (Chelsea, New York, 1970).

[86] J. J. Derksen. Numerical simulation of solids suspension in a stirred tank. *AIChE Journal*, 49(11):2700–2714, 2003.

[87] X.-Q. Chen and J. C. F. Pereira. Computation of particle dispersion in turbulent liquid flows using an efficient lagrangian trajectory model. *International Journal for Numerical Methods in Fluids*, 26(3):345–364, 1998.

[88] M. Marquillie, J.-P. Laval, and R. Dolganov. Direct numerical simulation of a separated channel flow with a smooth profile. *Journal of Turbulence*, page N1, 2008.

[89] S. J. Scott, A. U. Karnik, and J. S. Shrimpton. On the quantification of preferential accumulation. *International Journal of Heat and Fluid Flow*, 30(4):789–795, 2009.

[90] S. Goto and J. C. Vassilicos. Sweep-stick mechanism of heavy particle clustering in fluid turbulence. *Phys. Rev. Lett.*, 100:054503, Feb 2008.

[91] A. M. Mollinger and F. T. M. Nieuwstadt. Measurement of the lift force on a particle fixed to the wall in the viscous sublayer of a fully developed turbulent boundary layer. *Journal of Fluid Mechanics*, 316:285–306, 1996.

[92] L. Zeng, F. Najjar, S. Balachandar, and P. Fischer. Forces on a finite-sized particle located close to a wall in a linear shear flow. *Physics of Fluids*, 21(3):033302, 2009.

[93] E. Rabinovich and H. Kalman. Incipient motion of individual particles in horizontal particle-fluid systems: A. experimental analysis. *Powder Technology*, 192(3):318–325, 2009.

[94] D. Leighton and A. Acrivos. The lift on a small sphere touching a plane in the presence of a simple shear flow. *Zeitschrift für Angewandte Mathematik und Physik (ZAMP)*, 36:174–178, 1985.

[95] P. G. Saffman. The lift on a small sphere in a slow shear flow. *Journal of Fluid Mechanics*, 22 (02):385–400, 1965.

[96] D. Leighton and A. Acrivos. Viscous resuspension. *Chemical Engineering Science*, 41(6): 1377–1384, 1986.

[97] B. V. Derjaguin, V. M. Muller, and Yu. P. Toporov. Effect of contact deformations on the adhesion of particles. *Journal of Colloid and Interface Science*, 53(2):314–326, 1975.

[98] K. L. Johnson, K. Kendall, and A. D. Roberts. Surface energy and the contact of elastic solids. *Proceedings of the Royal Society*, A324:301–313, 1971.

[99] D.S. Rimai and D.J. Quesnel. Particle adhesion. In M. Chaudhury and A.V. Pocius, editors, *Surfaces, Chemistry and Applications*, pages 139–191. Elsevier Science B.V., Amsterdam, 2002. ISBN 978-0-44-451140-9.

[100] P. Vainshtein, G. Ziskind, M. Fichman, and C.Gutfinger. Kinetic model of particle resuspension by drag force. *Physical Review Letters*, 78(3):551–554, 1997.

[101] J. N. Israelachvili. *Intermolecular and Surface Forces, 2nd Edition*. Academic Press, 1992. ISBN 978012391927.

[102] S. Eichenlaub, C. Chan, and S. P. Beaudoin. Hamaker constants in integrated circuit metalization. *Journal of Colloid and Interface Science*, 248(2):389–397, 2002.

[103] H. D. Ackler, R. H. French, and Y. Chiang. Comparisons of hamaker constants for ceramic systems with intervening vacuum or water: From force laws and physical properties. *Journal of Colloid and Interface Science*, 179(2):460–469, 1996.

[104] R. H. French, R. M. Cannon, L. K. DeNoyer, and Y. M. Chiang. Full spectral calculation of non-retarded hamaker constants for ceramic systems from interband transition strengths. *Solid State Ionics*, 75:13–33, 1995.

[105] D. Maugis. Adhesion of spheres: The jkr-dmt transition using a dugdale model. *Journal of Colloid and Interface Science*, 150(1):243–269, 1992.

[106] R. Jones, H. M. Pollock, D. Geldart, and A. Verlinden. Inter-particle forces in cohesive powders studied by afm: effects of relative humidity, particle size and wall adhesion. *Powder Technology*, 132(2-3):196–210, 2003.

[107] P.A. Cundall and O.D.L. Strack. A discrete numerical model for granular assemblies. *Geotechnique*, 29:47–65, 1979.

[108] T. J. Goda and F. Ebert. Three-dimensional discrete element simulations in hoppers and silos. *Powder Technology*, 158:58–68, 2005.

[109] S. Laín and M. Sommerfeld. Euler/lagrange computations of pneumatic conveying in a horizontal channel with different wall roughness. *Powder Technology*, 184(1):76–88, 2008.

[110] J.S. Marshall. Discrete-element modeling of particulate aerosol flows. *Journal of Computational Physics*, 228(5):1541–1561, 2009.

[111] Q. Zhang and E. Schmidt. Modelling of particle layer detachment - role of transient kinetic effects. *Particuology*, 7(1):45–51, 2009.

[112] N. Maw, J. R. Barber, and J. N. Fawcett. The oblique impact of spheres. *Wear*, 38(1): 101–114, 1976.

[113] H. Kruggel-Emden, M. Sturm, S. Wirtz, and V. Scherer. Selection of an appropriate time integration scheme for the discrete element method (dem). *Computers and Chemical Engineering*, 32(10):2263–2279, 2008.

[114] H. Kruggel-Emden, S.Wirtz, and V. Scherer. An analytical solution of different configurations of the linear viscoelastic normal and frictional-elastic tangential contact model. *Chemical Engineering Science*, 62(23):6914–6926, 2007.

[115] H. Kruggel-Emden, S.Wirtz, and V. Scherer. A study on tangential force laws applicable to the discrete element method (dem) for materials with viscoelastic or plastic behavior. *Chemical Engineering Science*, 63(6):1523–1541, 2008.

[116] R. Chandramohan and M.S. Powell. Measurement of particle interaction properties for incorporation in the discrete element method simulation. *Minerals Engineering*, 18(12): 1142–1151, 2005.

[117] M.M. Mollanouri Shamsi and A.A. Mirghasemi. Numerical simulation of 3d semi-real-shaped granular particle assembly. *Powder Technology*, 221(0):431–446, 2012. ISSN 0032-5910. <ce:title>Selected papers from 2010 AIChE Annual Meeting</ce:title>.

[118] J. Ai, J.F. Chen, J.M. Rotter, and J.Y. Ooi. Assessment of rolling resistance models in discrete element simulations. *Powder Technology*, 206(3):269–282, 2011.

[119] P. Prokopovich, S. Perni, *et al*. Multiasperity contact adhesion model for universal asperity height and radius of curvature distributions. *Langmuir*, 26(22):17028, 2010.

[120] B. Brogliato. *Nonsmooth mechanics : models, dynamics, and control*. Communications and control engineering. Springer, London, 2nd edition, 1999. ISBN 1852331437.

[121] P.W. Cleary and M.L. Sawley. Dem modelling of industrial granular flows: 3d case studies and the effect of particle shape on hopper discharge. *Applied Mathematical Modelling*, 26(2): 89–111, 2002.

[122] H. Hu. A multigrid navier-stokes cfd code for rotor computations. *Computer methods in applied mechanics and engineering*, 167(1):127–137, 1998.

[123] R.E. Brown and A.J. Line. Efficient high-resolution wake modeling using the vorticity transport equation. *AIAA journal*, 43(7):1434–1443, 2005.

[124] N. Hariharan and L.N. Sankar. A review of computational techniques for rotor wake modeling. In *38th AIAA Aerospace Sciences Meeting*, page 2000, Reno, NV, USA, Jan 2000.

[125] WJ McCroskey. Vortex wakes of rotorcraft. In *33rd Aerospace Sciences Meeting and Exhibit*, Reno, NV, USA, January 1995. American Institue of Aeronautics and Astronautics.

[126] B. Sanderse, SP Pijl, and B. Koren. Review of computational fluid dynamics for wind turbine wake aerodynamics. *Wind Energy*, 14(7):799–819, 2011.

[127] A. J. Landgrebe. The wake geometry of a hovering helicopter rotor and its influence on rotor performance. *Journal of the American Helicopter Society*, 17(4):3–15, 1972.

[128] D. A. Griffiths, S. Ananthan, and J. G. Leishman. Predictions of rotor performance in ground effect using a free-vortex wake model. *Journal of the American Helicopter Society*, 50 (4):302–314, 2005.

[129] R.E. Brown and G.R. Whitehouse. Modelling rotor wakes in ground effect. *Journal of the American Helicopter Society*, 49(3):238–249, 2004.

[130] D. Griffiths. A study of dual-rotor interference and ground effect using a free-vortex wake model. In *AHS International, 58 th Annual Forum Proceedings*, volume 1, pages 592–612, 2002.

[131] M.J. Bhagwat and J.G. Leishman. Time-accurate free-vortex wake model for dynamic rotor response. In *American Helicopter Society Specialist Meeting*, 2000.

[132] P. Li and R. Chen. Rotor unsteady aerodynamics model using an efficient free-vortex method. *Aircraft Engineering and Aerospace Technology*, 84(5):311–320, 2012.

[133] A. Bagai and JG Leishman. Rotor free-wake modeling using a pseudoimplicit relaxation algorithm. *Journal of aircraft*, 32(6):1276–1285, 1995.

[134] D. P. Pulla. *A study of helicopter aerodynamics in ground effect*. Ph. d. thesis, Ohio State University, 2006.

[135] J.S. Light. Tip vortex geometry of a hovering helicopter rotor in ground effect. *Journal of the American helicopter society*, 38(2):34–42, 1993.

[136] F.X. Caradonna and C. Tung. Experimental and analytical studies of a model helicopter rotor in hover. *Vertica*, 5(2):149–161, 1981.

[137] D.J. Lee and S.U. Na. Numerical simulations of wake structure generated by rotating blades using a time marching, free vortex blob method. *European Journal of Mechanics-B/Fluids*, 18(1):147–159, 1999.

[138] J. Steinhoff and D. Underhill. Modification of the euler equations for 'vorticity confinement': Application to the computation of interacting vortex rings. *Physics of Fluids*, 6:2738, 1994.

[139] C.B. Allen. Parallel simulation of unsteady hovering rotor wakes. *International journal for numerical methods in engineering*, 68(6):632–649, 2006.

[140] L. Xu and P. Weng. Rotor wake capture improvement based on high-order spatially accurate schemes and chimera grids. *Applied Mathematics and Mechanics*, 32(12):1565–1576, 2011.

[141] A. Wissink, M. Potsdam, V. Sankaran, J. Sitaraman, Z. Yang, and D. Mavriplis. A coupled unstructured-adaptive cartesian cfd approach for hover prediction. In *American Helicopter Society 66th Annual Forum*, 2010.

[142] T. Kalra, V. Lakshminarayan, J. Baeder, and S. Thomas. Methodological improvements for computational study of hovering micro-rotor in ground effect. In *Fluid Dynamics and Co-located Conferences*, pages –. American Institute of Aeronautics and Astronautics, June 2011.

[143] S. Thomas, S. Ananthan, and J. D. Baeder. Wake-coupling cfd-csd analysis of helicopter rotors in steady and maneuvering flight conditions. In *AHS Specialists' Conference on Aeromechanics*, San Francisco, CA, January 2010.

[144] OJ Boelens, VH van der, B. Oskam, and AA Hassan. Accurate and efficient vortex-capturing for a helicopter rotor in hover. In *EUROPEAN ROTORCRAFT FORUM*, volume 26, pages 51–51. Citeseer, 2000.

[145] Philips and Brown. The effect of helicopter configuration on the fluid dynamics of brownout. *34th European Rotorcraft Forum, UK*, 2008.

[146] J.N. Sørensen and C.W. Kock. A model for unsteady rotor aerodynamics. *Journal of wind engineering and industrial aerodynamics*, 58(3):259–275, 1995.

[147] R. Mikkelsen, J.N. Sørensen, S. Øye, and N. Troldborg. Analysis of power enhancement for a row of wind turbines using the actuator line technique. In *Journal of Physics: Conference Series*, volume 75, page 012044. IOP Publishing, 2007.

[148] R. Mikkelsen. *Actuator disc methods applied to wind turbines*. PhD thesis, Technical University of Denmark, 2003.

[149] N. Troldborg, J.N. Sørensen, and R. Mikkelsen. Actuator line simulation of wake of wind turbine operating in turbulent inflow. In *Journal of Physics: Conference Series*, volume 75, page 012063. IOP Publishing, 2007.

[150] N. Troldborg, J.N. Sorensen, and R. Mikkelsen. Numerical simulations of wake characteristics of a wind turbine in uniform inflow. *Wind Energy*, 13(1):86–99, 2010.

[151] C. S. Watters and C. Masson. Modeling of lifting-device aerodynamics using the actuator surface concept. *International journal for numerical methods in fluids*, 62(11):1264–1298, 2010.

[152] I. Dobrev, F. Massouh, and M. Rapin. Actuator surface hybrid model. In *Journal of Physics: Conference Series*, volume 75, page 012019. IOP Publishing, 2007.

[153] M. Biava, W. Khier, and L. Vigevano. Cfd prediction of air flow past a full helicopter configuration. *Aerospace Science and Technology*, 19(1):3–18, 2012.

[154] H Dumitrescu, V. Cardoş, A. Dumitrache, and F. Frunzulică. Vortex theory of the ideal wind turbine. *INCAS Bulletin*, 1(2):90–101, 2009.

[155] *ANSYS ® Fluent 12.0 Theory Guide*. Ansys Inc., April 2009.

[156] S. Ananthan, J. Gordon Leishman, and M. Ramasamy. The role of filament stretching in the free-vortex modelling of rotor wakes. In *58th Annual Forum and Technology Display of the American Helicopter Society*, Montreal, Canada, June 2002.

[157] PJ Roache. Perspective: a method for uniform reporting of grid refinement studies. *Journal of Fluids Engineering*, 116:405–405, 1994.

[158] L. F. Richardson. The approximate arithmetical solution by finite differences of physical problems involving differential equations, with an application to the stresses in a masonry dam. *Philosophical Transactions of the Royal Society of London. Series A, Containing Papers of a Mathematical or Physical Character*, 210(459–470):307–357, 1911.

[159] P.J. Roache. *Computational Fluid Dynamics. 1972*. Hermosa, Denver, Colorado, 1972.

[160] I. C. Cheeseman and W. E. Bennett. The effect of the ground on a helicopter rotor in forward flight. Reports and Memoranda 3021, Aeronautical Research Council, 1955.

[161] J.S. Hayden. The effect of the ground on helicopter hovering power required. In *32nd Annual Forum of the American Helicopter Society, Washington, DC*, pages 10–12, 1976.

[162] J.G. Leishman. *Principles of helicopter aerodynamics*. Cambridge University Press, 2006.

[163] A. Shields. Application of similarity principles and turbulence research to bed-load movement. mitt. preuss. versuchsanst. wasserbau schiffbau, berlin. In W.P. Ott, J.C. Uchelen, and W.M. Kech, editors, *Laboratory of Hydraulics and Water Resources*, number 167. California Institute of Technology, Pasadena, California (translators), 1936.

[164] N.D. Nathan and R.B. Green. Flow visualisation of the helicopter brown-out phenomenon. *Aeronautical Journal*, 113(1145):467–478, 2009.

[165] J. McAlpine, D. Koracin, D. Boyle, J. Gillies, and E. McDonald. Development of a rotorcraft dust-emission parameterization using a cfd model. *Environmental Fluid Mechanics*, 10: 691–710, 2010. 10.1007/s10652-010-9191-y.

[166] C. Phillips and R. E. Brown. Eulerian simulation of the fluid dynamics of helicopter brownout. In *64th American Helicopter Society Annual Forum*, 2008.

[167] J R Calvert and R A Farrar, editors. *An Engineering Data Book*. Palgrave, 1999. ISBN 0333516613.

[168] M. W. Reeks and D. Hall. Kinetic models for particle resuspension in turbulent flows: theory and measurement. *Journal of Aerosol Science*, 32(1):1–31, 2001.

[169] Sir Horace Lamb. *Hydrodynamics*. Cambridge University Press, 1932.

[170] H. B. Squires. The growth of a vortex in a turbulent flow. *Aeronautical Quarterly*, 16: 302–306, August 1965.

[171] Alexander Weigand and Morteza Gharib. On the decay of a turbulent vortex ring. *Physics of Fluids*, 6(12):3806–3808, 1994.

[172] H. XU, J. LU, and X. LIU. Non-uniform sediment incipient velocity. *International Journal of Sediment Research*, 23(1):69–75, 2008.

[173] J.C. Yang, Y. Zhang, D.Y. Liu, and X.L. Wei. CFD-DEM simulation of three-dimensional aeolian sand movement. *Science China Physics, Mechanics & Astronomy*, 53(7):1306–1318, 2010.

[174] L. Kang, L. Guo, and D. Liu. Reconstructing the vertical distribution of the aeolian saltation mass flux based on the probability distribution of lift-off velocity. *Geomorphology*, 96(1):1–15, 2008.

[175] L. Kang and X. Zou. Vertical distribution of wind–sand interaction forces in aeolian sand transport. *Geomorphology*, 125(3):361–373, 2011.

[176] John Heald, Ian McEwan, and Simon Tait. Sediment transport over a flat bed in a unidirectional flow: simulations and validation. *Philosophical Transactions A*, 362(1822): 1973, 2004.

[177] Mikio Sakai and Seiichi Koshizuka. Large-scale discrete element modeling in pneumatic conveying. *Chemical Engineering Science*, 64(3):533–539, 2009.

[178] J. J. Derksen and R. A. Larsen. Drag and lift forces on random assemblies of wall-attached spheres in low-reynolds-number shear flow. *Journal of Fluid Mechanics*, 673:548–573, 2011.

[179] Thomas G Drake and Joseph Calantoni. Discrete particle model for sheet flow sediment transport in the nearshore. *Journal of Geophysical Research: Oceans (1978–2012)*, 106(C9): 19859–19868, 2001.

[180] E. Rougier, A. Munjiza, and N. W. M. John. Numerical comparison of some explicit time integration schemes used in dem, fem/dem and molecular dynamics. *International Journal for Numerical Methods in Engineering*, 61:856–879, 2004.

[181] F. Y. Fraige and P. A. Langston. Integration schemes and damping algorithms in distinct element models. *Advanced Powder Technology*, 15:227–245, 2004.

[182] Y-h. Taguchi. New origin of a convective motion: Elastically induced convection in granular materials. *Physical Review Letters*, 69(9):1367–1370, Aug 1992.

[183] M. H. Sadd, Q. Tai, and A. Shukla. Contact law effects on wave propagation in particulate materials using distinct element modeling. *International Journal of Non-Linear Mechanics*, 28 (2):251–265, 1993.

[184] J.H. Ovesen, H.G. Petersen, and J.W. Perram. Comparison of two methods for solving linear equations occurring in molecular dynamics applications. *Computer Physics Communications*, 94:1–18, March 1996.

[185] S. Sundaram and L. R. Collins. Numerical considerations in simulating a turbulent suspension of finite-volume particles. *Journal of Computational Physics*, 124(2):337–350, 1996.

[186] F.P. Di Maio and A. Di Renzo. Analytical solution for the problem of frictional-elastic collisions of spherical particles using the linear model. *Chemical Engineering Science*, 59(16): 3461–3475, 2004.

[187] A. B. Yu and B. H. Xu. Particle-scale modelling of gas-solid flow in fluidisation. *Journal of Chemical Technology & Biotechnology*, 78(2-3):111–121, 2003.

[188] A. Samimi, A. Hassanpour, and M. Ghadiri. Single and bulk compressions of soft granules: Experimental study and dem evaluation. *Chemical Engineering Science*, 60(14): 3993–4004, 2005.

[189] J. Härtl and J.Y. Ooi. Numerical investigation of particle shape and particle friction on limiting bulk friction in direct shear tests and comparison with experiments. *Powder Technology*, 212(1):231–239, 2011.

[190] Y.C. Zhou, B.H. Xu, A.B. Yu, and P. Zulli. An experimental and numerical study of the angle of repose of coarse spheres. *Powder Technology*, 125(1):45–54, 2002.

[191] R. Albert, MA Pfeifer, A.L. Barabási, and P. Schiffer. Slow drag in a granular medium. *Physical Review Letters*, 82(1):205–208, 1999.

[192] G. Frenning, G. Alderborn, L.B. Kish, and D. Mahlin. Spectral analysis of force fluctuations during probe penetration into cohesive powders. *Powder Technology*, 187(1):62–67, 2008.

[193] L.J. Gibson and M.F. Ashby. *Cellular solids: structure and properties*. Cambridge university press, 1999. ISBN 0521495601.

[194] P.A. Langston, U. Tüzün, and D.M. Heyes. Discrete element simulation of granular flow in 2d and 3d hoppers: Dependence of discharge rate and wall stress on particle interactions. *Chemical Engineering Science*, 50(6):967–987, 1995.

[195] E.C. Ifeachor and B.W. Jervis. *Digital signal processing: a practical approach*. Pearson Education, 2002. ISBN 0201596199.